LUND UNIVERSITY

Radome Diagnostics: utilizing Source Reconstruction based on Surface Integral Representations

Persson, Kristin

2013

Radome Diagnostics: utilizing Source Reconstruction based on Surface Integral Representations

Kristin Persson

Doctoral Dissertation
Electromagnetic Theory

Lund University
Lund, Sweden
2013

Doctoral dissertation which, by due permission of the Faculty of Engineering at Lund University, will be publicly defended on June 14th, 2013, at 10.15 a.m. in lecture hall E:1406, Ole Römers väg 3, Lund, for the degree of Doctor of Philosophy in Engineering.

Department of Electrical and Information Technology
Electromagnetic Theory
Lund University
P.O. Box 118, S-221 00 Lund, Sweden

Series of licentiate and doctoral theses
No. 49
ISSN 1654-790X
ISBN 978-91-7473-523-9 (printed version)
ISBN 978-91-7473-524-6 (pdf)

Printed in Sweden by Tryckeriet i E-huset, Lund University, Lund.
May 2013

Till Elias och Michael.

June 18, 2013

Errata

Page		**Reads**	**Should read**
8	caption Fig. 7	a RNZAF	an RNZAF
8	caption Fig. 7	source: New Zealand Air Force	source: Royal New Zealand Air Force
25	Fig. 22	Known electric field	Known (measured) electric field
65	par. 2, line 2^-	summation limits N_m and N_p are	summation limit N_m is
66	par. 1, line 1	quadratic	square matrices
66	par. 1, line 7	orthogonal	unitary
84	par. 1, line 2^-	summation limits N_m and N_p are	summation limit N_m is
84	line 10^-	quadratic	square matrices
84	line 4^-	orthogonal	unitary
137	line 4	This can be corrected by probe compensation where the antenna aperture is mathematically translated to the center of rotation [12].	Sentence is deleted.
164	eq. (4.1)	$P_{\mathrm{n}}^{\mathrm{co}} + P_{\mathrm{n}}^{\mathrm{cross}}$	$P^{\mathrm{co}} + P^{\mathrm{cross}}$

Abstract

In this thesis, an inverse source reconstruction method with great potential in radome diagnostics is presented. A radome is a cover that encloses an antenna in order to protect it from environmental influences. Radome diagnostics are acquired in the design process, the delivery control, and in performance verification of repaired and newly developed radomes. A measured near or far field may indicate deviations, *e.g.*, beam deflection, but the origins of the flaws are not uncovered. In this thesis, radome diagnostics is performed by imaging the tangential electromagnetic fields on radome surfaces, disclosing the radome influence on the electromagnetic fields as well as the positions and influences of defects.

The source reconstruction is based on a surface integral representation together with the extinction theorem. The extinction theorem and its associated surface integral equation ensure that the reconstructed tangential electromagnetic fields have their sources within the radome. The presence of axial symmetry in the measurement set-up enables usage of the fast Fourier transform to reduce the computational complexity. Furthermore, the problem is solved by an in-house body of revolution method of moments (MoM) code utilizing a singular value decomposition (SVD) for regularization. The reconstruction is performed on a fictitious surface in free space, located precisely outside the physical surface of the radome, *i.e.*, no *a priori* information of the material of the radome is requested. Moreover, both synthetic and measured data are used to verify the method.

In Papers I-III, the measurement set-up is a reflector antenna covered by a monolithic radome, and the near field is measured on a cylindrical surface. The height of the radome corresponds to $29 - 43$ wavelengths in the frequency interval $8.0 - 12.0\,\text{GHz}$. The amplitude and phase of the tangential electromagnetic fields are reconstructed on the radome surface and the influence of the radome is investigated. Moreover, the alteration of the phase due to the transmission of the radome, the insertion phase delay (IPD), is imaged. Defects in the form of square copper patches, with an edge length corresponding to $1.6 - 2.4$ wavelengths in the considered frequency interval, are attached to the radome wall. These might serve as a model for *e.g.*, a lightning conductor or a Pitot tube. The attached patches alter the near field, and by applying source reconstruction, the disturbances of the patches are focused and detectable.

In Paper IV, the field is measured on a spherical sector in the far-field region at $10.0\,\text{GHz}$. Two set-ups with dielectric defects attached to the radome surface, are investigated. The aim is to investigate if variations in the electrical thickness of the radome wall can be detected. It is concluded that it is possible to discover dielectric patches of various edge sizes ($0.5 - 2.0$ wavelengths), and with the smallest thickness corresponding to a phase shift of a couple of degrees.

In Paper V, a frequency selective (FSS) radome corresponding to a height of 51 wavelengths at the frequency $9.35\,\text{GHz}$ is investigated. The electrical performance of an FSS radome depends on the periodic structure of the elements in the radome frame. The periodic structure of the investigated radome is disrupted by horizontal defects (vertical displacements of elements) and vertical defects (a col-

umn of missing elements). The far-field data is measured on a spherical sector, and the far-field data reveals that the radome changes the radiation properties. The tangential electromagnetic fields on the radome surface are reconstructed for several antenna illuminations to image the cause of these alterations. Furthermore, it is shown that the different components of the electromagnetic fields are affected differently by the defects, implying that both co- and cross-components of the electric and magnetic fields need to be considered. Moreover, the Poynting's vector is employed to visualize how the defects block the field from the antenna.

Populärvetenskaplig sammanfattning (in Swedish)

Elektromagnetiska fält finns idag överallt och är en förutsättning för att det moderna samhället ska fungera. Utan att fundera närmare på det, använder vi oss ständigt av de elektromagnetiska fältens förmåga att trådlöst överföra information och energi. Några exempel är; uppvärmning av mat i mikron och på induktionshällen, samtal i mobiltelefonen, uppdatering av status på Facebook oavsett var vi befinner oss, samt volyminställning på TV och stereo med fjärrkontrollen.

För att omvandla en elektrisk ström i en apparat till elektromagnetiska fält som breder ut sig i luften, eller tvärt om, används antenner. En antenn kan behöva skyddas från väderpåverkan och insyn. Ett sådant skydd kallas radom och sitter som ett hölje över antennen. Ett exempel på en radom är noskonen på ett flygplan.

Radomen ska helst vara elektriskt genomskinlig, det vill säga den ska inte förändra de elektromagnetiska fälten som antennen skickar ut eller tar emot. Elektrisk genomskinlighet är dock mycket svårt att uppnå eftersom det är många faktorer som man måste ta hänsyn till vid radomtillverkning. En noskon på ett flygplan är väldigt utsatt där den sitter längst fram. Radomen måste vara robust för att stå emot kraftiga mekaniska påfrestningar såsom regn- och hagelstormar, samtidigt som den inte ska vara alltför tung. Flygplanets hastighetsmätare sitter oftast som ett metallrör längst fram i radomens nos. Detta rör attraherar blixten, vilket betyder att ett kraftigt blixtskydd är nödvändigt. Dessutom ska radomen även vara aerodynamiskt utformad. Alla dessa krav på radomen går inte att till fullo uppfylla samtidigt. Detta innebär att den elektriska genomskinligheten kommer att påverkas, det vill säga, radomen kommer till viss del att påverka och förändra antennens elektriska prestanda.

Innan leverans av nya radomer, samt vid tester på lagade radomer, genomförs oftast fjärrfältsmätningar för att avgöra om uppsatta specifikationer uppnås. Med hjälp av fjärrfältsdata kan man se om något är fel men inte vad felet beror på. För att hitta orsaken till felet måste ytterligare undersökningar göras. Exempelvis kan man undersöka om det elektromagnetiska fältets fas påverkas som det är tänkt då fältet passerar genom radomväggen. En annan metod som används för att t.ex. hitta sprickor i radomväggen är ultraljud. I denna avhandling föreslås ett nytt sätt att diagnostisera radomer. Metoden är baserad på källrekonstruktion vilket innebär att ett uppmätt elektromagnetiskt fält ”backas tillbaka” till radomytan. Genom att åskådliggöra fälten på den tredimensionella radomkroppen kan defekter lokaliseras och deras inverkan på de elektromagnetiska fälten kan studeras. Resultaten är mycket positiva och metoden har stor potential att kunna utvecklas till ett industriellt anpassat diagnostiseringsverktyg.

Preface

This doctoral dissertation in Engineering summarizes the research I have carried out at the Department of Electrical and Information Technology, formerly the Department of Electroscience, Lund University, Lund, Sweden. The first part consists of a General Introduction followed by the scientific papers as listed below.

List of included papers

I. K. Persson and M. Gustafsson. Reconstruction of equivalent currents using a near-field data transformation – with radome applications, *Progress in Electromagnetics Research*, vol. 54, pp. 179–198, 2005.

II. K. Persson and M. Gustafsson. Reconstruction of equivalent currents using the scalar surface integral representation, Technical Report LUTEDX/(TEAT-7131), pp. 1–25, 2005, Department of Electrical and Information Technology, Lund University, Sweden.[1] `http://www.eit.lth.se`

III. K. Persson, M. Gustafsson, and G. Kristensson. Reconstruction and visualization of equivalent currents on a radome using an integral representation formulation, *Progress in Electromagnetics Research B*, vol. 20, pp. 65–90, 2010.

IV. K. Persson, M. Gustafsson, G. Kristensson, and B. Widenberg. Radome diagnostics – source reconstruction of phase objects with an equivalent currents approach, Technical Report LUTEDX/(TEAT-7223), pp. 1–22, 2012, Department of Electrical and Information Technology, Lund University, Sweden.[2] `http://www.eit.lth.se`

V. K. Persson, M. Gustafsson, G. Kristensson, and B. Widenberg. Source reconstruction by far-field data for imaging of defects in frequency selective radomes, *IEEE Antennas and Wireless Propagation Letters*, vol. 12, pp. 480–483, 2013.

Other publications by the author

VI. K. Persson and M. Gustafsson. Reconstruction of equivalent currents using a near-field data transformation - with radome applications, *Proceedings EMB04*, Computational Electromagnetics - Methods and Applications (EMB 04), Göteborg, Sweden, pp. 124–131, October 18–19, 2004.

VII. K. Persson and M. Gustafsson. Near field to equivalent currents transformation with radome applications, *Proceedings International Symposium on Electromagnetic Theory*, International Symposium on Electromagnetic Theory (URSI EMTS 2004), Pisa, Italy, pp. 1122–1124, May 23–27, 2004.[3]

[1] The technical report is based on the material in Paper I, however, it contains additional results regarding phase reconstruction and visualization techniques.

[2] Submitted for publication.

[3] Honored with a Young Scientist Award.

VIII. K. Persson, M. Gustafsson, and G. Kristensson. Experimental validation of reconstructed equivalent currents on a radome, *International Conference on Electromagnetic Near-Field Characterization & Imaging (ICONIC 2005)*, Barcelona, Spain, pp. 35-40, June 8–10, 2005.

IX. K. Persson, M. Gustafsson, and G. Kristensson. Usage of a surface integral representation to reconstruct equivalent currents - with radome applications, *Proceedings of Radiovetenskap och kommunikation*, Nordic Conference on Radio Science and Communications (RVK 05), Linköping, Sweden, June 14–16, 2005.

X. S. Nordebo, M. Gustafsson, K. Persson. Sensitivity analysis for antenna near-field imaging. *IEEE Transactions on Signal Processing*, vol. 55, no. 1, pp. 94-101, 2007.

XI. K. Persson, M. Gustafsson, G. Kristensson, and B. Widenberg. Source reconstruction for radome diagnostics. *The 34th Progress In Electromagnetics Research Symposium (PIERS)*, Stockholm, Sweden, August 12–15, 2013.[4]

[4]Accepted for publication.

Summary of included papers

Paper I: Reconstruction of equivalent currents using a near-field data transformation – with radome applications

In this paper, it is investigated how the amplitude of the dominant co-polarized component of the electric near field can be reconstructed on a radome surface close to the source of radiation. The method is based on a surface integral representation together with the extinction theorem. The representation describes an inverse source problem with the dominant co-polarized component of the electric field and its normal derivative on the radome surface as unknowns. The experimental set-up is axially symmetric, such that the complexity of the problem can be reduced by employing a Fourier transform. The linear system is regularized by a singular value decomposition (SVD). The measurement set-up consists of a reflector antenna and a radome. The height of the radome corresponds to 29 wavelength at 8 GHz, and the electric near field is measured on a cylindrical surface.

Three different configurations are considered in the frequency range $8 - 12$ GHz; antenna only, antenna with radome, and antenna with defect radome. The defect radome has two copper plates attached to its surface. The formulation is validated for synthetic data. Furthermore, it is showed that the measured electric field can be reconstructed on the radome surface in an accurate way, where the effects of the copper plates, not seen in the measured near field, are localized. Moreover, the used technique is verified by comparing the far field, calculated from the reconstructed fields employing a near- to far-field transformation, to a measured far field.

Contributions of the author:
The author of this dissertation is the main contributor to this paper. She has carried out a major part of the analysis and the algorithm implementation. The author is also responsible for the numerical simulations, and the writing of the paper.

Paper II: Reconstruction of equivalent currents using the scalar surface integral representation

This paper is a continuation of Paper I. An extended analysis of the measurement data from Paper I is performed, whereas the theoretical parts remain unchanged. Specifically, the phase of the electric field is taken into account. The phase delay caused by the radome, referred to as the insertion phase delay (IPD), is investigated. Furthermore, different ways of visualizing the results are discussed and presented.

Contributions of the author:
The author of this dissertation is the main contributor to this paper. She has carried out a major part of the analysis and the algorithm implementation. The author is also responsible for the numerical simulations, and the writing of the paper.

Paper III: Reconstruction and visualization of equivalent currents on a radome surface using an integral representation formulation

In this paper, the inverse source problem is solved by utilizing the surface integral representation combined with a surface integral equation originating from the extinction theorem. Both co- and cross-components are taken into account, and the coupling between the components of the fields increases the complexity of the problem. The problem is solved in a similar way as in Papers I-II, *i.e.*, the integral representation and equation are written as linear systems and solved by a body of revolution method of moments (MoM) approach. An SVD is employed to invert the matrices and the singular values are filtered to regularize the problem.

The three radome configurations are investigated at 8 GHz; antenna only, antenna with radome, and antenna with defect radome (attached copper plates). All components of the measured near field are now analyzed, and both co- and cross-components of the equivalent surface currents are reconstructed. These currents reveal in what ways the radome changes the radiation pattern of the antenna. The copper plates attached to the radome alter the measured electric field. However, the cause of the distortion is not seen in the measured near field. In this paper, it is shown that both components of the magnetic equivalent surface current can be used to localize the effects of the copper plates. The influence of the radome on the phase of the field, the IPD, is also investigated. An estimation of the thickness of the radome wall from the calculated IPD verifies the results.

Contributions of the author:
The author of this dissertation is the main contributor to this paper. She has carried out a major part of the analysis and the algorithm implementation, except the MoM-kernel, which is based on an in-house MoM-code. The author is also responsible for the numerical simulations, and the writing of the paper.

Paper IV: Radome diagnostics – source reconstruction of phase objects with an equivalent currents approach

In this paper, the reconstruction algorithm is utilized to diagnose deviations in the electrical thickness of the radome wall. These deviations are modeled by attaching several patches of dielectric tape (defects) to the radome wall. The electrical properties of the tape are similar to the electrical properties of the radome wall.

Two different far-field measurement series were employed at 10 GHz, each series containing three separate set-up configurations; antenna only, antenna with radome, and antenna with defect radome (attached dielectric patches). The height of the radome corresponds to 36 wavelengths. The IPD is reconstructed, and the dielectric patches of various edge sizes (0.5-2 wavelengths), and with the smallest thickness corresponding to a phase shift of a couple of degrees, are imaged.

Contributions of the author:
The author of this dissertation is the main contributor to this paper. She has carried out a major part of the planning of the measurements, the analysis, and the algorithm implementation, except the MoM-kernel, which is based on an in-house

MoM-code. The author is also responsible for the numerical simulations, and the writing of the paper.

Paper V: Source reconstruction by far-field data for imaging of defects in frequency selective radomes

In this last paper, defects in the periodic lattice of a frequency selective radome are investigated by the reconstruction code. Specifically, a line defect, *i.e.*, a column of missing elements, and a horizontal defect that is due to a small vertical displacement of the elements, are imaged. The far field is measured at 9.35 GHz for two set-ups; antenna only and antenna with radome, where the height of the radome corresponds to 51 wavelengths. Several measurement series, illuminating different parts of the radome wall, are employed to determine the equivalent surface currents and image the disturbances on the radome surface.

Contributions of the author:
The author of this dissertation is the main contributor to this paper. She has carried out a major part of the planning of the measurements, the analysis, and the algorithm implementation, except the MoM-kernel, which is based on an in-house MoM-code. The author is also responsible for the numerical simulations, and the writing of the paper.

Acknowledgments

First and foremost, I would like to express my deep gratitude to my supervisors Prof. Gerhard Kristensson and Prof. Mats Gustafsson. Without your great knowledge within the area of electromagnetic theory, your guidance, and your effort to always have time for discussions, I would not have made it this far. Taking part of your positive spirit, eagerness to find intuitive understanding of complex problems, and your remarkable stress hardiness, has been a great source of inspiration.

The work reported in this thesis was made possible by a grant from the Swedish Defense Material Administration (Försvarets materielverk), and their funding is gratefully acknowledged. Furthermore, I am indebted to Saab Bofors Dynamics and GKN Applied Composites AB for providing measurement data.

In discussing the concepts of radomes, Michael Andersson (Licentiate in Engineering), Björn Widenberg (Ph.D.), and Sören Poulsen (Ph.D.) at GKN Applied Composites AB have been most helpful, and their assistance is most appreciated. Michael, Björn, and Prof. Rebecca Seviour have also been proofreading and giving me valuable comments on parts of this thesis, which I am grateful for.

Thanks are due to the technical and administrative staff at the department for their helpful support during all these years. The assistance of the staff at the library of the E-building are also very appreciated.

I thank all colleges, both former and current, who during my stay at the department have created a friendly and relaxed atmosphere with interesting, fruitful, humorous, and really odd conversation topics during lunches and coffee breaks. In order to not forget any I just say a great thanks to all of you!

I would also like to thank all my friends outside the E-building. You are all very important to me and I am thankful that you have put up with me during this last year when work and family have occupied all my time.

A great gratitude goes to my parents, Gunvor and Sven-Eric, and my brother, Anders, who have given me solid support throughout my life and always believed in me.

Finally, I am forever thankful to my beloved husband, Michael, and our wonderful son, Elias, for your unconditional love, encouragement, and your way of setting things in perspective. Tack för att ni finns!

Lund, April 2013

Kristin Persson

Contents

Abstract v
Populärvetenskaplig sammanfattning (in Swedish) vii
Preface ix
List of included papers ix
Other publications by the author ix
Summary of included papers xi
Acknowledgments xv
Contents xvii
General Introduction 1
1 Introduction 3
2 Radomes 5
2.1 Disturbances of electrical performance 6
2.2 Materials and configurations of the radome wall 9
2.3 Modeling approaches and fabrication techniques 11
2.4 Verification methods of electrical properties 12
2.5 Verification of electrical properties by source reconstruction 16
3 Inverse source problems 20
3.1 Plane wave spectrum 21
3.2 Modal expansion 22
3.3 Surface integral representations 23
4 Conclusion and future challenges 31
A Surface integral representations and equations 34
A.1 Introduction of the scalar free-space Green's function 35
A.2 Introduction of the Maxwell equations 39
A.3 Values of the integral equations on the bounding surface 40
A.4 The exterior problem 43
I Reconstruction of equivalent currents using a near-field data transformation – with radome applications 57
1 Introduction 59
2 Near-field measurements 61
3 The surface integral representation 63
3.1 Angular Fourier transformation 64
3.2 Inversion with singular value decomposition 66
4 Implementation 66
5 Results using measured near-field data 68
6 Discussions and conclusions 71
II Reconstruction of equivalent currents using the scalar surface integral representation 75
1 Introduction 77
1.1 Ranges of application 77
1.2 History 78
1.3 The scalar surface integral representation 78
1.4 Results 79

1.5 Outline 80
2 Near-field measurements 81
3 The surface integral representation 82
3.1 Angular Fourier transformation 83
3.2 Inversion with singular value decomposition 84
4 Implementation 85
5 Results using measured near-field data 87
6 Alternative ways to visualize the electromagnetic currents 93
6.1 Amplitude of the reconstructed currents 93
6.2 Differences between the measurement configurations 93
6.3 Propagation of the reconstructed fields 95
7 Discussions and conclusions 96
III Reconstruction of equivalent currents on a radome using an integral representation formulation 103
1 Introduction 105
2 Prerequisites 106
2.1 General case 106
2.2 Body of revolution 108
3 Near-field measurements 111
4 Results 115
5 Conclusions 123
IV Radome diagnostics — source reconstruction of phase objects with an equivalent currents approach 131
1 Introduction and background 133
2 Radome diagnostics 135
2.1 Measurement data and set-up 135
2.2 IPD and visualization options 138
3 Reconstruction algorithm 140
4 Reconstruction results 143
4.1 Reference measurement 143
4.2 Imaging of dielectric material 144
5 Conclusions and discussions 148
A Induced currents due to dielectrics 150
V Source reconstruction by far-field data for imaging of defects in frequency selective radomes 155
1 Introduction and background 157
2 Measurement data and set-up 158
3 Reconstruction algorithm 160
4 Reconstruction results 161
5 Conclusions and discussions 166

General Introduction

Kristin Persson

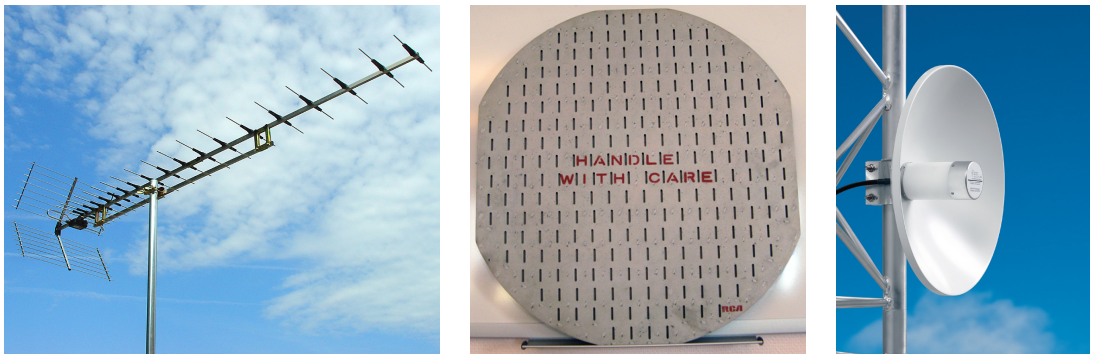

(a) (b) (c)

Figure 1: Examples of antennas: a) Television antenna of Yagi-Uda type. Photo courtesy of: Antennlaget, Växjö, Sweden. b) Aircraft slot antenna. Photo courtesy of: Björn Widenberg, GKN Aerospace Applied Composites, Linköping, Sweden. c) Parabolic reflector antenna. Photo courtesy of: Mattias Hellgren, Smarteq Wireless AB, Enebyberg, Sweden.

1 Introduction

Electromagnetic fields and its ability to transfer information and energy is essential in modern life. Without thinking, we use electromagnetic fields as information and energy carrier thousands of times every day; the breakfast oatmeal is cooked in the microwave oven. Opening the garage door is convenient with the remote key and the need of "old fashion" maps are abandoned in favor of GPS, keeping track of our position around the clock. If a Facebook update cannot be posted at any time, or from any location, we get really annoyed. Needless to say, we would stand bewildered without the functionality of the electromagnetic waves.

The antenna is the physical link between the radiation in free space and the electronic devices interpenetrating and translating the electromagnetic waves, to speech in a mobile phone or to dots representing airplanes on a radar screen. If the antenna operates in receiving mode it collects electromagnetic waves from free space, and if it works as a transmitter it sends out electromagnetic waves. Examples of different types of antennas are depicted in Figure 1.

In a direct problem, the sources of the electromagnetic fields on an antenna aperture are known. The primary goal is to determine the electromagnetic fields radiated by the antenna, see Figure 2 and [13, 69, 103, 136]. In this thesis, an inverse source problem is considered, where the electromagnetic field is measured and known in a set of points at a distance from the source, and the cause of the radiation is unknown [8, 24, 27, 34, 56, 60]. The challenge is to reconstruct the sources, to back propagate the measured field to find the electromagnetic fields close to the surface, or often on the surface of the radiator, see Figure 3. The inverse source problem is ill-posed, which means that small perturbations (noise) in the measured field are greatly amplified in the reconstruction of the sources, if not carefully considered.

An advantage of using source reconstruction in diagnostics is its non-destructive

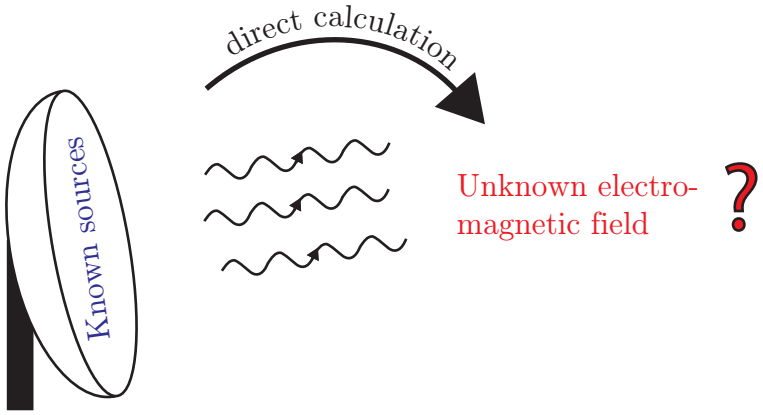

Figure 2: A direct source problem.

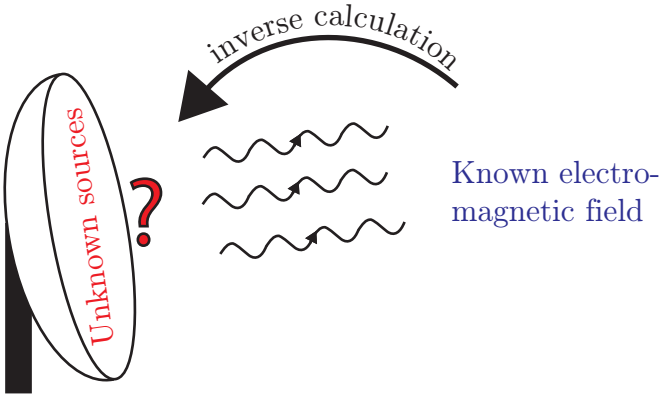

Figure 3: An inverse source problem.

nature, where the object under test is not affected. Source reconstruction as a diagnostics tool is applied in many areas, a few examples are given here, and a brief review is found in Section 3. In this thesis, the influences of defects attached to radomes are investigated. Specifically, defects, such as metal patches, Papers I-III, dielectric patches, Paper IV, and dislocations in a frequency selective radome, Paper V, are investigated. The changes in the phase and the amplitude of the electromagnetic fields, due to the radome and the defects, are imaged on the radome surface. These alterations of the electromagnetic fields give rise to unwanted deviations in the far-field data; transmission loss, beam deflection, changes of side-lobe levels, and the formation of flash lobes, see Papers I-V. The developed diagnostics tool has the potential to provide an understanding of what causes these deviations.

In Figure 4a, the influences of dielectric patches attached to a radome, 0.3 mm and 0.9 mm thick, are reconstructed on the radome surface. Other areas of interest are antenna diagnostics, [22, 35, 38, 57, 58, 78, 79], investigation of mobile phone radiation [39], and base station safety distances [151]. An example of antenna diagnostics is shown in Figure 4b, where the reconstructed electric field on a horn

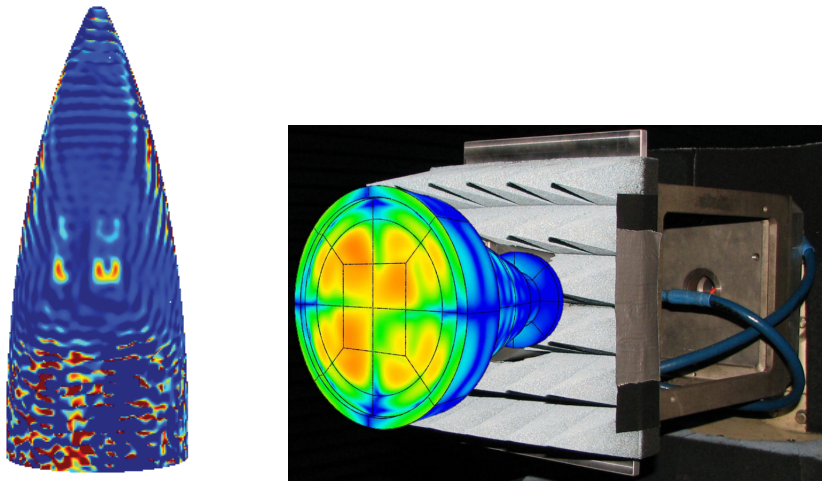

(a) (b)

Figure 4: a) A reconstruction revealing dielectric patches in the shape of the letters LU attached to the radome surface, see Paper IV. b) A diagnosed horn antenna unveiling an error in the antenna feed. Generated by DIATOOL of TICRA. Photo courtesy of TICRA.

antenna reveals an unexpected error in the antenna feed. Applications within the area of electromagnetic compatibility are found in *e.g.*, [76], where the radiation of printed circuits boards is characterized.

The main focus of this thesis is radome diagnostics by a source reconstruction method based on a surface integral representation and the extinction theorem. This introduction is intended to give the reader an brief description of what a radome is, and the advantage of a diagnostics tool to evaluate its electrical properties, see Section 2. The contributions of the author within the field of non-destructive radome diagnostics are shortly reviewed in Section 2.5. In Section 3, a background of the source reconstruction field is given with main focus on the method based on surface integral representations and equations utilized in this thesis. Finally, future challenges and conclusions are discussed in Section 4. The interested reader can find the derivation of the surface integral representations and equations in Appendix A. Furthermore, some sections in the General Introduction are based on [98].

2 Radomes

A radome encloses an antenna to protect it from environmental influences. Radomes shield antennas on various platforms, *e.g.*, on ships, satellites, airplanes, submarines, vehicles, high towers, or on the ground. Three examples are given in Figure 5. The word radome originates from the words “radar” and “dome” and it is believed to be coined by the staff at the Signal Corps’ Aircraft Radiation Laboratory, USA, during the years of World War II [107, 140].

(a) (b) (c)

Figure 5: Different radome applications: a) Nose cone protecting aircraft radar, JAS-39 Gripen. Copyright Gripen International. Photo: Katsuhiko Tokunaga. b) Station monitoring tectonic motions of the volcano Popocatepetl in Mexico. Photo courtesy of Enrique Cabral-Cano. c) Aircraft surveillance, Bromma airport, Sweden. Photo courtesy of Maciej Swic.

Depending on the properties of the shielding antenna and the environment in which it operates, the radomes have different styles and qualities. The size and form are very much dependent on the antenna and its electrical properties. The radar antenna on an airplane is very exposed, since it is located at the front to get a free line of sight. The radome covering the antenna needs to be aerodynamically designed, but also protect from snow, icing, wind, lightning, and hail *i.e.*, hard weather conditions, *cf.*, Figure 6. In military applications, the radome is often designed to have stealth properties, aiming for low monostatic reflection at frequencies outside the transmitting band of the antenna [107]. Stealth properties are commonly implemented by frequency selective surfaces (FSS) [90, 146]. Frequency selective surfaces is also an asset in environments with many receiving and transmitting antennas where shielding between electrical systems is desirable [65]. Another application is energy saving windows, where the FSS is designed to reduce heat transmission — the heat is kept indoors in the winter and shut out during the summer — without interfering with frequencies used for communications [44, 146].

2.1 Disturbances of electrical performance

Ideally, a radome is expected to be electrically transparent, which means that the amplitude and phase of the transmitted or received field should be unaffected by the radome [19, 65]. However, tradeoffs are necessary to fulfill properties such as aerodynamics, robustness, lightweight, weather persistency *etc.*, and it is impossible to completely avoid alterations in the antenna characteristics.

An example of a tradeoff, affecting the electrical performance, is the lightning protection attached to an airplane nose cone, *i.e.*, the Pitot tube, the lightning conductor, and the lightning-diverter strips [19, 65]. The Pitot tube indicates the speed of the airplane by pressure measurements, but serves also as a lightning attraction (*cf.*, Figure 10). Thus, the Pitot tube diverts the lightning, via a lightning con-

Figure 6: The nose cone of a cargo Boing airplane, after flying through a severe hail storm. Photo courtesy of Dave Subelack.

ductor attached on the inside of the radome, to the hull of the aircraft [147]. The consequences of a severe stroke of lightning, are shown in Figure 7a. Another example is shown in Figure 7b, where a radome from the 1970's was not equipped with lightning-diverter stripes. Instead, existing wires, the ones attached to the Pitot tube, were dimensioned to manage a stroke of lightning [9].

Other attachments that have an influence on the electromagnetic performance are plastic or metallic rain caps, located at the tip of the radome, which protect from rain erosion. A metallic cap may also reduce the mechanical stress at the tip of a nose-cone radome of an aircraft [19]. Different tradeoffs also occur when dealing with large space frame radomes. These are assembled by several panels where the framework, either metallic or dielectric, interacts with the electromagnetic fields, see Figure 8, where a space frame with a metallic framework is shown [65, 120]. Yet, another example appears when utilizing periodic structures in the design of bandpass radomes. The periodicity is disturbed by the double-curved radome surface, which gives undesired alterations in the electromagnetic performance of the radome [90, 107, 137, 146].

All these tradeoffs affect the electrical performance of the radome in different ways. Furthermore, the amplitude, phase and polarization or the electromagnetic field, are also changed in the radome wall and by interactions at the material interfaces. The results of all these factors are transmission loss (gain reduction) and beam deflection. Moreover, beam width, side-lobe levels, null depths are changed, and flash or image lobes appear [5, 19, 65, 140, 147].

The transmission loss reduces the detection range of the antenna, whereas higher side-lobe levels, caused by, *e.g.*, lightning-diverter strips [19], give rise to increased

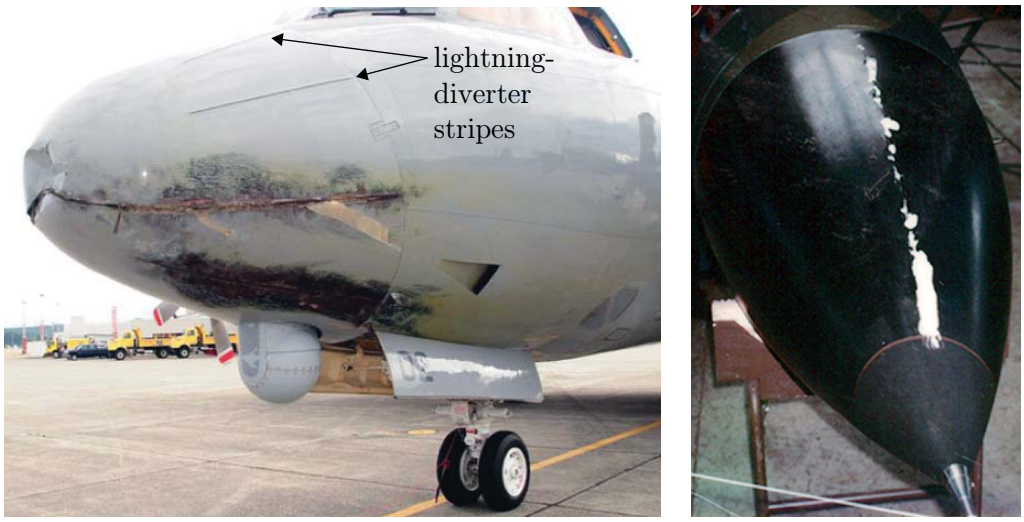

(a) (b)

Figure 7: a) Damaged radome, on a RNZAF Orion aircraft, due to a stroke of lightning. The arrows point out lightning-diverter stripes. New Zealand Crown Copyright, source: New Zealand Air Force (RNZAF), `http://www.airforce.mil.nz`. b) Damaged radome due to a stroke of lightning at the Pitot tube, resulting in an explosion of a heating wire. Copyright Saab AB.

clutter, and susceptibility to jamming [5, 147]. The flash or image lobes are caused by reflections on the inside of the radome wall and reflections within the wall [19, 65, 140]. These artifacts result in faulty registered objects of, *e.g.*, a radar system, giving an increased false-alarm rate [5, 147]. The electromagnetic wave changes its angle of incidence on the antenna when passing through the radome, and thereby also its phase relatively to air, and if not properly compensated for, boresight errors (BSE or beam deflection) and boresight error slope (BSES) occur [19, 65, 140]. The boresight error slope is the ratio of the change of the boresight error as function of the antenna scan angle [65]. These errors imply that the signal is believed to originate from a faulty direction, *cf.*, the discussion on this subject in Section 2.4.2. BSE can have severe consequences in navigating systems. Moreover, interaction between the radome wall and the antenna may further reduce the antenna performance if not carefully considered [65].

Some of the above-mentioned deviations are depicted in Figure 9, where a cross section of the measured far field is viewed. The co-polarization is showed, for the antenna alone and the antenna together with the radome, respectively. The antenna is a standard 18 inch slot antenna operating in the frequency band $9.2 - 9.5$ GHz, see Figure 1b. The radome consists of a frequency selective surface (FSS) with deviations in the periodic lattice, see Paper V for more details. Observe, the far field pattern does not reveal the causes of the deflections, to find these a diagnostics tool is required.

Figure 8: Photo of a metallic space frame radome protecting an antenna for satellite communications. The diameter is 13.7 m. Located at Chitose, Hokkaido, Japan. Photo courtesy of L-3 ESSCO Collins Limited.

2.2 Materials and configurations of the radome wall

The material of which the radome is manufactured must be electrically transparent, but also sustainable and persistent against environmental stress. The desire to find a strong, but radio frequency transparent material, is often contradictory, when it comes to material parameters and compromises are required. In the 1940's, when the manufacturing of radomes started to boom, the choice of material was plywood. However, plywood absorbs moisture, and it was soon abandoned in favor of plexiglass and later fiberglass [65]. Common choices of radome material today are different composite materials or ceramics [5]. Ceramics is utilized when high temperatures, *i.e.*, high velocities, are attained [65].

Composite radomes can be divided into subcategories — solids (monolithic), multilayered (sandwich), and metal-loaded radomes. Here, a short review is given, and the interested reader is referred to the literature for more details [19, 20, 65, 107, 125, 138, 140]. Solid radomes, also called monolithic radomes, can be of either thin-wall or half-wave design. The thickness of a thin-wall design should be less than $\lambda/10$, whereas the thickness of the wall in the half-wave design is a multiple of $\lambda/2$, where λ is the wavelength in the radome wall [19, 65]. The monolithic radomes consist of reinforced resin, where common choices of resin are; polyester, epoxy, or cyanate ester, whereas the reinforcement consist of *e.g.*, fiberglass or kevlar [19, 65, 147]. Multiple layers are used in sandwich radomes, where layers of material with a high permittivity (fiber-reinforced resin system) are alternated by materials with low

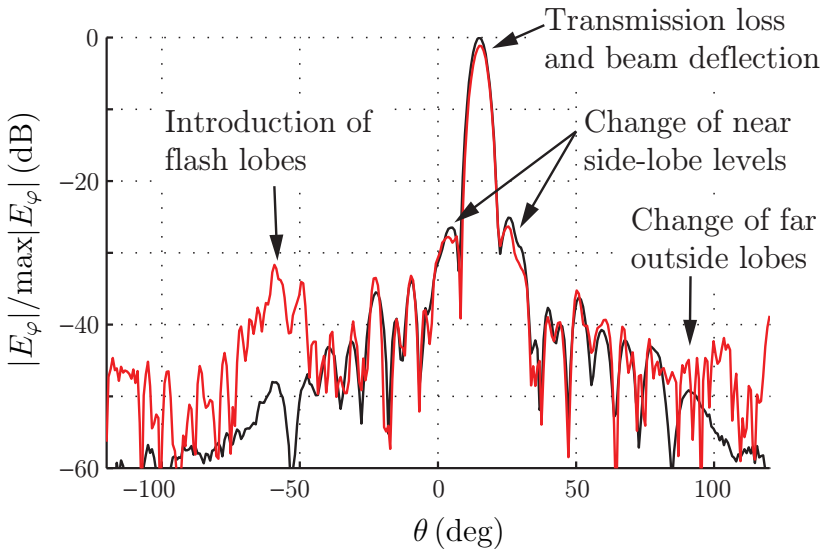

Figure 9: Changes in the electromagnetic performance due to the radome. The co-component, E_φ, of the far field is depicted, where the black line describes the antenna case and the red one the radome case. Negative θ-values correspond to the back side of the radome, whereas positive ones represent the front side where the main lobe hits the radome wall.

permittivity (honeycomb or dielectric foam) in different combinations, A-sandwich, B-sandwich, *etc.* [19, 65].

Introducing metal in a dielectric multilayered structure gives a metal-loaded radome [19]. Adding a periodic structure of elements provides frequency filtering properties, resulting in a radome that either transmits or reflects electromagnetic fields in specific frequency spans. Walls of this type is called frequency selective surfaces (FSS) [90, 95, 137, 143, 146, 148]. The periodic structures of an FSS usually consist of thin metal films serving as layers in a multilayered structure. Another type of FSS structure is the artificial puck plate (APP) design [106, 107, 148]. The APP consists of a thick perforated conducting frame, where the apertures in the periodic lattice are filled with dielectric pucks. These dielectric pucks act as short waveguide sections [107].

Monolithic radomes are common in ground-based or shipboard applications, where a simple design and construction is preferred, and the weight of the radome is of less importance [19]. Moreover, many fighter radomes are half-wave monolithic, since this construction is extremely persistent and sustainable [5]. Sandwich radomes are the most common ones in lower-speed aircraft, since they are more broadband and have a higher strength-to-weight ratio than the solid ones [5]. Metal-loaded radomes can be utilized in environments where the coupling with other antennas, using different frequency bands, needs to be low [65]. Moreover, stealth radomes consist of frequency selective structures, and they are designed by a careful choice of materials and geometries, to have a low radar cross section, *i.e.*, to be "invisible" [66, 90, 107]. Large antenna systems require large radomes, and these can

consist of an air-supported electrically thin dielectric fabric or a space frame, *cf.*, Figure 8 and [65, 120, 138].

2.3 Modeling approaches and fabrication techniques

Attaining all the desired properties of the radome is a delicate matter. The design and manufacturing process consists of several iterative steps, where prototypes are built, analyzed, and optimized. To speed up this process, analytical models of the transmission/reflection within the wall, and the propagation within the radome cavity, are available [19, 65]. Often a planar design is employed in the first iterative steps [147]. To get reliable results, it is crucial that the representation of the field radiated by the antenna, the input data, is well-known [5]. One modeling approach is based on physical optics (PO) [4, 83, 123]. A PO-MoM hybrid method is presented in [53, 85, 150], where the authors of [53] take the mutual coupling between the antenna and radome into consideration. In [84], fast multipoles are utilized in the PO-MoM hybrid to calculate the influence of an electrically large radome.

The antenna-radome interaction is often not negligible. For example, a change of the antenna matching can be caused by fields reflected by the radome wall back to the antenna aperture [65]. The interaction between the antenna and radome is considered in [50, 51], where surface integral equations are applied to investigating the change in antenna parameters of an Archimedean spiral antenna-radome system.

There are many manufacturing methods in use today. Three of the most popular ones are wet layup, usage of prepreg sheets, and resin infusion processes [147]. The main features of these are given here, whereas thorough descriptions are given in [30, 65, 75, 131, 140], where also other methods are outlined.

In wet layup, dry cloths of fiberglass are placed on a mandrel shaped as the radome. After each layer, resin is brushed on, and with this method, it is difficult to get an uniform ratio of resin and fiberglass. To avoid this, the pieces of fiberglass are soaked in resin and weighted before application, in order to get a controlled resin to fiber ratio [65].

There exists a number of different resin infusion technologies, which slightly differ from each other [131]. One example is the vacuum infusion processing, where all layers of the dry fiberglass are applied to a mold and sealed by a vacuum bag [131]. The resin is then introduced and spread by applying vacuum at strategic points. An advantage of this method is the improvement in work environment due to low emissions of harmful volatile substances, such as styrene and isocyanates [30]. Vacuum infusion is also an efficient and inexpensive method to use in production of large and complex shaped radomes [131]. However, a drawback is the difficulty of obtaining a uniform resin level [131].

Today, many radomes are built from commercially available preimpregnated sheets, prepregs, which are sticky cheats of fiber impregnated with resin [131]. The prepregs have a well-defined resin to fiber ratio and is available in a range of predefined thicknesses [65]. The main disadvantages are the price as well as their limited storage life. In order to prevent hardening of the resin, the prepregs need to be freezer stored. However, the hardening process is slowed down at low tempera-

tures, but not entirely stopped [147]. Moreover, frequency selective surfaces (FSS) are often designed as flat sheets, on which the periodic structure has been printed. These sheets are not very flexible, which makes the draping of them, on the radome frame, quite complex [137]. Regardless of which method used, the radome needs to be cured. Common methods utilize pressure and heat either by vacuum-bag or autoclave molding [30, 131, 140].

2.4 Verification methods of electrical properties

The design of radomes is a delicate art of engineering as many choices and parameters are to be considered. Consequently, there is a demand for diagnostics tools verifying the electrical properties of the radome. Delivery controls of new radomes must fulfill specified requirements and repaired radomes must be checked according to international standards and manufacturers maintenance manuals [65]. The evaluations can be divided into non-destructive or destructive, depending on the need of impact on the radome wall. The non-destructive ones are often the most desirable.

2.4.1 Measurement ranges

The performance of a radome is usually defined in operational parameters, such as *e.g.*, transmission loss and beam deflection (*cf.*, Section 2.1). A functional test is commonly performed by evaluation of far-field data [52]. The far field can be measured at an indoor (anechoic chamber) or an outdoor far-field range. The distance between the radome-antenna system and the range antenna, the size of the test range, depends on the electrical size of the radome [12, 65, 66].

A smaller far-field test range is the compact range where a plane wave is produced by using one or several reflector screens [145], see Figure 10. Measuring the near field, the chamber can be smaller still, however probe compensation becomes necessary [46, 149]. The far field is then determined by a near-field to far-field transformation [16, 40, 104, 117, 132, 133]. Figure 11 shows a photo of an anechoic chamber utilized for both near- and far-field measurements, depending on the size of the object under test and the frequency.

Far-field graphs can reveal antenna pattern degradations such as transmission loss, beam deflection, changes of side-lobe levels, and introduction of flash lobes (*cf.*, Figure 9 and Section 2.1). However, these graphs do not reveal the source of the error. To do so, skilled and highly experienced labour, or some further post-processing of the data, is required (*cf.*, Section 2.5).

2.4.2 Insertion phase delay

In performance evaluations of radomes, the phase shift of the electromagnetic field, due to the passage through the radome wall, is important. This quantity is called the electrical thickness of the radome or the insertion phase delay (IPD). The IPD relates the phase shift in the radome wall to the phase shift in free space [19], and

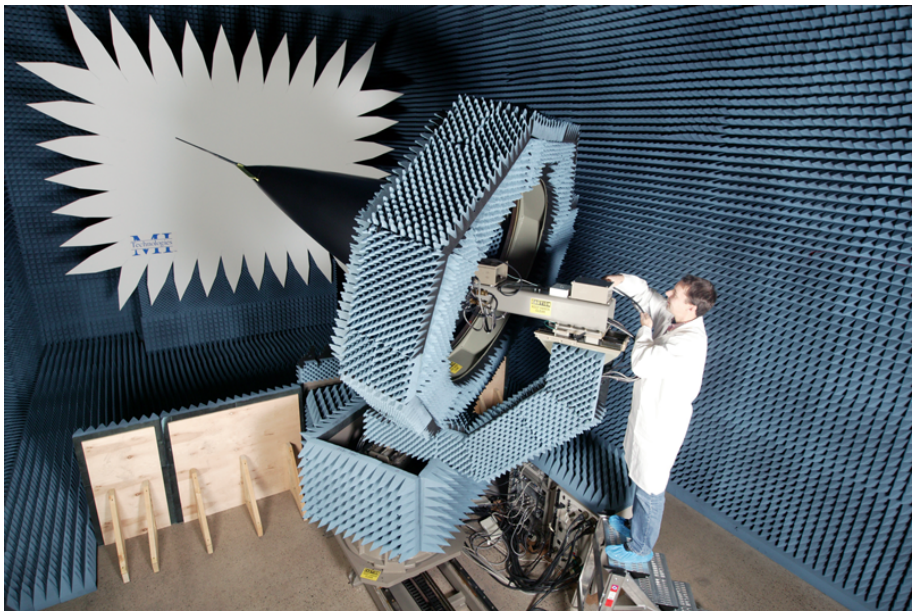

Figure 10: A compact test range from MI Technologies, at GKN Aerospace Applied Composites, Linköping, Sweden. The radome belongs to the aircraft Gripen. Attached to the tip of the radome is a Pitot tube. Size of chamber: $6.0(\text{width}) \times 5.4(\text{height}) \times 12(\text{length})\,\text{m}^3$, frequency range: $8.0 - 18.0\,\text{GHz}$. Photo courtesy of GKN Aerospace Applied Composites.

for a plane wave

$$\text{IPD} = \angle T - \frac{\omega}{\text{c}_0} d \cos\theta_\text{i} \tag{2.1}$$

where T is the complex transmission coefficient, which depends on the incidence angle, the parameters of the radome wall, and the polarization of the electromagnetic field [19]. The last term of (2.1) removes the phase shift of free space, where ω is the angular frequency, c_0 is the speed of light in free space, d is the thickness of the radome wall, and θ_i is the incident angle of the plane wave.

Having a non-constant phase shift (IPD) over the illuminated area or the radome surface can cause bore sight errors (BSE or beam deflection). This can be understood by thinking of the phase shift as a delay of the electromagnetic field in the radome wall relative to free space propagation. The angle of incidence may vary considerably for a double-curved radome, see Figure 12, and a large angle of incidence generally introduces a large IPD (if all other parameters are held constant), *i.e.*, a large delay. This is illustrated in Figure 12, where the BSE-effect is highly exaggerated to explain the concept. The wall at point a, where the field have a small angle of incidence, only delays the field a little, whereas the wall at point b, have a larger angle of incidence, and thereby delays the field a bit more *etc.*. Altogether, the main beam changes its direction. This change of direction is denoted beam deflection or BSE. The antenna can in some cases avert a predicted BSE by a compensation in the antenna software [19].

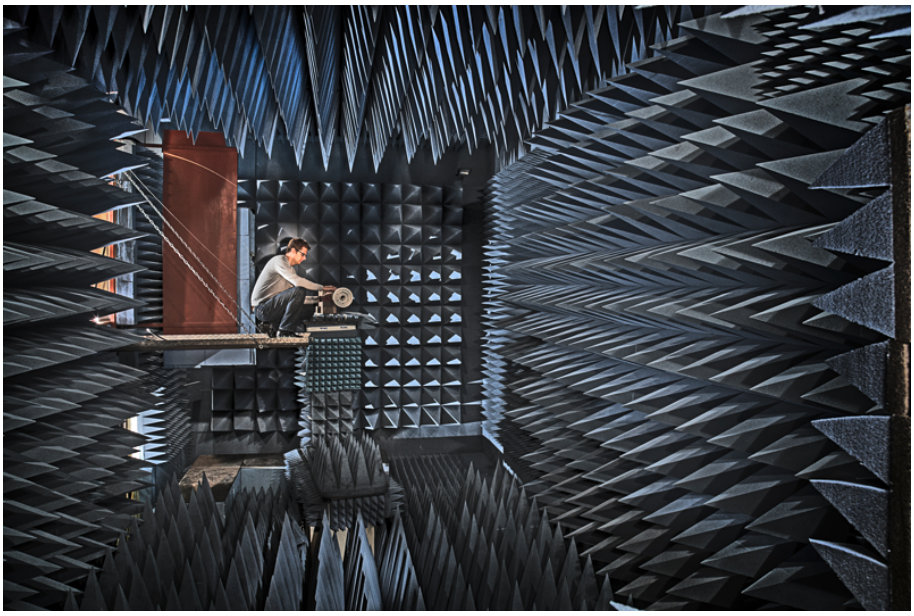

Figure 11: Anechoic chamber at RUAG Space, Göteborg, Sweden, for both near- and far-field measurements. Size of chamber: $5(\text{width}) \times 5(\text{height}) \times 9(\text{length})\,\text{m}^3$, frequency range: $0.8 - 40.0\,\text{GHz}$. Photo courtesy of RUAG Space AB.

One of the techniques to measure the electrical thickness (IPD) is by locating two horn antennas, on each side of the radome wall. A suitable choice is to locate them in such a way that the incident angle of the field coincide with the Brewster angle [31, 122]. This choice of incident angle minimizes the reflected field, and the disturbances due to back scattering into the radiating horn antenna are reduced. To calculate the IPD, the phase of the transmitted field is subtracted from the phase of the measured field with no radome present between the horn antennas. However, it is not always possible to measure at the Brewster angle due to radome geometry and set-up. Moreover, the radome performance is usually required for multiple incidence angles [31]. Another method is described in [29], where a modulated scattering technique is utilized [15]. Exterior to the radome, a transmitting and a receiving linear (1D) slot antenna scan the surface. Inside the radome, an array of small modulated sensors is located. The field scattered by the sensors is modulated and detected by the receivers. Due to the known modulation, the phase shift caused by the radome can be derived. Non-modulated signals, such as reflections in the radome wall or interaction between the receiving and transmitting antennas are discriminated.

In the case of a monolithic radome, the radome wall can be trimmed to achieve the required IPD-values [5, 147]. Trimming means that areas with a too high electrical thickness are ground, whereas areas with a too low IPD are patched, by applying cloths of reinforced fabric or using a spray gun that simultaneously sprays out chopped cloths of reinforced fabric, resin, and setting agent into a thin layer [131]. Care must be taken since a thickness change of the radome wall may affect other

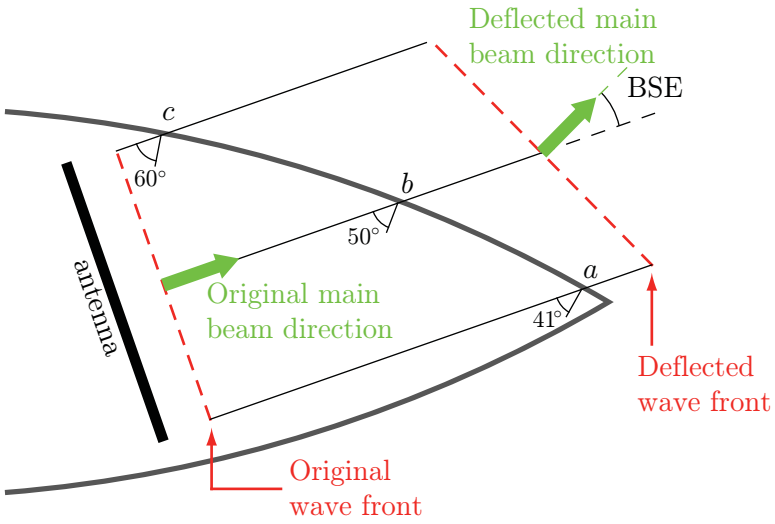

Figure 12: Beam deflection due to a non-constant phase shift over the illuminated radome wall [107].

parameters, *e.g.*, side and flash lobes, in an undesirable way.

2.4.3 Other non-destructive evaluation techniques

Due to mishaps in the production or impacts on the radome wall when in use, cracks may accrue. In a multilayered structure also debonds, *i.e.*, air pockets between the layers, arise [5, 131, 144, 147]. Below, a brief listing of some of the non-destructive evaluation techniques is presented, whereas the interested reader is referred to the literature [10, 11, 116, 119, 126, 131, 144].

A very easy way to obtain a first indication if cracks and debonds are present is to use coin tapping, also called the tap test [144]. In this test, one listens to sound deviations when a coin is tapped against the radome wall. A more sophisticated method, and one of the most commonly used, is ultrasonics [131], where the reflection of acoustic waves is measured. The time delay of the pulse is highly affected by density changes in the material, *i.e.*, cracks and debonds. Another method is shearography, which uses the fact that a defect in the surface reflects coherent light differently than an unaffected surface when subjected to stress produced by a mechanical or thermal excitation [10, 119].

To find moisture ingression in a damaged radome, a camera sensitive to infrared light can be utilized [11]. Modern techniques involve embedded optical fiber sensors. One example is the *e.g.*, optical time domain reflectometry, where a bend of the fiber induces a small reflection, that can be detected with a sensitive reflectrometer. Another example is the fiber bragg grating sensors, which are designed to reflect light of a specific wavelength, and if strained, the wavelength of the reflected light is shifted. More details of optical fiber sensors are found in [10, 116, 126].

2.4.4 Destructive methods

Figure 13: The radome diagnosed in Papers I-IV. The missing pieces at the bottom have been used for material characterization.

Sofar, non-destructive methods have been described, but in some tests it is hard to avoid damage to the radome wall. In production, the radome is sometimes made slightly longer than the blueprint indicates. This is done in order to attach the radome correctly to the fixture of the manufacturing tool, and the excess length is later cut off [147]. However, pieces can be cut from the extended region to ensure that the ratio of air to resin to fiber is correct in the wall (*cf.*, Figure 13). This is achieved by weighing the cut before and after the resin and reinforcement are separated by melting the resin [147]. The surface of the cut may also be inspected for debonds in a multilayered structure [147]. Moreover, the thickness of each layer can also be verified [147]. Other destructive tests, harming the radome, are lightning tests, and bird-collision tests [5].

2.5 Verification of electrical properties by source reconstruction

In this thesis, a novel approach, utilizing a non-destructive source reconstruction method to diagnose radomes, is proposed. The method is based on an inverse source problem where a measured far or near field is related to the equivalent surface currents on the radome surface by integral representations, see Papers I-V. A detailed review of the method is given in Section 3. Similar approaches have recently been used to diagnose antennas [1, 35, 57, 58, 78, 108, 110].

As mentioned in Section 2.4.1, graphs of the far field may indicate errors such as transmission loss, beam deflection, changes of side lobes and introduction of flash lobes, see Figure 9. However, the origin of the flaws is not revealed. To get an understanding of the cause, the equivalent surface currents — the tangential electromagnetic fields, see (3.1) — are reconstructed on the 3D-radome body. It is not feasibly to measure these fields directly, since a measurement of the electromagnetic fields close to a radiating body or scatterer is affected by the interaction of the measurement probe and the radiator or the scatterer. This interaction contaminates the measurement [46, 113, 149].

To evaluate the potential of the source reconstruction method as a diagnostics tool, defects of different kinds have been introduced to the radome surface. These defects are metal patches (Papers I-III), representing *e.g.*, lightning-diverter strips or Pitot tubes, dielectric patches (Paper IV), modeling deviations in the electrical thickness of the radome wall, and finally interruptions in the lattice of a frequency selective surface (Paper V). The aim is to localize the defects and to visualize their influences on the amplitude and phase of the electromagnetic fields. Attention is paid to different visualization options, such as different scales and components

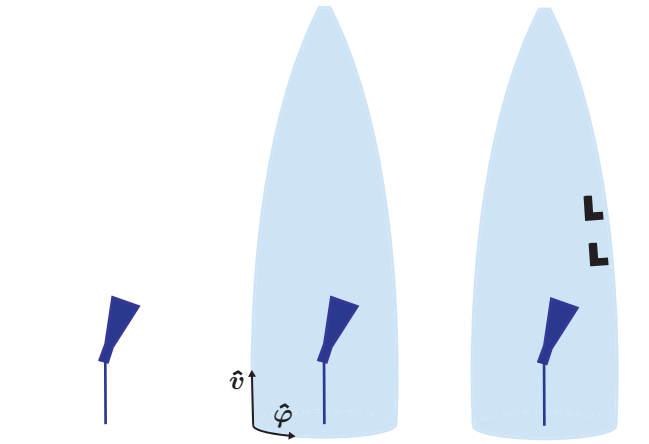

Figure 14: Sketch and notation of the measured set-up configurations in Papers I-IV. The middle figure shows the unit vectors of the coordinate system in which the reconstructed fields are expressed.

of the fields; co- or cross-polarizations of the electric or magnetic components, or the Poynting's vector, to reveal as many properties as possible of the fields on the radome surface. Some examples of the main diagnostics results are reviewed in the following paragraphs, whereas the full analysis and details are found in Papers I-V. Throughout this section, the configurations of the measurements are referred to as indicated in Figure 14; conf. (0) - antenna only, conf. (1) - antenna with radome, and conf. (2) - antenna with defect radome. The configuration number is indicated as a superscript on the fields, whereas the field component is showed by a subscript, *i.e.*, $H_{\mathrm{v}}^{(0)}$ is the magnetic component directed along the height of the radome surface when only the antenna is present.

The influence of metal patches, 1.6×1.6 wavelengths^2 at 8.0 GHz, is investigated in Papers I-III. A measured near field is utilized to find the tangential electromagnetic fields on a radome surface, with a height corresponding to 29 wavelengths. Three different set-ups are measured; antenna only, antenna with radome, and antenna with defect radome (two metal patches attached), see the sketch in Figure 14. The measured near field shows that the main beam is deflected and attenuated, and the side lobes are altered when the metal patches are present, see Figure 15. However, the origin of the deviations is unknown. Figure 16 depicts the difference between the radome and the defect radome cases for the reconstructed co-component of the tangential electric field on the radome surface. In Figure 16a, the patches are localized in a dB-scale, where the influence of the phase is included since the difference imaged is $|E_{\mathrm{v}}^{(1)} - E_{\mathrm{v}}^{(2)}|$. The linear scale in Figure 16b depicts the difference of the amplitudes, *i.e.*, $|E_{\mathrm{v}}^{(1)}| - |E_{\mathrm{v}}^{(2)}|$. The area with a negative field amplitude, just above the lower patch, reveals a field contribution that is probably attributed to scattering from the patch. The radome's introduction of flash (or image) lobes and the alteration of these due to the presence of metal patches are visualized for the

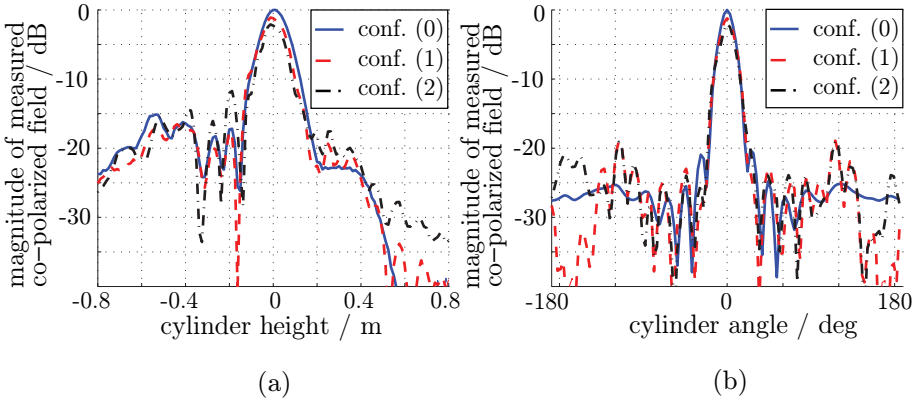

Figure 15: The measured co-polarized electric field on the measurement cylinder. (a) The angle is fixed at $\varphi = 0$ (front side), and the fields are normalized to the maximum value when no radome is present — conf. (0). (b) The height is fixed at $z = 0$, and the fields are normalized to the maximum value when no radome is present.

electric co-component in Figure 17.

Localization and analysis of dielectric patches, cloths of fiberglass, are carried out in Paper IV. The utilized reinforced fiber tape is employed in trimming of monolithic radomes to achieve a smooth insertion phase delay (IPD) and to reduce the bore sight errors (BSE), *cf.*, Section 2.4.2. The dielectric material mainly effects the phase of the field, and one layer of tape, 0.15 mm, gives rise to a phase shift of $2° - 3°$. Again, three different set-ups are measured; antenna only, antenna with radome, and antenna with defect radome, see Figure 14. However, the measurements are carried out in a compact range and far-field data at 10.0 GHz is employed in the reconstruction. The height of the radome corresponds to 36 wavelengths. Two measurement series are conducted where the sizes and thicknesses of the defects are shown in Figure 18. Figures 19a and 20a depict the patches attached to the radome and Figures 19b and 20b visualize the illumination of the defects when the radome is present, *i.e.*, conf. (1). The dielectric squares and letters are localized by the phase difference between the radome and the defect radome cases, *i.e.*, conf. (1) and (2), see Figures 19c and 20c. Further analysis concludes that the dielectric squares of size 2λ — one layer thick, the squares of size 1λ — two layer thick, and the squares of size 0.5λ — 4 layer thick, are clearly visible in the reconstructed phase differences. Furthermore, the dielectric tapes of two layers and the smallest dimension of 0.5λ in the form of the letters LU are resolved. The phase shifts of the larger squares, and the letters, coincide well with the approximated theoretical values of $2° - 3°$ per layer. It is conjectured that the diagnostics method, can be used in constructing a trimming mask for the illuminated areas of a radome. A trimming mask indicates which areas that are too thin or too thick, and thereby need correction.

The electrical performance of a frequency selective (FSS) radome depends on the periodic structure of the elements in the radome frame. Due to the double

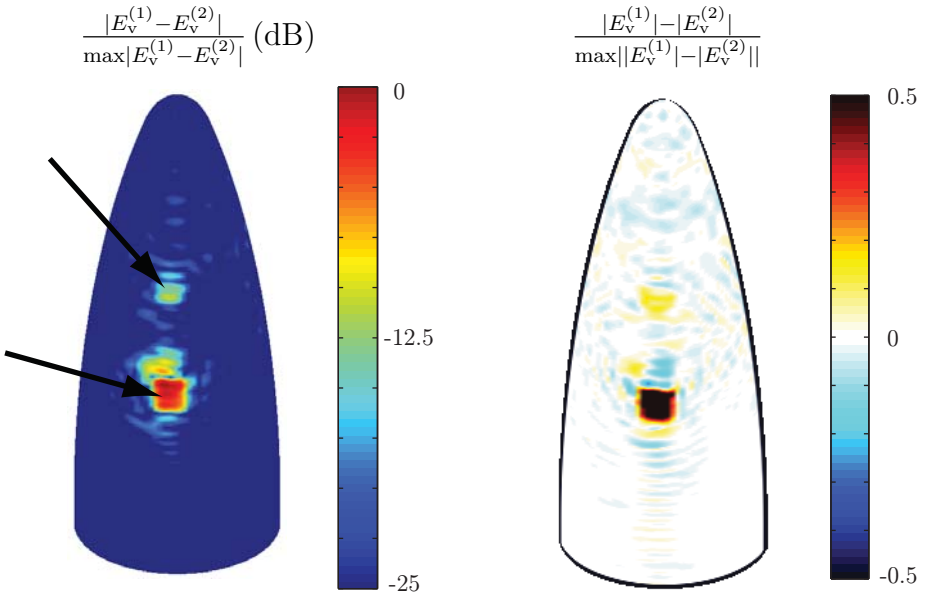

(a) (b)

Figure 16: Metal patches, localized in the reconstructed field difference between conf. (1) and (2). a) The logarithmic differences. The arrows point out the locations of the copper plates. b) The linear differences.

curvature of the wall, the size, or other manufacturing difficulties, the periodicity may be disrupted. In Paper V, the influence of disturbances, such as displacements of the elements and missing elements, is visualized, see Figure 21. The far field is measured at 9.35 GHz for two set-ups; antenna and antenna together with the FSS radome, *i.e.*, conf. (0) and (1), where the height of the radome now corresponds to 51 wavelengths. The far field is illustrated in Figure 9, where it is clear that the antenna pattern is altered due to the presence of the radome. However, the appearance of the fields on the radome surface, and how these differ from the ones predicted by *e.g.*, a simulation tool, are unknown, *i.e.*, the cause of the altered far field pattern is unknown. One example of the reconstruction of the fields on the radome surface is visualized in Figure 21b, where the difference of the Poynting's vector between the antenna and the radome cases — conf. (0) and (1), depicts how the field is blocked (negative power flow) by the defects.

A correct description of the electromagnetic fields, radiated by the antenna, is vital in the numerical modeling of the radome wall (*cf.*, a discussion in Section 2.3). Reconstruction of the tangential electromagnetic fields in conf. (0), close to or on the antenna aperture, gives an accurate depiction of the antenna radiation [1, 35, 57, 58, 78, 108, 110].

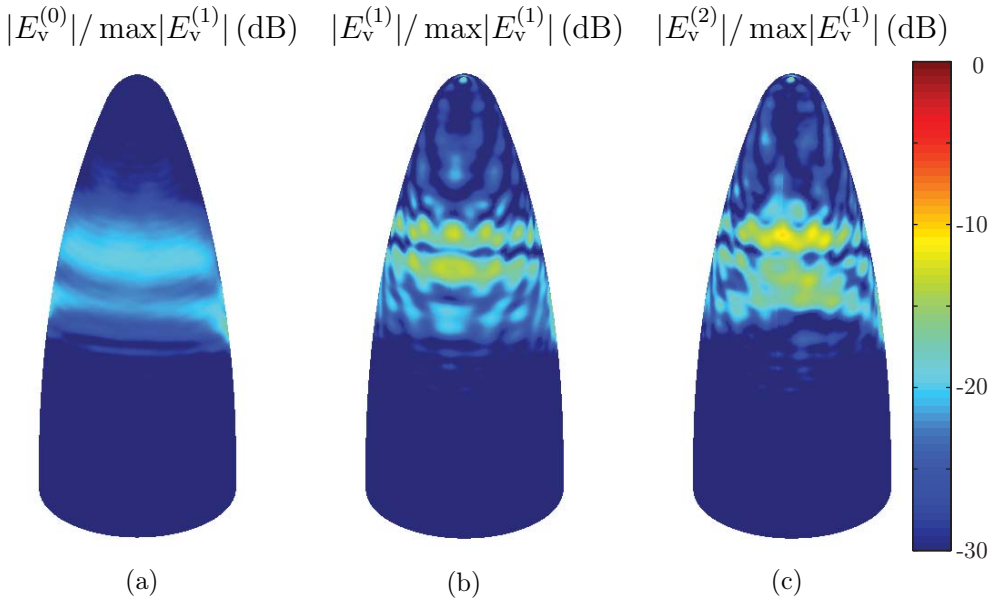

Figure 17: The back side of the radome displaying the flash lobes in the different configurations. (a) Antenna only — conf. (0), *i.e.*, no flash lobe present. (b) Radome present — conf. (1). (c) Defect radome present — conf. (2).

3 Inverse source problems

Inverse problems have applications within a variety of disciplines, such as, radar, medicine, non-destructive testing, and geophysical exploration. Depending on the problem to be solved, different equations and solution methodologies are applied [8, 24, 34, 47, 60, 92, 96, 118, 135]. In this thesis, focus is on electromagnetic problems modeled by the Maxwell equations. Specifically, attention is paid to the *inverse source problems* [34, 56], where the aim is to reconstruct the source or the electromagnetic fields close to the source, *i.e.*, the main interest of the investigation is the electromagnetic sources and not the object itself. Moreover, usually some *a priori* information of the object is given, *e.g.*, geometry or material parameters.

In addition to the inverse source problems, there are the *inverse scattering problems*, where information about the scattering object is requested [24, 96, 118]. In these problems, the incident field and a model for the field-obstacle interaction, are utilized to determine the physical properties of the object, such as shape and material. Multiple illuminations are usually employed. It is worth noting that the division between the inverse scattering problem and inverse source problem is not strict.

As stated, the focus in this thesis is the inverse source problem, and the following sections give a background of the field of research, in particular, the diagnostics applications. The technique to be employed depends on, the geometry of the surface where the field is measured, the geometry of the body where the fields are to be reconstructed, and the material of the body of the equivalent currents — the

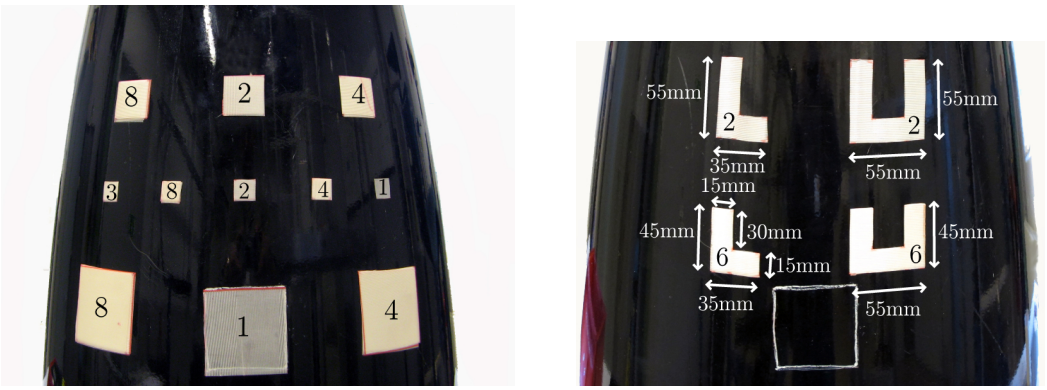

(a) (b)

Figure 18: The dielectric defects attached to the radome. The numbers on the patches indicate the number of tape layers. a) The size of the squares are; $30 \times 30\,\mathrm{mm}^2$ on the top row, $15 \times 15\,\mathrm{mm}^2$ on the middle row, and $60 \times 60\,\mathrm{mm}^2$ on the bottom row. b) Each "leg" has a width of 15 mm. The drawn square shows where the centered lower square in the left figure was located.

most common ones are the perfect magnetic conductor (PMC), the perfect electric conductor (PEC), or free space.

In Sections 3.1 and 3.2 decomposition in plane waves and modal expansions are discussed as reconstruction techniques. Integral representations, as a method to solve the inverse source problems, are then introduced in Section 3.3. This section starts with a presentation of the equivalent surface currents, the surface integral representation, and the surface integral equations. A brief review is then given of how others employ the representations, and their results within diagnostics.

3.1 Plane wave spectrum

A numerically fast technique is the method utilizing the plane wave spectrum (PWS) [17, 28, 45, 48, 91, 141]. This technique was one of the first employed, and in this approach the measured field is expanded in plane waves. The PWS is the Fourier transformation of the radiated far field in the lateral variables [46, 49]. The near field on a plane, arbitrarily close to the radiator, can then be obtained by an inverse Fourier transform. Both spherical and planar measurement surfaces can be used, as well as measurements in the near field or in the far field, since accurate transformations between the different geometries and the fields are available [18].

The PWS is used to determine the specific absorption rate (SAR) of mobile phones [39]. Instead of scanning the electric field strength in the whole volume of a phantom, it is enough to measure the amplitude of the electric field on two planes. The phase of the electric field is retrieved by an iterative process and the expansion of the field in its plane wave spectrum is utilized to evaluate the electric field and thereby the SAR on other planes in the phantom. The method is also applied to localize defects, patches of absorbers (Eccosorb), attached to a planar antenna

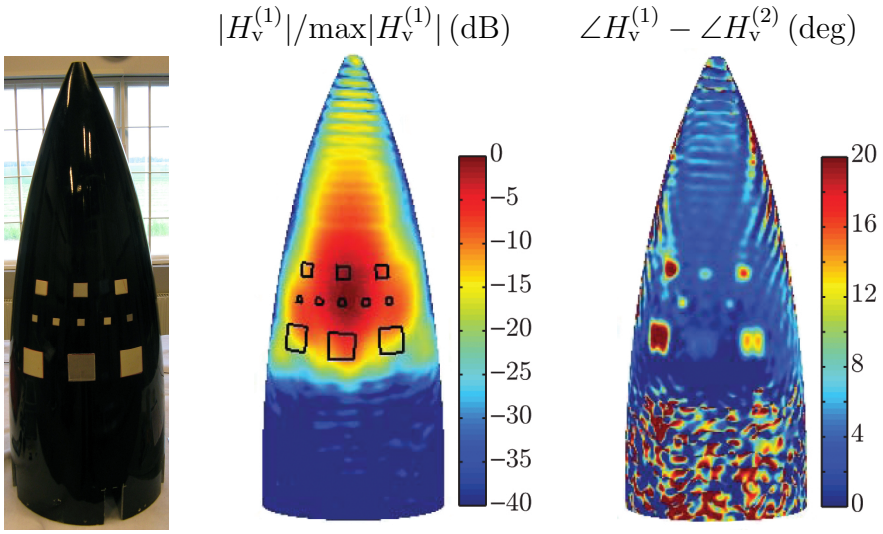

Figure 19: a) A photo of the radome with the attached dielectric squares (defects). b) The reconstructed field, H_v, on the radome — conf. (1). The drawn squares indicate where the defects will be located to create conf. (2). c) The phase of the reconstructed field difference between conf. (1) and (2).

array [74]. Another application is the reconstruction of the near field on the surface of a parabolic antenna, where an iterative scheme and geometrical relationships make it possible to find the fields on the non-planar parabolic surface [111, 112, 115]. Moreover, an early attempt to determine radome influences, using plane wave decomposition, is found in [41].

3.2 Modal expansion

A modal expansion of the field can be employed if the reconstruction surface is cylindrical or spherical [46, 49, 129]. The field is then expressed as a sum of cylindrical or spherical vector waves. The radial dependence in the expansion is given in cylindrical or spherical Bessel functions, respectively. The angular part contains trigonometric functions, and in the spherical case associated Legendre functions [46, 49, 129]. The method is only valid outside the smallest cylinder/sphere enclosing the radiating body, *i.e.*, equivalent currents can only be obtained on radiating bodies shaped as cylinders or spheres. The resolution obtained with spherical wave expansion (SWE) can be higher than the resolution achieved using the plane wave spectrum (PWS) [42]. More general geometries, *e.g.*, needle shaped objects and flat disks, can be handled by expanding the field in spheroidal wave functions [127, 128]. As with the spherical vector waves, the solution is only valid outside the smallest spheroid enclosing the radiating body.

In [42], the SWE is employed to calculate the insertion phase delay (IPD) and to detect defects in the wall of a spherical radome, *i.e.*, deviations in the dielectric constant and the wall thickness. The method is also utilized in antenna near-field imaging problems to find the relation between accuracy and resolution [93, 94]. The

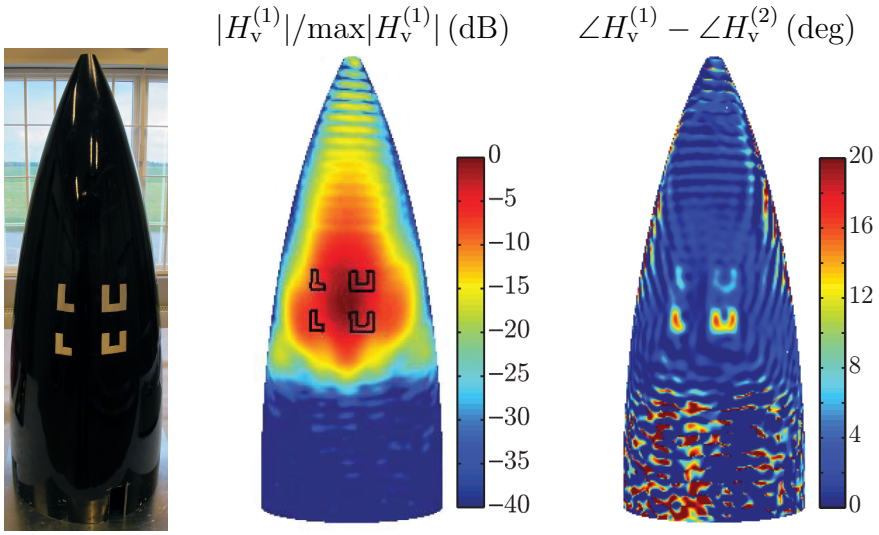

Figure 20: a) A photo of the radome with the attached dielectric letters LU (defects). b) The reconstructed field, H_{v}, on the radome — conf. (1). The drawn lines indicate where the letters will be located to create conf. (2). c) The phase of the reconstructed field difference between conf. (1) and (2).

Cramér-Rao bound gives a lower bound on the estimation error and a fundamental physical limit on system accuracy. This bound is related, via the Fisher information matrix [61], to the resolution as a function of the number of vector waves included [93]. The mathematical frame-work is applied to an electric field, measured on a cylindrical surface, and it is shown in which regions the result is trustworthy.

A combination of SWE and plane wave expansion (PWE) is employed in [21, 23]. The electric field of a spherical near-field measurement is expanded in spherical vector waves. Utilizing an extended transform of [33], the field is expressed in its plane wave spectrum, whereby the field on a plane close to the origin can be retrieved through an inverse fast Fourier transform. The method combines the high resolution of the SWE with the ability to come very close to the antenna under test provided by the PWE. This diagnostics technique is demonstrated by introducing errors; feed tilt, Gaussian shaped metallic bump, and dishes of aluminum, on an offset reflector antenna. These deviations are localized in the recreated field on a plane surface just in front of the antenna [22].

Another combination of modal expansion and PWE is utilized by [151], where the safety perimeter of base station antennas is investigated. The electric field, measured on a cylindrical surface, is expanded in cylindrical vector waves and the far field is calculated. The far field is expanded in PWS, and the field on different planes close to the antenna is retrieved.

3.3 Surface integral representations

The interest in applying surface integral representations in non-destructing diagnostics has increased rapidly over the last years. The problem is a linear inverse source

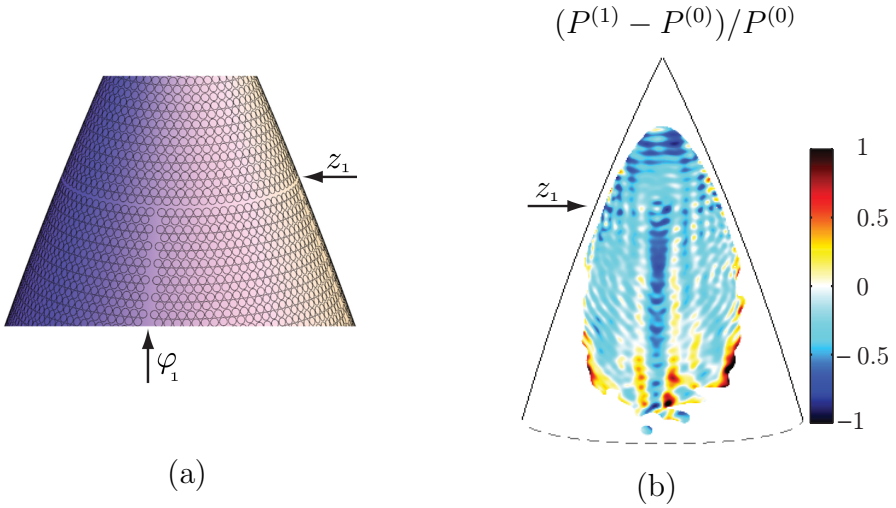

Figure 21: a) Part of the radome visualizing a vertical line defect — a column of missing elements — at φ_1. A horizontal defect occurs at z_1 due to a small vertical displacement of the elements. b) The time average power density through the radome is depicted in areas illuminated down to −15 dB. A pointwise normalization is utilized to reduce the influence of a non-even illumination, see details in Paper V.

problem, and it is solved by a method of moments (MoM) approach. Compared to the previously described methods, the measurement surface and the surface where the sources are reconstructed are not limited to certain shapes, and with the rapid development of computer technology, the computational complexity becomes less of a problem. Initial diagnostics studies, employing a surface integral representation and the extinction theorem, assuming no *a priori* information on the material of the object, were reported in [99, 100], also attached as Papers I-II. This method and variations thereof have then been utilized for numerous diagnostics purposes, see Section 3.3.3 and [1, 2, 35, 36, 38, 57–59, 78, 79, 97, 101, 102, 108–110]. In 2011 two commercial software tools, based on the reconstruction technique, were launched, *i.e.*, DIATOOL by TICRA[1] and INSIGHT by SATIMO[2].

3.3.1 Surface integral representations and equations

In this thesis, a surface integral representation and a surface integral equation are utilized for radome diagnostics. A typical set-up is depicted in Figure 22. The amplitude and phase of an electric field (E_z and E_φ) are sampled in the near- or far-field region. The goal is to reconstruct the equivalent surface currents (J_v, J_φ, M_v, M_φ) on a radome-shaped surface in order to diagnose the electrical performance of the radiating system. The equivalent surface currents are defined as the tangential

[1]TICRA. `http://www.ticra.com`, *2013-04-03*.
[2]SATIMO. `http://www.satimo.com`, *2013-04-03*.

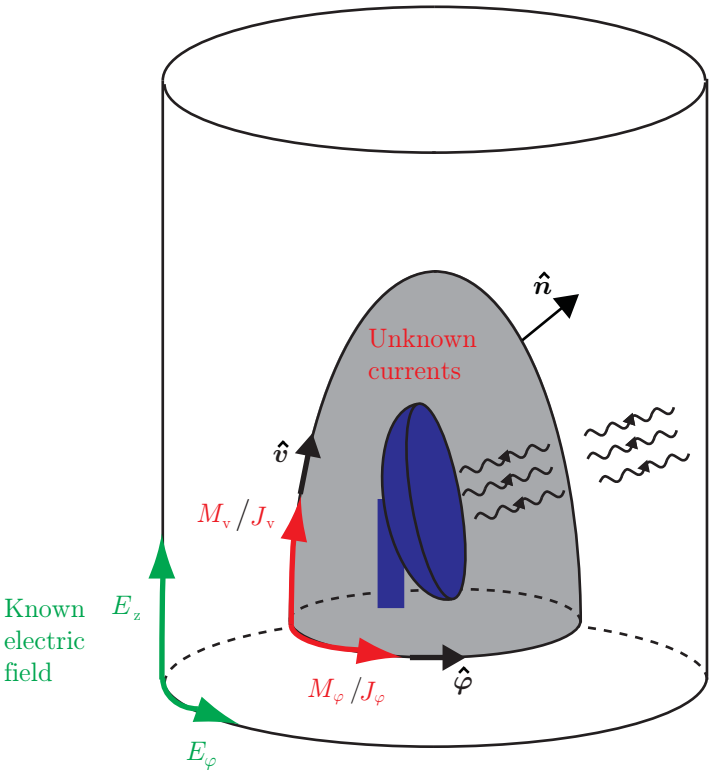

Figure 22: Description of the inverse source problem, and notation for parametrization of the electromagnetic and equivalent surface currents components. The shape of the sample surface is arbitrary, however, it is here depicted as a cylindrical geometry in the near-field region.

components of the electromagnetic fields on the surface [13, 54];

$$\begin{cases} \boldsymbol{J} = \hat{\boldsymbol{n}} \times \boldsymbol{H} \\ \boldsymbol{M} = -\,\hat{\boldsymbol{n}} \times \boldsymbol{E} \end{cases} \tag{3.1}$$

where $\boldsymbol{J}$ is the equivalent electric surface current[3], $\boldsymbol{M}$ is the equivalent magnetic surface current[3], $\boldsymbol{E}$ is the electric field, $\boldsymbol{H}$ is the magnetic field, respectively, and $\hat{\boldsymbol{n}}$ is the outward pointing unit vector as shown in Figure 22.

The equivalent surface currents on the radome surface are decomposed into two tangential components along the horizontal, $\hat{\boldsymbol{\varphi}}$, and vertical, $\hat{\boldsymbol{v}}$, arc lengths coordinates, *i.e.*, $[\hat{\boldsymbol{\varphi}}, \hat{\boldsymbol{v}}, \hat{\boldsymbol{n}}]$ forms a right-handed coordinate system, see Figure 22. The relations between the components of the tangential fields on the surface and the equivalent surface currents are then; $H_{\mathrm{v}} = \boldsymbol{H} \cdot \hat{\boldsymbol{v}} = -J_{\varphi}$, $H_{\varphi} = \boldsymbol{H} \cdot \hat{\boldsymbol{\varphi}} = J_{\mathrm{v}}$, $E_{\varphi} = \boldsymbol{E} \cdot \hat{\boldsymbol{\varphi}} = -M_{\mathrm{v}}$, and $E_{\mathrm{v}} = \boldsymbol{E} \cdot \hat{\boldsymbol{v}} = M_{\varphi}$. In this thesis, both terms — equivalent

[3]In a more stringent terminology, the currents are equivalent surface current densities. However, the word density is commonly suppressed in the literature and the subscript S or eq is employed [13, 25, 54]. Moreover, equivalent surface currents are the only currents present in this thesis, and since measurement configuration and field polarization are expressed as sub- and superscript, the simplified notation in (3.1) is applied.

surface currents and tangential electromagnetic fields — are used when the sources are discussed.

A surface integral representation expresses the electric field (E_z, E_φ in Figure 22) in a homogeneous and isotropic region in terms of the tangential surface current values on the bounding surface (J_v, J_φ, M_v, M_φ). In our case, the bounding surface, S_{radome}, is a fictitious surface, located just outside the physical radome surface, with smoothly capped top and bottom surfaces to form a closed surface. This fictitious surface is located in free space, but for convenience, it is referred to as the radome surface throughout the thesis. Combining the source-free Maxwell equations and vector identities gives a surface integral representation of the electric field [27, 54, 55, 63, 69, 86, 89, 130, 139, 142]. A derivation is found in Appendix A, and the result is

$$\iint\limits_{S_{\text{radome}}} \Big(\mathrm{j}k\eta_0 \; g(\boldsymbol{r}', \boldsymbol{r}) \big[\hat{\boldsymbol{n}}(\boldsymbol{r}') \times \boldsymbol{H}(\boldsymbol{r}') \big] - \mathrm{j}\frac{\eta_0}{k} \; \nabla' g(\boldsymbol{r}', \boldsymbol{r}) \Big\{ \nabla'_S \cdot \big[\hat{\boldsymbol{n}}(\boldsymbol{r}') \times \boldsymbol{H}(\boldsymbol{r}') \big] \Big\} + \nabla' g(\boldsymbol{r}', \boldsymbol{r}) \times \big[\hat{\boldsymbol{n}}(\boldsymbol{r}') \times \boldsymbol{E}(\boldsymbol{r}') \big] \Big) \, \mathrm{d}S' = \begin{cases} -\boldsymbol{E}(\boldsymbol{r}) & \boldsymbol{r} \text{ outside } S_{\text{radome}} \\ \boldsymbol{0} & \boldsymbol{r} \text{ inside } S_{\text{radome}} \end{cases} \tag{3.2}$$

where the time convention used is $\mathrm{e}^{\mathrm{j}\omega t}$, ω is the angular frequency, and η_0 is the intrinsic wave impedance of free space. The surface divergence is denoted $\nabla_S \cdot$ [27], the unit normal $\hat{\boldsymbol{n}}$ points outward, and the scalar free-space Green's function is $g(\boldsymbol{r}', \boldsymbol{r}) = \frac{\mathrm{e}^{-\mathrm{j}k|\boldsymbol{r}-\boldsymbol{r}'|}}{4\pi|\boldsymbol{r}-\boldsymbol{r}'|}$, where the wave number is $k = \omega/\mathrm{c}_0$, and c_0 is the speed of light in free space. The representation (3.2) states that if the tangential electromagnetic fields on a bounding surface is known, the electric field in the volume, outside of S_{radome}, can be determined [55, 130].

If the integrals in (3.2) are evaluated at a point $\boldsymbol{r}$ lying in the volume enclosed by S_{radome}, the integrals cancel each other — the extinction theorem [25, 130]. This statement does not necessarily mean that the field $\boldsymbol{E}$ is identically zero inside S_{radome}, it only says that the values of the integrals cancel. The use of the extinction theorem together with the surface integral representation, *i.e.*, both representations in (3.2), guaranties that the sources of the reconstructed surface currents are located inside S_{radome}.

In Papers I-II, the surface integral representation in (3.2) is applied to a measured near field with a dominating co-polarized component. The representation is combined with the extinction theorem, where $\boldsymbol{r}$ in (3.2) is located inside the radome at a small distance from the inner radome wall.

In Papers III-V, both polarizations of the measured electric field are considered, and the lower representation in (3.2) is transformed into a surface integral equation letting $\boldsymbol{r}$ approach S_{radome} from the inside. However, care must be taken since the integrands become singular as $\boldsymbol{r}$ approaches the surface, see Appendix A and [27, 63, 87, 130]. To simplify the notation, the equivalent surface currents in (3.1), as

well as the operators $\mathcal{L}$ and $\mathcal{K}$ are introduced as [54]

$$\begin{cases} \mathcal{L}(\boldsymbol{X})(\boldsymbol{r}) = \mathrm{j}k \iint\limits_{S_{\text{radome}}} \left\{ g(\boldsymbol{r}', \boldsymbol{r})\boldsymbol{X}(\boldsymbol{r}') - \dfrac{1}{k^2} \nabla' g(\boldsymbol{r}', \boldsymbol{r}) \left[\nabla'_S \cdot \boldsymbol{X}(\boldsymbol{r}') \right] \right\} \mathrm{d}S' \\ \mathcal{K}(\boldsymbol{X})(\boldsymbol{r}) = \iint\limits_{S_{\text{radome}}} \nabla' g(\boldsymbol{r}', \boldsymbol{r}) \times \boldsymbol{X}(\boldsymbol{r}') \, \mathrm{d}S' \end{cases}$$

In this notation, the surface integral representation yields

$$\mathcal{L}\left(\eta_0 \boldsymbol{J}\right)(\boldsymbol{r}) - \mathcal{K}\left(\boldsymbol{M}\right)(\boldsymbol{r}) = -\boldsymbol{E}(\boldsymbol{r}) \qquad \boldsymbol{r} \in S_{\text{meas}} \tag{3.3}$$

where S_{meas} is the set of sample points. The surface integral equation for the electric field (EFIE) reads

$$\hat{\boldsymbol{n}}(\boldsymbol{r}) \times \left\{ \mathcal{L}\left(\eta_0 \boldsymbol{J}\right)(\boldsymbol{r}) - \mathcal{K}\left(\boldsymbol{M}\right)(\boldsymbol{r}) \right\} = \frac{1}{2} \boldsymbol{M}(\boldsymbol{r}) \qquad \boldsymbol{r} \in S_{\text{radome}} \tag{3.4}$$

In a similar manner, a surface integral equation of the magnetic field (MFIE) is derived,

$$\hat{\boldsymbol{n}}(\boldsymbol{r}) \times \left\{ \mathcal{L}\left(\boldsymbol{M}\right)(\boldsymbol{r}) + \mathcal{K}\left(\eta_0 \boldsymbol{J}\right)(\boldsymbol{r}) \right\} = -\frac{\eta_0}{2} \boldsymbol{J}(\boldsymbol{r}) \qquad \boldsymbol{r} \in S_{\text{radome}} \tag{3.5}$$

No *a priori* assumption on the material parameters of the radome is employed in (3.3)-(3.5). As pointed out above, the reconstruction of the equivalent currents is performed in free space on a fictitious surface just outside the physical surface of the radome, *i.e.*, S_{radome} is located in free space. The main purpose of the diagnostics is to find unknown deviations, *e.g.*, regions where the parameters of the material differs from the ones in the design model, the *a priori* information. By reconstruction of the equivalent surface currents, in free space, precisely outside the physical radome surface, these defects can be imaged.

The surface integral equations (3.3)-(3.5) are commonly simplified by assuming the material inside the surface of reconstruction to be a perfect electric conductor (PEC) or a perfect magnetic conductor (PMC), see references in Section 3.3.3. The boundary conditions state that the tangential electric field on a PEC and the tangential magnetic field on a PMC vanish — $\boldsymbol{M} = \boldsymbol{0}$ or $\boldsymbol{J} = \boldsymbol{0}$, respectively.

By using EFIE or MFIE separately, it is well known that internal resonances can occur when solving the direct scattering problem [25, 26, 87, 121]. The resonances are not the same for EFIE and MFIE, thus a combination of them, *e.g.*, a CFIE- or a PMCHWT-formulation, removes the problem with the internal resonances [25, 54, 64, 87, 139]. Another approach is suggested in [124], where dual-surface integral equations are employed to avoid the resonances.

In the inverse source problem, a slightly different approach is used, where the surface integral equations, EFIE and/or MFIE, are combined with a surface integral representation. In this thesis, the problem is solved by using both EFIE (3.4) and MFIE (3.5) separately together with the representation (3.2). The results do not

differ significantly from each other, and it is concluded that there are no problems with internal resonances for the employed set-ups and choice of operators.

The inverse source problems with unknown volume current densities can contain non-radiating volume current densities. This problem is well known and this means that there exist volume current densities that produce a zero field outside a finite region [14, 32, 77, 81, 136]. This implies that a non-radiating volume current density can be added to the solution without affecting the electromagnetic field outside the finite region, *i.e.*, the inverse source problem is non-unique. However, we have not encountered any difficulties when solving for the equivalent surface currents (3.1) in (3.2)-(3.5). This suggests that either are non-radiating surface currents not present or suppressed by the regularization.

The surface integral representation can also be derived by utilizing Love's equivalence principle. This subject is only briefly described here, and the interested reader is referred to the literature concerning the details of Love's form of the equivalence principle [12, 49, 80, 110, 114]. Employing Love's equivalence principle, equivalent currents are defined in analogy to those in (3.1) on a fictitious surface that encloses the original sources. Specifically, equivalent surface currents are constructed in such a way that they produce the same electromagnetic fields, as the original sources, outside the fictitious surface, but a zero field inside.

Love's equivalence theorem states that different sets of equivalent surface currents can be obtained depending of the choice of the material (*e.g.*, free space, PEC, or PMC) inside the fictitious surface [12, 49, 114]. Either one of these sets of surface currents gives rise to the same electromagnetic field outside the fictitious surface as the original sources. In this thesis, the fictitious surface, S_{radome}, is located in free space just outside the radome surface. Moreover, the surface integral representation is combined with a surface integral equation, (3.4) or (3.5), in which the material parameters are set to free space. Further discussion about the implications of using a surface integral representation alone, compared to combining it with a surface integral equation is found in [110].

3.3.2 Reconstruction algorithm

The algorithm of the inverse source problem is given in Paper III, and the procedure is reviewed here. To find the unknown equivalent surface currents in (3.3)-(3.5), the integral equations are written in their weak forms, *i.e.*, they are multiplied with test functions and integrated by parts over their domain [16, 37, 68, 87, 103]. The set-up, see Figure 22, is axially symmetric. Consequently, a Fourier expansion in the azimuth angle of rotational symmetry reduces the problem by one dimension, *i.e.*, the problem can be solved independently for each Fourier mode [82, 103, 105]. Moreover, the Fourier spectrum of the measured field is truncated at a certain Fourier index, above which the energy contents is too low, see details in Papers III-IV.

The system of equations in (3.3)–(3.5) is solved by a body of revolution method of moments (MoM) code [6, 82], and the Green's functions are evaluated based on [43]. The basis function in the $\hat{\boldsymbol{\varphi}}$-direction consists of a piecewise constant function, and a

global function, a Fourier basis, of coordinate φ. Moreover, the basis function in the $\hat{\boldsymbol{v}}$-direction consists of a piecewise linear function, 1D rooftop, of the coordinate v, and the same global function as the basis function in the $\hat{\boldsymbol{\varphi}}$-direction, see Figure 22 for notations. Test functions are chosen according to Galerkin's method [16]. The surface is described by a second order approximation, and to form a closed surface, a smooth top and bottom are added to the radome surface. The MoM code is based on an in-house MoM code, and it is verified by perfectly conducting or dielectric scattering spheres [136].

The inversion of the surface integral representation (3.2) is ill-posed, which means that small errors in the measured data can produce large errors in the reconstructed equivalent surface currents, *i.e.*, the problem needs to be regularized [8, 62, 68]. In this thesis, the problem is regularized by a truncated singular value decomposition (SVD), where the influence of small singular values is reduced [8, 34, 47]. In Papers IV-V, a reference measurement series is performed to set the regularizing parameter used in the subsequent series. The inversion of the matrix system is verified using synthetic data. Moreover, the results, which localize the given defects, serve as verifications.

3.3.3 Source reconstruction utilizing surface integral representations

The interest in surface integral representations and surface integral equations as tools in diagnostics has increased rapidly over the last years, where different combinations and formulations based on an integral representation, the electric (EFIE), and magnetic (MFIE) field integral equation, are utilized. This section contains a brief overview presenting a selection of the results accomplished within the field of research. More extensive reviews are given in [1, 110].

If the object on which the equivalent surface currents are to be reconstructed is metallic, a perfect electric conductor (PEC), the magnetic equivalent surface current is eliminated in (3.2). This is often a legitimate approximation in diagnostics of metallic antenna apertures. For example, in [134] an electric surface integral representation is employed together with measured near-field data of a cylindrical PEC having apertures of various sizes on its surface. The very near field is reconstructed to demonstrate how to localize and diagnose leakage points in metallic wires.

A common approach is to utilize the equivalence theorem together with image theory, *cf.*, a short discussion in Section 3.3.1 and [12, 49, 114]. In this method, the volume inside the surface containing the sources is replaced by a body of a perfect electric conductor (PEC) or a perfect magnetic conductor (PMC), leaving only one of the equivalent surface currents. By employing the image technique, the remaining equivalent surface current is calculated on a planar surface in front of the object. This technique is convenient in diagnostics of flat antenna structures, see *e.g.*, [73], where an equivalent magnetic current together with *a priori* knowledge of the antenna geometry is utilized to diagnose a low-directivity printed antenna. A development of the method is given in [71], where a base station antenna is enclosed by two infinite planes, one aligned with the front antenna aperture and one aligned with the back aperture, on which the magnetic equivalent current is

recreated. The magnetic equivalent current is then employed to find the safety perimeter of the base station antenna by recreating the radiating field on planes at various distances in front of and behind the antenna. In [3], the equivalence principle and the image technique are utilized to diagnose radiated noise in electronic circuits by reconstructing the electric equivalent surface current on a plane above the circuit. In addition to diagnostics, the utilization of the equivalence theorem together with image theory is also applied in near-field to far-field transformations [70, 72, 104, 117, 132].

A first attempt to recreate both electric and magnetic equivalent surface currents on a 3D body is published in [99], *i.e.*, Papers I-II, where an electric field with a dominating co-component is utilized to image electromagnetic deviations due to copper plates attached on a radome surface. The problem is solved by a dual-surface integral representation and regularized with a singular value decomposition (SVD). This work is followed by [97, 101, 102], *i.e.*, Papers III-V, where the surface integral representation is combined with the EFIE and applied to the co- and cross-components of the measured electric field — measured in the near field in [97] and measured in the far field in [101, 102]. Diagnostics of radomes are performed with special interest in metallic defects [97], dielectric defects [101], and defects in the lattice of a frequency selective radome [102].

A slightly different approach is found in [57–59], where defect elements on a satellite antenna [58], and on a circular array antenna [57], are imaged. Specifically, the integral representation, the EFIE, and the MFIE are solved utilizing higher order bases functions in a MoM solver. The problem is regularized with a generalized truncated singular value decomposition in [59], a Tikhonov regularization in [58], and an iterative regularization scheme in [57], respectively.

In [38, 108–110], the surface integral representation is combined with EFIE or MFIE that is evaluated on a surface located inside the surface of reconstruction, *i.e.*, a dual-surface approach is employed, and the matrix system is solved by an iterative conjugate-gradient solver. The dual-surface strategy is employed to find and exclude radiation contributions from leaky cables and support structures in [108], and in [38], antennas are characterized. A comparison between a single surface integral representation and a dual-equation formulation (a surface integral representation combined with EFIE or MFIE) is performed in [109, 110], which shows that the dual-equation formulation is in favour.

Yet another approach is given in [1, 2, 78, 79], where a surface integral representation alone is applied together with an iterative conjugate-gradient solver. The electric current on the walls of a PEC, pyramidal horn antenna, is visualized in [2]. In [78], a conjugate-gradient solver and a singular value decomposition are shown to give similar results. Moreover, measured near-field and far-field data is employed to image the electric equivalent surface current on a radome covered log-periodic wide-band antenna. A parallelized algorithm implemented on graphic processing units is employed in [79] to image the equivalent surface currents on a base station antenna and a helix antenna.

A single surface integral representation involving the dyadic Green's function is employed by [35, 36]. In [36], the surface integral representation is solved by

using fast multipoles and an iterative solver based on generalized minimal residual. The electric equivalent current is reconstructed on a PEC flat surface in front of a reflector antenna and on the chassis of a car where an array of monopole antennas is located. In [35], the authors make use of higher order basis functions and multilevel fast multipoles to recreate the electric and magnetic equivalent surface currents on a base station antenna from probe corrected near-field measurements.

4 Conclusion and future challenges

In this thesis a novel approach of source reconstruction for radome diagnostics is investigated. A radome covers an antenna and protects it from environmental influences. The radome is ideally electrically transparent in the frequency band of operation. However, several aspects affecting the electric performance, such as aerodynamics, robustness, lightweight, and lightning protection, must be considered in the design. The electrical performance is usually defined by operational parameters, *e.g.*, beam deflection and transmission loss, which are commonly evaluated by far-field measurements. Moreover, it is in general very difficult to determine the cause of a performance deviation from far-field data alone. Source reconstruction for radome diagnostics is presented in this thesis, where the tangential electromagnetic fields are imaged on the radome surface, and the influences of defects and their locations are revealed.

Previously, source reconstruction for diagnostics has been performed on canonical shaped bodies (planes, cylinders, and spheres), by utilizing plane wave decomposition, modal expansion or combinations thereof [21–23, 39, 41, 42, 74, 111, 112, 115, 151]. The source reconstruction method, in this thesis, is based on a surface integral representation together with the extinction theorem. The representation relates the unknown tangential electromagnetic fields on the 3D-radome body to the measured electric near or far field. The extinction theorem guarantees that the sources are located inside the radome. The tangential electromagnetic fields are reconstructed in free space just outside the physical surface of the radome, *i.e.*, no *a priori* information of material parameters are required. The problem is an ill-posed inverse source problem, regularized with a truncated singular value decomposition (SVD).

Surface integral representations have been employed in source reconstruction prior to the work in [99], included as Paper I. However, to our knowledge, the surface integral representation has earlier only been applied by itself to a perfect electric conductor (PEC) or a perfect magnetic conductor (PMC), where one equivalent surface current is reduced in the surface integral representation [3, 71, 73, 134]. Lately, the method utilizing a surface integral representation, commonly in combination with a surface integral equation or variations thereof, have been employed in antenna diagnostics to find both the electric and the magnetic equivalent surface currents [2, 35, 36, 38, 57, 58, 78, 79, 108]. Furthermore, two commercial tools have been launched[4].

[4]DIATOOL by TICRA, `http://www.ticra.com`,
and INSIGHT by SATIMO, `http://www.satimo.com`. *2013-04-03.*

The objective of the thesis is to demonstrate the potential of the source reconstruction method as a diagnostics tool for radomes. The technique is non-destructive and can be applied to both near- and far-field measurements. The electrical performance of the radome wall, and defects attached to or in the wall, have successfully been investigated. Specifically, influences of attached metal patches (representing *e.g.*, lightning-diverter strips or Pitot tubes), attached dielectric patches (modeling deviations in the electrical thickness of the radome wall), and interruptions in the lattice of a frequency selective surface (*e.g.*, seams between printed circuits boards), have been imaged and analyzed. Attention is paid to both amplitude and phase of the reconstructed fields, as well as different visualization options, such as different scales and components of the fields (co- or cross-polarizations of the electric or magnetic components), or the Poynting's vector, to discover as much properties as possible of the electromagnetic fields on the radome surface.

Based on the investigations within the scope of this thesis, it is concluded that the source reconstruction method has great potential of becoming a useful diagnostics tool in radome design and evaluation processes. Below, some suggestions of how the method can be incorporated as a diagnostics tool, together with further development proposals, are listed.

- Source reconstruction can be utilized in delivery controls to guarantee manufacturing tolerances, *e.g.*, the insertion phase delay (IPD), for specific antenna illuminations.

  This is demonstrated in Papers II-V, where the IPD of the radome wall is investigated.

- In performance validations, there is a need to understand the cause of deviations in far-field data; transmission loss, beam deflection, side-lobe deviations *etc.* A comparison, between the reconstructed tangential electromagnetic fields on the radome surface and the expected ones derived from the theoretical design, is suggested to reveal the errors and their influences. Another example is the requirement of a trimming mask to reduce beam deflection caused by a monolithic radome. A proposal is to utilize source reconstruction for a couple of set-ups where the illuminations (the antenna positions) are directed towards the areas on the radome that give rise to the largest beam deflections. Images of the phase shifts (IPD) on the radome surface reveal areas of the wall that are either too thick or too thin, and thereby need trimming.

  Several defects and their influences on the electromagnetic fields are investigated in Papers I-V. Specifically, thickness deviations of the radome wall are explored in Paper IV.

- Placement of Pitot tubes, lightning conductors, the attachment of the radome to the hull of the aircraft, and errors in the periodic lattice of a frequency selective surface, change the electrical performance of the radome. Reconstruction of the tangential electromagnetic fields on the radome surface gives an understanding of these influences. To get detailed information about a certain defect, a couple of illuminations can be employed in the reconstruction. The

idea is that different visualization techniques (such as, division of the tangential electromagnetic field in different components, imaging in different scales, and applying filtering masks) reveal properties of the defect. Employing carefully chosen illuminations, *i.e.*, relevant polarizations and incident angles, one might be able to diagnose blockage of different field components, interference patterns, edge effects, introduction of side and flash lobes, *etc.*.

The concept is visualized in Papers I-V, where metallic and dielectric attachments have been studied in the Papers I-IV, whereas deviations in an frequency selective radome is imaged in V.

- A correct representation of the antenna radiation is essential as input in radome design software tools in order to model the antenna characteristics accurately. This can be achieved by the source reconstruction method, see [2, 22, 35, 36, 38, 57, 58, 71, 73, 74, 78, 79, 108, 111, 112, 115, 134, 151].

- Source reconstruction can also been utilized as a local verification tool in the design of radome design software tools. These design tools commonly predict the far field by modelling the propagation of the antenna radiation through the radome wall. However, if the predicted far field contains errors, it is hard to track the cause, *i.e.*, the area of the radome surface that is incorrectly modeled by the software. These areas are identified by making a local comparison against the reconstructed electromagnetic fields.

- In the future, it will be feasible to filter the influence of a defect. For example, assume a radome that gives rise to beam deflection. The radome is diagnosed by reconstruction of the IPD, which indicate that the radome has a too thick wall at a specific area, and it is proposed that the wall needs to be locally ground. The plan is to make a numerical simulation of the suggested surface alteration, in order to ensure that the proposed step (here grinding) creates the desired effect in the far-field data. That is, the reconstructed IPD is virtually manipulated in such a way that the change corresponds to the physical thinning of the wall. This IPD is then employed to calculate the far field to make sure that the proposed grinding does not change *e.g.*, side lobes in an undesirably way. This procedure guaranties that the suggested modifications lead to the required effects in the far-field data.

- Today, the regularization parameter in the SVD is set manually. Studies have shown that, for the investigated set-ups, the choice of this parameter within an interval leads to stable results, and the parameter needs only to be set once for a whole measurement series, see Paper IV. However, in future work, it is desirably to automatically set the regularization parameter. This can for example be achieved by employing a Tikhonov regularization with the associated L-curve [47, 67].

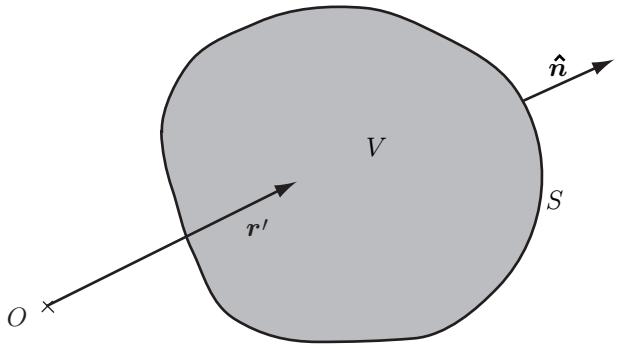

Figure 23: The domain V of integration and the variable of integration $\boldsymbol{r}'$.

Appendix A Surface integral representations and equations

There are several ways to derive surface integral representations and surface integral equations of the Maxwell equations [27, 54, 55, 63, 86, 89, 130, 139]. In this appendix, an alternative way is demonstrated [69, 142]. The aim is to give a basic understanding of the derivation, and rigorous mathematical definitions of function spaces *etc.*, are ignored.

The surface integral representation expresses the electromagnetic field in a homogeneous and isotropic region in terms of its values on the bounding surface. The representation states that if the electromagnetic field on a surface of a volume is known, the electromagnetic field in the volume can be determined [55, 130].

The representation is derived starting with two arbitrary scalar fields, $\phi(\boldsymbol{r}')$ and $\psi(\boldsymbol{r}')$, defined in a bounded domain V. The domain V is bounded by the surface S with outward pointing normal vector $\hat{\boldsymbol{n}}(\boldsymbol{r}')$, see Figure 23. *The Green's theorem*, reads [7, 129]

$$\iint_S [\phi(\boldsymbol{r}')\nabla'\psi(\boldsymbol{r}') - \psi(\boldsymbol{r}')\nabla'\phi(\boldsymbol{r}')] \cdot \hat{\boldsymbol{n}}(\boldsymbol{r}') \, \mathrm{d}S' = \iiint_V \left[\phi(\boldsymbol{r}')\nabla'^2\psi(\boldsymbol{r}') - \psi(\boldsymbol{r}')\nabla'^2\phi(\boldsymbol{r}')\right] \mathrm{d}v' \quad \text{(A.1)}$$

Proceeding to the representation of vector fields, let the scalar field $\phi(\boldsymbol{r}')$ in (A.1) be $[\boldsymbol{a} \cdot \boldsymbol{F}(\boldsymbol{r}')]$, where $\boldsymbol{a}$ is an arbitrary constant vector and $\boldsymbol{F}(\boldsymbol{r}')$ is a vector field. We have

$$\iint_S \Big\{[\boldsymbol{a} \cdot \boldsymbol{F}(\boldsymbol{r}')]\nabla'\psi(\boldsymbol{r}') - \psi(\boldsymbol{r}')\nabla'[\boldsymbol{a} \cdot \boldsymbol{F}(\boldsymbol{r}')]\Big\} \cdot \hat{\boldsymbol{n}}(\boldsymbol{r}') \, \mathrm{d}S' = \iiint_V \Big\{[\boldsymbol{a} \cdot \boldsymbol{F}(\boldsymbol{r}')]\nabla'^2\psi(\boldsymbol{r}') - \psi(\boldsymbol{r}')\nabla'^2[\boldsymbol{a} \cdot \boldsymbol{F}(\boldsymbol{r}')]\Big\} \, \mathrm{d}v'$$

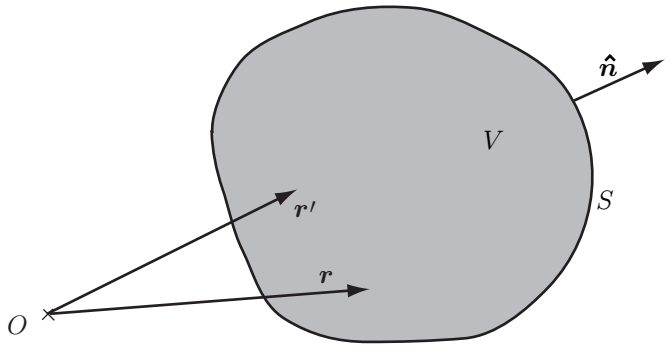

Figure 24: The domain V of integration. The variable of integration is denoted $\boldsymbol{r}'$ and the observation point $\boldsymbol{r}$.

Tedious algebra using differentiation rules of the nabla operator and the divergence theorem give [54, 88, 129]

$$\begin{aligned}
&\iint_S \Big(\psi(\boldsymbol{r}') \Big\{ \hat{\boldsymbol{n}}(\boldsymbol{r}') \times [\nabla' \times F(\boldsymbol{r}')] \Big\} + \nabla'\psi(\boldsymbol{r}') \big[\hat{\boldsymbol{n}}(\boldsymbol{r}') \cdot \boldsymbol{F}(\boldsymbol{r}') \big] \\
&\qquad - \psi(\boldsymbol{r}') \big[\nabla' \cdot F(\boldsymbol{r}') \big] \hat{\boldsymbol{n}}(\boldsymbol{r}') - \nabla'\psi(\boldsymbol{r}') \times \big[\hat{\boldsymbol{n}}(\boldsymbol{r}') \times \boldsymbol{F}(\boldsymbol{r}') \big] \Big) \, \mathrm{d}S' \\
&= \iiint_V \left(\boldsymbol{F}(\boldsymbol{r}') \, \nabla'^2 \psi(\boldsymbol{r}') + \psi(\boldsymbol{r}') \Big\{ \nabla' \times [\nabla' \times \boldsymbol{F}(\boldsymbol{r}')] - \nabla' [\nabla' \cdot \boldsymbol{F}(\boldsymbol{r}')] \Big\} \right) \mathrm{d}v' \qquad \text{(A.2)}
\end{aligned}$$

This equation is the foundation for finding integral representations of vector fields.

A.1 Introduction of the scalar free-space Green's function

Let the scalar field ψ in (A.2) be the scalar free-space Green's function,

$$g(\boldsymbol{r}, \boldsymbol{r}') = \frac{\mathrm{e}^{-\mathrm{j}k|\boldsymbol{r}-\boldsymbol{r}'|}}{4\pi|\boldsymbol{r}-\boldsymbol{r}'|}$$

using the time convention $\mathrm{e}^{\mathrm{j}\omega t}$. The variable of integration is denoted $\boldsymbol{r}'$ and the observation point $\boldsymbol{r}$, see Figure 24. Assume $\boldsymbol{r} \notin S$. The Green's function satisfies,

$$\nabla'^2 g(\boldsymbol{r}, \boldsymbol{r}') + k^2 g(\boldsymbol{r}, \boldsymbol{r}') = 0 \qquad\qquad \boldsymbol{r}' \neq \boldsymbol{r} \qquad\qquad \text{(A.3)}$$

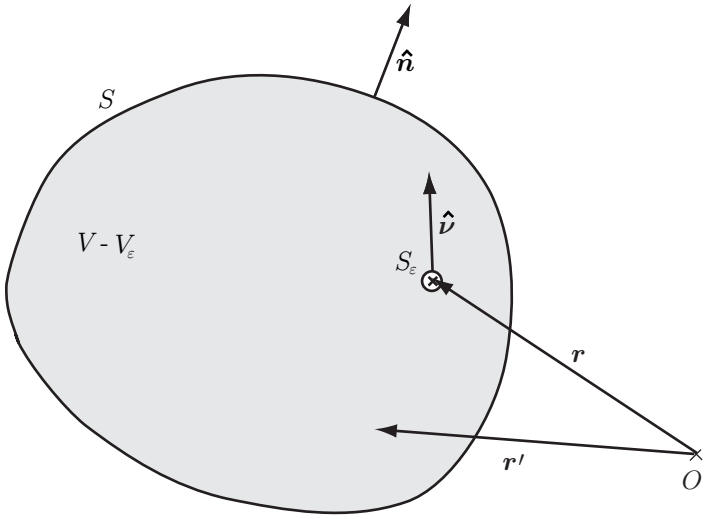

Figure 25: The geometry for the evaluation of the limit process. The volume V is punctuated by a ball of radius r_ϵ centered at the observation point $\boldsymbol{r}$. The bounding surface of this ball is S_ϵ and its volume is denoted V_ϵ.

where k is the wave number of the material. Replacing ψ in (A.2) with the scalar free-space Green's function and utilizing (A.3) gives

$$\begin{aligned}\iint_S \Big(& g(\boldsymbol{r},\boldsymbol{r}')\Big\{\hat{\boldsymbol{n}}(\boldsymbol{r}')\times\big[\nabla'\times\boldsymbol{F}(\boldsymbol{r}')\big]\Big\} + \nabla' g(\boldsymbol{r},\boldsymbol{r}')\big[\hat{\boldsymbol{n}}(\boldsymbol{r}')\cdot\boldsymbol{F}(\boldsymbol{r}')\big] \\ & - g(\boldsymbol{r},\boldsymbol{r}')\big[\nabla'\cdot\boldsymbol{F}(\boldsymbol{r}')\big]\hat{\boldsymbol{n}}(\boldsymbol{r}') - \nabla' g(\boldsymbol{r},\boldsymbol{r}')\times\big[\hat{\boldsymbol{n}}(\boldsymbol{r}')\times\boldsymbol{F}(\boldsymbol{r}')\big]\Big)\,\mathrm{d}S' \\ = \iiint_V & \Big(g(\boldsymbol{r},\boldsymbol{r}')\Big\{\nabla'\times\big[\nabla'\times\boldsymbol{F}(\boldsymbol{r}')\big] - \nabla'\big[\nabla'\cdot\boldsymbol{F}(\boldsymbol{r}')\big] - k^2\boldsymbol{F}(\boldsymbol{r}')\Big\}\Big)\,\mathrm{d}v' \end{aligned} \tag{A.4}$$

Now, let us investigate what happens when the observation point belongs to the volume V, *i.e.*, $\boldsymbol{r}\in V$. The Green's function is singular at the point $\boldsymbol{r}'=\boldsymbol{r}$ and this point must be avoided. Here, the integrals are investigated in the limit of classical integrals. That is, a small ball V_ϵ, centered at the singularity $\boldsymbol{r}$, is excluded. The radius of this ball is r_ϵ and its spherical bounding surface is denoted S_ϵ, see Figure 25. Letting the radius of the sphere approach zero, in (A.4), gives

$$\iint_S \ldots\ \mathrm{d}S' + \lim_{r_\epsilon\to 0}\iint_{S_\epsilon}\ldots\ \mathrm{d}S' = \iiint_V \ldots\ \mathrm{d}v' - \lim_{r_\epsilon\to 0}\iiint_{V_\epsilon}\ldots\ \mathrm{d}v' \tag{A.5}$$

The surface S_ϵ is parameterized in spherical coordinates, *i.e.*, $r_\epsilon>0$, $0\leqslant\varphi\leqslant 2\pi$, and $0\leqslant\theta\leqslant\pi$, with $\hat{\boldsymbol{e}}_z$ as the symmetry axis. The used notation is, *cf.*, Figure 26,

$$\begin{aligned} r_\epsilon &= |\boldsymbol{r}'-\boldsymbol{r}| & \mathrm{d}S &= r_\epsilon^2\sin\theta\,\mathrm{d}\varphi\,\mathrm{d}\theta \\ \hat{\boldsymbol{n}} &= -\hat{\boldsymbol{\nu}} & \mathrm{d}v &= r_\epsilon^2\sin\theta\,\mathrm{d}r_\epsilon\,\mathrm{d}\varphi\,\mathrm{d}\theta \end{aligned} \tag{A.6}$$

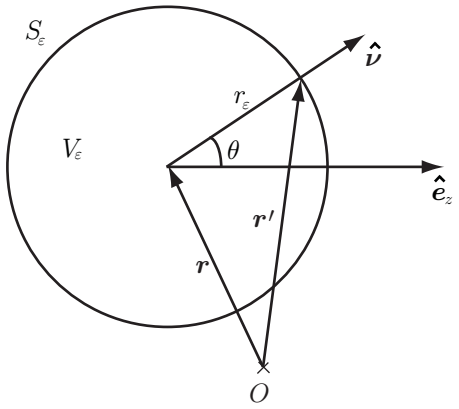

Figure 26: The geometry and notation for the evaluation of integrals over the sphere S_ϵ.

$$\begin{aligned}\hat{\boldsymbol{\nu}} &= \frac{\boldsymbol{r}'-\boldsymbol{r}}{r_\epsilon} = \cos\varphi\sin\theta\,\hat{\boldsymbol{e}}_x + \sin\varphi\sin\theta\,\hat{\boldsymbol{e}}_y + \cos\theta\,\hat{\boldsymbol{e}}_z \\ \nabla' g(\boldsymbol{r},\boldsymbol{r}') &= \frac{(\boldsymbol{r}-\boldsymbol{r}')\,\mathrm{e}^{-\mathrm{j}k|\boldsymbol{r}-\boldsymbol{r}'|}}{4\pi|\boldsymbol{r}-\boldsymbol{r}'|^3}\big[1+\mathrm{j}k|\boldsymbol{r}-\boldsymbol{r}'|\big] = \hat{\boldsymbol{n}}\,\frac{\mathrm{e}^{-\mathrm{j}kr_\epsilon}}{4\pi r_\epsilon}\left[\frac{1}{r_\epsilon}+\mathrm{j}k\right]\end{aligned} \tag{A.7}$$

where $\hat{\boldsymbol{e}}$ denotes the Cartesian orthonormal basis vectors in the x-, y-, and z-direction, respectively.

In the integrals over the small sphere S_ϵ, the normal unit vector $\hat{\boldsymbol{\nu}}$ varies rapidly over the integral domain while the fields $\boldsymbol{F}$, $[\nabla\cdot\boldsymbol{F}]$, $[\nabla\times\boldsymbol{F}]$, $\{\nabla\times\big[\nabla\times\boldsymbol{F}\big]\}$, and $\{\nabla\big[\nabla\cdot\boldsymbol{F}\big]\}$ are assumed to vary more slowly. Provided these fields are continuous, the mean value theorem for integrals implies that in the limit of $r_\epsilon\to 0$, the fields can be evaluated at the singular point $\boldsymbol{r}$ [27]. Letting $r_\epsilon\to 0$, results in the following limits for the different parts in (A.4).

$$\begin{aligned}&\lim_{r_\epsilon\to 0}\iint_{S_\epsilon} g(\boldsymbol{r},\boldsymbol{r}')\Big\{\hat{\boldsymbol{n}}(\boldsymbol{r}')\times\big[\nabla'\times\boldsymbol{F}(\boldsymbol{r}')\big]\Big\}\,\mathrm{d}S' \\ &\quad=\lim_{r_\epsilon\to 0}\iint_{S_\epsilon}\frac{\mathrm{e}^{-\mathrm{j}kr_\epsilon}}{4\pi r_\epsilon}\Big\{\hat{\boldsymbol{n}}(\boldsymbol{r}')\times\big[\nabla'\times\boldsymbol{F}(\boldsymbol{r}')\big]\Big\}\,r_\epsilon^2\sin\theta'\,\mathrm{d}\varphi'\,\mathrm{d}\theta' = \boldsymbol{0} \\ &\lim_{r_\epsilon\to 0}\iint_{S_\epsilon}\nabla' g(\boldsymbol{r},\boldsymbol{r}')\big[\hat{\boldsymbol{n}}(\boldsymbol{r}')\cdot\boldsymbol{F}(\boldsymbol{r}')\big]\,\mathrm{d}S' \\ &\quad=\lim_{r_\epsilon\to 0}\iint_{S_\epsilon}\hat{\boldsymbol{n}}(\boldsymbol{r}')\,\frac{\mathrm{e}^{-\mathrm{j}kr_\epsilon}}{4\pi r_\epsilon}\left[\frac{1}{r_\epsilon}+\mathrm{j}k\right]\big[\hat{\boldsymbol{n}}(\boldsymbol{r}')\cdot\boldsymbol{F}(\boldsymbol{r}')\big]\,r_\epsilon^2\sin\theta'\,\mathrm{d}\varphi'\,\mathrm{d}\theta' \\ &\quad=\frac{1}{4\pi}\iint_{S_\epsilon}\hat{\boldsymbol{n}}(\boldsymbol{r}')\,\big[\hat{\boldsymbol{n}}(\boldsymbol{r}')\cdot\boldsymbol{F}(\boldsymbol{r})\big]\sin\theta'\,\mathrm{d}\varphi'\,\mathrm{d}\theta' = \frac{1}{3}\boldsymbol{F}(\boldsymbol{r})\end{aligned}$$

$$\lim_{r_\epsilon\to 0}\iint\limits_{S_\epsilon} g(\boldsymbol{r},\boldsymbol{r}')\big[\nabla'\cdot\boldsymbol{F}(\boldsymbol{r}')\big]\hat{\boldsymbol{n}}(\boldsymbol{r}')\,\mathrm{d}S'$$

$$=\lim_{r_\epsilon\to 0}\iint\limits_{S_\epsilon}\frac{\mathrm{e}^{-\mathrm{j}kr_\epsilon}}{4\pi r_\epsilon}\big[\nabla'\cdot\boldsymbol{F}(\boldsymbol{r}')\big]\,\hat{\boldsymbol{n}}(\boldsymbol{r}')\,r_\epsilon^2\sin\theta'\,\mathrm{d}\varphi'\,\mathrm{d}\theta'=\boldsymbol{0}$$

$$\lim_{r_\epsilon\to 0}\iint\limits_{S_\epsilon}\nabla' g(\boldsymbol{r},\boldsymbol{r}')\times\big[\hat{\boldsymbol{n}}(\boldsymbol{r}')\times\boldsymbol{F}(\boldsymbol{r}')\big]\,\mathrm{d}S'$$

$$=\lim_{r_\epsilon\to 0}\iint\limits_{S_\epsilon}\hat{\boldsymbol{n}}(\boldsymbol{r}')\frac{\mathrm{e}^{-\mathrm{j}kr_\epsilon}}{4\pi r_\epsilon}\left[\frac{1}{r_\epsilon}+\mathrm{j}k\right]\times\big[\hat{\boldsymbol{n}}(\boldsymbol{r}')\times\boldsymbol{F}(\boldsymbol{r}')\big]\,r_\epsilon^2\sin\theta'\,\mathrm{d}\varphi'\,\mathrm{d}\theta'$$

$$=\frac{1}{4\pi}\iint\limits_{S_\epsilon}\hat{\boldsymbol{n}}(\boldsymbol{r}')\times\big[\hat{\boldsymbol{n}}(\boldsymbol{r}')\times\boldsymbol{F}(\boldsymbol{r})\big]\sin\theta'\,\mathrm{d}\varphi'\,\mathrm{d}\theta'$$

$$=\frac{1}{4\pi}\iint\limits_{S_\epsilon}\Big\{\hat{\boldsymbol{n}}(\boldsymbol{r}')\big[\hat{\boldsymbol{n}}(\boldsymbol{r}')\cdot\boldsymbol{F}(\boldsymbol{r})\big]-\boldsymbol{F}(\boldsymbol{r})\big[\hat{\boldsymbol{n}}(\boldsymbol{r}')\cdot\hat{\boldsymbol{n}}(\boldsymbol{r}')\big]\Big\}\sin\theta'\,\mathrm{d}\varphi'\,\mathrm{d}\theta'$$

$$=\frac{1}{4\pi}\Big[\frac{4\pi}{3}\boldsymbol{F}(\boldsymbol{r})-4\pi\boldsymbol{F}(\boldsymbol{r})\Big]=-\frac{2}{3}\boldsymbol{F}(\boldsymbol{r})$$

$$\lim_{r_\epsilon\to 0}\iiint\limits_{V_\epsilon} g(\boldsymbol{r},\boldsymbol{r}')\Big\{\nabla'\times\big[\nabla'\times\boldsymbol{F}(\boldsymbol{r}')\big]-\nabla'\big[\nabla'\cdot\boldsymbol{F}(\boldsymbol{r}')\big]-k^2\boldsymbol{F}(\boldsymbol{r}')\Big\}\,\mathrm{d}v'$$

$$=\lim_{r_\epsilon\to 0}\iiint\limits_{V_\epsilon}\frac{\mathrm{e}^{-\mathrm{j}kr_\epsilon}}{4\pi r_\epsilon}\Big\{\nabla'\times\big[\nabla'\times\boldsymbol{F}(\boldsymbol{r}')\big]-\nabla'\big[\nabla'\cdot\boldsymbol{F}(\boldsymbol{r}')\big]$$

$$-k^2\boldsymbol{F}(\boldsymbol{r}')\Big\}\,r_\epsilon^2\sin\theta'\,\mathrm{d}r_\epsilon\,\mathrm{d}\varphi'\,\mathrm{d}\theta'=\boldsymbol{0}$$

The parts are inserted into (A.5) giving

$$\iint\limits_S \ldots\,\mathrm{d}S'+\boldsymbol{F}(\boldsymbol{r})=\iiint\limits_V \ldots\,\mathrm{d}v'\qquad \boldsymbol{r}\in V$$

Until now we have assumed that $\boldsymbol{r}$ belongs to the volume V. If $\boldsymbol{r}\notin V$ the integrals in (A.4) are not singular. The results are collected in the following integral representation

$$\begin{aligned}&\iiint\limits_V\left(g(\boldsymbol{r},\boldsymbol{r}')\Big\{\nabla'\times\big[\nabla'\times\boldsymbol{F}(\boldsymbol{r}')\big]-\nabla'\big[\nabla'\cdot\boldsymbol{F}(\boldsymbol{r}')\big]-k^2\boldsymbol{F}(\boldsymbol{r}')\Big\}\right)\mathrm{d}v'\\&-\iint\limits_S\Big(g(\boldsymbol{r},\boldsymbol{r}')\Big\{\hat{\boldsymbol{n}}(\boldsymbol{r}')\times\big[\nabla'\times\boldsymbol{F}(\boldsymbol{r}')\big]\Big\}+\nabla' g(\boldsymbol{r},\boldsymbol{r}')\big[\hat{\boldsymbol{n}}(\boldsymbol{r}')\cdot\boldsymbol{F}(\boldsymbol{r}')\big]\\&\quad-g(\boldsymbol{r},\boldsymbol{r}')\big[\nabla'\cdot\boldsymbol{F}(\boldsymbol{r}')\big]\hat{\boldsymbol{n}}(\boldsymbol{r}')-\nabla' g(\boldsymbol{r},\boldsymbol{r}')\times\big[\hat{\boldsymbol{n}}(\boldsymbol{r}')\times\boldsymbol{F}(\boldsymbol{r}')\big]\Big)\,\mathrm{d}S'\\&=\begin{cases}\boldsymbol{F}(\boldsymbol{r}) & \boldsymbol{r}\in V\\ \boldsymbol{0} & \boldsymbol{r}\notin V\end{cases}\end{aligned}\tag{A.8}$$

This is a general representation of a vector field $\boldsymbol{F}$. The field $\boldsymbol{F}$ is represented as a volume integral of its values in V and as a surface integral of its values over the bounding surface S of V. If these integrals are evaluated at a point $\boldsymbol{r}$ that lies outside the volume V, these integrals cancel each other — the extinction theorem [25, 130]. It is important to notice that this does not necessarily mean that the field $\boldsymbol{F}$ is identically zero outside the volume V — only the values of the integrals cancel. As stated above, it is assumed that $\boldsymbol{r} \notin S$.

A.2 Introduction of the Maxwell equations

So far, the vector field $\boldsymbol{F}$ has been an arbitrary vector field. This field can be chosen as the electric or magnetic field that satisfies the source-free Maxwell equations with the time convention $\mathrm{e}^{\mathrm{j}\omega t}$, *i.e.*,

$$\begin{cases} \nabla \times \boldsymbol{E} = -\mathrm{j}\omega \boldsymbol{B} \\ \nabla \times \boldsymbol{H} = \mathrm{j}\omega \boldsymbol{D} \end{cases} \tag{A.9}$$

Moreover, assuming that the material inside the volume V is isotropic and homogeneous, the constitutive relations are given by

$$\begin{cases} \boldsymbol{D} = \epsilon_0 \epsilon \boldsymbol{E} \\ \boldsymbol{B} = \mu_0 \mu \boldsymbol{H} \end{cases} \tag{A.10}$$

Combination of (A.9) and (A.10) give

$$\begin{cases} \nabla \times \boldsymbol{E} = -\mathrm{j}\omega \mu_0 \mu \boldsymbol{H} \\ \nabla \times \boldsymbol{H} = \mathrm{j}\omega \epsilon_0 \epsilon \boldsymbol{E} \end{cases} \tag{A.11}$$

$$\begin{cases} \nabla \times (\nabla \times \boldsymbol{E}) = k^2 \boldsymbol{E} \\ \nabla \times (\nabla \times \boldsymbol{H}) = k^2 \boldsymbol{H} \end{cases} \tag{A.12}$$

$$\begin{cases} \nabla \cdot \boldsymbol{E} = 0 \\ \nabla \cdot \boldsymbol{H} = 0 \end{cases} \tag{A.13}$$

where ϵ_0 is the permittivity of free space, ϵ the relative permittivity, μ_0 the permeability of free space, μ the relative permeability, ω the angular frequency, and $k = \omega\sqrt{\epsilon_0 \mu_0 \epsilon \mu}$ the wave number.

Let $\boldsymbol{F}$ in (A.8) be the electric field $\boldsymbol{E}$. Together with (A.11)-(A.13) a surface integral representation for the electric field, is obtained

$$\begin{aligned} \iint_S \Big\{ & \mathrm{j}\omega\mu_0\mu \; g(\boldsymbol{r}, \boldsymbol{r}') \big[\hat{\boldsymbol{n}}(\boldsymbol{r}') \times \boldsymbol{H}(\boldsymbol{r}')\big] - \nabla' g(\boldsymbol{r}, \boldsymbol{r}') \big[\hat{\boldsymbol{n}}(\boldsymbol{r}') \cdot \boldsymbol{E}(\boldsymbol{r}')\big] \\ & + \nabla' g(\boldsymbol{r}, \boldsymbol{r}') \times \big[\hat{\boldsymbol{n}}(\boldsymbol{r}') \times \boldsymbol{E}(\boldsymbol{r}')\big] \Big\} \, \mathrm{d}S' = \begin{cases} \boldsymbol{E}(\boldsymbol{r}) & \boldsymbol{r} \text{ inside } S \\ \boldsymbol{0} & \boldsymbol{r} \text{ outside } S \end{cases} \end{aligned} \tag{A.14}$$

where the surface S is shown in Figure 24. Observe that the volume integral is zero and only the surface integral remains. If $\boldsymbol{F}$ is interchanged by the magnetic field $\boldsymbol{H}$, a surface integral representation for the magnetic field is attained. The surface integral representation (A.14) contains both the normal and the tangential components of the electromagnetic field. In practice, it is more convenient to work only with the tangential fields. The normal component, the second term in (A.14), can be written in terms of a tangential component by an application of the Maxwell equations (A.9)-(A.10),

$$\hat{\boldsymbol{n}}(\boldsymbol{r}) \cdot \boldsymbol{E}(\boldsymbol{r}) = -\mathrm{j}\frac{1}{\omega\epsilon_0\epsilon}\ \hat{\boldsymbol{n}}(\boldsymbol{r}) \cdot \big[\nabla \times \boldsymbol{H}(\boldsymbol{r})\big] = \mathrm{j}\frac{1}{\omega\epsilon_0\epsilon}\ \nabla_S \cdot \big[\hat{\boldsymbol{n}}(\boldsymbol{r}) \times \boldsymbol{H}(\boldsymbol{r})\big]$$

where the identity $\nabla_S \cdot (\hat{\boldsymbol{n}} \times \boldsymbol{a}) = -\hat{\boldsymbol{n}} \cdot (\nabla \times \boldsymbol{a})$ is used with $\boldsymbol{a}$ denoting an arbitrary vector and $\nabla_S \cdot$ the surface divergence [27]. That gives *a surface integral representation for the electric field* consisting of only tangential components on the surface S,

$$\iint_S \Bigg(\mathrm{j}\omega\mu_0\mu\ g(\boldsymbol{r},\boldsymbol{r}')\big[\hat{\boldsymbol{n}}(\boldsymbol{r}') \times \boldsymbol{H}(\boldsymbol{r}')\big] - \mathrm{j}\frac{1}{\omega\epsilon_0\epsilon}\ \nabla' g(\boldsymbol{r},\boldsymbol{r}')\Big\{\nabla'_S \cdot \big[\hat{\boldsymbol{n}}(\boldsymbol{r}') \times \boldsymbol{H}(\boldsymbol{r}')\big]\Big\} + \nabla' g(\boldsymbol{r},\boldsymbol{r}') \times \big[\hat{\boldsymbol{n}}(\boldsymbol{r}') \times \boldsymbol{E}(\boldsymbol{r}')\big] \Bigg)\ \mathrm{d}S' = \begin{cases} \boldsymbol{E}(\boldsymbol{r}) & \boldsymbol{r} \text{ inside } S \\ \boldsymbol{0} & \boldsymbol{r} \text{ outside } S \end{cases} \tag{A.15}$$

A.3 Values of the integral equations on the bounding surface

The integral representation in (A.15) is defined for all $\boldsymbol{r} \notin S$. To include the surface into the domain it must be studied what happens as $\boldsymbol{r}$ approaches S. At this stage of the derivation it is not even clear that these limit values exist at all. The integrands in (A.15) become singular as $\boldsymbol{r}$ moves toward the surface. This singularity can be treated in several ways. Here, a classic approach is used, where the limit is investigated by adding a half sphere from the outside and the inside, respectively [139].

Starting with the approach from the outside, the surface integral representation (A.15) reads

$$\iint_S \Bigg(\mathrm{j}\omega\mu_0\mu\ g(\boldsymbol{r},\boldsymbol{r}')\big[\hat{\boldsymbol{n}}(\boldsymbol{r}') \times \boldsymbol{H}(\boldsymbol{r}')\big] - \mathrm{j}\frac{1}{\omega\epsilon_0\epsilon}\ \nabla' g(\boldsymbol{r},\boldsymbol{r}')\Big\{\nabla'_S \cdot \big[\hat{\boldsymbol{n}}(\boldsymbol{r}') \times \boldsymbol{H}(\boldsymbol{r}')\big]\Big\} + \nabla' g(\boldsymbol{r},\boldsymbol{r}') \times \big[\hat{\boldsymbol{n}}(\boldsymbol{r}') \times \boldsymbol{E}(\boldsymbol{r}')\big] \Bigg)\ \mathrm{d}S' = \boldsymbol{0} \qquad \boldsymbol{r} \notin V$$

and it is applied to a volume V_{punc}, which is slightly deformed compared to the original volume V, *i.e.*, a small half ball of radius r_ϵ is excluded. The bounding surface of the volume V_{punc} is denoted S' and consists of two parts; the punctuated

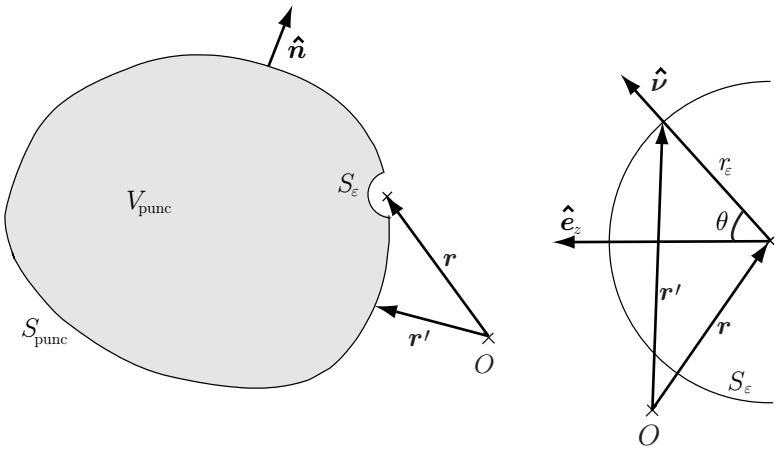

(a) (b)

Figure 27: (a) The geometry and notation for the evaluation of the limit process taken from the outside. (b) The parametrization of the half sphere S_ϵ. Notice that $\hat{\boldsymbol{n}} = -\hat{\boldsymbol{\nu}}$.

surface S_{punc}, and a half sphere S_ϵ of radius r_ϵ, *i.e.*, $S' = S_{\text{punc}} \cup S_\epsilon$, see Figure 27a. In the limit $r_\epsilon \to 0$ the surface $S' \to S$ and $V_{\text{punc}} \to V$, *i.e.*,

$$\lim_{r_\epsilon \to 0} \iint\limits_{S'} \ldots \, \mathrm{d}S' = \iint\limits_{S} \ldots \, \mathrm{d}S' + \lim_{r_\epsilon \to 0} \iint\limits_{S_\epsilon} \ldots \, \mathrm{d}S' \tag{A.16}$$

where the integral $\iint \ldots \, \mathrm{d}S$ denotes Cauchy's principal value [105].

To investigate the limit of the integral over the surface S_ϵ, this surface is parameterized by the spherical angles $0 \leqslant \varphi \leqslant 2\pi$ and $0 \leqslant \theta \leqslant \pi/2$ with the direction $\boldsymbol{e}_z$ as the symmetry axis, see Figure 27b and (A.6)-(A.7). The normal unit vector $\hat{\boldsymbol{\nu}}$ varies rapidly over the small half sphere S_ϵ, while the electromagnetic fields $\boldsymbol{E}$ and $\boldsymbol{H}$ are assumed to vary more slowly. Provided these fields are continuous, the mean value theorem for integrals implies that in the limit of $r_\epsilon \to 0$ the fields can be evaluated at the point $\boldsymbol{r}$ [27]. Letting $r_\epsilon \to 0$, results in the following limits for the different parts

$$\begin{aligned}
&\lim_{r_\epsilon \to 0} \iint\limits_{S_\epsilon} g(\boldsymbol{r}, \boldsymbol{r}') \big[\hat{\boldsymbol{n}}(\boldsymbol{r}') \times \boldsymbol{H}(\boldsymbol{r}')\big] \, \mathrm{d}S' \\
&\qquad = \lim_{r_\epsilon \to 0} \iint\limits_{S_\epsilon} \frac{\mathrm{e}^{-\mathrm{j}kr_\epsilon}}{4\pi r_\epsilon} \big[-\hat{\boldsymbol{\nu}}(\boldsymbol{r}') \times \boldsymbol{H}(\boldsymbol{r}')\big] \, r_\epsilon^2 \sin\theta' \, \mathrm{d}\varphi' \, \mathrm{d}\theta' = \boldsymbol{0} \\
&\lim_{r_\epsilon \to 0} \iint\limits_{S_\epsilon} -\mathrm{j}\frac{1}{\omega\epsilon_0\epsilon} \, \nabla' g(\boldsymbol{r}, \boldsymbol{r}') \Big\{ \nabla'_S \cdot \big[\hat{\boldsymbol{n}}(\boldsymbol{r}') \times \boldsymbol{H}(\boldsymbol{r}')\big] \Big\} \, \mathrm{d}S' \\
&\qquad = \lim_{r_\epsilon \to 0} \iint\limits_{S_\epsilon} -\nabla' g(\boldsymbol{r}, \boldsymbol{r}') \big[\hat{\boldsymbol{n}}(\boldsymbol{r}') \cdot \boldsymbol{E}(\boldsymbol{r}')\big] \, \mathrm{d}S'
\end{aligned}$$

$$= \lim_{r_\epsilon \to 0} \iint\limits_{S_\epsilon} \hat{\boldsymbol{\nu}}(\boldsymbol{r}') \, \frac{\mathrm{e}^{-\mathrm{j}kr_\epsilon}}{4\pi r_\epsilon} \left[\frac{1}{r_\epsilon} + \mathrm{j}k\right] \left[-\hat{\boldsymbol{\nu}}(\boldsymbol{r}') \cdot \boldsymbol{E}(\boldsymbol{r}')\right] r_\epsilon^2 \sin\theta' \, \mathrm{d}\varphi' \, \mathrm{d}\theta'$$

$$= -\frac{1}{4\pi} \iint\limits_{S_\epsilon} \hat{\boldsymbol{\nu}}(\boldsymbol{r}') \left[\hat{\boldsymbol{\nu}}(\boldsymbol{r}') \cdot \boldsymbol{E}(\boldsymbol{r})\right] \sin\theta' \, \mathrm{d}\varphi' \, \mathrm{d}\theta' = -\frac{1}{6}\boldsymbol{E}(\boldsymbol{r})$$

$$\lim_{r_\epsilon \to 0} \iint\limits_{S_\epsilon} \nabla' g(\boldsymbol{r}, \boldsymbol{r}') \times \left[\hat{\boldsymbol{n}}(\boldsymbol{r}') \times \boldsymbol{E}(\boldsymbol{r}')\right] \, \mathrm{d}S'$$

$$= \lim_{r_\epsilon \to 0} \iint\limits_{S_\epsilon} -\hat{\boldsymbol{\nu}}(\boldsymbol{r}') \, \frac{\mathrm{e}^{-\mathrm{j}kr_\epsilon}}{4\pi r_\epsilon} \left[\frac{1}{r_\epsilon} + \mathrm{j}k\right] \times \left[-\hat{\boldsymbol{\nu}}(\boldsymbol{r}') \times \boldsymbol{E}(\boldsymbol{r}')\right] r_\epsilon^2 \sin\theta' \, \mathrm{d}\varphi' \, \mathrm{d}\theta'$$

$$= \frac{1}{4\pi} \iint\limits_{S_\epsilon} \hat{\boldsymbol{\nu}}(\boldsymbol{r}') \times \left[\hat{\boldsymbol{\nu}}(\boldsymbol{r}') \times \boldsymbol{E}(\boldsymbol{r})\right] \sin\theta' \, \mathrm{d}\varphi' \, \mathrm{d}\theta'$$

$$= \frac{1}{4\pi} \int_{\theta'=0}^{\pi/2} \int_{\varphi'=0}^{2\pi} \Big\{\hat{\boldsymbol{\nu}}(\boldsymbol{r}') \big[\hat{\boldsymbol{\nu}}(\boldsymbol{r}') \cdot \boldsymbol{E}(\boldsymbol{r})\big] - \boldsymbol{E}(\boldsymbol{r}) \big[\hat{\boldsymbol{\nu}}(\boldsymbol{r}') \cdot \hat{\boldsymbol{\nu}}(\boldsymbol{r}')\big]\Big\} \sin\theta' \, \mathrm{d}\varphi' \, \mathrm{d}\theta'$$

$$= \frac{1}{4\pi} \Big[\frac{2\pi}{3}\boldsymbol{E}(\boldsymbol{r}) - 2\pi\boldsymbol{E}(\boldsymbol{r})\Big] = -\frac{1}{3}\boldsymbol{E}(\boldsymbol{r})$$

The limit values above are plugged into (A.16), giving

$$\iint\limits_S \Bigg(\mathrm{j}\omega\mu_0\mu \; g(\boldsymbol{r}, \boldsymbol{r}') \big[\hat{\boldsymbol{n}}(\boldsymbol{r}') \times \boldsymbol{H}(\boldsymbol{r}')\big] - \mathrm{j}\frac{1}{\omega\epsilon_0\epsilon} \; \nabla' g(\boldsymbol{r}, \boldsymbol{r}') \Big\{\nabla'_S \cdot \big[\hat{\boldsymbol{n}}(\boldsymbol{r}') \times \boldsymbol{H}(\boldsymbol{r}')\big]\Big\}$$

$$+ \nabla' g(\boldsymbol{r}, \boldsymbol{r}') \times \big[\hat{\boldsymbol{n}}(\boldsymbol{r}') \times \boldsymbol{E}(\boldsymbol{r}')\big]\Bigg) \, \mathrm{d}S' = \frac{1}{2}\,\boldsymbol{E}(\boldsymbol{r}) \qquad \boldsymbol{r} \in S \quad \text{(A.17)}$$

which is the limit value of the surface integral representation for the electric field when approaching from the outside.

If the limit is taken from the inside instead, the surface integral representation, (A.15),

$$\iint\limits_S \Bigg(\mathrm{j}\omega\mu_0\mu \; g(\boldsymbol{r}, \boldsymbol{r}') \big[\hat{\boldsymbol{n}}(\boldsymbol{r}') \times \boldsymbol{H}(\boldsymbol{r}')\big] - \mathrm{j}\frac{1}{\omega\epsilon_0\epsilon_\mathrm{r}} \; \nabla' g(\boldsymbol{r}, \boldsymbol{r}') \Big\{\nabla'_S \cdot \big[\hat{\boldsymbol{n}}(\boldsymbol{r}') \times \boldsymbol{H}(\boldsymbol{r}')\big]\Big\}$$

$$+ \nabla' g(\boldsymbol{r}, \boldsymbol{r}') \times \big[\hat{\boldsymbol{n}}(\boldsymbol{r}') \times \boldsymbol{E}(\boldsymbol{r}')\big]\Bigg) \, \mathrm{d}S' = \boldsymbol{E}(\boldsymbol{r}) \qquad \boldsymbol{r} \in V \quad \text{(A.18)}$$

is applied to a volume V_punc shown in Figure 28a. The derivation is similar to the analysis above. The difference is that now $\hat{\boldsymbol{n}} = \hat{\boldsymbol{\nu}}$. This changes the sign in the limit processes, which inserted in (A.18) give the same final surface integral equation, *i.e.*, (A.17).

The representation (A.17) consists of three components, two describing the tangential field and one describing the normal component of the field. Since the normal

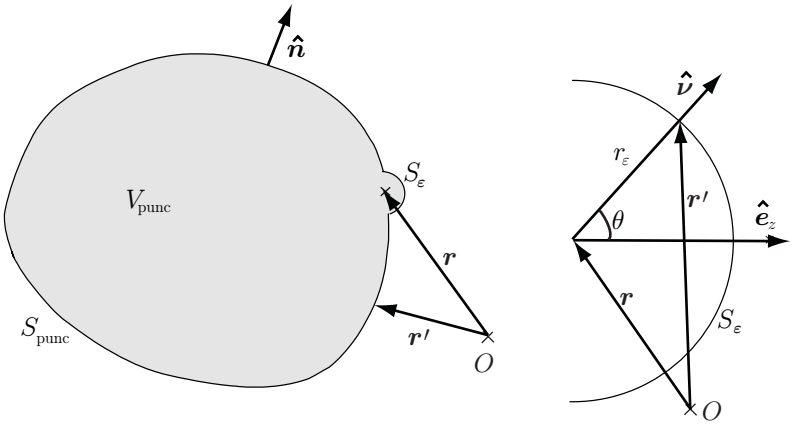

(a) (b)

Figure 28: (a) The notation and geometry for the evaluation of the limit process taken from the inside. (b) The parametrization of the half sphere S_ϵ. Observe that now $\hat{\boldsymbol{n}} = \hat{\boldsymbol{\nu}}$.

component can be determined by the knowledge of the tangential parts, the normal component can be eliminated [89], giving

$$\hat{\boldsymbol{n}}(\boldsymbol{r})\times\iint_S\Big(\mathrm{j}\omega\mu_0\mu\; g(\boldsymbol{r},\boldsymbol{r}')\big[\hat{\boldsymbol{n}}(\boldsymbol{r}')\times\boldsymbol{H}(\boldsymbol{r}')\big]-\mathrm{j}\frac{1}{\omega\epsilon_0\epsilon}\;\nabla' g(\boldsymbol{r},\boldsymbol{r}')\Big\{\nabla'_S\cdot\big[\hat{\boldsymbol{n}}(\boldsymbol{r}')\times\boldsymbol{H}(\boldsymbol{r}')\big]\Big\}$$
$$+\nabla' g(\boldsymbol{r},\boldsymbol{r}')\times\big[\hat{\boldsymbol{n}}(\boldsymbol{r}')\times\boldsymbol{E}(\boldsymbol{r}')\big]\Big)\;\mathrm{d}S'=\frac{1}{2}\,\hat{\boldsymbol{n}}(\boldsymbol{r})\times\boldsymbol{E}(\boldsymbol{r})\qquad \boldsymbol{r}\in S \quad \text{(A.19)}$$

A.4 The exterior problem

Sofar, we have derived a surface integral representation (A.15) and a surface integral equation (A.19), where the regions are defined in Figure 29a. Observe that all sources are assumed to be outside the surface S and that the electric field inside S can be determined by the electromagnetic fields on the border. The expressions do not give any information of the electromagnetic field outside the surface S.

In this thesis, the surface integral representation and equation are applied to the exterior problem (*cf.*, Figure 29b). That is, all sources are assumed to be inside the surface S and the electric field outside can be determined by the fields on the border. The outside volume is not bounded. However, employing the Silver-Müller radiation conditions, the solution of the Maxwell equations satisfies the following

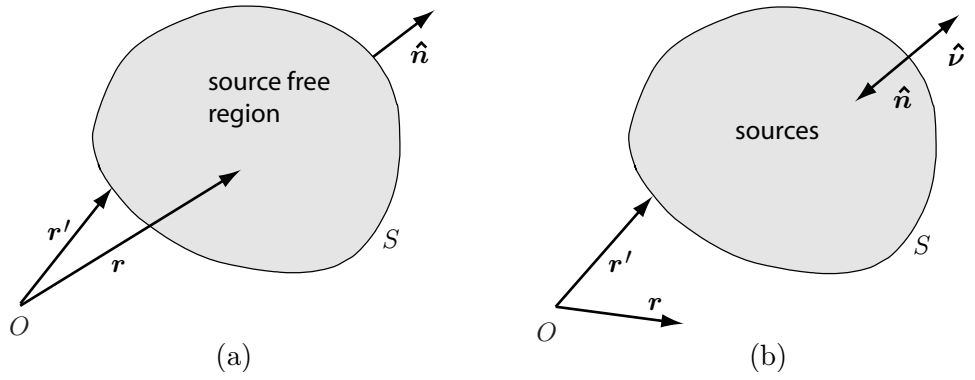

Figure 29: (a) The interior problem. (b) The exterior problem.

surface integral representation and equation [63, 89, 125, 130]

$$\begin{cases} \displaystyle\iint_S \Big(\mathrm{j}k\eta_0\; g(\boldsymbol{r},\boldsymbol{r}')\big[\hat{\boldsymbol{\nu}}(\boldsymbol{r}')\times\boldsymbol{H}(\boldsymbol{r}')\big] - \mathrm{j}\frac{\eta_0}{k}\;\nabla' g(\boldsymbol{r},\boldsymbol{r}')\Big\{\nabla'_S\cdot\big[\hat{\boldsymbol{\nu}}(\boldsymbol{r}')\times\boldsymbol{H}(\boldsymbol{r}')\big]\Big\} \\ \qquad + \nabla' g(\boldsymbol{r},\boldsymbol{r}')\times\big[\hat{\boldsymbol{\nu}}(\boldsymbol{r}')\times\boldsymbol{E}(\boldsymbol{r}')\big]\Big)\,\mathrm{d}S' = \begin{cases} -\boldsymbol{E}(\boldsymbol{r}) & \boldsymbol{r}\text{ outside }S \\ \boldsymbol{0} & \boldsymbol{r}\text{ inside }S \end{cases} \\ \hat{\boldsymbol{\nu}}(\boldsymbol{r})\times\displaystyle\iint\!\!\!\!\!\!-_S \Big(\mathrm{j}k\eta_0\; g(\boldsymbol{r},\boldsymbol{r}')\big[\hat{\boldsymbol{\nu}}(\boldsymbol{r}')\times\boldsymbol{H}(\boldsymbol{r}')\big] - \mathrm{j}\frac{\eta_0}{k}\;\nabla' g(\boldsymbol{r},\boldsymbol{r}')\Big\{\nabla'_S\cdot\big[\hat{\boldsymbol{\nu}}(\boldsymbol{r}')\times\boldsymbol{H}(\boldsymbol{r}')\big]\Big\} \\ \qquad + \nabla' g(\boldsymbol{r},\boldsymbol{r}')\times\big[\hat{\boldsymbol{\nu}}(\boldsymbol{r}')\times\boldsymbol{E}(\boldsymbol{r}')\big]\Big)\,\mathrm{d}S' = -\frac{1}{2}\,\hat{\boldsymbol{\nu}}(\boldsymbol{r})\times\boldsymbol{E}(\boldsymbol{r}) \qquad \boldsymbol{r}\in S \end{cases}$$

where the change of signs is due to the choice of normal, $\hat{\boldsymbol{\nu}} = -\hat{\boldsymbol{n}}$. Furthermore, the volume outside S is set to free space, *i.e.*, the intrinsic wave impedance being $\eta_0 = \sqrt{\frac{\mu_0}{\epsilon_0}}$ and the wave number is $k = \omega/c_0$, where c_0 is the speed of light in free space.

The tangential fields on the surface can be expressed as the electric and magnetic equivalent surface currents, $\boldsymbol{J}$ and $\boldsymbol{M}$, defined as [13, 54]

$$\begin{cases} \boldsymbol{J}(\boldsymbol{r}) = \hat{\boldsymbol{\nu}}(\boldsymbol{r})\times\boldsymbol{H}(\boldsymbol{r}) \\ \boldsymbol{M}(\boldsymbol{r}) = -\,\hat{\boldsymbol{\nu}}(\boldsymbol{r})\times\boldsymbol{E}(\boldsymbol{r}) \end{cases}$$

To further simplify the expressions, the operators $\mathcal{L}$ and $\mathcal{K}$ are introduced as [54]

$$\begin{cases} \mathcal{L}(\boldsymbol{X})(\boldsymbol{r}) = \mathrm{j}k\displaystyle\iint_S \Big\{ g(\boldsymbol{r}',\boldsymbol{r})\boldsymbol{X}(\boldsymbol{r}') - \frac{1}{k^2}\;\nabla' g(\boldsymbol{r}',\boldsymbol{r})\big[\nabla'_S\cdot\boldsymbol{X}(\boldsymbol{r}')\big]\Big\}\,\mathrm{d}S' \\ \mathcal{K}(\boldsymbol{X})(\boldsymbol{r}) = \displaystyle\iint_S \nabla' g(\boldsymbol{r}',\boldsymbol{r})\times\boldsymbol{X}(\boldsymbol{r}')\,\mathrm{d}S' \end{cases} \tag{A.20}$$

All collected, giving a surface integral representation and a surface integral equation

of the electric field

$$\begin{cases} \mathcal{L}\left(\eta_0 \boldsymbol{J}\right)(\boldsymbol{r}) - \mathcal{K}\left(\boldsymbol{M}\right)(\boldsymbol{r}) = \begin{cases} -\boldsymbol{E}(\boldsymbol{r}) & \boldsymbol{r} \text{ outside } S \\ \boldsymbol{0} & \boldsymbol{r} \text{ inside } S \end{cases} \\ \hat{\boldsymbol{\nu}}(\boldsymbol{r}) \times \left\{ \mathcal{L}\left(\eta_0 \boldsymbol{J}\right)(\boldsymbol{r}) - \mathcal{K}\left(\boldsymbol{M}\right)(\boldsymbol{r}) \right\} = \dfrac{1}{2}\boldsymbol{M}(\boldsymbol{r}) \qquad \boldsymbol{r} \in S \end{cases}$$

where the regions are depicted in Figure 29b, and the integrals are interpreted as Cauchy's principle value [27, 105] when necessary.

Sometimes it is preferable to utilize a surface integral equation of the magnetic field together with the surface integral representation. This equation can be derived in a similar way as shown above by letting the vector $\boldsymbol{F}$ in (A.8) be the magnetic field $\boldsymbol{H}$, resulting in

$$\hat{\boldsymbol{\nu}}(\boldsymbol{r}) \times \left\{ \mathcal{L}\left(\boldsymbol{M}\right)(\boldsymbol{r}) + \mathcal{K}\left(\eta_0 \boldsymbol{J}\right)(\boldsymbol{r}) \right\} = -\frac{\eta_0}{2}\boldsymbol{J}(\boldsymbol{r}) \qquad \boldsymbol{r} \in S$$

References

[1] Y. Alvarez, F. Las-Heras, and C. Garciain. The sources reconstruction method for antenna diagnostics and imaging applications. In A. Kishk, editor, *Solutions and Applications of Scattering, Propagation, Radiation and Emission of Electromagnetic Waves*. InTech, 2012.

[2] Y. Alvarez, F. Las-Heras, and M. R. Pino. Reconstruction of equivalent currents distribution over arbitrary three-dimensional surfaces based on integral equation algorithms. *IEEE Trans. Antennas Propagat.*, **55**(12), 3460–3468, 2007.

[3] Y. Alvarez, M. Rodríguez, F. Las-Heras, and M. M. Hernando. On the use of the source reconstruction method for estimating radiated EMI in electronic circuits. *Instrumentation and Measurement, IEEE Transactions on*, **59**(12), 3174–3183, 2010.

[4] M. Andersson. Software for analysis of radome performance. In *Proc. International Conference on Electromagnetics in Advanced Applications (ICEAA'05)*, pages 537–539, Torino, Italy, 2005.

[5] Andersson, Michael. Radomes & Antennas, GKN Aerospace Applied Composites, Garvaren, Stationsgatan 2, SE-341 60 Ljungby, Sweden, *Private communication*, 2013.

[6] M. Andreasen. Scattering from bodies of revolution. *IEEE Trans. Antennas Propagat.*, **13**(2), 303–310, 1965.

[7] G. Arfken. *Mathematical Methods for Physicists*. Academic Press, Orlando, third edition, 1985.

[8] R. Aster, B. Borchers, and C. Thurber. *Parameter Estimation and Inverse Problems*. Academic Press, New York, 2005.

[9] Bäckström, Mats. Saab Aeronautics, SE-581 88 Linköping, Sweden, *Private communication*, 2013.

[10] D. Balageas, S. Bourasseau, M. Dupont, E. Bocherens, V. Dewynter-Marty, and P. Ferdinand. Comparison between non-destructive evaluation techniques and integrated fiber optic health monitoring systems for composite sandwich structures. *Journal of intelligent material systems and structures*, **11**(6), 426–437, 2000.

[11] D. Balageas and P. Levesque. EMIR: a photothermal tool for electromagnetic phenomena characterization. *Revue générale de Thermique*, **37**(8), 725–739, 1998.

[12] C. A. Balanis. *Antenna Theory*. John Wiley & Sons, New Jersey, third edition, 2005.

[13] C. A. Balanis. *Advanced Engineering Electromagnetics*. John Wiley & Sons, New York, 1989.

[14] N. Bleistein and J. K. Cohen. Non-uniqueness in the inverse source problem in acoustics and electromagnetics. *J. Math. Phys.*, **18**(2), 194–201, 1977.

[15] J.-C. Bolomey and F. E. Gardiol. *Engineering applications of the modulated scatterer technique*. Artech House Publishers, 2001.

[16] A. Bondeson, T. Rylander, and P. Ingelström. *Computational Electromagnetics*. Springer-Verlag, Berlin, 2005.

[17] H. G. Booker and P. C. Clemmow. The concept of an angular spectrum of plane waves and its relation to that of polar diagram and aperture distribution. *Proc. Inst. Elec. Eng.*, **97**(1), 11–16, 1950.

[18] A. Boström, G. Kristensson, and S. Ström. Transformation properties of plane, spherical and cylindrical scalar and vector wave functions. In V. V. Varadan, A. Lakhtakia, and V. K. Varadan, editors, *Field Representations and Introduction to Scattering*, Acoustic, Electromagnetic and Elastic Wave Scattering, chapter 4, pages 165–210. Elsevier Science Publishers, Amsterdam, 1991.

[19] D. G. Burks. Radomes. In J. L. Volakis, editor, *Antenna engineering handbook*. pub-mcgraw, fourth edition, 2007.

[20] W. M. Cady, M. B. Karelitz, and L. A. Turner. *Radar Scanners and Radomes*, volume 26 of *Radiation Laboratory Series*. McGraw-Hill, New York, 1948.

[21] C. Cappellin, O. Breinbjerg, and A. Frandsen. Properties of the transformation from the spherical wave expansion to the plane wave expansion. *Radio Sci.*, **43**(1), 2008.

[22] C. Cappellin, A. Frandsen, and O. Breinbjerg. Application of the SWE-to-PWE antenna diagnostics technique to an offset reflector antenna. *IEEE Antennas and Propagation Magazine*, **50**(5), 204–213, 2008.

[23] C. Cappellin. *Antenna diagnostics for spherical near-field antenna measurements*. PhD thesis, Technical University of Denmark, 2007.

[24] M. Cheney and B. Borden. *Fundamentals of radar imaging*, volume 79. Society for Industrial Mathematics, 2009.

[25] W. C. Chew, M. S. Tong, and B. Hu. *Integral equation methods for electromagnetic and elastic waves*, volume 12. Morgan & Claypool, 2008.

[26] W. C. Chew, E. Michielssen, J. Song, and J. Jin. *Fast and efficient algorithms in computational electromagnetics*. Artech House, Inc., 2001.

[27] D. Colton and R. Kress. *Integral Equation Methods in Scattering Theory*. John Wiley & Sons, New York, 1983.

[28] L. E. Corey and E. B. Joy. On computation of electromagnetic fields on planar surfaces from fields specified on nearby surfaces. *IEEE Trans. Antennas Propagat.*, **29**(2), 402–404, 1981.

[29] G. Cottard, J. Y. Simon, J.-C. Bolomey, and D. Picard. Rapid IPD measurements by means of microwave imaging techniques. In *Proc. 6th European Electromagnetic Structures Conf.*, pages 313–320, Friedrichshafen, Germany, Sept. 1991.

[30] H. Damberg. *Kompositthandboken: polymerbaserade fiberkompositer*. Sveriges verkstadsindustrier (VI), Industrilitteratur AB, Stockholm, 2001. (In Swedish).

[31] A. Delogu and M. Mwanya. Design and testing of a radome for a beam steering radar antenna. In *Proc. International Conference on Electromagnetics in Advanced Applications (ICEAA'05)*, pages 505–508, Torino, Italy, 2005.

[32] A. J. Devaney and E. Wolf. Radiating and nonradiating classical current distributions and the fields they generate. *Phys. Rev. D*, **8**(4), 1044–1047, 1973.

[33] A. J. Devaney and E. Wolf. Multipole expansions and plane wave representations of the electromagnetic field. *J. Math. Phys.*, **15**(2), 234–244, 1974.

[34] A. J. Devaney. *Mathematical foundations of imaging, tomography and wavefield inversion*. Cambridge University Press, 2012.

[35] T. F. Eibert, E. Kaliyaperumal, and C. H. Schmidt. Inverse equivalent surface current method with hierarchical higher order basis functions, full probe correction and multilevel fast multipole acceleration. *Progress In Electromagnetics Research*, **106**, 377–394, 2010.

[36] T. F. Eibert and C. H. Schmidt. Multilevel fast multipole accelerated inverse equivalent current method employing Rao-Wilton-Glisson discretization of electric and magnetic surface currents. *IEEE Trans. Antennas Propagat.*, **57**(4), 1178–1185, 2009.

[37] L. C. Evans. *Partial Differential Equations*. American Mathematical Society, Providence, Rhode Island, 1998.

[38] L. J. Foged, L. Scialacqua, F. Saccardi, J. L. Araque Quijano, G. Vecchi, and M. Sabbadini. Practical application of the equivalent source method as an antenna diagnostics tool. *IEEE Antennas and Propagation Magazine*, **54**(5), 243–249, 2012.

[39] J. Fridén, H. Isaksson, B. Hansson, and B. Thors. Robust phase-retrieval for quick whole-body SAR assessment using dual plane amplitude-only data. *Electronics Letters*, **45**(23), 1155–1157, 2009.

[40] C. Gennarelli, A. Capozzoli, L. J. Foged, J. Fordham, and D. J. van Rensburg. Recent advances in near-field to far-field transformation techniques. *International Journal of Antennas and Propagation*, **2012**, 2012.

[41] E. Gimonet, A. Sarremejean, J. P. David, and P. Bossuet. Determination of radome pertubation by inverse transform of radiation pattern. In *Proc. of 5th European Electromagnetic Windows Conference*, pages 183–190, Juan-les-Pins, France, 1989.

[42] M. G. Guler and E. B. Joy. High resolution spherical microwave holography. *IEEE Trans. Antennas Propagat.*, **43**(5), 464–472, 1995.

[43] M. Gustafsson. Accurate and efficient evaluation of modal Green's functions. *Journal of Electromagnetic Waves and Applications*, **24**(10), 1291–1301, 2010.

[44] M. Gustafsson, A. Karlsson, A. P. Rebelo, and B. Widenberg. Design of frequency selective windows for improved indoor outdoor communication. *IEEE Trans. Antennas Propagat.*, **54**, 1897–1900, 2006.

[45] J. Hanfling, G. Borgiotti, and L. Kaplan. The backward transform of the near field for reconstruction of aperture fields. *IEEE Antennas and Propagation Society International Symposium*, **17**, 764–767, 1979.

[46] J. E. Hansen, editor. *Spherical Near-Field Antenna Measurements*. Number 26 in IEE electromagnetic waves series. Peter Peregrinus Ltd., Stevenage, UK, 1988. ISBN: 0-86341-110-X.

[47] P. C. Hansen. *Discrete inverse problems: insight and algorithms*, volume 7. Society for Industrial & Applied, 2010.

[48] T. B. Hansen and A. D. Yaghjian, editors. *Plane-wave theory of time-domain fields: near-field scanning applications*. IEEE electromagnetic wave theory. IEEE Press, New York, 1999. ISBN: 0-7803-3428-0.

[49] R. F. Harrington. *Time Harmonic Electromagnetic Fields*. McGraw-Hill, New York, 1961.

[50] M. He. On the characteristics of radome enclosed Archimedean spiral antennas. *Antennas and Propagation, IEEE Transactions on*, **56**(7), 1867–1874, 2008.

[51] M. He, X. Xu, B. Hu, and Y. Zheng. Accurate analysis of arbitrarily shaped wire antenna-dielectric radome structures. *Antennas and Wireless Propagation Letters, IEEE*, **6**, 408–410, 2007.

[52] D. W. Hess, R. Luna, and J. McKenna. Electromagnetic radome measurements: a review of automated systems. In *Proc. Loughborough Antennas Prop. Conf.*, Loughborough, England, 2005. CD-ROM.

[53] B. Hu, X. Xu, M. He, and Y. Zheng. More accurate hybrid PO-MOM analysis for an electrically large antenna-radome structure. *Progress in Electromagnetics Research*, **92**, 255–265, 2009.

[54] J. M. Jin. *Theory and computation of electromagnetic fields*. Wiley Online Library, 2010.

[55] D. S. Jones. *Acoustic and Electromagnetic Waves*. Oxford University Press, New York, 1986.

[56] D. S. Jones. *Methods in Electromagnetic Wave Propagation*. IEEE Press, Piscataway, NJ, second edition, 1994.

[57] E. Jörgensen, D. W. Hess, P. Meincke, O. Borries, C. Cappellin, and J. Fordham. Antenna diagnostics on planar arrays using a 3D source reconstruction technique and spherical near-field measurements. In *Antennas and Propagation (EUCAP), Proceedings of the 6th European Conference on*, pages 2547–2550. IEEE, 2012.

[58] E. Jörgensen, P. Meincke, and C. Cappellin. Advanced processing of measured fields using field reconstruction techniques. In *Antennas and Propagation (EUCAP), Proceedings of the 5th European Conference on*, pages 3880–3884. IEEE, 2011.

[59] E. Jörgensen, P. Meincke, C. Cappellin, and M. Sabbadini. Improved source reconstruction technique for antenna diagnostics. In *Proceeedings of the 32nd ESA Antenna Workshop*, 2010.

[60] J. Kaipio and E. Somersalo. *Statistical and computational inverse problems*. Springer-Verlag, New York, 2005.

[61] S. M. Kay. *Fundamentals of Statistical Signal Processing, Estimation Theory*. Prentice-Hall, Inc., NJ, 1993.

[62] A. Kirsch. *An Introduction to the Mathematical Theory of Inverse Problems*. Springer-Verlag, New York, 1996.

[63] R. E. Kleinman and G. F. Roach. Boundary integral equations for the three-dimensional Helmholtz equation. *SIAM Review*, **16**(2), 214–236, 1974.

[64] B. M. Kolundžija and A. R. Djordjević. *Electromagnetic modeling of composite metallic and dielectric structures*. Artech House, Boston, London, 2002.

[65] D. J. Kozakoff. *Analysis of Radome-Enclosed Antennas*. Artech House, Boston, London, 1997.

[66] J. D. Kraus and R. J. Marhefka. *Antennas*. McGraw-Hill, New York, third edition, 2002.

[67] D. Krawczyk-Stańdo and M. Rudnicki. The use of L-curve and U-curve in inverse electromagnetic modelling. In S. Wiak, A. Krawczyk, and I. Dolezel, editors, *Intelligent Computer Techniques in Applied Electromagnetics*, volume 119. Springer Verlag, 2008.

[68] R. Kress. *Linear Integral Equations*. Springer-Verlag, Berlin Heidelberg, second edition, 1999.

[69] G. Kristensson. *Spridningsteori med antenntillämpningar*. Studentlitteratur, Lund, 1999. (In Swedish).

[70] F. Las-Heras, B. Galocha, and J. L. Besada. Far-field performance of linear antennas determined from near-field data. *IEEE Trans. Antennas Propagat.*, **50**(3), 408–410, 2002.

[71] F. Las-Heras, M. R. Pino, S. Loredo, Y. Alvarez, and T. K. Sarkar. Evaluating near-field radiation patterns of commercial antennas. *IEEE Trans. Antennas Propagat.*, **54**(8), 2198–2207, 2006.

[72] F. Las-Heras and T. K. Sarkar. Radial field retrieval in spherical scanning for current reconstruction and NF–FF transformation. *IEEE Trans. Antennas Propagat.*, **50**(6), 866–874, 2002.

[73] J.-J. Laurin, J.-F. Zürcher, and F. E. Gardiol. Near-field diagnostics of small printed antennas using the equivalent magnetic current approach. *IEEE Trans. Antennas Propagat.*, **49**(5), 814–828, 2001.

[74] J. Lee, E. M. Ferren, D. P. Woollen, and K. M. Lee. Near-field probe used as a diagnostic tool to locate defective elements in an array antenna. *IEEE Trans. Antennas Propagat.*, **36**(6), 884–889, 1988.

[75] S. M. Lee. *Handbook of composite reinforcements*. Wiley-VCH, 1992.

[76] P. Li and L. J. Jiang. Source reconstruction method-based radiated emission characterization for PCBs. *IEEE Transactions on Electromagnetic Compatibility*, 2013.

[77] I. V. Lindell. *Methods for Electromagnetic Field Analysis*. Clarendon Press, Oxford, 1992.

[78] Y. A. Lopez, F. Las-Heras Andres, M. R. Pino, and T. K. Sarkar. An improved super-resolution source reconstruction method. *Instrumentation and Measurement, IEEE Transactions on*, **58**(11), 3855–3866, 2009.

[79] J. A. Lopez-Fernandez, M. Lopez-Portugues, Y. Alvarez Lopez, C. G. Gonzalez, D. Martínez, and F. Las-Heras. Fast antenna characterization using the sources reconstruction method on graphics processors. *Progress In Electromagnetics Research*, **126**, 185–201, 2012.

[80] A. E. H. Love. The integration of the equations of propagation of electric waves. *Proceedings of the Royal Society of London*, **68**(442-450), 19–21, 1901.

[81] E. A. Marengo and R. W. Ziolkowski. Nonradiating and minimum energy sources and their fields: Generalized source inversion theory and applications. *IEEE Trans. Antennas Propagat.*, **48**(10), 1553–1562, October 2000.

[82] J. R. Mautz and R. F. Harrington. Radiation and scattering from bodies of revolution. *Appl. Scientific Research*, **20**(1), 405–435, 1969.

[83] P. McNair. Radome degradation of radar adaptive array performance. In *Radar, 2006 IEEE Conference on*, pages 162–165, 2006.

[84] H. F. Meng and W. B. Dou. Fast analysis of electrically large radome in millimeter wave band with fast multipole acceleration. *Progress In Electromagnetics Research*, **120**, 371–385, 2011.

[85] M. A. A. Moneum, Z. Shen, J. L. Volakis, and O. Graham. Hybrid PO-MoM analysis of large axi-symmetric radomes. *Antennas and Propagation, IEEE Transactions on*, **49**(12), 1657–1666, 2001.

[86] P. Monk. *Finite Element Methods for Maxwell's Equations*. Oxford University Press, Oxford, 2003.

[87] N. Morita, N. Kumagai, and J. R. Mautz. *Integral Equation Methods for Electromagnetics*. Artech House, Boston, London, 1990.

[88] P. M. Morse and H. Feshbach. *Methods of Theoretical Physics*, volume 2. McGraw-Hill, New York, 1953.

[89] C. Müller. *Foundations of the Mathematical Theory of Electromagnetic Waves*. Springer-Verlag, Berlin, 1969.

[90] B. Munk. *Frequency Selective Surfaces: Theory and Design*. John Wiley & Sons, New York, 2000.

[91] M. S. Narasimhan and B. P. Kumar. A technique of synthesizing the excitation currents of planar arrays or apertures. *IEEE Trans. Antennas Propagat.*, **38**(9), 1326–1332, 1990.

[92] P. Neittaanmäki, M. Rudnicki, and A. Savini. *Inverse problems and optimal design in electricity and magnetism*, volume 35. Oxford University Press, 1996.

[93] S. Nordebo, M. Gustafsson, and K. Persson. Sensitivity analysis for antenna near-field imaging. *IEEE Trans. Signal Process.*, **55**(1), 94–101, January 2007.

[94] S. Nordebo and M. Gustafsson. Statistical signal analysis for the inverse source problem of electromagnetics. *IEEE Trans. Signal Process.*, **54**(6), 2357–2361, June 2006.

[95] E. A. Parker. The gentleman's guide to frequency selective surfaces. In *17th QMW Antenna Symposium*, pages 1–18, 1991.

[96] M. Pastorino. Modern microwave inverse-scattering techniques for image reconstruction. *IEEE Instrumentation & Measurement Magazine*, pages 20–25, December 1998.

[97] K. Persson, M. Gustafsson, and G. Kristensson. Reconstruction and visualization of equivalent currents on a radome using an integral representation formulation. *Progress In Electromagnetics Research*, **20**, 65–90, 2010.

[98] K. Persson. *Retrieval of equivalent currents by the use of an integral representation and the extinction theorem — radome applications*. Licentiate thesis, Lund University, Department of Electrical and Information Technology, P.O. Box 118, S-221 00 Lund, Sweden, 2010. `http://www.eit.lth.se`.

[99] K. Persson and M. Gustafsson. Reconstruction of equivalent currents using a near-field data transformation – with radome applications. *Progress in Electromagnetics Research*, **54**, 179–198, 2005.

[100] K. Persson and M. Gustafsson. Reconstruction of equivalent currents using the scalar surface integral representation. Technical Report LUTEDX/(TEAT-7131)/1–25/(2005), Lund University, Department of Electrical and Information Technology, P.O. Box 118, S-221 00 Lund, Sweden, 2005. `http://www.eit.lth.se`.

[101] K. Persson, M. Gustafsson, G. Kristensson, and B. Widenberg. Radome diagnostics - source reconstruction of phase objects with an equivalent currents approach. Technical Report LUTEDX/(TEAT-7223)/1–22/(2012), Lund University, Department of Electrical and Information Technology, P.O. Box 118, S-221 00 Lund, Sweden, 2012. `http://www.eit.lth.se`.

[102] K. Persson, M. Gustafsson, G. Kristensson, and B. Widenberg. Source reconstruction by far-field data for imaging of defects in frequency selective radomes. *IEEE Antennas and Wireless Propagation Letters*, **12**, 480–483, 2013.

[103] A. F. Peterson, S. L. Ray, and R. Mittra. *Computational Methods for Electromagnetics*. IEEE Press, New York, 1998.

[104] P. Petre and T. K. Sarkar. Planar near-field to far-field transformation using an equivalent magnetic current approach. *IEEE Trans. Antennas Propagat.*, **40**(11), 1348–1356, 1992.

[105] A. J. Poggio and E. K. Miller. Integral equation solutions of three-dimensional scattering problems. In R. Mittra, editor, *Computer Techniques for Electromagnetics*. Pergamon, New York, 1973.

[106] S. Poulsen. Artificial puck plate radomes. In *Proc. International Conference on Electromagnetics in Advanced Applications (ICEAA'05)*, Torino, Italy, 2005.

[107] S. Poulsen. *Stealth radomes*. PhD thesis, Lund University, Department of Electroscience, Lund University, P.O. Box 118, S-221 00 Lund, Sweden, 2006.

[108] J. L. A. Quijano, L. Scialacqua, J. Zackrisson, L. J. Foged, M. Sabbadini, and G. Vecchi. Suppression of undesired radiated fields based on equivalent currents reconstruction from measured data. *Antennas and Wireless Propagation Letters, IEEE*, **10**, 314–317, 2011.

[109] J. L. A. Quijano and G. Vecchi. Improved-accuracy source reconstruction on arbitrary 3-D surfaces. *IEEE Antennas & Wireless Propagat. Lett.*, **8**, 1046–1049, 2009.

[110] J. L. A. Quijano and G. Vecchi. Field and source equivalence in source reconstruction on 3D surfaces. *Progress In Electromagnetics Research*, **103**, 67–100, 2010.

[111] Y. Rahmat-Samii. Surface diagnosis of large reflector antennas using microwave holographic metrology: an iterative approach. *Radio Sci.*, **19**(5), 1205–1217, 1984.

[112] Y. Rahmat-Samii and J. Lemanczyk. Application of spherical near-field measurements to microwave holographic diagnosis of antennas. *IEEE Trans. Antennas Propagat.*, **36**(6), 869–878, 1988.

[113] Y. Rahmat-Samii, L. I. Williams, and R. G. Yaccarino. The UCLA bi-polar planar-near-field antenna-measurement and diagnostics range. *IEEE Antennas and Propagation Magazine*, **37**(6), 16–35, December 1995.

[114] S. R. Rengarajan and Y. Rahmat-Samii. The field equivalence principle: Illustration of the establishment of the non-intuitive null fields. *Antennas and Propagation Magazine, IEEE*, **42**(4), 122–128, 2000.

[115] D. J. Rochblatt and B. L. Seidel. Microwave antenna holography. *IEEE Trans. Microwave Theory Tech.*, **40**(6), 1294–1300, 1992.

[116] T. Rougier. Damage detection in composite by optical fibre sensors. In *International Conference on Adaptive Structures and Technologies, 10 th, Paris, France*, pages 431–435, 2000.

[117] T. K. Sarkar and A. Taaghol. Near-field to near/far-field transformation for arbitrary near-field geometry utilizing an equivalent electric current and MoM. *IEEE Trans. Antennas Propagat.*, **47**(3), 566–573, March 1999.

[118] J. K. Seo and E. J. Woo. *Nonlinear Inverse Problems in Imaging*. John Wiley & Sons, West Sussex, United Kingdom, 2013.

[119] W. N. Sharpe Jr. *Springer handbook of experimental solid mechanics*. Springer, 2008.

[120] R. Shavit, A. P. Smolski, E. Michielssen, and R. Mittra. Scattering analysis of high performance large sandwich radomes. *IEEE Transactions on Antennas and Propagation*, **40**(2), 126–133, 1992.

[121] X. Q. Sheng and W. Song. *Essentials of Computational Electromagnetics*. Wiley, 2012.

[122] Z. Shengfang, G. Dongming, K. Renke, J. Zhenyuan, S. Aifeng, and J. Tian. Research on microwave and millimeter-wave IPD measurement system for radome. In *Microwave and Millimeter Wave Technology, 2004. ICMMT 4th International Conference on, Proceedings*, pages 711–714. IEEE, 2004.

[123] J. A. Shifflett. CADDRAD: A physical optics radar/radome analysis code for arbitrary 3D geometries. *IEEE Antennas and Propagation Magazine*, **6**(39), 73–79, 1997.

[124] R. A. Shore and A. D. Yaghjian. Dual-surface integral equations in electromagnetic scattering. *IEEE Trans. Antennas Propagat.*, **53**(5), 1706–1709, 2005.

[125] S. Silver. *Microwave Antenna Theory and Design*, volume 12 of *Radiation Laboratory Series*. McGraw-Hill, New York, 1949.

[126] J. S. Sirkis, C. C. Chang, and B. T. Smith. Low velocity impact of optical fiber embedded laminated graphite/epoxy panels. part I: macro-scale. *Journal of composite materials*, **28**(14), 1347–1370, 1994.

[127] J. C.-E. Sten. Reconstruction of electromagnetic minimum energy sources in a prolate spheroid. *Radio Sci.*, **39**(2), 2004.

[128] J. C.-E. Sten and E. A. Marengo. Inverse source problem in an oblate spheroidal geometry. *IEEE Trans. Antennas Propagat.*, **54**(11), 3418–3428, 2006.

[129] J. A. Stratton. *Electromagnetic Theory*. McGraw-Hill, New York, 1941.

[130] S. Ström. Introduction to integral representations and integral equations for time-harmonic acoustic, electromagnetic and elastodynamic wave fields. In V. V. Varadan, A. Lakhtakia, and V. K. Varadan, editors, *Field Representations and Introduction to Scattering*, volume 1 of *Handbook on Acoustic, Electromagnetic and Elastic Wave Scattering*, chapter 2, pages 37–141. Elsevier Science Publishers, Amsterdam, 1991.

[131] A. B. Strong. *Fundamentals of composites manufacturing: materials, methods and applications*. Society of Manufacturing Engineers, 2008.

[132] A. Taaghol and T. K. Sarkar. Near-field to near/far-field transformation for arbitrary near-field geometry, utilizing an equivalent magnetic current. *IEEE Trans. Electromagn. Compatibility*, **38**(3), 536–542, 1996.

[133] A. Taflove and S. C. Hagness. *Computational electrodynamics: The Finite-Difference Time-Domain Method*. Artech House, Boston, London, 2000.

[134] F. Thérond, J. C. Bolomey, N. Joachmowicz, and F. Lucas. Electromagnetic diagnosis technique using spherical near-field probing. In *Proc. EUROEM'94*, pages 1218–1226, Bordeaux, France, 1994.

[135] A. G. Tijhuis. *Electromagnetic Inverse Profiling. Theory and Numerical Implementation*. VNU Science Press BV, Utrecht, 1987.

[136] J. G. Van Bladel. *Electromagnetic Fields*. IEEE Press, Piscataway, NJ, second edition, 2007.

[137] J. C. Vardaxoglou. *Frequency Selective Surfaces (Analysis and Design)*. Research Studies Press, 1997.

[138] J. A. Vitale. Large radomes. In R. C. Hansen, editor, *Microwave scanning antennas: Apertures*, volume 1. Academic Press, New York and London, 1964.

[139] J. L. Volakis and K. Sertel. *Integral Equation Methods for Electromagnetics*. Scitech publishing, 2012.

[140] J. D. Walton. *Radome engineering handbook: design and principles*, volume 1. M. Dekker, 1970.

[141] J. J. H. Wang. An examination of the theory and practices of planar near-field measurement. *IEEE Trans. Antennas Propagat.*, **36**(6), 746–753, 1988.

[142] J. J. H. Wang. *Generalized Moment Methods in Electromagnetics: Formulation and Computer Solution of Integral Equations*. John Wiley & Sons, New York, 1991.

[143] Z. L. Wang, K. Hashimoto, N. Shinohara, and H. Matsumoto. Frequency-selective surface for microwave power transmission. *Microwave Theory and Techniques, IEEE Transactions on*, **47**(10), 2039–2042, 1999.

[144] R. F. Wegman and T. R. Tullos. *Handbook of adhesive bonded structural repair*. Noyes Publications, 1992.

[145] B. Widenberg. Advanced compact test range for both radome and antenna measurement. In *11th European Electromagnetic Structures Conference*, pages 183–186, Torino, Italy, 2005.

[146] B. Widenberg. *Thick Frequency Selective Structures*. PhD thesis, Lund Institute of Technology, Department of Electroscience, Lund Institute of Technology, P.O. Box 118, S-221 00 Lund, Sweden, 2003. ISSN 1402-8662.

[147] Widenberg, Björn. Radomes & Antennas, GKN Aerospace Applied Composites, P.O Box 13070, SE-580 13 Linköping, Sweden, *Private communication*, 2013.

[148] T. K. Wu, editor. *Frequency Selective Surface and Grid Array*. John Wiley & Sons, New York, 1995.

[149] A. D. Yaghjian. An overview of near-field antenna measurements. *IEEE Trans. Antennas Propagat.*, **34**(1), 30–45, January 1986.

[150] W. J. Zhao, Y. B. Gan, L. W. Li, and C. F. Wang. Effects of an electrically large airborne radome on radiation patterns and input impedance of a dipole array. *Antennas and Propagation, IEEE Transactions on*, **55**(8), 2399–2402, 2007.

[151] A. Ziyyat, L. Casavola, D. Picard, and J. C. Bolomey. Prediction of BTS antennas safety perimeter from NF to NF transformation: an experimental validation. In *Proc. Antenna Measurement Techniques Association (AMTA)*, pages 22–26, Denver, US, 2001.

Reconstruction of equivalent currents using a near-field data transformation – with radome applications

Paper I

Kristin Persson and Mats Gustafsson

Based on: K. Persson and M. Gustafsson. Reconstruction of equivalent currents using a near-field data transformation – with radome applications, *Progress in Electromagnetics Research*, vol. 54, pp. 179–198, 2005.

Abstract

Knowledge of the current distribution on a radome can be used to improve radome design, detect manufacturing errors, and to verify numerical simulations. In this paper, the transformation from near-field data to its equivalent current distribution on a surface of arbitrary material, *i.e.*, the radome, is analyzed. The transformation is based on the scalar surface integral representation that relates the equivalent currents to the near-field data. The presence of axial symmetry enables usage of the fast Fourier transform (FFT) to reduce the computational complexity. Furthermore, the problem is regularized using a singular value decomposition (SVD). Both synthetic and measured data are used to verify the method. The quantity of data is large since the height of the radome corresponds to $29 - 43$ wavelengths in the frequency interval $8.0 - 12.0$ GHz. It is shown that the method gives an accurate description of the field radiated from an antenna, on a surface enclosing it. Moreover, disturbances introduced by copper plates attached to the radome surface, not localized in the measured near field, are focused and detectable in the equivalent currents.

1 Introduction

There are several applications of a near field to equivalent currents transformation. For example, in the radome industry it is important to have accurate models of the field radiated from the antenna placed inside the radome. It is hard to measure this field directly since the radome often is placed very close to the antenna and at these distances, there is a substantial interaction between the antenna and the measuring probe [5, 10, 16]. Another field of application is in the manufacturing of radiating bodies, *e.g.*, radomes, antenna arrays, when the radiation pattern from the body does not exhibit the expected form. By determination of the equivalent currents on the radiating body the malfunctioning areas or components can be found.

A common method, transforming near field to equivalent currents and vice versa, is to use modal-expansions of the electric field [5]. This is a very efficient method for radiating bodies with certain geometrical symmetries, *i.e.*, planar, cylindrical, and spherical. Having a planar aperture, the plane wave spectrum of the field is utilized in the back transformation [3, 4]. The fact that the expression of the far field originating from a planar surface is equal to the Fourier transform of the radiating field on the aperture has been investigated in [9, 10]. The paper [9] also illustrates that defects, patches of Eccosorb, can be detected on the aperture. If the radiating body is of cylindrical or spherical geometry, the radial solutions contain cylindrical and spherical Bessel functions, while the angular solutions are described by trigonometric functions and the associated Legendre functions [5, 14]. For general geometrical symmetries, where modal-expansions do not exist, the modal-expansion is less applicable.

Later on different combinations of the electric- and magnetic-field integral equations (EFIE and MFIE) derived from the Maxwell equations, have been used to back propagate fields towards their sources. By this method it is possible to handle

a wider class of geometries [10]. In [15] the dual-surface magnetic and electric-field integral equations are investigated. The fields are transformed back to a cubic perfect electric conductor by solving the dual-surface magnetic-field integral equation using the conjugate gradient method. Other work using the integral equations is reported in [11], where the near field is measured on a arbitrary surface and later inverted to a planar, perfectly conducting surface by using a singular value decomposition (SVD) for regularization.

In this paper, the approach is to investigate a scalar surface integral representation that does not require the aperture to be a perfect electric or magnetic conductor. The representation provides a relation relating the unknown electric and magnetic equivalent currents on a surface to the measured electric field. An additional relation is given by the fact that the equivalent currents are constructed such that the integral is zero inside the volume, on which surface the currents exist, *i.e.*, the extinction theorem [13].

The integral relations are discretized into matrix linear equations. The matrix equations include an azimuthal convolution which is solved with a fast Fourier transform (FFT) in the angular coordinate. The fast Fourier transform brings down the complexity of the problem, *i.e.*, the original surface-to-surface linear map is decomposed into a set of line-to-line linear maps. A singular value decomposition (SVD) is used to invert each of these linear maps. As most inverse problems it is ill-posed, *i.e.*, small errors in the near-field data can produce large errors in the equivalent currents. Thus, the problem needs to be regularized by suppression of small singular values when inverted.

In this paper, the measured electric field is presumed to be scalar, *i.e.*, the scalar surface integral representation is utilized. The assumption is acceptable since the used near-field data, supplied by SAAB Bofors Dynamics and Chelton Applied Composites, Sweden, clearly have one dominating component in the main lobe, see Figure 3. The measured data is given for three different antenna and radome configurations, *viz.*, antenna, antenna together with radome, and antenna together with defect radome. The height of the radome corresponds to $29 - 43$ wavelengths in the frequency interval $8.0 - 12.0$ GHz.

As a start, synthetic data is used to verify the method. Verification is also performed by a comparison between the measured far field and the far field calculated from the equivalent currents on the radome. The calculated far field agrees well with the measured far field. We show that the method can describe the field radiated from an antenna, on a surface enclosing it. When the radome is introduced the field is scattered and flash lobes arise. The equivalent currents on the radome, that produce the electric field measured in the near-field area, are identified and the flash lobes are accurately detected.

Manufacturing errors, not localized in the measured near-field data, can be focused and detected in the equivalent currents on the radome surface. In this paper, it is shown that the field scattered by copper plates attached on the radome, is focused back towards the original position of the copper plates. The length of the side of the square copper plates is 6 cm, *i.e.*, $1.6 - 2.4$ wavelengths corresponding to the frequency span $8.0 - 12.0$ GHz.

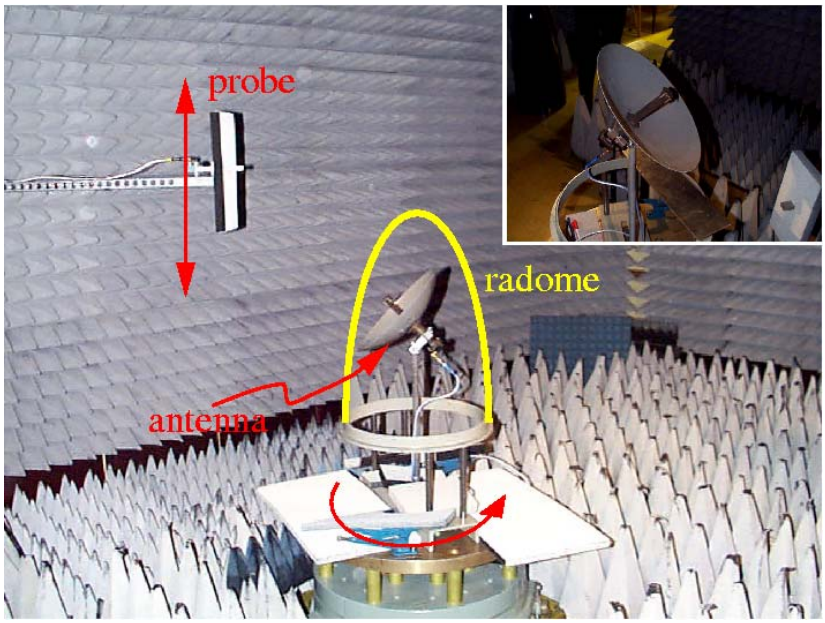

Figure 1: Photo of the cylindrical near-field range at SAAB Bofors Dynamics, Sweden. The antenna under test is rotated and the probe is moved in the vertical direction. A close up of the reflector antenna is shown in the upper right corner.

In Section 2 the experimental set-up is described and the measured near-field data is presented. The scalar surface integral representation is introduced and adapted to the specific problem in Section 3. Section 4 discusses the implementation process of the scalar surface integral representation. Results, using synthetic near-field data and the error of the method is elucidated. The results, when using the experimental near-field data, are shown and examined in Section 5. The paper ends with the achieved conclusions in Section 6.

2 Near-field measurements

The near-field data, used in this paper, was supplied by SAAB Bofors Dynamics and Chelton Applied Composites, Sweden. The set-up with relevant dimensions indicated is shown in Figures 1 and 2a. Three different measurements were performed; data measured without the radome, data measured with the radome, and data measured with the defect radome. The defect radome has two copper plates attached to its surface.

A reflector antenna fed by a symmetrically placed wave-guide generates the near-field data, see Figure 1. The diameter of the antenna is 0.32 m and its focal distance is 0.1 m. The main lobe of the antenna is vertically polarized relative to the horizontal plane. The standing wave ratio (SWR) is approximately 1.4 in the frequency range $8.2 - 9.5$ GHz. The antenna is poorly adapted for other frequencies.

The radome surface is axially symmetric and its radius, in terms of the height

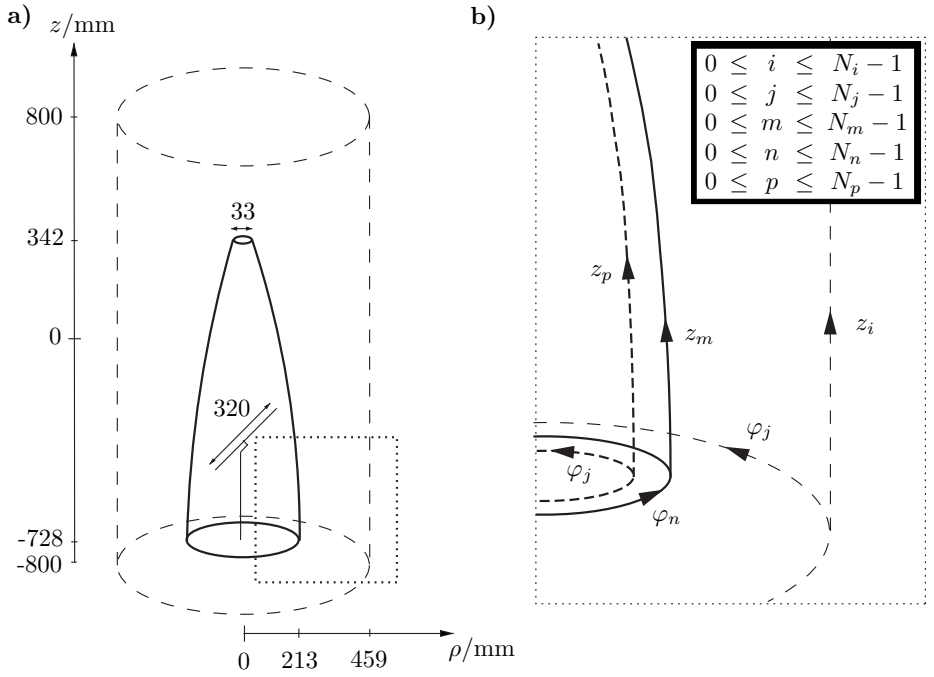

Figure 2: (a) The dimensions of the reflector antenna, the radome, and the cylinder where the electric near field is measured. (b) A close-up showing the discretized geometric variables.

coordinate, is modeled by

$$\rho(z) = \begin{cases} 0.213\,\mathrm{m} & -0.728\,\mathrm{m} \le z \le -0.663\,\mathrm{m} \\ -(bz'+d) + \sqrt{(bz'+d)^2 - a(z')^2 - 2cz' - e} & -0.663\,\mathrm{m} < z \le 0.342\,\mathrm{m} \end{cases} \tag{2.1}$$

where $z' = z + 0.728\,\mathrm{m}$ and the constants are $a = 0.122$, $b = 0.048$, $c = -0.018\,\mathrm{m}$, $d = 0.148\,\mathrm{m}$, and $e = -0.108\,\mathrm{m}^2$. The near-field measurement probe consists of a wave-guide for which no compensation is made in the final data. The cylindrical surface, where the electric field is measured, is placed in both the reactive near-field zone and the radiating near-field zone [2].

The amplitude and phase of the electric field are measured in the frequency interval $8.0-12.0\,\mathrm{GHz}$ on a cylindrical surface by moving the probe in the z-direction and rotating the antenna under test, see Figure 1. Applying this measurement set-up, the fields on the top and the bottom of the cylindrical surface could not be collected. It would have been preferable to measure the fields on an infinite cylinder. However, the size of the cylinder is chosen due to the influence of the turntable below the radome and the low field amplitudes above $z = 800\,\mathrm{mm}$, *cf.*, Figures 2a and 3. In the azimuth angle, 120 points are measured between $-180°$ and $180°$ in steps of $3°$. The z-dimension is divided into 129 points, every two points separated by 12.5 mm. This means that at 8.0 GHz the electric field is measured 3 times per wavelength, in the z-direction, and 1.5 times per wavelength, in the azimuth direction, respectively. Together, a total of $120 \times 129 = 15480$ measurement points are used for each radome

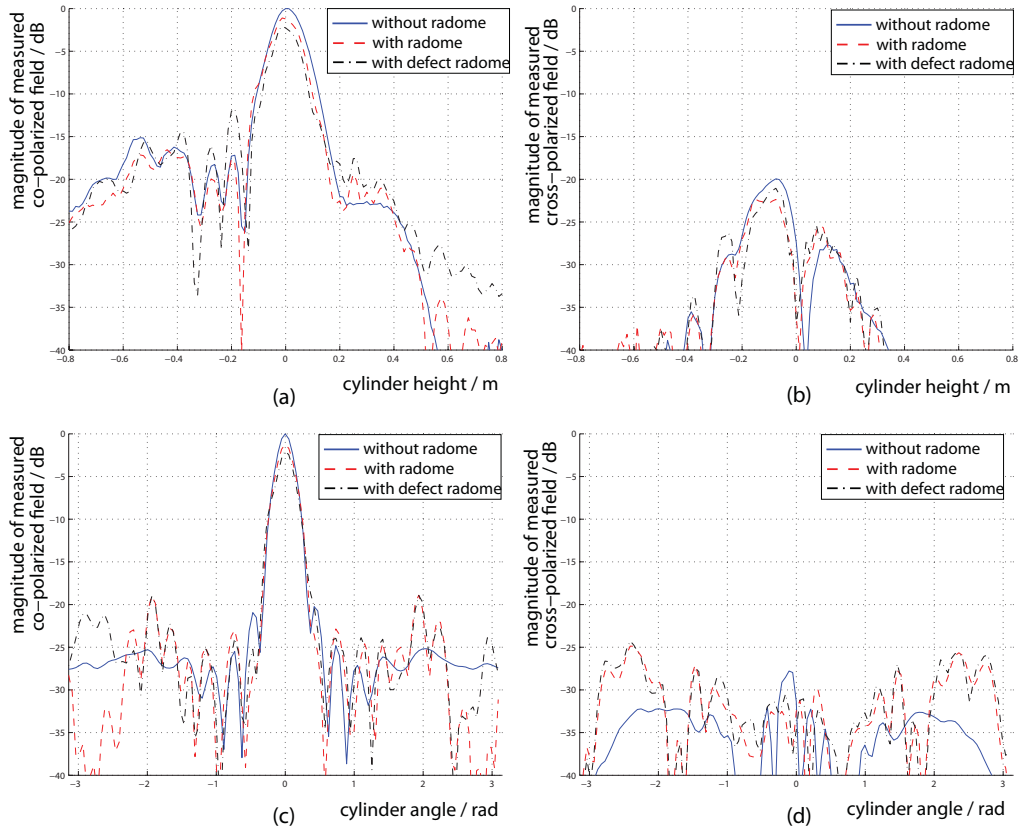

Figure 3: The measured co- and cross-polarized electric field on the measurement cylinder at 8.0 GHz. In (a) and (b) the angle is fixed at $\varphi = 0$, and the fields are normalized to the maximum value when no radome is present in (a). In (c) and (d) the height is fixed at $z = 0$, and the fields are normalized to the maximum value when no radome is present in (c).

configuration and frequency. The co- and cross-polarized measured electric fields are shown in Figure 3. The differences between the three different antenna and radome cases arise from constructive and destructive interference between the radiated field and the scattered field. In Figure 3 it is also observed that the electric field consists of a dominating co-component in the main lobe, *i.e.*, a dominating z-component since the antenna is vertically polarized.

3 The surface integral representation

The surface integral representation expresses the electromagnetic field in a homogeneous and isotropic region in terms of its values on the bounding surface. The representation states that if the electromagnetic field on a surface of a volume is known, the electromagnetic field in the volume can be determined [7, 13]. The representation is derived starting from the time harmonic Maxwell equations with the time convention $e^{j\omega t}$. The Maxwell equations transform into the vector Helmholtz

equation

$$\nabla^2 \boldsymbol{E}(\boldsymbol{r}) + k^2 \boldsymbol{E}(\boldsymbol{r}) = 0 \tag{3.1}$$

since the material (air) is source free, homogeneous, and isotropic.

Assume that the electric field only consists of a component in the z-direction. This is a good approximation dealing with the specific measurements described in Section 2 since our prime interest is to reconstruct the electric field in the main lobe, where the z-component is clearly the dominating one, *cf.*, Figure 3.

Working with a scalar field, the surface integral representation only depends on the scalar electric field, E_z, and its normal derivative, $\partial E_z/\partial n$, *i.e.*, the magnetic field is not taken into account as it must in the full three dimensional expression [7]. The scalar surface integral representation is derived using the free space Green's function $g(\boldsymbol{r}, \boldsymbol{r}') = \mathrm{e}^{-\mathrm{j}k|\boldsymbol{r}-\boldsymbol{r}'|}/4\pi|\boldsymbol{r}-\boldsymbol{r}'|$ [13]

$$\iint\limits_S \left[\frac{\partial g(\boldsymbol{r}, \boldsymbol{r}')}{\partial n} E_z(\boldsymbol{r}) - g(\boldsymbol{r}, \boldsymbol{r}') \frac{\partial E_z(\boldsymbol{r})}{\partial n} \right] \mathrm{d}S = \begin{cases} -E_z(\boldsymbol{r}') & \boldsymbol{r}' \in V \\ 0 & \boldsymbol{r}' \notin V \end{cases} \tag{3.2}$$

where V is the volume spanning from the outside of the radome to infinity. The closed surface S is the radome surface with an added top and bottom surface. Observe that the electric field does not have to be zero outside the volume, *i.e.*, inside the radome. The surface integral representation (3.2) only states that the left-hand side of the equation is zero if the vector $\boldsymbol{r}'$ points outside the volume V, *i.e.*, the extinction theorem [13].

The equivalent surface currents are introduced as

$$M(\boldsymbol{r}) \equiv E_z(\boldsymbol{r}) \quad \text{and} \quad M'(\boldsymbol{r}) \equiv \frac{\partial E_z(\boldsymbol{r})}{\partial n} \tag{3.3}$$

which are inserted in (3.2) to give

$$\iint\limits_{\text{radome}} \left[\frac{\partial g(\boldsymbol{r}, \boldsymbol{r}')}{\partial n} M(\boldsymbol{r}) - g(\boldsymbol{r}, \boldsymbol{r}') M'(\boldsymbol{r}) \right] \mathrm{d}S = \begin{cases} -E_z^{\mathrm{cyl}}(\boldsymbol{r}') & \boldsymbol{r}' \in \text{cylinder} \\ 0 & \boldsymbol{r}' \in \text{surface inside radome} \end{cases} \tag{3.4}$$

where E_z^{cyl} is the z-component of the electric field on the measurement cylinder. The continuous variables are discretized to give linear matrix equations. The discretized cylindrical coordinate system is described by the integer indices displayed in Figure 2b.

3.1 Angular Fourier transformation

The transformation, the Green's function, is axially symmetric due to the measurement set-up, see Section 2. Observe that the symmetry only applies to the transformation, not to the electric field. Thus, the left-hand side in (3.4) represents a convolution and by using a Fourier transformation of the azimuth coordinate the computational complexity can be brought down one dimension. This reduction of

one dimension, can be understood by writing the left-hand side in (3.4) as a matrix X. This matrix is a circulant matrix, *i.e.*, every row is shifted one step to the right compared to the previous row. The eigenvectors of all circulant matrices are the column vectors of the Fourier matrix F. When a circulant matrix is multiplied with the Fourier matrix. *i.e.*, performing the Fourier transformation, the result is $FX = F\Lambda$ where Λ is a diagonal matrix, which can be seen as a reduction of one dimension [12].

Discretization and Fourier transformation, in the azimuth coordinate, of (3.4) give

$$\sum_{m=0}^{N_m-1} \left[\widehat{\mathcal{G}}'_{im\hat{\jmath}} \widehat{M}_{m\hat{\jmath}} \; - \widehat{\mathcal{G}}_{im\hat{\jmath}} \widehat{M}'_{m\hat{\jmath}} \right] = -\widehat{E}^{\text{cyl}}_{i\hat{\jmath}} \qquad \text{for all } \; i, \hat{\jmath} \tag{3.5}$$

and

$$\sum_{m=0}^{N_m-1} \left[\widehat{\mathsf{G}}'_{pm\hat{\jmath}} \widehat{M}_{m\hat{\jmath}} \; - \widehat{\mathsf{G}}_{pm\hat{\jmath}} \widehat{M}'_{m\hat{\jmath}} \right] = 0 \qquad \text{for all } \; p, \hat{\jmath} \tag{3.6}$$

where $\mathcal{G}$ and G are the surface integrals, taken over the radome, of the Green's function multiplied with the basis functions used in the discretization process. $\mathcal{G}$ has the discretized space variable $\boldsymbol{r}'$ belonging to the measurement cylinder and G has the discretized space variable $\boldsymbol{r}'$ belonging to a surface inside the radome, respectively. The prime denotes the normal derivative of the Green's function, $\hat{\jmath}$ is the integer index belonging to the Fourier transformed azimuth component, and the "hat" denotes the Fourier transformed variables. The summation limits N_m and N_p are described in Figure 2b.

To solve the scalar surface integral representation, a limit process of (3.6) should be performed, letting the fictitious surface inside the radome approach the radome surface [2, 8]. To avoid singularities, we let the fictitious surface be located at a finite distance from the radome surface. This provides us with a simple and feasible method to allocate the surface currents, *i.e.*, the extinction theorem is used as an approximate solution to the integral representation in (3.6).

Reduction of M' in (3.5) and (3.6) gives

$$\sum_{m=0}^{N_m-1} \left\{ \widehat{\mathcal{G}}'_{im\hat{\jmath}} - \sum_{p=0}^{N_p-1} \sum_{q=0}^{N_m-1} \widehat{\mathcal{G}}_{iq\hat{\jmath}} (\widehat{\mathsf{G}}^{-1})_{qp\hat{\jmath}} \widehat{\mathsf{G}}'_{pm\hat{\jmath}} \right\} \widehat{M}_{m\hat{\jmath}} \; = -\widehat{E}^{\text{cyl}}_{i\hat{\jmath}} \quad \text{for all } \; i, \hat{\jmath} \tag{3.7}$$

Equation (3.7) can also be written as $\hat{\jmath}$ matrix equations

$$\widehat{\boldsymbol{G}}^{\text{radome}}_{\hat{\jmath}} \widehat{\boldsymbol{M}}_{\hat{\jmath}} \; = -\widehat{\boldsymbol{E}}^{\text{cyl}}_{\hat{\jmath}} \qquad \text{for all } \; \hat{\jmath} \tag{3.8}$$

where the matrices are defined as $\widehat{\boldsymbol{M}}_{\hat{\jmath}} \equiv [\widehat{M}_{m1}]_{\hat{\jmath}}$, $\widehat{\boldsymbol{E}}^{\text{cyl}}_{\hat{\jmath}} \equiv [\widehat{E}^{\text{cyl}}_{i1}]_{\hat{\jmath}}$, and

$$\widehat{\boldsymbol{G}}^{\text{radome}}_{\hat{\jmath}} \equiv [\widehat{\mathcal{G}}'_{im}]_{\hat{\jmath}} - [\widehat{\mathcal{G}}_{im}]_{\hat{\jmath}} [\widehat{\mathsf{G}}_{mp}]^{-1}_{\hat{\jmath}} [\widehat{\mathsf{G}}'_{pm}]_{\hat{\jmath}} \tag{3.9}$$

The notation of matrices used here is that of [1].

3.2 Inversion with singular value decomposition

Since the matrices $\widehat{\boldsymbol{G}}_{\hat{\jmath}}^{\text{radome}}$ and $[\widehat{\mathsf{G}}_{mp}]_{\hat{\jmath}}$ in (3.8) and (3.9) are not quadratic, a regular inversion cannot be performed. A fast and easy way to solve this is to use the singular value decomposition (SVD) [12]. This method is used on both matrices, but the SVD-equations are only given here for $\widehat{\boldsymbol{G}}_{\hat{\jmath}}^{\text{radome}}$. The matrix system (3.8) can then be rewritten as

$$\widehat{\boldsymbol{U}}_{\hat{\jmath}}\widehat{\boldsymbol{S}}_{\hat{\jmath}}\widehat{\boldsymbol{V}}_{\hat{\jmath}}^{\dagger}\widehat{\boldsymbol{M}}_{\hat{\jmath}} = -\widehat{\boldsymbol{E}}_{\hat{\jmath}}^{\text{cyl}} \qquad \text{for all } \hat{\jmath} \tag{3.10}$$

where $\widehat{\boldsymbol{V}}_{\hat{\jmath}}^{\dagger}$ denotes the Hermitian conjugate of $\widehat{\boldsymbol{V}}_{\hat{\jmath}}$. Both $\widehat{\boldsymbol{U}}_{\hat{\jmath}}$ and $\widehat{\boldsymbol{V}}_{\hat{\jmath}}$ are orthogonal matrices. $\widehat{\boldsymbol{S}}_{\hat{\jmath}}$ is a diagonal matrix consisting of the singular values to $\widehat{\boldsymbol{G}}_{\hat{\jmath}}^{\text{radome}}$ in decreasing order. The singular values of both $\widehat{\boldsymbol{G}}_{\hat{\jmath}}^{\text{radome}}$ and $[\widehat{\mathsf{G}}_{mp}]_{\hat{\jmath}}$ exhibit the tendency shown by the curves in Figure 4a.

A cut-off value δ normalized to the operator L_2-norm of $\widehat{\boldsymbol{G}}_1^{\text{radome}}$ is chosen. The operator L_2-norm of $\widehat{\boldsymbol{G}}_1^{\text{radome}}$ is equal to the largest singular value (σ_1) of the largest Fourier transformed azimuth component [8]. All singular values smaller than δ are ignored during the inversion of $\widehat{\boldsymbol{S}}_{\hat{\jmath}}$ and are afterwards set to zero. If this is not done the small singular values create an uncontrolled growth of non-radiation currents when inverted. The mathematical formulation then fails since very small electric field contributions become dominating. Performing the inversion of (3.10) gives

$$\widehat{\boldsymbol{M}}_{\hat{\jmath}} = -\,\widehat{\boldsymbol{U}}_{\hat{\jmath}}^{\dagger}\widehat{\boldsymbol{S}}_{\hat{\jmath}}^{-1}\widehat{\boldsymbol{V}}_{\hat{\jmath}}\widehat{\boldsymbol{E}}_{\hat{\jmath}}^{\text{cyl}} \qquad \text{for all } \hat{\jmath} \tag{3.11}$$

Before the system of equations is solved it is necessary to convert it back from Fourier space by an inverse Fourier transformation

$$\boldsymbol{M}_{j} = \mathcal{F}^{-1}\left[-\widehat{\boldsymbol{U}}_{\hat{\jmath}}^{\dagger}\widehat{\boldsymbol{S}}_{\hat{\jmath}}^{-1}\widehat{\boldsymbol{V}}_{\hat{\jmath}}\widehat{\boldsymbol{E}}_{\hat{\jmath}}^{\text{cyl}}\right] \qquad \text{for all } j,\hat{\jmath} \tag{3.12}$$

where j, as before, denotes the integer index belonging to the discretized azimtuth component, see Figure 2b.

4 Implementation

Some adjustments of the formulas are made in the implementation process. To facilitate the calculations, the radome surface is reshaped into a closed surface by adding a smooth top and bottom surface. These extra surfaces are useful since the measurements are performed under non-ideal conditions. The table, on which the antenna and radome are placed, see Figure 1, reflects some of the radiation, which is taken care of by the bottom surface. The top surface represents the electric field that is reflected on the inside of the radome and then is passed out through the top hole. If these factors are not considered, unwanted edge effects occur since the

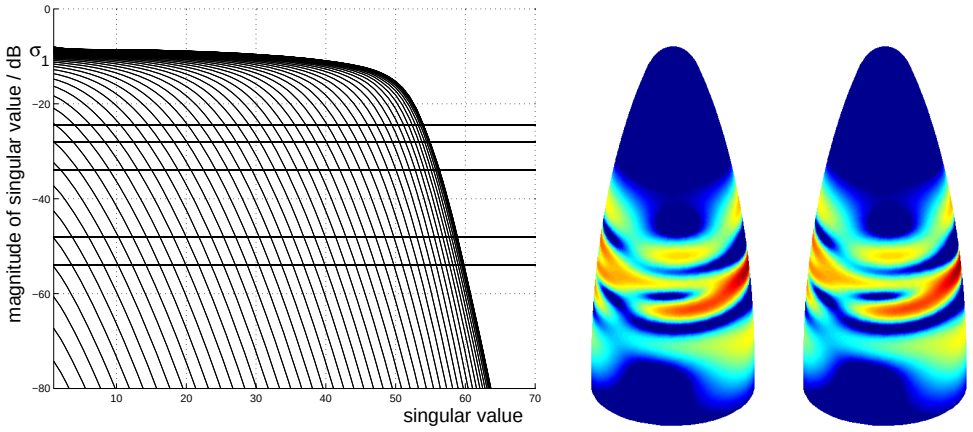

(a) (b) (c)

Figure 4: (a) The tendency of singular values of $\widehat{\boldsymbol{G}}_{\hat{\jmath}}^{\text{radome}}$ and $[\widehat{\mathsf{G}}_{mp}]_{\hat{\jmath}}$. Every curve represents the singular values of a Fourier transformed azimuth component, *i.e.*, different $\hat{\jmath}$. The horizontal lines describe the cut-off values $\delta = \sigma_1[0.15\ 0.1\ 0.05\ 0.01\ 0.005]$. (b) The synthetic equivalent current, originating from three dipoles, in dB-scale $[-15, 0]$, normalized to the highest current value, *i.e.*, the maximum current magnitude in figure c. (c) The reconstructed current in dB-scale $[-15, 0]$, normalized to its highest current value.

electric field originating from the table and the top of the radome is forced to arise from the radome itself.

The measured electric near field is measured 1.5 times per wavelength, in the angular direction, at the frequency 8.0 GHz, see Section 2. To be sure that the equivalent currents on the radome are recreated in an accurate way it is necessary to have a high sample density on the radome. This is achieved by increasing the number of discrete points, in the angular direction, on the radome surface by including extra angles between the already existing ones. Thus, the axial symmetry of the Green's transformation is kept. The sample density on the measurement cylinder contributes very little to the total error. The scalar surface integral representation creates currents on the radome such that the electric field is correct at the measurement points. However, if the Nyquist theorem is fulfilled, then the electric field is correct at all points on the measurement surface, *i.e.*, not only at the measurement points. As mentioned before, the problem is vast and the matrix $\widehat{\boldsymbol{G}}$, *cf.*, (3.9), has approximately 10^8 elements at the frequency 8.0 GHz when the sample density is 10 points per wavelength both in the angular direction and in the z-direction on the radome.

To verify and find the error of the method, synthetic data is used. A synthetic electric field, originating from three dipoles inside the radome is shown in Figure 4b. The corresponding reconstructed current on a surface shaped as the radome is shown in Figure 4c where the sample density is 10 points per wavelength both in the z-direction and in the angular direction. The inner fictitious surface is located one wavelength from the radome surface.

The error as a function of the Fourier transformed azimuth component is defined

as

$$\mathrm{Err}(\hat{\jmath}) = 20\log_{10}\frac{\| \widehat{\boldsymbol{M}}_{\hat{\jmath}} - \widehat{\boldsymbol{M}}_{\hat{\jmath}}^{\mathrm{correct}} \|_2}{\| \widehat{\boldsymbol{M}}_{\hat{\jmath}}^{\mathrm{correct}} \|_2} \tag{4.1}$$

$$= 20\log_{10}\frac{\sqrt{\sum_{m=0}^{N_m-1} \mid \widehat{M}_{m\hat{\jmath}} - \widehat{M}_{m\hat{\jmath}}^{\mathrm{correct}} \mid^2 \Delta S_m}}{\sqrt{\sum_{m=0}^{N_m-1} \mid \widehat{M}_{m\hat{\jmath}}^{\mathrm{correct}} \mid^2 \Delta S_m}} \quad \text{for all } \hat{\jmath} \tag{4.2}$$

where ΔS_m denotes the discretized area elements on the radome.

By using synthetic data and choosing appropriate cut-off values δ the error is shown to be below -60 dB for each existing Fourier transformed azimuth component. To obtain these low error levels, the measurement surface must be closed, *i.e.*, field values at the top and bottom surfaces of the cylindrical measurement surface must be included. The cut-off values depend on the complexity of the specific measurement set-up and must be investigated for each new set-up.

The total error of the scalar surface integral representation using the measured near field described in Section 2 is hard to define since the noise level and the amount of field spread outside the measurement cylinder are unknown parameters. Instead we rely on the fact that the method handles synthetic data well and that the results using measured data is satisfactory, see Section 5.

5 Results using measured near-field data

The measured near-field data, described in Section 2, is investigated. The inner fictitious surface is located one wavelength from the radome surface. The sample density on the radome is 10 points per wavelength both in the angular direction and in the z-direction. The cut-off values are determined in accordance with the discussion in Section 4.

Three different measurement configurations are investigated, *viz.*, antenna, antenna together with radome, and antenna together with defect radome. The studied frequency interval is $8.0 - 12.0$ GHz. The results for the different measurement configurations are shown in Figure 5a at the frequencies 8.0 GHz and 10.0 GHz. In Figure 5b the results for the defect radome case are shown for the frequencies 8.0 GHz, 9.0 GHz, 10.0 GHz, 11.0 GHz, and 12.0 GHz, respectively.

In the case when no radome is placed around the antenna the equivalent current is calculated on a surface shaped as the radome, see Figure 5aa' and 5ad'. The figures show that the near field close to the antenna is complex and hard to predict, *i.e.*, the diffraction pattern must be taken into account. The diffraction is explained as environmental reflections and an off-centered antenna feed.

The case when the radome is present, see Figure 5ab' and 5ae', shows in comparison to the case without radome that the used radome interacts with the antenna and hence disturbs the radiated field. However, the currents in the main lobe are hardly affected by the radome, as seen in Figure 6a. The influence of the radome is

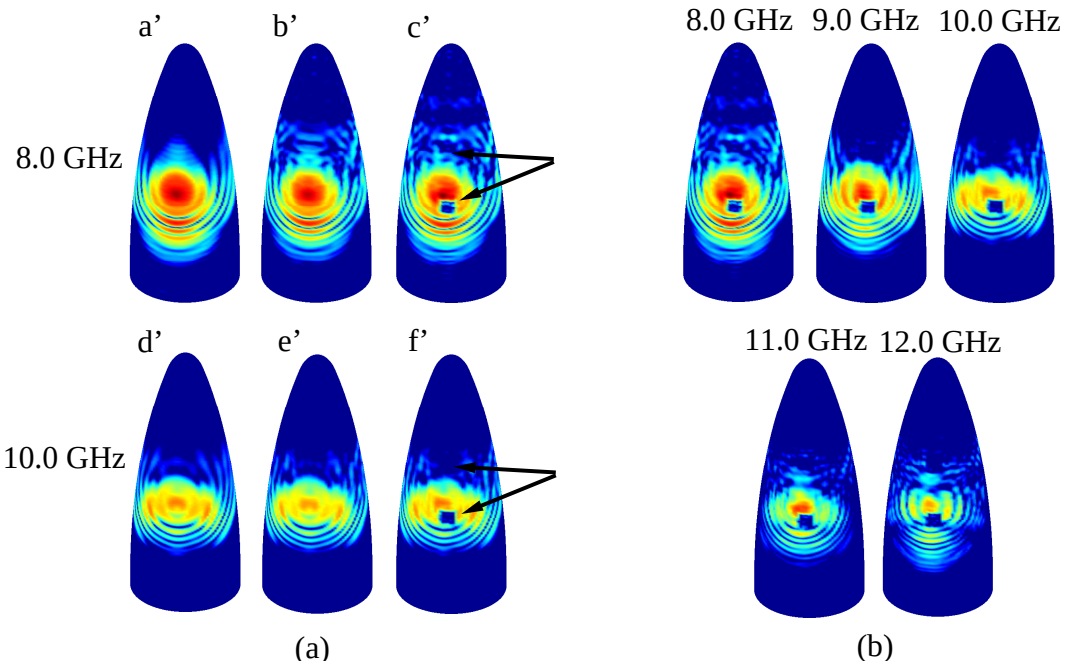

Figure 5: The reconstructed currents in dB-scale $[-30, 0]$, all normalized to the highest current value, *i.e.*, the maximum current magnitude in figure ac'. (a) The different measurement configurations are depicted at two different frequencies. From left to right; antenna without radome, antenna together with radome, and antenna together with defect radome, respectively. The arrows point out the location of the copper plates on the defect radome. (b) The defect radome case, shown at different frequencies.

clearly visible in the reconstructed currents on the back of the radome where flash lobes occur, see Figure 6b.

The defect radome has two copper plates attached to its surface. These are placed in the forward direction of the main lobe of the antenna and centered at the heights 41.5 cm and 65.5 cm above the bottom of the radome. The length of the side of the squared copper plates is 6 cm, which corresponds to 1.6 wavelengths at 8.0 GHz and 2.4 wavelengths at 12.0 GHz, respectively. The locations of the copper plates are detected as shown in Figure 5ac' and 5af', where the lower plate appears clearly. The other plate is harder to discern since it is placed in a region with small current magnitudes. However, a cross section graph through the main lobe detects even this copper plate, see Figure 6a. Observe that the effects of the copper plates cannot be localized directly in the near-field data, compare Figure 6a to Figure 3a. The near-field data only shows that the field is disturbed, not the location of the disturbance. Nevertheless, by using the scalar surface integral representation the effects of the plates are localized and focused. The defect radome also increases the backscattering as seen in Figure 6b. Due to the copper plates the flash lobes are different compared to the case with the non-defect radome.

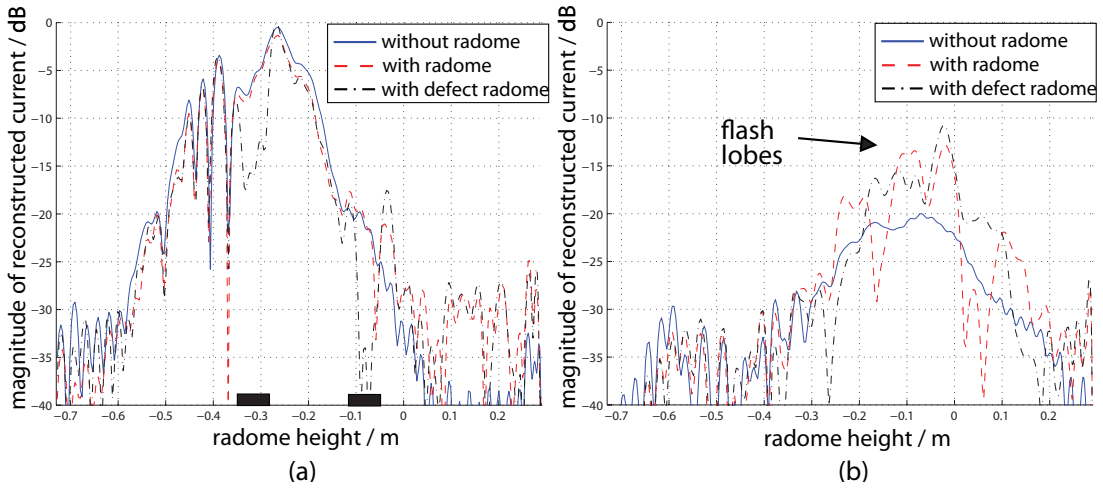

Figure 6: Cross section of the reconstructed current on the radome surface for the different measurement configurations, at 8.0 GHz. The current is shown as functions of the radome height for a fixed angle. All graphs are normalized to the highest current value, *i.e.*, the maximum current for the defect radome. (a) The graph representing the currents in the main lobe, *i.e.*, the front of the radome. The position of the copper plates are marked as thick lines on the horizontal axis. (b) The currents on the back of the radome.

As a final verification, the far-field amplitude on a sphere in the far-field region is studied. The electric field, originating from the equivalent currents on the radome, is calculated on the sphere,

$$\boldsymbol{E}_j^{\text{sph}} = -\mathcal{F}^{-1}\left[\widehat{\boldsymbol{G}}_{\hat{\jmath}}\widehat{\boldsymbol{M}}_{\hat{\jmath}}\right] \qquad \text{for all } j, \hat{\jmath} \tag{5.1}$$

in accordance with (3.8) and (3.12), except that $\widehat{\boldsymbol{G}}_{\hat{\jmath}}$ now describes the transformation from the radome to the inner fictitious surface and the far-field sphere, respectively. The denotations j and $\hat{\jmath}$ are, as before, the integer index belonging to the discretized azimuth component and the Fourier transformed discretized azimuth component, respectively.

The far-field amplitude F is derived as

$$F(\theta, \phi) = kr\, \mathrm{e}^{\mathrm{j}kr} E^{\text{sph}}(r, \theta, \phi) \qquad \text{as } r \to \infty \tag{5.2}$$

where (r, θ, ϕ) describes the spherical coordinate system [6]. The result is compared with measured far-field data, supplied by Chelton Applied Composites, as shown in Figure 7. The far field is depicted for the angles $\phi = 0$ and $\phi = \pi$, *i.e.*, a cross-section through the far field of the main lobe and the corresponding far field originating from the currents on the back of the radome. There is a lack of agreement between the measured far field and the calculated one in the angles corresponding to the top of the radome,*i.e.*, $\theta \approx 0$. This is due to the fact that fields originating hereof are not all included in the measured near-field data, since the measurement surface is a

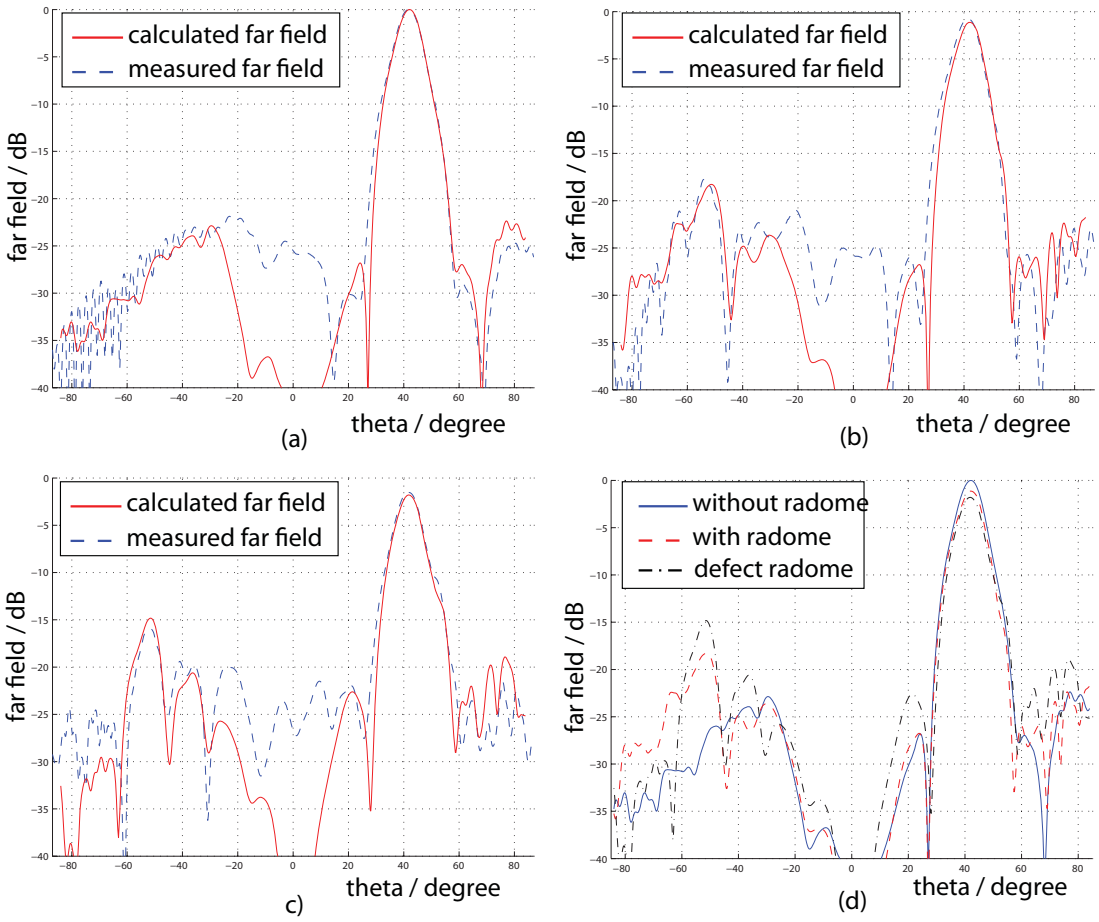

Figure 7: Comparison between the measured far-field data, supplied by Chelton Applied Composites, and the far field calculated from the equivalent currents on the radome surface. The far fields are normalized to the maximum value of the far field when no radome is present. (a) Antenna without radome. (b) Antenna together with radome. (c) Antenna together with defect radome. (d) The calculated far-field pattern for the three measurement configurations.

cylinder, see Figure 2a. The fact that the radome disturbs and reflects the electric field, as earlier seen in Figure 6b, can also be detected in the far field, see Figure 7d, where flash lobes appear when the radome is present.

6 Discussions and conclusions

The used scalar surface integral representation gives a linear map between the equivalent currents and the near-field data for general structures. It is here shown that this map can be inverted for axially symmetric geometries. The model can theoretically be adapted to geometries lacking symmetry axes. Although it is not a feasible approach for radome applications, demanding large quantities of measured data, with the present computer capacity.

The transformation method is stable and useful in radome design and for evaluation purposes. To investigate the electric field passing through the radome, the current distribution on the antenna or on a surface enclosing the antenna must be known. Using the surface integral representation, the equivalent currents, on a surface enclosing the antenna, can be described.

Another range of application within the radome industry is to study how *e.g.*, lightning conductors and Pitot tubes, often placed on radomes, influence the equivalent currents. We show that such influences and the field effects of the radome itself can be detected. In this paper, copper plates are attached on the radome, in the direction of the antenna main lobe. The length of the side of the square copper plates are $1.6-2.4$ wavelengths, corresponding to the frequency span $8.0-12.0$ GHz. The effects of the plates cannot be localized directly by using the near-field data, but by using the equivalent currents the effects are focused and detected on the radome surface. Thus, by transforming the near-field data to the radome surface, field defects introduced by the radome and other disturbances are focused back to their origins.

It is concluded that the transformation method based on the surface integral representation works very well and that the field of applications is large. A natural continuation is to elaborate the algorithm by including near field data with cross-polarization, *i.e.*, to implement the full Maxwell equations with a method of moments (MoM). Nevertheless, if the measured near-field data consists of one dominating component the use of the full Maxwell equations are not necessary, as shown in this paper.

Additional aspects to be investigated more thoroughly in the future are the resolution possibilities of manufacturing errors and other external field influences. Analysis of the phase information in the equivalent currents is also of interest. Moreover, a study regarding the detection of different materials attached to the radome surface is desirable.

Acknowledgments

The work reported in this paper is sponsored by Försvarets Materielverk (FMV), Sweden, which is gratefully acknowledged.

The authors also like to express their gratitude to the people at SAAB Bofors Dynamics, Sweden, and especially to Michael Andersson and Sören Poulsen at Chelton Applied Composites, Sweden, for supplying the near-field data and pictures of the experimental set-up.

References

[1] H. Anton. *Elementary Linear Algebra.* John Wiley & Sons, New York, 7 edition, 1994.

[2] C. A. Balanis. *Antenna Theory.* John Wiley & Sons, New York, second edition, 1997.

[3] L. E. Corey and E. B. Joy. On computation of electromagnetic fields on planar surfaces from fields specified on nearby surfaces. *IEEE Trans. Antennas Propagat.*, **29**(2), 402–404, 1981.

[4] J. Hanfling, G. Borgiotti, and L. Kaplan. The backward transform of the near field for reconstruction of aperture fields. *IEEE Antennas and Propagation Society International Symposium*, **17**, 764–767, 1979.

[5] J. E. Hansen, editor. *Spherical Near-Field Antenna Measurements.* Number 26 in IEE electromagnetic waves series. Peter Peregrinus Ltd., Stevenage, UK, 1988. ISBN: 0-86341-110-X.

[6] J. D. Jackson. *Classical Electrodynamics.* John Wiley & Sons, New York, second edition, 1975.

[7] D. S. Jones. *Acoustic and Electromagnetic Waves.* Oxford University Press, New York, 1986.

[8] R. Kress. *Linear Integral Equations.* Springer-Verlag, Berlin Heidelberg, second edition, 1999.

[9] J. Lee, E. M. Ferren, D. P. Woollen, and K. M. Lee. Near-field probe used as a diagnostic tool to locate defective elements in an array antenna. *IEEE Trans. Antennas Propagat.*, **36**(6), 884–889, 1988.

[10] Y. Rahmat-Samii, L. I. Williams, and R. G. Yaccarino. The UCLA bi-polar planar-near-field antenna-measurement and diagnostics range. *IEEE Antennas and Propagation Magazine*, **37**(6), 16–35, December 1995.

[11] T. K. Sarkar and A. Taaghol. Near-field to near/far-field transformation for arbitrary near-field geometry utilizing an equivalent electric current and MoM. *IEEE Trans. Antennas Propagat.*, **47**(3), 566–573, March 1999.

[12] G. Strang. *Introduction to applied mathematics.* Wellesley-Cambridge Press, Box 157, Wellesley MA 02181, 1986.

[13] S. Ström. Introduction to integral representations and integral equations for time-harmonic acoustic, electromagnetic and elastodynamic wave fields. In V. V. Varadan, A. Lakhtakia, and V. K. Varadan, editors, *Field Representations and Introduction to Scattering*, volume 1 of *Handbook on Acoustic, Electromagnetic and Elastic Wave Scattering*, chapter 2, pages 37–141. Elsevier Science Publishers, Amsterdam, 1991.

[14] V. V. Varadan, Y. Ma, V. K. Varadan, and A. Lakhtakia. Scattering of waves by spheres and cylinders. In V. V. Varadan, A. Lakhtakia, and V. K. Varadan,

editors, *Field Representations and Introduction to Scattering*, volume 1 of *Handbook on Acoustic, Electromagnetic and Elastic Wave Scattering*, chapter 4, pages 211–324. Elsevier Science Publishers, Amsterdam, 1991.

[15] M. B. Woodworth and A. D. Yaghjian. Derivation, application and conjugate gradient solution of dual-surface integral equations for three-dimensional, multi-wavelength perfect conductors. *Progress in Electromagnetics Research*, **5**, 103–129, 1991.

[16] A. D. Yaghjian. An overview of near-field antenna measurements. *IEEE Trans. Antennas Propagat.*, **34**(1), 30–45, January 1986.

Reconstruction of equivalent currents using the scalar surface integral representation

Paper II

Kristin Persson and Mats Gustafsson

Based on: K. Persson and M. Gustafsson. Reconstruction of equivalent currents using the scalar surface integral representation, Technical Report LUTEDX/(TEAT-7131), pp. 1–25, 2005, Department of Electrical and Information Technology, Lund University, Sweden. `http://www.eit.lth.se`

The technical report is a continuation of Paper I. An extended analysis of the measurement data is performed, whereas the theoretical parts remain unchanged. Specifically, the phase of the electric field is taken into account, and different visualization techniques are discussed and presented.

Abstract

Knowledge of the current distribution on a radome can be used to improve radome design, detect manufacturing errors, and to verify numerical simulations. In this paper, the transformation from near-field data to its equivalent current distribution on a surface of arbitrary material, *i.e.*, the radome, is analyzed. The transformation is based on the scalar surface integral representation that relates the equivalent currents to the near-field data. The presence of axial symmetry enables usage of the fast Fourier transform (FFT) to reduce the computational complexity. Furthermore, the problem is regularized using a singular value decomposition (SVD). Both synthetic and measured data are used to verify the method. The quantity of data is large since the height of the radome corresponds to $29 - 43$ wavelengths in the frequency interval $8.0 - 12.0$ GHz. It is shown that the method gives an accurate description of the field radiated from an antenna, on a surface enclosing it. Moreover, disturbances introduced by copper plates attached to the radome surface, not localized in the measured near field, are focused and detectable in the equivalent currents. The method also enables us to determine the phase shift of the field due to the passage of the radome, *cf.*, the insertion phase delay.

1 Introduction

This paper provides a wrap-up and a final report of the reconstruction of equivalent currents in the scalar approximation. The paper is a continuation of the work in [11]. An extended analysis of the measurement data is performed, whereas the theoretical parts remain unchanged. Specifically, the phase of the electric field is taken into account, and different visualization techniques are discussed and presented.

1.1 Ranges of application

There are several applications of a near field to equivalent currents transformation. For example, in the radome industry it is important to have accurate models of the field radiated from the antenna placed inside the radome. It is hard to measure this field directly since the radome often is located very close to the antenna and at these distances, there is a substantial interaction between the antenna and the measuring probe [6, 13, 19]. It is also important to have a powerful tool to determine the insertion phase delay (IPD), also known as the electrical thickness of the radome. The IPD is often one of the specified qualities given to characterize a radome. One way to measure the IPD is to place two horn antennas in such a way that the incident angle on the radome coincide with the Brewster angle, which is the angle where the transmitted field has its highest value [12]. To get the IPD, the phase of the transmitted field is subtracted from the phase of the measured field with no radome between the horn antennas. This process is very time consuming since it has to be repeated several times to cover the whole radome surface. Using the scalar surface integral equation, the phase shift due to the propagation through the radome is determined.

Another field of application is in the manufacturing of radiating bodies, *e.g.*, antenna arrays, when the radiation pattern from the body does not exhibit the expected form. By determination of the equivalent currents on the radiating body, the malfunctioning areas or components can be found.

1.2 History

A common method, transforming near field to equivalent currents and vice versa, is to use modal-expansions of the electric field [6]. This is a very efficient method for radiating bodies with certain geometrical symmetries, *i.e.*, planar, cylindrical, and spherical. Having a planar aperture, the plane wave spectrum of the field is utilized in the back transformation [3, 5]. The fact that the expression of the far field originating from a planar surface is equal to the Fourier transform of the radiating field on the aperture has been investigated in [10, 13]. The paper [10] also illustrates that defects, patches of Eccosorb, can be detected on the aperture. If the radiating body is of cylindrical or spherical geometry, the radial solutions contain cylindrical and spherical Bessel functions, while the angular solutions are described by trigonometric functions and the associated Legendre functions [6, 17]. For general geometrical symmetries, where modal-expansions do not exist, the modal-expansion is less applicable.

Moreover, different combinations of the electric- and magnetic-field integral equations (EFIE and MFIE) derived from the Maxwell equations, have been used to back propagate fields towards their sources. By this method it is possible to handle a wider class of geometries [13]. In [18] the dual-surface magnetic and electric-field integral equations are investigated. The fields are transformed back to a cubic perfect electric conductor by solving the dual-surface magnetic-field integral equation using the conjugate gradient method. Other work using the integral equations is reported in [14], where the near field is measured on a arbitrary surface and later inverted to a planar, perfectly conducting surface by using a singular value decomposition (SVD) for regularization.

1.3 The scalar surface integral representation

In this paper, the approach is to investigate a scalar surface integral representation that does not require the aperture to be a perfect electric or magnetic conductor. The representation provides a relation relating the unknown electric and magnetic equivalent currents on a surface to the measured electric field. An additional relation is given by the fact that the equivalent currents are constructed such that the integral is zero inside the volume, on which surface the currents exist, *i.e.*, the extinction theorem [16].

The integral relations are discretized into matrix linear equations. The matrix equations include an azimuthal convolution which is solved with a fast Fourier transform (FFT) in the angular coordinate. The fast Fourier transform brings down the complexity of the problem, *i.e.*, the original surface-to-surface linear map is decomposed into a set of line-to-line linear maps. A singular value decomposition (SVD)

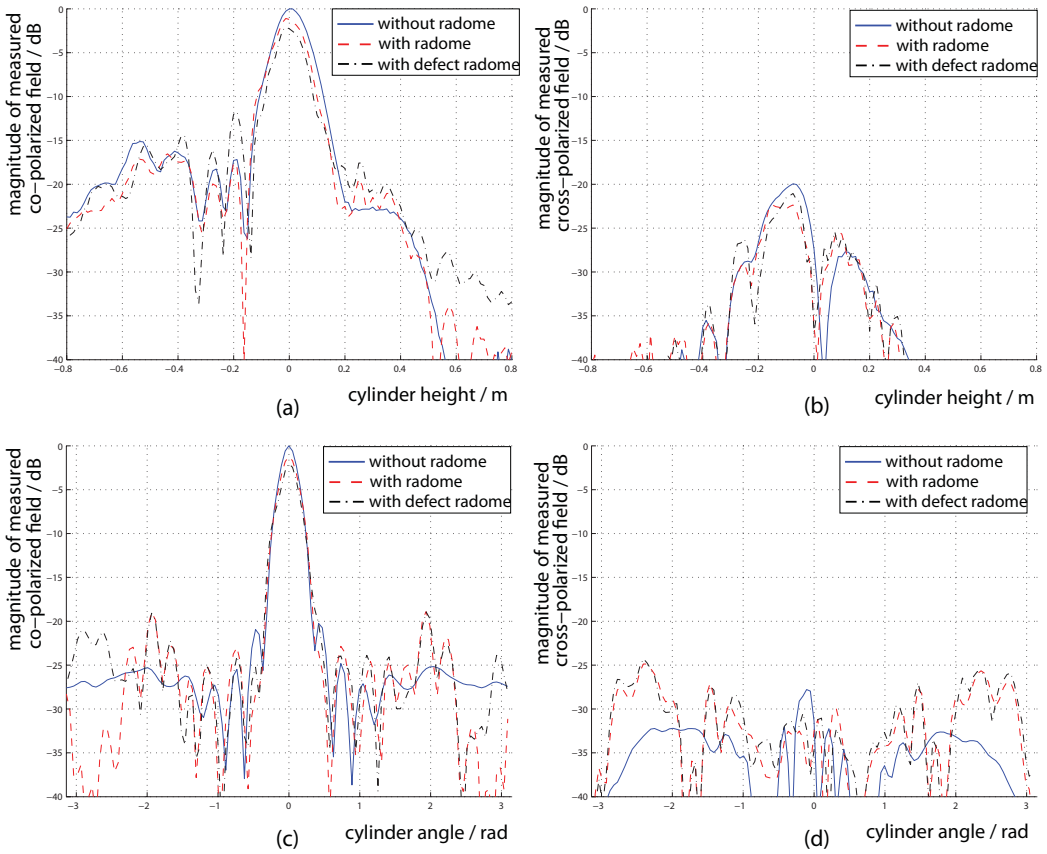

Figure 1: The measured co- and cross-polarized electric field on the measurement cylinder at 8.0 GHz. In (a) and (b) the angle is fixed at $\varphi = 0$, and the fields are normalized by the maximum value when no radome is present in (a). In (c) and (d) the height is fixed at $z = 0$, and the fields are normalized to the maximum value when no radome is present in (c).

is used to invert each of these linear maps. As most inverse problems it is ill-posed, *i.e.*, small errors in the near-field data can produce large errors in the equivalent currents. Thus, the problem needs to be regularized by suppression of small singular values when inverted.

1.4 Results

In this paper, the measured electric field is presumed to be scalar, *i.e.*, the scalar surface integral representation is utilized. The assumption is acceptable since the used near-field data, supplied by SAAB Bofors Dynamics and Applied Composites AB, Sweden, clearly have one dominating component in the main lobe, see Figure 1. The measured data is given for three different antenna and radome configurations, *viz.*, antenna, antenna together with radome, and antenna together with defect radome. The measurement set-up is shown in Figure 2. The height of the radome corresponds to $29 - 43$ wavelengths in the frequency interval $8.0 - 12.0$ GHz.

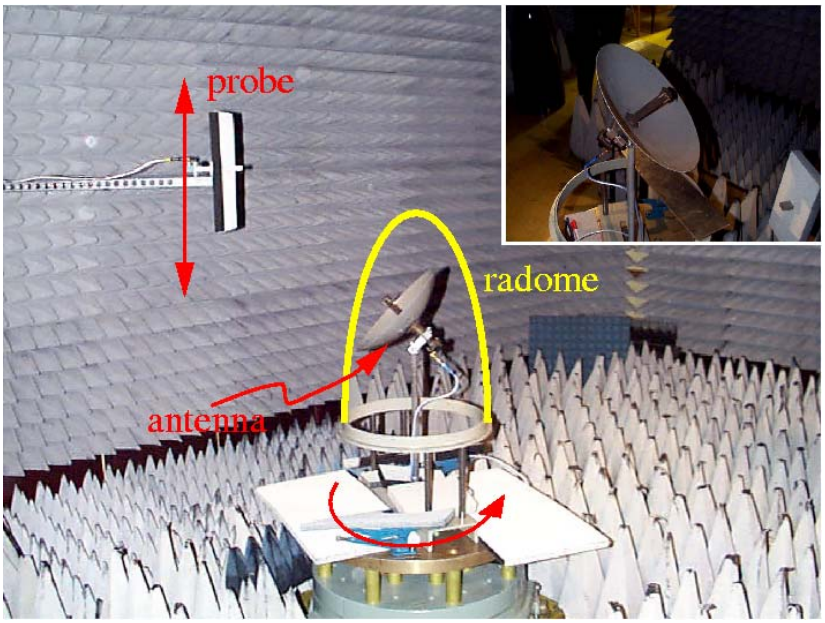

Figure 2: Photo of the cylindrical near-field range at SAAB Bofors Dynamics, Sweden. The antenna under test is rotated and the probe is moved in the vertical direction. A close up of the reflector antenna is shown in the upper right corner.

As a start, synthetic data is used to verify the method. Verification is also performed by a comparison between the measured far field and the far field calculated from the equivalent currents on the radome. The calculated far field agrees well with the measured far field. Moreover, when the radome is introduced, the field is scattered and flash lobes arise. The equivalent currents on the radome, due to these effects are identified and the flash lobes are accurately detected.

Manufacturing errors, not localized in the measured near-field data, can be focused and detected in the equivalent currents on the radome surface. In this paper, it is shown that the field scattered by copper plates attached on the radome, is focused back towards the original position of the copper plates. The length of the side of the square copper plates is 6 cm, *i.e.*, $1.6 - 2.4$ wavelengths corresponding to the frequency span $8.0 - 12.0$ GHz.

1.5 Outline

In Section 2, the experimental set-up is described and the measured near-field data is presented. The scalar surface integral representation is introduced and adapted to the specific problem in Section 3. Section 4 contains the implementation process of the scalar surface integral representation. Results, using synthetic near-field data, and the error of the method are presented. The results, when using the experimental near-field data, are shown and examined in Section 5. To give the reader a understanding of the field properties that can be extracted from the resulting data, Section 6 gives examples of ways to visualize the results. The paper ends with the achieved conclusions in Section 7.

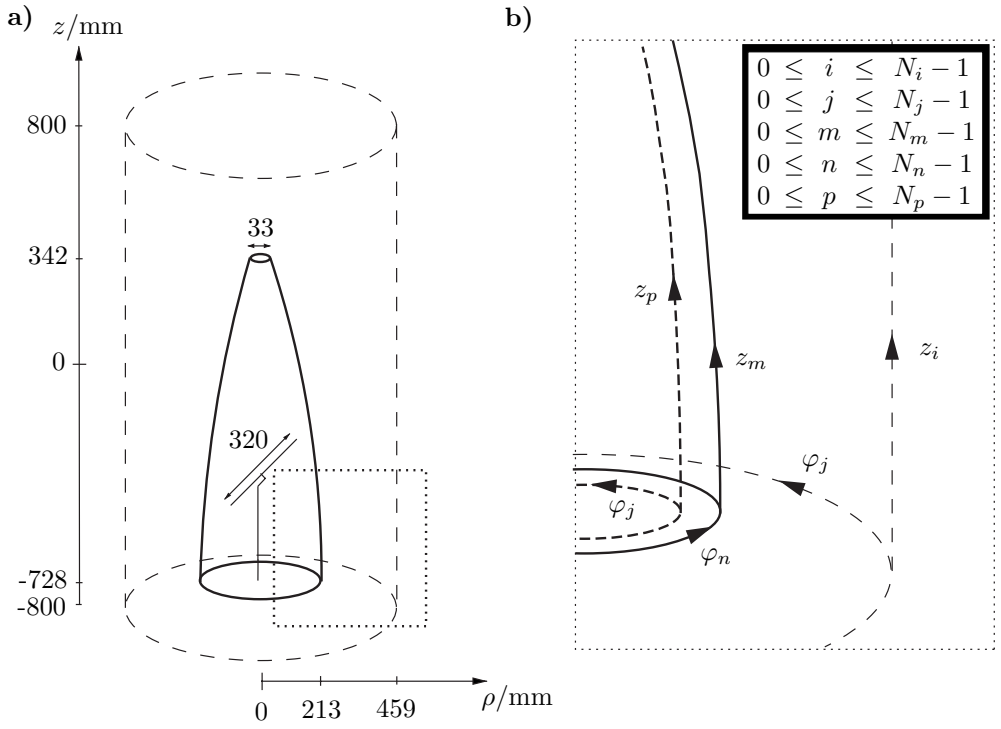

Figure 3: (a) The dimensions of the reflector antenna, the radome, and the cylinder where the electric near field is measured. (b) A close-up showing the inner fictitious surface and the discretized geometric variables.

2 Near-field measurements

The near-field data, used in this paper, was supplied by SAAB Bofors Dynamics and Applied Composites AB, Sweden. The set-up with relevant dimensions indicated is shown in Figures 2 and 3a. Three different measurements were performed; data measured without the radome, data measured with the radome, and data measured with the defect radome. The defect radome has two copper plates attached to its surface.

A reflector antenna, fed by a symmetrically located wave-guide, generates the near-field, see Figure 2. The diameter of the antenna is 0.32 m and its focal distance is 0.1 m. The main lobe of the antenna is vertically polarized relative to the horizontal plane. The standing wave ratio (SWR) is approximately 1.4 in the frequency range $8.2 - 9.5$ GHz. The antenna is poorly adapted for other frequencies.

The radome surface is axially symmetric and its radius, in terms of the height coordinate, is modeled by

$$\rho(z) = \begin{cases} 0.213\,\mathrm{m} & -0.728\,\mathrm{m} \le z \le -0.663\,\mathrm{m} \\ -(bz'+d) + \sqrt{(bz'+d)^2 - a(z')^2 - 2cz' - e} & -0.663\,\mathrm{m} < z \le 0.342\,\mathrm{m} \end{cases} \tag{2.1}$$

where $z' = z + 0.728\,\mathrm{m}$ and the constants are $a = 0.122$, $b = 0.048$, $c = -0.018\,\mathrm{m}$, $d = 0.148\,\mathrm{m}$, and $e = -0.108\,\mathrm{m}^2$, respectively. The material of the radome has a

relative permittivity of 4.32 and its loss tangent is 0.0144. The thickness of the wall of the radome varies between $7.6 - 8.2$ mm. The near-field measurement probe consists of a wave-guide for which no compensation is made in the final data. The cylindrical surface, where the electric field is measured, is located in the near-field zone [2].

The amplitude and phase of the electric field are measured in the frequency interval $8.0-12.0$ GHz on a cylindrical surface by moving the probe in the z-direction and rotating the antenna under test, see Figure 2. Applying this measurement set-up, the fields on the top and the bottom of the cylindrical surface could not be collected. It would have been preferable to measure the fields on an infinite cylinder. However, the size of the cylinder is chosen such that the turntable below the radome does not have a major influence of the measurements and such that the fields above $z = 800$ mm are negligible, *cf.*, Figures 1 and 3a. In the azimuth angle, 120 points are measured between -180° and 180° in steps of 3°. The z-dimension is divided into 129 points, separated by 12.5 mm. This means that at 8.0 GHz the electric field is measured 3 times per wavelength, in the z-direction, and 1.5 times per wavelength, in the azimuth direction, respectively. Together, a total of $120 \times 129 = 15480$ measurement points are used for each radome configuration and frequency. The co- and cross-polarized measured electric fields are shown in Figure 1. The differences between the three different antenna and radome cases arise from constructive and destructive interference between the radiated field and the scattered field. In Figure 1 it is also observed that the electric field consists of a dominating co-component in the main lobe, *i.e.*, a dominating z-component since the antenna is vertically polarized.

3 The surface integral representation

The surface integral representation expresses the electromagnetic field in a homogeneous, isotropic region in terms of its values on the bounding surface. The representation states that if the electromagnetic field on a surface of a volume is known, the electromagnetic field in the volume can be determined [8, 16]. The representation is derived starting from the time harmonic Maxwell equations with the time convention $\mathrm{e}^{\mathrm{j}\omega t}$. The Maxwell equations transform into the vector Helmholtz equation

$$\nabla^2 \boldsymbol{E}(\boldsymbol{r}) + k^2 \boldsymbol{E}(\boldsymbol{r}) = 0 \tag{3.1}$$

since the material (air) is source free, homogeneous, and isotropic.

Assume that the electric field only consists of a component in the z-direction. This is a good approximation dealing with the specific measurements described in Section 2 since our prime interest is to reconstruct the electric field in the main lobe, where the z-component is clearly the dominating one, *cf.*, Figure 1.

Working with a scalar field, the surface integral representation only depends on the scalar electric field, E_z, and its normal derivative, $\partial E_z/\partial n$, *i.e.*, not all components of the electric and magnetic fields need to be included. Observe that in the vector integral representation all tangential components of the electric and magnetic

fields must be taken into account [8]. The scalar surface integral representation is derived using the free space Green function $g(\boldsymbol{r},\boldsymbol{r}') = \mathrm{e}^{-\mathrm{j}k|\boldsymbol{r}-\boldsymbol{r}'|}/4\pi|\boldsymbol{r}-\boldsymbol{r}'|$ giving [16]

$$\iint\limits_S \left[\frac{\partial g(\boldsymbol{r},\boldsymbol{r}')}{\partial n} E_z(\boldsymbol{r}) - g(\boldsymbol{r},\boldsymbol{r}')\frac{\partial E_z(\boldsymbol{r})}{\partial n}\right] \mathrm{d}S = \begin{cases} -E_z(\boldsymbol{r}') & \boldsymbol{r}' \in V \\ 0 & \boldsymbol{r}' \notin V \end{cases} \tag{3.2}$$

where V is the volume exterior to the closed surface S which consists of the radome surface with an added top and bottom surface. Observe that the electric field does not have to be zero outside the volume, *i.e.*, inside the radome. The surface integral representation (3.2) only states that the left-hand side of the equation, evaluated at a point $\boldsymbol{r}'$ outside the volume V, is zero, *i.e.*, the extinction theorem [16].

The equivalent surface currents are introduced as

$$M(\boldsymbol{r}) \equiv E_z(\boldsymbol{r}) \quad \text{and} \quad M'(\boldsymbol{r}) \equiv \frac{\partial E_z(\boldsymbol{r})}{\partial n} \tag{3.3}$$

which inserted in (3.2) give

$$\iint\limits_{\text{radome}} \left[\frac{\partial g(\boldsymbol{r},\boldsymbol{r}')}{\partial n} M(\boldsymbol{r}) - g(\boldsymbol{r},\boldsymbol{r}')M'(\boldsymbol{r})\right] \mathrm{d}S = \begin{cases} -E_z^{\text{cyl}}(\boldsymbol{r}') & \boldsymbol{r}' \in \text{cylinder} \\ 0 & \boldsymbol{r}' \in \text{inside radome} \end{cases} \tag{3.4}$$

where E_z^{cyl} is the z-component of the electric field on the measurement cylinder. The fictitious surface, inside the radome, is shaped as the radome and located close to the radome wall.

3.1 Angular Fourier transformation

Due to the measurement set-up, the transformation, the Green's function, is axially symmetric, see Section 2. The symmetry only applies to the transformation, not to the electric field. Thus, the left-hand side in (3.4) represents a convolution and by using a Fourier transformation of the azimuth coordinate, the computational complexity can be brought down one dimension. This reduction of one dimension, can be understood by writing the left-hand side in (3.4) as a matrix, X. This matrix is a circulant matrix, *i.e.*, every row is shifted one step to the right compared to the previous row. The eigenvectors of all circulant matrices are the column vectors of the Fourier matrix, F. Multiplying a circulant matrix with the Fourier matrix, *i.e.*, performing the Fourier transformation, gives $FX = F\Lambda$ where Λ is a diagonal matrix, which can be seen as a reduction of one dimension [15].

The continuous variables in (3.4) are discretized to give linear matrix equations. The discretized cylindrical coordinate system is described by the integer indices depicted in Figure 3b. Discretization and Fourier transformation, in the azimuth coordinate, of (3.4) give

$$\sum_{m=0}^{N_m-1} \left[\widehat{\mathcal{G}}'_{im\hat{\jmath}}\widehat{M}_{m\hat{\jmath}} \;\; - \widehat{\mathcal{G}}_{im\hat{\jmath}}\widehat{M}'_{m\hat{\jmath}}\right] = -\widehat{E}_{i\hat{\jmath}}^{\text{cyl}} \qquad \text{for all } \; i,\hat{\jmath} \tag{3.5}$$

and

$$\sum_{m=0}^{N_m-1}\left[\widehat{\mathsf{G}}'_{pm\hat{\jmath}}\widehat{M}_{m\hat{\jmath}} \;-\widehat{\mathsf{G}}_{pm\hat{\jmath}}\widehat{M}'_{m\hat{\jmath}}\right]=0 \qquad \text{for all } p,\hat{\jmath} \tag{3.6}$$

where $\mathcal{G}$ and G are the surface integrals, taken over the radome, of the Green's function multiplied with the basis functions used in the discretization process. $\mathcal{G}$ has the discretized space variable $\boldsymbol{r}'$ belonging to the measurement cylinder and G has the discretized space variable $\boldsymbol{r}'$ belonging to the fictitious surface inside the radome, respectively. The prime denotes the normal derivative of the Green's function, $\hat{\jmath}$ is the integer index belonging to the Fourier transformed azimuth component, and the "hat" denotes the Fourier transformed variables. The summation limits N_m and N_p are given in Figure 3b.

To solve the scalar surface integral representation, a limit process of (3.6) should be performed, letting the fictitious surface inside the radome approach the radome surface [2, 9]. To avoid singularities, we let the fictitious surface be located at a finite distance from the radome surface. This provides us with a simple and feasible method to allocate the surface currents, *i.e.*, the extinction theorem is used as an approximate solution to the integral representation in (3.6).

Reduction of M' in (3.5) and (3.6) gives

$$\sum_{m=0}^{N_m-1}\left\{\widehat{\mathcal{G}}'_{im\hat{\jmath}}-\sum_{p=0}^{N_p-1}\sum_{q=0}^{N_m-1}\widehat{\mathcal{G}}_{iq\hat{\jmath}}\,(\widehat{\mathsf{G}}^{-1})_{qp\hat{\jmath}}\,\widehat{\mathsf{G}}'_{pm\hat{\jmath}}\right\}\widehat{M}_{m\hat{\jmath}} \;=-\widehat{E}^{\text{cyl}}_{i\hat{\jmath}} \quad \text{for all } i,\hat{\jmath} \tag{3.7}$$

Equation (3.7) can also be written as $\hat{\jmath}$ matrix equations

$$\widehat{\boldsymbol{G}}^{\text{radome}}_{\hat{\jmath}}\,\widehat{\boldsymbol{M}}_{\hat{\jmath}} \;=-\widehat{\boldsymbol{E}}^{\text{cyl}}_{\hat{\jmath}} \qquad \text{for all } \hat{\jmath} \tag{3.8}$$

where the matrices are defined as $\widehat{\boldsymbol{M}}_{\hat{\jmath}}\equiv[\widehat{M}_{m1}]_{\hat{\jmath}}$, $\widehat{\boldsymbol{E}}^{\text{cyl}}_{\hat{\jmath}}\equiv[\widehat{E}^{\text{cyl}}_{i1}]_{\hat{\jmath}}$, and

$$\widehat{\boldsymbol{G}}^{\text{radome}}_{\hat{\jmath}}\equiv[\widehat{\mathcal{G}}'_{im}]_{\hat{\jmath}}-[\widehat{\mathcal{G}}_{im}]_{\hat{\jmath}}[\widehat{\mathsf{G}}_{mp}]^{-1}_{\hat{\jmath}}[\widehat{\mathsf{G}}'_{pm}]_{\hat{\jmath}} \qquad \text{for all } \hat{\jmath} \tag{3.9}$$

The used notation of matrices is that of [1].

3.2 Inversion with singular value decomposition

Since the matrices $\widehat{\boldsymbol{G}}^{\text{radome}}_{\hat{\jmath}}$ and $[\widehat{\mathsf{G}}_{mp}]_{\hat{\jmath}}$ in (3.8) and (3.9) are not quadratic, a regular inversion cannot be performed. A fast and easy way to solve this is to use the singular value decomposition (SVD) [15]. This method is used on both matrices, but the SVD-equations are only given here for $\widehat{\boldsymbol{G}}^{\text{radome}}_{\hat{\jmath}}$. The matrix system (3.8) can then be rewritten as

$$\widehat{\boldsymbol{U}}_{\hat{\jmath}}\widehat{\boldsymbol{S}}_{\hat{\jmath}}\widehat{\boldsymbol{V}}^{\dagger}_{\hat{\jmath}}\widehat{\boldsymbol{M}}_{\hat{\jmath}}=-\widehat{\boldsymbol{E}}^{\text{cyl}}_{\hat{\jmath}} \qquad \text{for all } \hat{\jmath} \tag{3.10}$$

where $\widehat{\boldsymbol{V}}^{\dagger}_{\hat{\jmath}}$ denotes the Hermitian conjugate of $\widehat{\boldsymbol{V}}_{\hat{\jmath}}$. Both $\widehat{\boldsymbol{U}}_{\hat{\jmath}}$ and $\widehat{\boldsymbol{V}}_{\hat{\jmath}}$ are orthogonal matrices. $\widehat{\boldsymbol{S}}_{\hat{\jmath}}$ is a diagonal matrix consisting of the singular values to $\widehat{\boldsymbol{G}}^{\text{radome}}_{\hat{\jmath}}$ in decreasing order. The singular values of both $\widehat{\boldsymbol{G}}^{\text{radome}}_{\hat{\jmath}}$ and $[\widehat{\mathsf{G}}_{mp}]_{\hat{\jmath}}$ exhibit the tendency shown by the curves in Figure 4a.

A cut-off value, δ, normalized to the operator L_2-norm of $\widehat{\boldsymbol{G}}_1^{\text{radome}}$ is chosen. The operator L_2-norm of $\widehat{\boldsymbol{G}}_1^{\text{radome}}$ is equal to the largest singular value (σ_1) of the largest Fourier transformed azimuth component [9]. All singular values smaller than δ are ignored during the inversion of $\widehat{\boldsymbol{S}}_{\hat{\jmath}}$ and are afterwards set to zero. If this is not done the small singular values create an uncontrolled growth of non-radiation currents when inverted. The mathematical formulation then fails since very small electric field contributions become dominating. Performing the inversion of (3.10) gives

$$\widehat{\boldsymbol{M}}_{\hat{\jmath}} = - \widehat{\boldsymbol{V}}_{\hat{\jmath}} \widehat{\boldsymbol{S}}_{\hat{\jmath}}^{-1} \widehat{\boldsymbol{U}}_{\hat{\jmath}}^{\dagger} \widehat{\boldsymbol{E}}_{\hat{\jmath}}^{\text{cyl}} \qquad \text{for all } \hat{\jmath} \tag{3.11}$$

Before the system of equations is solved, it is necessary to convert it back from Fourier space by an inverse Fourier transformation

$$\boldsymbol{M}_j = \mathcal{F}^{-1} \left[-\widehat{\boldsymbol{V}}_{\hat{\jmath}} \widehat{\boldsymbol{S}}_{\hat{\jmath}}^{-1} \widehat{\boldsymbol{U}}_{\hat{\jmath}}^{\dagger} \widehat{\boldsymbol{E}}_{\hat{\jmath}}^{\text{cyl}} \right] \qquad \text{for all } j, \hat{\jmath} \tag{3.12}$$

where j, as above, denotes the integer index belonging to the discretized azimuth component, see Figure 3b.

4 Implementation

Some adjustments of the formulas are made in the implementation process. To facilitate the calculations, the radome surface is reshaped into a closed surface by adding a smooth top and bottom surface. These extra surfaces are useful since the measurements are performed under non-ideal conditions. The turntable, on which the antenna and radome are located, see Figure 2, reflects some of the radiation, which is taken care of by the added bottom surface. The top surface takes care of the electric field that is reflected on the inside of the radome and then radiated through the top hole. If these factors are not considered, unwanted edge effects occur since the electric field originating from the turntable and the top of the radome is forced to arise from the radome itself.

The measured electric near field is measured 1.5 times per wavelength, in the azimuth direction, at the frequency 8.0 GHz, see Section 2. To be sure that the equivalent currents on the radome are recreated in an accurate way, it is necessary to have a high sample density on the radome. This is achieved by increasing the number of discrete points, in the azimuth direction, on the radome surface by including extra angles between the already existing ones. Thus, the axial symmetry of the Green's transformation is preserved.

The sample density on the measurement cylinder contributes very little to the total error. The scalar surface integral representation creates currents on the radome such that the electric field is correct at the measurement points. However, if the Nyquist theorem is fulfilled, then the electric field is correct at all points on the measurement surface, *i.e.*, not only at the measurement points [15]. As mentioned

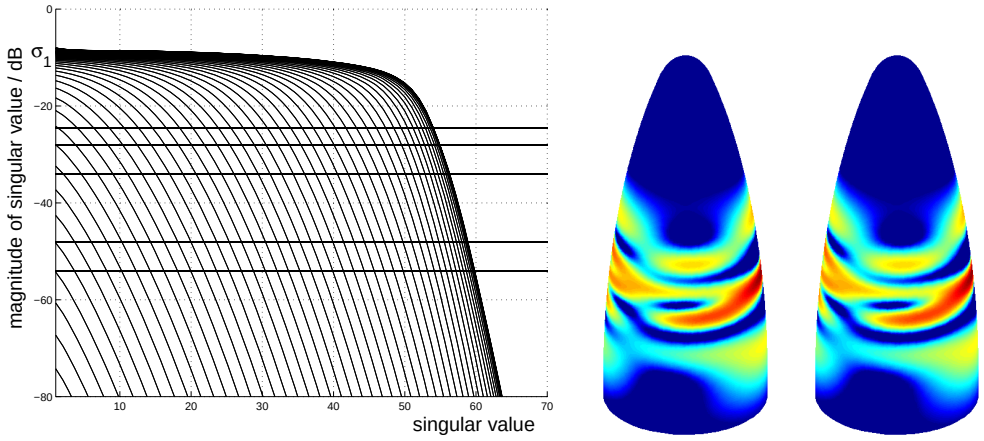

(a) (b) (c)

Figure 4: (a) The typical behavior of singular values of $\widehat{\boldsymbol{G}}_{\hat{\jmath}}^{\text{radome}}$ and $[\widehat{\mathsf{G}}_{mp}]_{\hat{\jmath}}$. Every curve represents the singular values of a Fourier transformed azimuth component, *i.e.*, different $\hat{\jmath}$. The horizontal lines describe the cut-off values, $\delta = \sigma_1[0.15\ 0.1\ 0.05\ 0.01\ 0.005]$. (b) The synthetic equivalent currents, originating from three dipoles, in a dB-scale $[-15, 0]$, normalized to the highest current value, *i.e.*, the maximum current magnitude in subfigure c. (c) The reconstructed currents in dB-scale $[-15, 0]$, normalized to its highest current value.

above, the amount of data is large and the matrix $\widehat{\boldsymbol{G}}^{\text{radome}}$, *cf.*, (3.9), has approximately 10^8 elements at the frequency 8.0 GHz when the sample density is 10 points per wavelength both in the azimuth direction and in the z-direction on the radome.

To verify and find the error of the method, synthetic data is used. A synthetic electric field, originating from three dipoles inside the radome is shown in Figure 4b. The corresponding reconstructed currents on a surface shaped as the radome are shown in Figure 4c where the sample density is 10 points per wavelength both in the z-direction and in the azimuth direction. The inner fictitious surface is located one wavelength from the radome surface.

The error as a function of the Fourier transformed azimuth component is defined as

$$\begin{aligned} \text{Err}(\hat{\jmath}) &= 20\log_{10}\frac{\| \widehat{\boldsymbol{M}}_{\hat{\jmath}} - \widehat{\boldsymbol{M}}_{\hat{\jmath}}^{\text{correct}} \|_2}{\| \widehat{\boldsymbol{M}}_{\hat{\jmath}}^{\text{correct}} \|_2} \\ &= 20\log_{10}\frac{\sqrt{\sum_{m=0}^{N_m-1} | \widehat{M}_{m\hat{\jmath}} - \widehat{M}_{m\hat{\jmath}}^{\text{correct}} |^2 \, \Delta S_m}}{\sqrt{\sum_{m=0}^{N_m-1} | \widehat{M}_{m\hat{\jmath}}^{\text{correct}} |^2 \, \Delta S_m}} \quad \text{for all } \hat{\jmath} \end{aligned} \tag{4.1}$$

where ΔS_m denotes the discretized area elements on the radome.

By using synthetic data and choosing appropriate cut-off values, δ, the error is shown to be below -60 dB for each existing Fourier transformed azimuth component. To obtain these low error levels, the measurement surface must be closed, *i.e.*, field

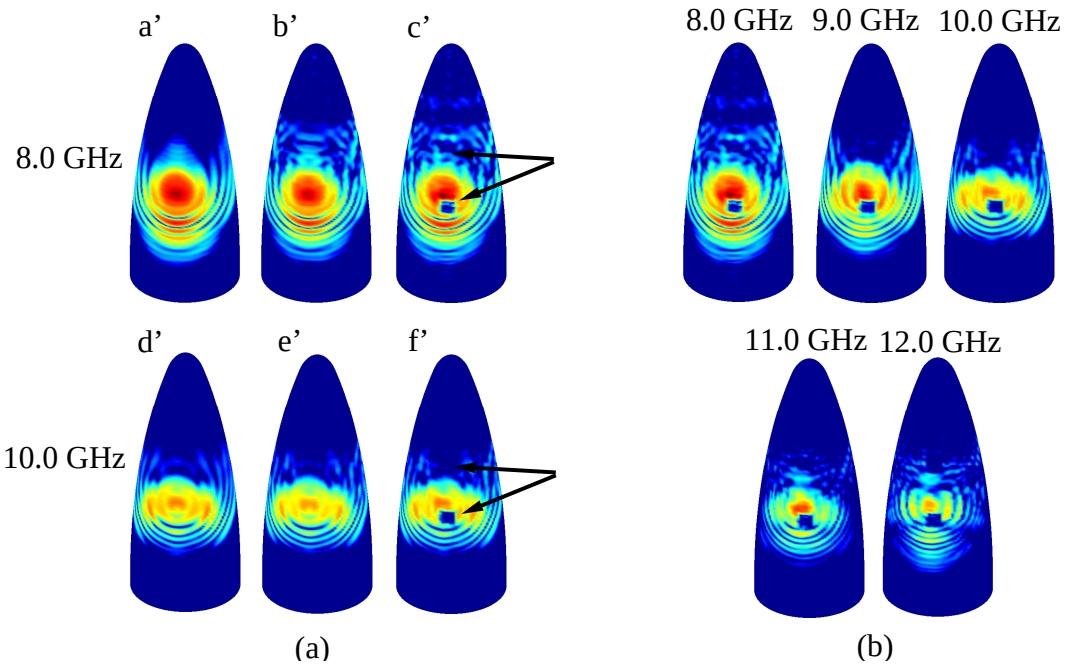

Figure 5: The reconstructed currents in dB-scale $[-30, 0]$, all normalized to the highest current value, *i.e.*, the maximum current magnitude in figure ac'. (a) The different measurement configurations are depicted at two different frequencies. From left to right; antenna without radome, antenna together with radome, and antenna together with defect radome, respectively. The arrows point out the location of the copper plates on the defect radome. (b) The defect radome case, shown at different frequencies.

values at the top and bottom surfaces of the cylindrical measurement surface must be included. The cut-off values depend on the complexity of the specific measurement set-up and must be investigated for each new set-up.

The total error of the scalar surface integral representation using the measured near field described in Section 2 is hard to define since the noise level and the amount of field spread outside the measurement cylinder are unknown parameters. Instead, we rely on the fact that the method handles synthetic data well and that the results using measured data is satisfactory, see Section 5.

5 Results using measured near-field data

The measured near-field data, described in Section 2, is investigated. The inner fictitious surface is located one wavelength from the radome surface. The sample density on the radome is 10 points per wavelength both in the azimuth direction and in the z-direction. The cut-off values are determined in accordance with the discussion in Section 4.

Three different measurement configurations are investigated, *viz.*, antenna, an-

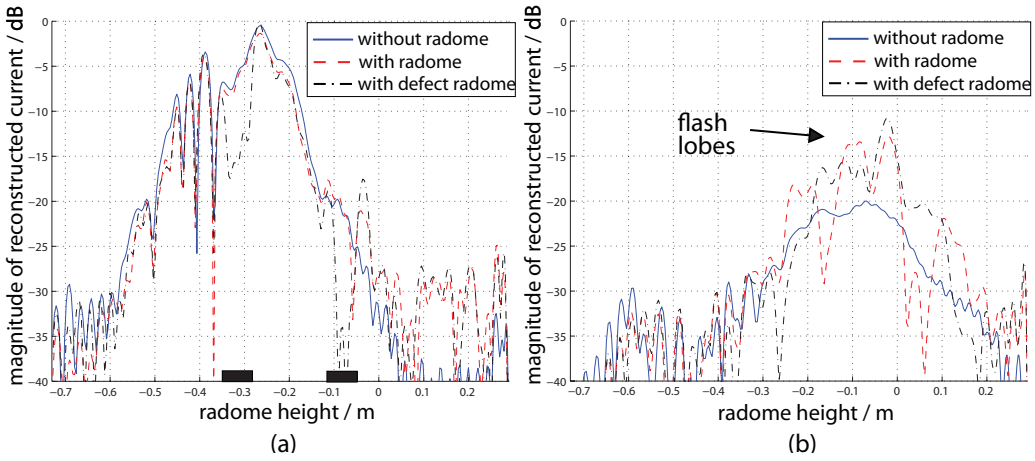

Figure 6: Cross section of the reconstructed currents, on the radome surface, for the different measurement configurations at 8.0 GHz. The currents are shown as functions of the radome height for a fixed angle. All graphs are normalized to the highest current value, *i.e.*, the maximum current for the defect radome case. (a) The graph representing the currents in the main lobe, *i.e.*, the front of the radome. The positions of the copper plates are marked by thick lines on the horizontal axis. (b) The currents on the back of the radome.

tenna together with radome, and antenna together with defect radome. The studied frequency interval is $8.0 - 12.0$ GHz. The results for the different measurement configurations are shown in Figure 5a at the frequencies 8.0 GHz and 10.0 GHz. In Figure 5b the results for the defect radome case are shown for the frequencies 8.0 GHz, 9.0 GHz, 10.0 GHz, 11.0 GHz, and 12.0 GHz, respectively.

In the case when no radome is located around the antenna, the equivalent currents are calculated on a surface shaped as the radome, see Figure 5aa' and 5ad'. The figures show that the near field close to the antenna is complex and hard to predict, *i.e.*, the diffraction pattern must be taken into account. The diffraction is explained as environmental reflections and an off-centered antenna feed.

The case when the radome is present, see Figure 5ab' and 5ae', shows in comparison to the case without radome that the radome interacts with the antenna and hence disturbs the radiated field. However, the currents in the main lobe are hardly affected by the radome, as seen in Figure 6a. The influence of the radome is clearly visible in the reconstructed currents on the back of the radome where flash lobes occur, see Figure 6b.

The defect radome has two copper plates attached to its surface. These are located in the forward direction of the main lobe of the antenna and centered at the heights 41.5 cm and 65.5 cm above the bottom of the radome. The length of the side of the squared copper plates is 6 cm, which corresponds to 1.6 wavelengths at 8.0 GHz and 2.4 wavelengths at 12.0 GHz, respectively. The locations of the copper plates are detected as shown in Figure 5ac' and 5af', where the lower plate appears clearly. The other plate is harder to discern since it is located in a region with low

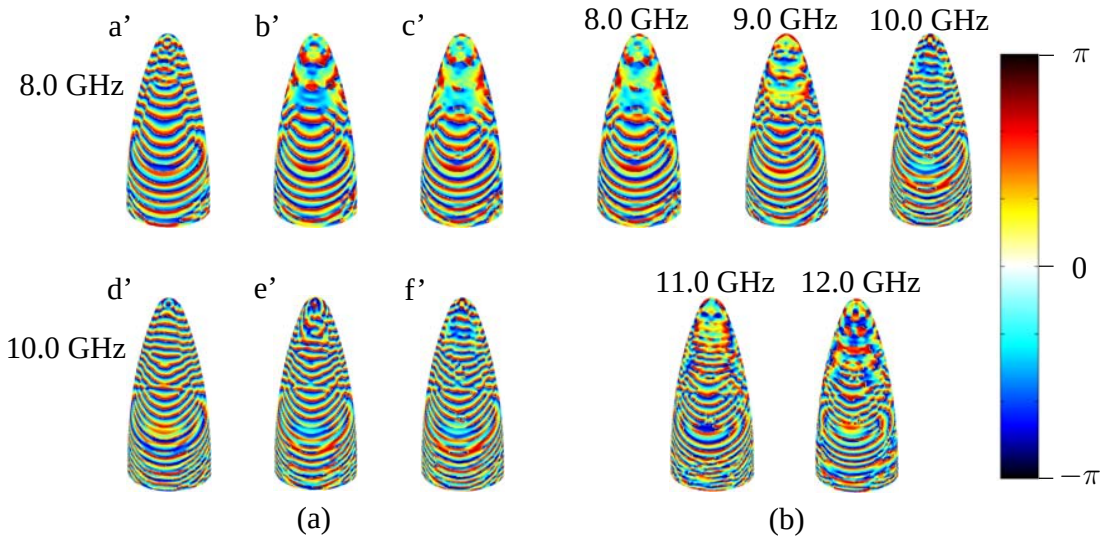

Figure 7: The reconstructed phase of the currents on the front of the radome. (a) The different measurement configurations are depicted at two different frequencies. From left to right; antenna without radome, antenna together with radome, and antenna together with defect radome, respectively. (b) The defect radome case, shown at different frequencies.

amplitudes. However, a cross section graph through the main lobe detects even this copper plate, see Figure 6a. Observe that the effects of the copper plates cannot be localized directly in the near-field data, compare Figure 6a to Figure 1a. The near-field data only shows that the field is disturbed, not the location of the disturbance. Nevertheless, by using the scalar surface integral representation, the effects of the plates are localized and focused. The defect radome also increases the backscattering as seen in Figure 6b. Due to the copper plates, the flash lobes are different compared to the case with the non-defect radome.

Until now only the amplitude of the reconstructed currents has been investigated. The phase of the currents is depicted in Figure 7. The vertical lines above the main lobe in Figure 7a' and 7d' are due to phase jumps and are caused by the low amplitude of the currents in these areas. The phase difference (antenna - antenna with radome) reveals how the the phase is changed due to the influence of the radome, see Figure 8. The phase shift, denoted Δ_φ, is only known modulus 2π. The phase shift in the main lobe is almost constant, especially for the low frequencies, which is more clearly seen by looking at the cross section of the front side of the radome, see Figure 9. What is noticeable in this image is the region between $z = -0.4\,\mathrm{m}$ and $z = 0\,\mathrm{m}$, *i.e.*, the main lobe where the phase shift is nearly constant. In areas where the amplitude of the field is small, *cf.*, Figure 6a, the phase of the field is not well defined, *i.e.*, it is dominated by noise. This almost constant phase shift, for the low frequencies, confirms that the radome is quite well adapted to the frequencies $8.0 - 9.0\,\mathrm{GHz}$, which is also the frequency interval where the antenna is well matched, see Section 2.

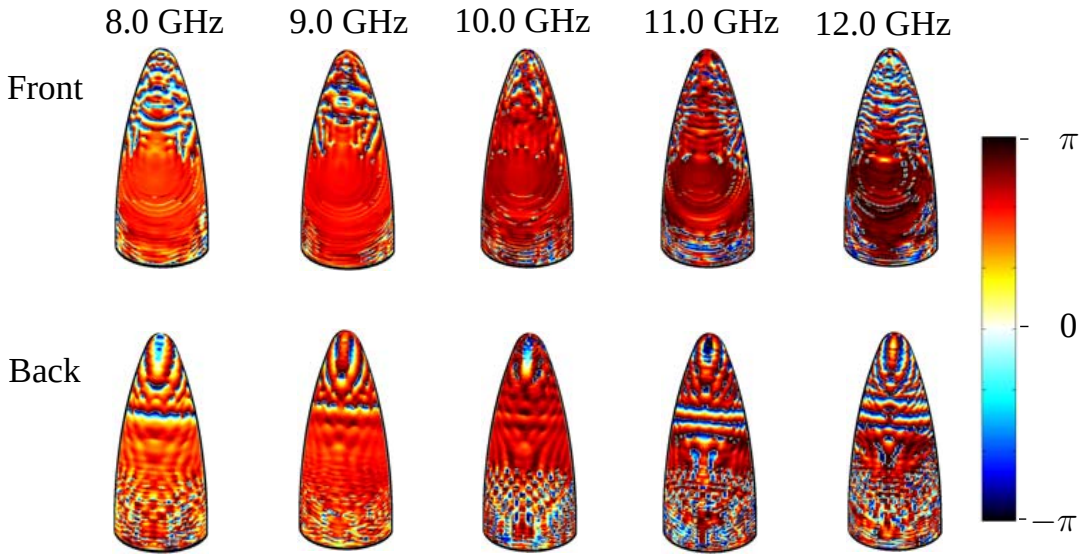

Figure 8: The phase difference (antenna - antenna with radome) for several frequencies.

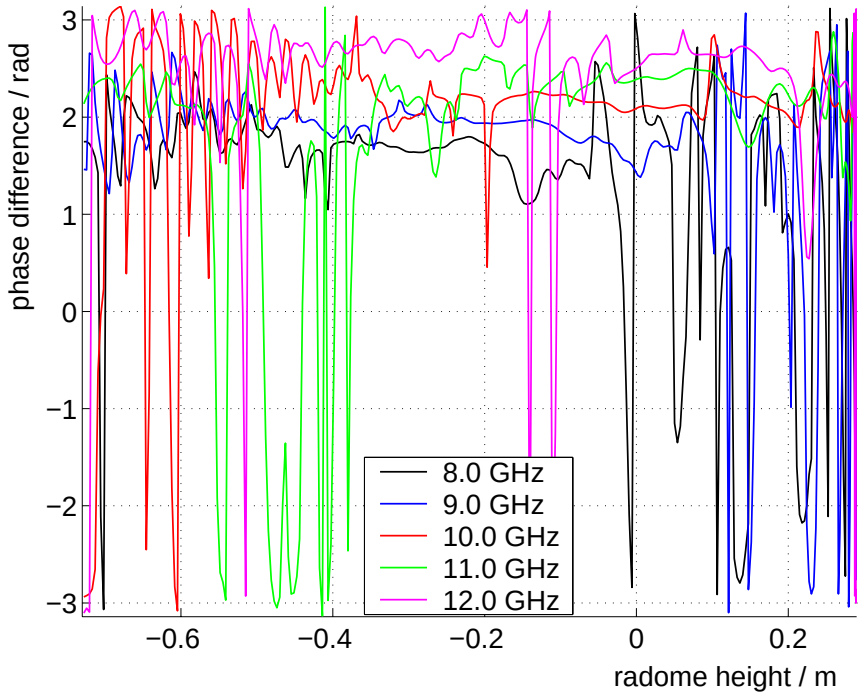

Figure 9: Cross section of the phase difference (antenna - antenna with radome) on the front of the radome. Observe that in areas where the amplitude of the currents are small, *cf.*, Figure 6a, the phase of the field is not well defined, *i.e.*, it is dominated by noise.

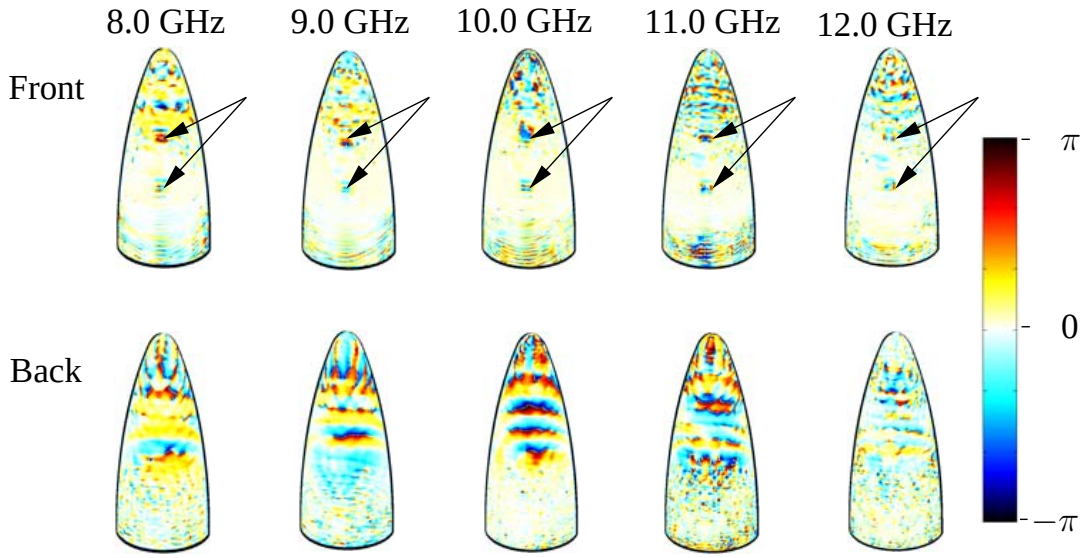

Figure 10: The phase difference (antenna with radome - antenna with defect radome) for several frequencies. The arrows point out the location of the copper plates.

Sometimes, when dealing with phase information, the figures can be clarified by using phase unwrapping [4]. It means that the jump in the scale between 0 and 2π is removed. In our case phase unwrapping gives us no new information since the area of interest is the main lobe and the phase shift there is almost constant.

To validate the calculation of the phase shift, the propagation distance of the field through the radome, *i.e.*, the actual propagation path of the field in the radome material, is estimated and compared to the actual thickness of the radome given in Section 2. The propagation distance of the field through the radome is longer than the wall thickness since the field has an incident angle larger than zero. The phase difference between two fields propagating the distance d in air and in the radome material, respectively, can be written as [12]

$$\Delta_\varphi = \mathrm{Re}\left[2\pi f\sqrt{\epsilon_0\epsilon_r\mu_0(1-\mathrm{j}\tan\delta)}\right] d - 2\pi f\sqrt{\epsilon_0\mu_0}\, d \tag{5.1}$$

where f is the frequency, d the propagation distance of the field, ϵ_0 the permittivity of free space, and μ_0 the permeability of free space, respectively. The parameters belonging to the radome, described in Section 2, are the relative permittivity, ϵ_r, and the loss tangent, $\tan\delta$. Since only an estimation of the propagation distance is performed, we assume that this distance is the same in both air and the radome material. We assume perpendicular incidence and neglect all reflections. According to Section 2, the thickness of the radome is between $7.6 - 8.2\,\mathrm{mm}$. The almost constant phase shifts in the main lobe are approximated from Figure 9 for all frequencies. Solving for d in (5.1) results in a propagation distance of $9.3 - 9.7\,\mathrm{mm}$ for all frequencies, which is considered constant due to the crude approximations of the phase shifts. The phase shift, Δ_φ, is comparable to the insertion phase delay (IPD) often used in the radome industry.

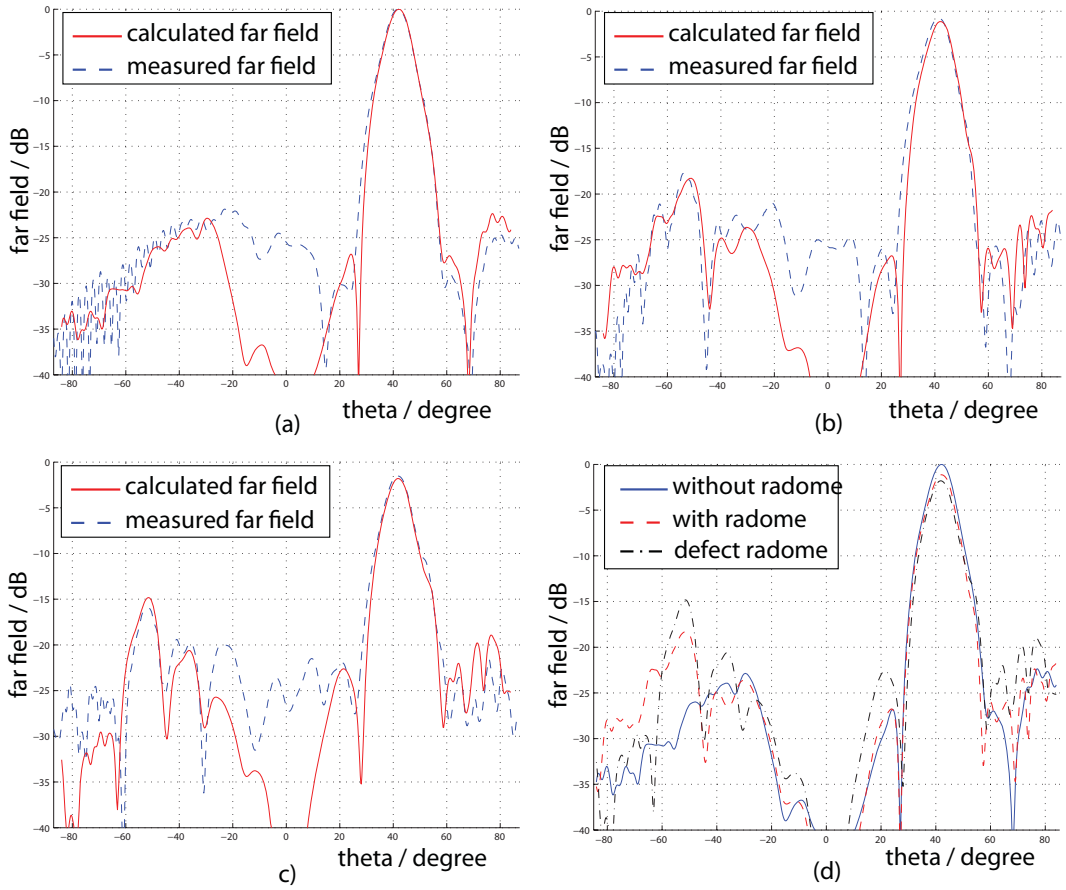

Figure 11: Comparison between the measured far-field data, supplied by Applied Composites AB, and the far field calculated from the equivalent currents on the radome surface. The far fields are normalized to the maximum value of the far field when no radome is present. (a) Antenna without radome. (b) Antenna together with radome. (c) Antenna together with defect radome. (d) The calculated far-field pattern for the three measurement configurations.

The phase images in Figure 7b are not appropriate for finding the location of the copper plates. Instead, the phase difference (antenna with radome - antenna with defect radome) is useful, see Figure 10. These images reveal the change of the phase due to the attached copper plates on the defect radome.

As a final verification of the method, the amplitude on a sphere in the far-field region is studied. The electric field, originating from the equivalent currents on the radome, is calculated on the sphere, *i.e.*,

$$\boldsymbol{E}_j^{\text{sph}} = -\mathcal{F}^{-1}\left[\widehat{\boldsymbol{G}}_{\hat{\jmath}}\widehat{\boldsymbol{M}}_{\hat{\jmath}}\right] \qquad \text{for all } j,\hat{\jmath} \tag{5.2}$$

in accordance with (3.8) and (3.12), except that $\widehat{\boldsymbol{G}}_{\hat{\jmath}}$ now describes the transformation from the radome to the inner fictitious surface and to the far-field sphere. The denotations j and $\hat{\jmath}$ are, as above, the integer index belonging to the discretized

azimuth component and the Fourier transformed discretized azimuth component, respectively.

The far-field amplitude F is derived as

$$F(\theta, \phi) = kr\, \mathrm{e}^{\mathrm{j}kr} E^{\mathrm{sph}}(r, \theta, \phi) \qquad \text{as } r \to \infty \tag{5.3}$$

where (r, θ, ϕ) denotes the spherical coordinate system [7]. The result is compared with measured far-field data, supplied by Applied Composites AB, as shown in Figure 11. The far field is depicted for the angles $\phi = 0$ and $\phi = \pi$, *i.e.*, a cross-section through the far field of the main lobe and the corresponding far field originating from the currents on the back of the radome. There is a lack of agreement between the measured far field and the calculated one at the angles corresponding to the top of the radome, *i.e.*, $\theta \approx 0$. This is due to the fact that fields originating hereof are not all included in the measured near-field data, since the measurement surface is a cylinder, see Figure 3a. The fact that the radome disturbs and reflects the electric field, as earlier seen in Figure 6b, can also be detected in the far field, see Figure 11d, where flash lobes appear when the radome is present.

6 Alternative ways to visualize the electromagnetic currents

6.1 Amplitude of the reconstructed currents

In the previous section, the amplitude and the phase of the reconstructed currents have been visualized by showing the amplitude in dB-scale over the front side of the radome in Figure 5, and over a cross section of the front and the back in Figure 6. These ways of presenting the results are in this section supplemented in an attempt to see what possibilities other visualization approaches offer. First, the back side of the radome is shown in a dB-scale in Figure 12. The absolute value of the currents is also displayed in a linear scale on the front and the back of the radome in Figures 13 and 14, respectively. The flash lobes clearly appear in both dB- and linear scale, see Figures 12 and 14. Notice that the top copper plate is not resolved very well in the linear scale compared to the dB-scale in Figure 5.

6.2 Differences between the measurement configurations

To further demonstrate the distinctions between the three radome configurations their differences are calculated. The difference (|antenna| - |antenna with radome|) is shown in Figure 15 in a dB-scale, and in Figure 16 in a linear scale. The images show the influence of the radome and the appearance of flash lobes at the back of the radome. The dB-scale, Figure 15, has the advantage that also small current values are made visible. The advantage with the linear scale is that the sign of the difference is visible. In Figure 16, on the front of the radome, the field originating from the antenna is the strongest, *i.e.*, the difference is positive, while on the back of the radome, the field passing through the radome as flash lobes is the strongest,

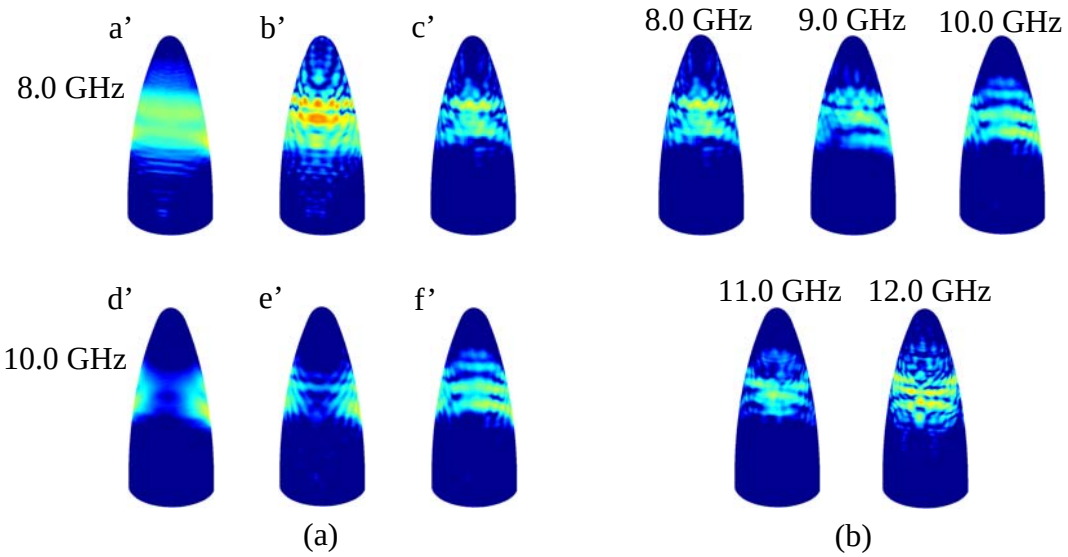

Figure 12: The reconstructed currents on the back of the radome in a dB-scale $[-30, 0]$, all normalized to the highest current value, *i.e.*, the maximum current magnitude in Figure 5ac'. (a) The different measurement configurations are depicted at two different frequencies. From left to right; antenna without radome, antenna together with radome, and antenna together with defect radome, respectively. (b) The defect radome case, shown at different frequencies.

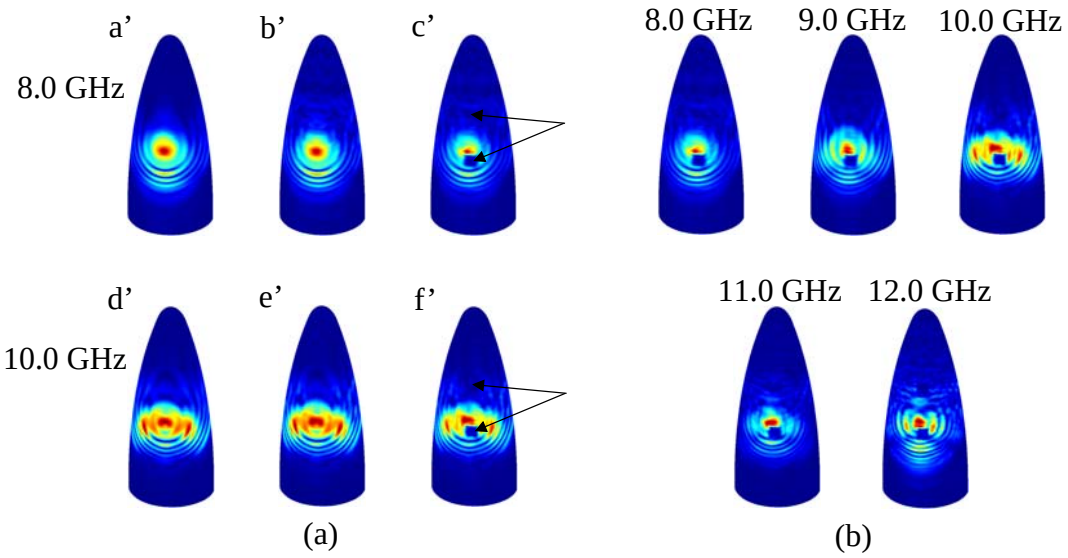

Figure 13: The reconstructed currents on the front of the radome in a linear scale, all normalized to the highest current value, *i.e.*, the maximum current magnitude in figure ac'. (a) The different measurement configurations are depicted at two different frequencies. From left to right; antenna without radome, antenna together with radome, and antenna together with defect radome, respectively. The arrows point out the location of the copper plates on the defect radome. (b) The defect radome case, shown at different frequencies.

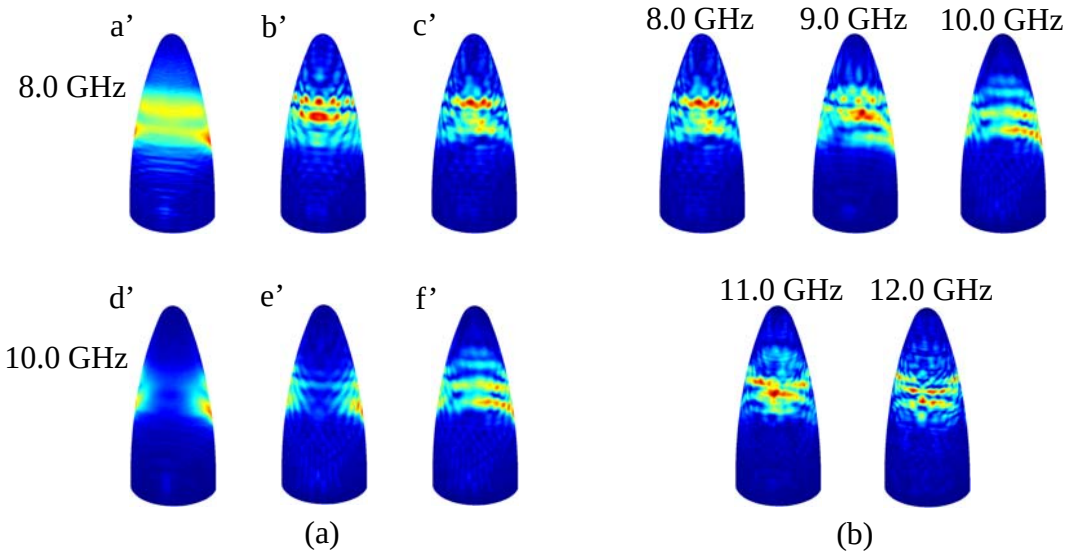

Figure 14: The reconstructed currents on the back of the radome in a linear scale, all normalized to the highest current value, *i.e.*, the maximum current magnitude in Figure 13ac'. (a) The different measurement configurations are depicted at two different frequencies. From left to right; antenna without radome, antenna together with radome, and antenna together with defect radome, respectively. (b) The defect radome case, shown at different frequencies.

i.e., the difference is negative. This conclusion cannot be drawn by looking at the dB-scale in Figure 15, where only the amplitude of the difference is displayed.

To emphasize the contribution of the defect radome, the difference (|antenna with radome| - |antenna with defect radome|) is studied in a dB-scale, see Figure 17 and in a linear scale, see Figure 18. The effect of the lower copper plate is clearly detectable in both figures, while the top plate is hard to discern in both scales, *i.e.*, these figures are useful to get an overview, but when it comes to details, other visualizations approaches are needed. The tricky part with the dB-scale is to choose its lower limit. If a too low value is used, too much noise appears and blurs the image. However, if instead a too high value is picked, the field effects caused by the copper plates are hidden. To reveal the exact positions of the copper plates, cross section graphs through the front of the radome are presented in a linear and in a dB-scale in Figure 19 for the frequency 8.0 GHz. The effects of the copper plates are clearly seen in both scales, but their positions are somewhat off-centered. This is probably due to the fact that the copper plates cause diffractions and reflections, which do not occur when only the radome is present. There is also an uncertainty in the measurement set-up.

6.3 Propagation of the reconstructed fields

To see how the waves propagate on the radome-shaped surface, the field values, *i.e.*, $\mathrm{Re}\,(\boldsymbol{M}\,\mathrm{e}^{\mathrm{j}\omega t})$ for $0 \leqslant \omega t \leqslant 2\pi$, are presented as a movie on `http://www.eit.lth.se/staff/kristin.persson` under the link `Research`. The distinctions between the

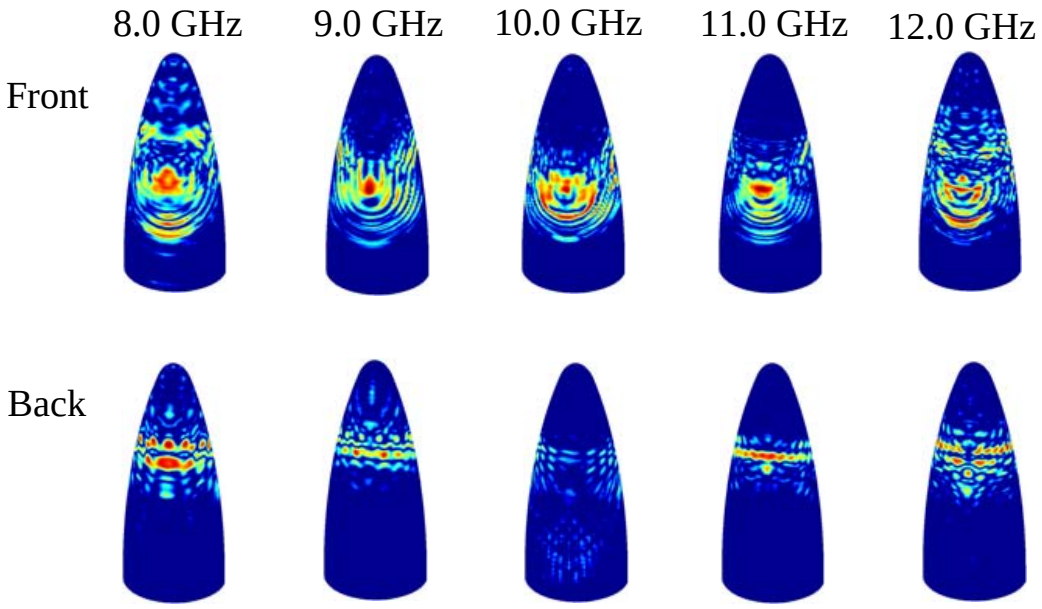

Figure 15: The amplitude difference abs(|antenna| - |antenna with radome|) for several frequencies. The amplitude differences are normalized to the highest value at each frequency and are all depicted in a dB-scale $[-20, 0]$.

different frequencies and radome configurations are revealed on both the front and the back side of the radome surface.

7 Discussions and conclusions

The scalar surface integral representation gives a linear map between the equivalent currents and the near-field data for general geometries. It is shown that this map can be inverted for axially symmetric geometries. The model can theoretically be adapted to geometries lacking symmetry axes. Although it is not a feasible approach for radome applications, demanding large quantities of measured data, with the present computer capacity.

The transformation method is stable and useful in radome design and for evaluation purposes. To investigate the electric field passing through the radome, the current distribution on the antenna or on a surface enclosing the antenna must be known. Using the surface integral representation, the equivalent currents, on a surface enclosing the antenna, can be described. The insertion phase delay is estimated by investigating the phase of the reconstructed currents.

In this paper, copper plates are attached on the radome, in the direction of the antenna main lobe. The length of the side of the square copper plates is $1.6 - 2.4$ wavelengths, corresponding to the frequency span $8.0 - 12.0$ GHz. The effects of the plates cannot be localized directly by using the near-field data, but by using the equivalent currents, the effects are focused and detected on the radome

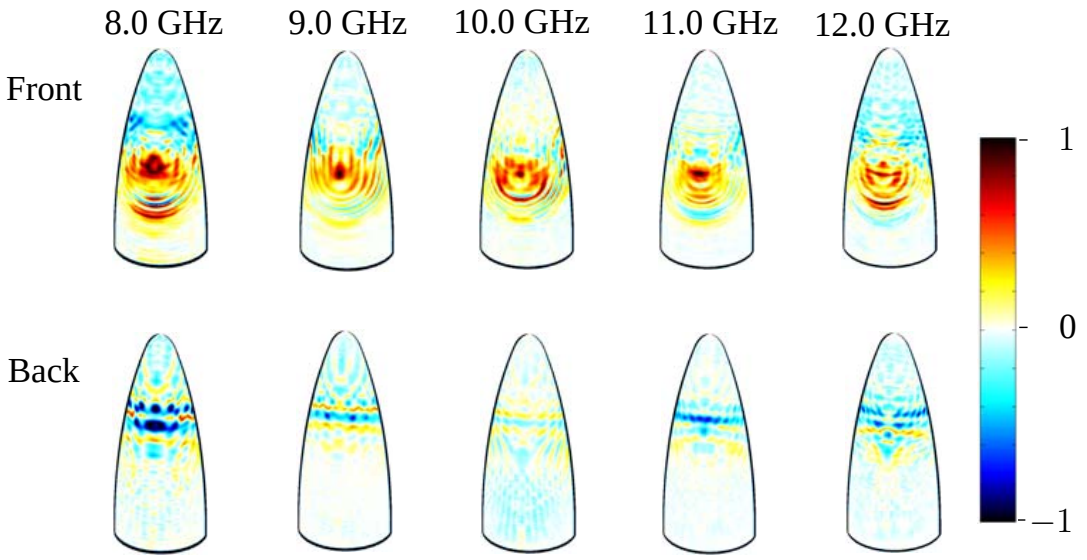

Figure 16: The amplitude difference (|antenna| - |antenna with radome|) for several frequencies. The amplitude differences are normalized to the highest value at each frequency and are all depicted in a linear scale.

surface. Thus, by transforming the near-field data to the radome surface, field defects introduced by the radome and other disturbances are focused back to their origins. Another range of application within the radome industry is to study how *e.g.*, lightning conductors and Pitot tubes, often placed on radomes, influence the equivalent currents. We predict that such influences and the field effects of the radome itself can be detected.

It is concluded that the transformation method based on the scalar surface integral representation works very well and that the field of applications is large. A natural continuation is to elaborate the algorithm by including near-field data with cross-polarization, *i.e.*, to implement the full Maxwell equations with a method of moments (MoM). Nevertheless, if the measured near-field data consists of one dominating component, the use of the full Maxwell equations are not necessary, as shown in this paper.

Additional aspects to be investigated more thoroughly in the future are the resolution possibilities of manufacturing errors and other external field influences. Moreover, a study regarding the detection of different materials attached to the radome surface is desirable.

Acknowledgments

The work reported in this paper is sponsored by Försvarets Materielverk (FMV), Sweden, which is gratefully acknowledged.

The authors also like to express their gratitude to SAAB Bofors Dynamics, Sweden, and especially to Michael Andersson and Sören Poulsen at Applied Composites

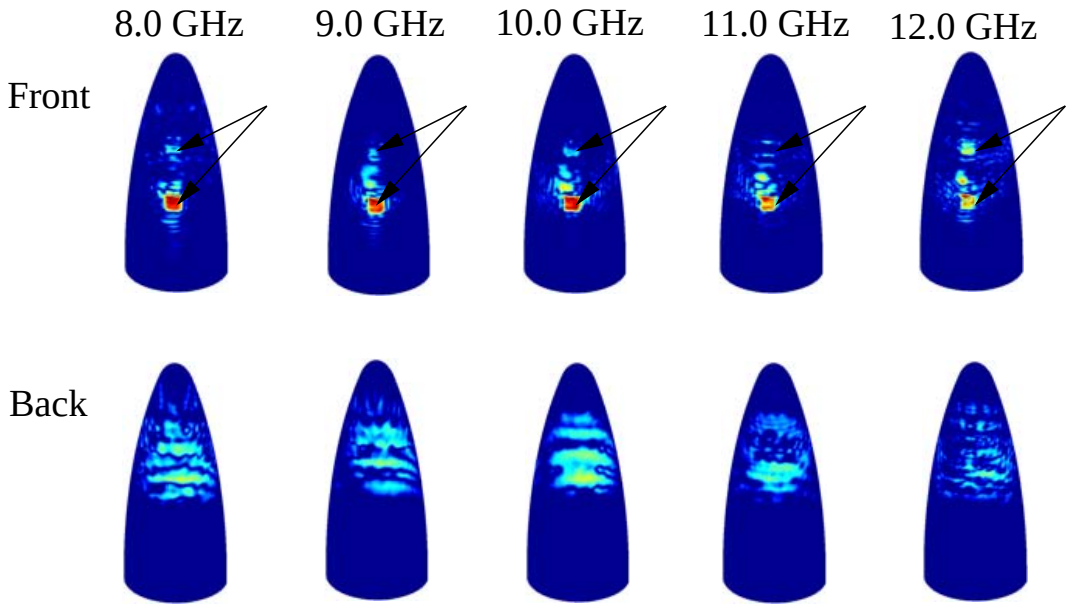

Figure 17: The amplitude difference abs(|antenna with radome| - |antenna with defect radome|) for several frequencies. The amplitude differences are normalized to the highest value at each frequency and are all depicted in a dB-scale $[-30, 0]$. The arrows point out the location of the copper plates.

AB, Sweden, for supplying the near-field data and pictures of the experimental set-up.

References

[1] H. Anton. *Elementary Linear Algebra.* John Wiley & Sons, New York, 7 edition, 1994.

[2] C. A. Balanis. *Antenna Theory.* John Wiley & Sons, New York, second edition, 1997.

[3] L. E. Corey and E. B. Joy. On computation of electromagnetic fields on planar surfaces from fields specified on nearby surfaces. *IEEE Trans. Antennas Propagat.*, **29**(2), 402–404, 1981.

[4] D. C. Ghiglia and M. d. Pritt. *Two-Dimensional Phase Unwrapping: theory, algorithms, and software.* John Wiley & Sons, New York, 1998.

[5] J. Hanfling, G. Borgiotti, and L. Kaplan. The backward transform of the near field for reconstruction of aperture fields. *IEEE Antennas and Propagation Society International Symposium*, **17**, 764–767, 1979.

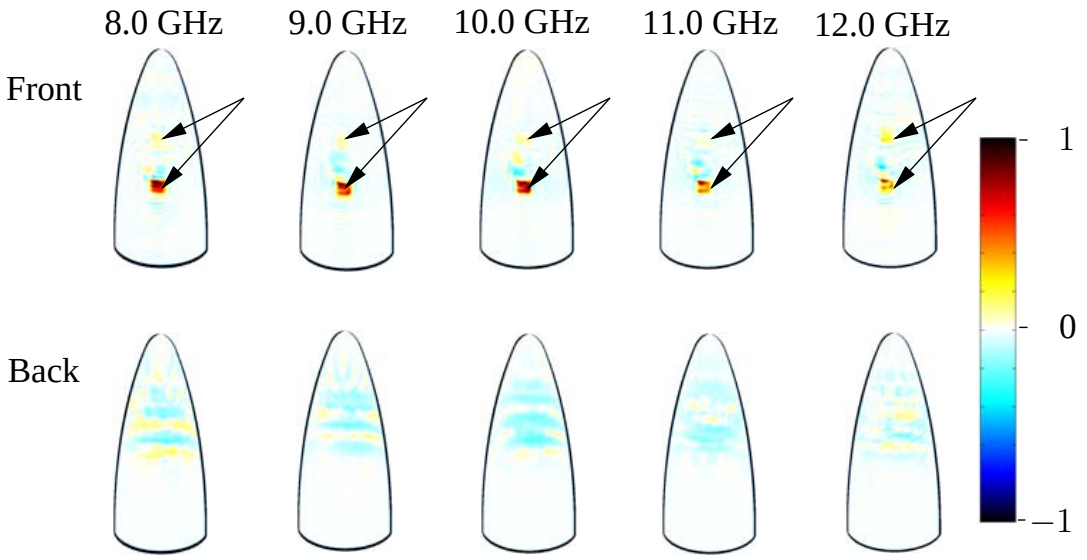

Figure 18: The amplitude difference (|antenna with radome| - |antenna with defect radome|) for several frequencies. The amplitude differences are normalized to the highest value at each frequency and are all depicted in a linear scale. The arrows point out the location of the copper plates.

[6] J. E. Hansen, editor. *Spherical Near-Field Antenna Measurements*. Number 26 in IEE electromagnetic waves series. Peter Peregrinus Ltd., Stevenage, UK, 1988. ISBN: 0-86341-110-X.

[7] J. D. Jackson. *Classical Electrodynamics*. John Wiley & Sons, New York, second edition, 1975.

[8] D. S. Jones. *Acoustic and Electromagnetic Waves*. Oxford University Press, New York, 1986.

[9] R. Kress. *Linear Integral Equations*. Springer-Verlag, Berlin Heidelberg, second edition, 1999.

[10] J. Lee, E. M. Ferren, D. P. Woollen, and K. M. Lee. Near-field probe used as a diagnostic tool to locate defective elements in an array antenna. *IEEE Trans. Antennas Propagat.*, **36**(6), 884–889, 1988.

[11] K. Persson and M. Gustafsson. Reconstruction of equivalent currents using a near-field data transformation – with radome applications. *Progress in Electromagnetics Research*, **54**, 179–198, 2005.

[12] D. M. Pozar. *Microwave Engineering*. John Wiley & Sons, New York, 1998.

[13] Y. Rahmat-Samii, L. I. Williams, and R. G. Yaccarino. The UCLA bi-polar planar-near-field antenna-measurement and diagnostics range. *IEEE Antennas and Propagation Magazine*, **37**(6), 16–35, December 1995.

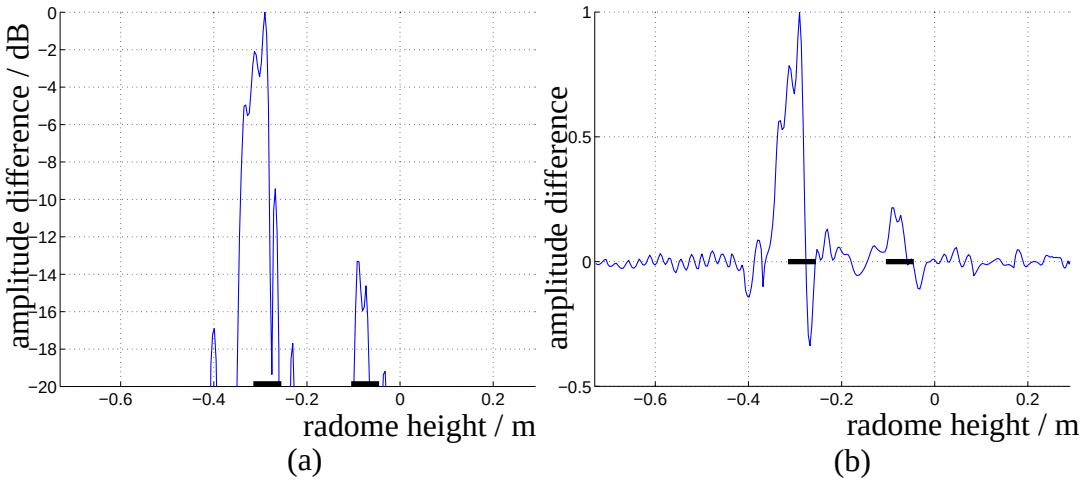

Figure 19: Cross section of the amplitude difference (|antenna with radome| - |antenna with defect radome|) at 8.0 GHz. The graphs show the difference on the front of the radome as a function of the radome height for a fixed angle. They are both normalized to their highest values. The positions of the copper plates are marked by thick lines on the horizontal axis. (a) The difference abs(|antenna with radome| - |antenna with defect radome|) in dB-scale. (b) The difference (|antenna with radome| - |antenna with defect radome|) in a linear scale.

[14] T. K. Sarkar and A. Taaghol. Near-field to near/far-field transformation for arbitrary near-field geometry utilizing an equivalent electric current and MoM. *IEEE Trans. Antennas Propagat.*, **47**(3), 566–573, March 1999.

[15] G. Strang. *Introduction to applied mathematics*. Wellesley-Cambridge Press, Box 157, Wellesley MA 02181, 1986.

[16] S. Ström. Introduction to integral representations and integral equations for time-harmonic acoustic, electromagnetic and elastodynamic wave fields. In V. V. Varadan, A. Lakhtakia, and V. K. Varadan, editors, *Field Representations and Introduction to Scattering*, volume 1 of *Handbook on Acoustic, Electromagnetic and Elastic Wave Scattering*, chapter 2, pages 37–141. Elsevier Science Publishers, Amsterdam, 1991.

[17] V. V. Varadan, Y. Ma, V. K. Varadan, and A. Lakhtakia. Scattering of waves by spheres and cylinders. In V. V. Varadan, A. Lakhtakia, and V. K. Varadan, editors, *Field Representations and Introduction to Scattering*, volume 1 of *Handbook on Acoustic, Electromagnetic and Elastic Wave Scattering*, chapter 4, pages 211–324. Elsevier Science Publishers, Amsterdam, 1991.

[18] M. B. Woodworth and A. D. Yaghjian. Derivation, application and conjugate gradient solution of dual-surface integral equations for three-dimensional, multi-wavelength perfect conductors. *Progress in Electromagnetics Research*, **5**, 103–129, 1991.

[19] A. D. Yaghjian. An overview of near-field antenna measurements. *IEEE Trans. Antennas Propagat.*, **34**(1), 30–45, January 1986.

Reconstruction of equivalent currents on a radome using an integral representation formulation

Paper III

Kristin Persson, Mats Gustafsson, and Gerhard Kristensson

Based on: K. Persson, M. Gustafsson, and G. Kristensson. Reconstruction of equivalent currents on a radome using an integral representation formulation, *Progress in Electromagnetics Research B*, vol. 20, pp. 65–90, 2010.

Extended version published as: K. Persson, M. Gustafsson, and G. Kristensson. Reconstruction and visualization of equivalent currents on a radome surface using an integral representation formulation, Technical Report LUTEDX/(TEAT-7184), pp. 1–45, 2010, Department of Electrical and Information Technology, Lund University, Sweden. `http://www.eit.lth.se`

Abstract

In this paper an inverse source problem is investigated. The measurement set-up is a reflector antenna covered by a radome. Equivalent currents are reconstructed on a surface shaped as the radome in order to diagnose the radome's interaction with the radiated field. To tackle this inverse source problem an analysis of a full-wave integral representation, with the equivalent currents as unknowns, is used. The extinction theorem and its associated integral equation ensure that the reconstructed currents represent sources within the radome. The axially symmetric experimental set-up reduces the computational complexity of the problem. The resulting linear system is inverted by using a singular value decomposition. We visualize how the presence of the radome alters the components of the equivalent currents. The method enables us to determine the phase shift of the field due to the transmission of the radome, *i.e.*, the IPD (insertion phase delay). Also, disturbances due to defects, not observable in the measured near field, are localized in the equivalent currents.

1 Introduction

The aim of this paper is to calculate and visualize the sources of a measured electric field on a radome-shaped surface. The electric field is originating from an antenna inside the radome and is measured in the near-field zone outside the radome. The electrical size of the radome is 29 wavelengths at the frequency 8.0 GHz.

This kind of calculations are important in antenna diagnostics, radome design, *etc.*, since the field close to the body of interest is difficult to measure directly. By doing so, the interaction between the source and the measurement probe can give incorrect results [14, 36, 49]. In the process of designing a radome, the electric field close to the antenna is input to software calculating the field propagation through the radome wall [1, 39]. To get reliable results, it is crucial that the representation of the field radiated from the antenna, *i.e.*, the input data, is well known. To determine the performance of the radome it is eligible to quantify *e.g.*, beam deflection, transmission efficiency, pattern distortion, and the electrical thickness of the radome wall, *i.e.*, the insertion phase delay (IPD). It is also of interest to see how the mounting device and *e.g.*, lightning conductors and Pitot tubes, often placed on radomes, interact with the electric field.

One of the first techniques developed to solve the inverse source problems of this kind employs the plane wave expansion [10, 23, 37]. The method works very well when the equivalent currents are reconstructed on a planar surface. One recent area of application is the determination of the specific absorption rate of mobile phones [12]. A modal expansion of the field can be utilized if the reconstruction surface is cylindrical or spherical [14, 24, 29]. This method has been used to calculate the insertion phase delay (IPD) and to detect defects on a spherical radome [13]. More general geometries, *e.g.*, needle shaped objects and flat disks, can be handled by expanding the field in spheroidal wave functions [45]. A combination of the plane wave spectrum and the modal expansion has been utilized in [7, 8] and [50] where

flat antenna structures are diagnosed and safety perimeter of base stations' antennas is investigated, respectively. Further references in the area can be found in [43].

To be able to handle a wider class of geometries, diagnostics techniques based on integral representations, which are solved by a method of moments approach, are applied. The drawback is the computational complexity. If the object on which the currents are to be reconstructed is metallic, *i.e.*, a perfect electric conductor (PEC), either the electric or magnetic field integral equation (EFIE or MFIE) can be employed [48] or combinations thereof [33, 40]. The equivalence principle is conveniently used when analyzing flat antenna structures [21, 22, 38]. An integral representation together with *a priori* information of the object and iterative solvers is used by [20] and [11] to find the electric current on the walls of a PEC for diagnostics of a pyramidal horn antenna and a monopole placed on the chassis of a car. In [35] a dual-surface approach is compared to the single-equation formulation.

In this paper we propose a technique using the integral representations to relate the unknown equivalent currents to a known measured near field. In addition to the integral representation, we also use an integral equation, originating from the extinction theorem [9]. By using the extinction theorem together with the integral representation, we secure that the sources of the reconstructed currents only exist inside the enclosing volume [47]. The equivalent currents can be reconstructed on a surface arbitrarily close to the antenna. No *a priori* information of the material of the object just inside the surface is utilized.

2 Prerequisites

In this section, we review the basic equations employed in this paper. We start with a general geometry, and specialize to a body of revolution in Section 2.2. More technical details are given in [32].

2.1 General case

The surface integral representation expresses the electromagnetic field in a homogeneous, isotropic region in terms of its values on the closed bounding surface. We engage the integral representations to a domain outside a closed, bounded surface S_{rad}. Carefully employing the Silver-Müller radiation conditions, the solution of the Maxwell equations satisfy the following integral representation [16, 27, 42, 47]

$$\begin{aligned}\iint_{S_{\text{rad}}} \Big(& -\mathrm{j}\omega\mu_0\mu\; g(\boldsymbol{r}_1,\boldsymbol{r}_2)\big[\hat{\boldsymbol{n}}(\boldsymbol{r}_1)\times\boldsymbol{H}(\boldsymbol{r}_1)\big] \\ & + \frac{\mathrm{j}}{\omega\epsilon_0\epsilon}\,\nabla_1 g(\boldsymbol{r}_1,\boldsymbol{r}_2)\Big\{\nabla_{1S}\cdot\big[\hat{\boldsymbol{n}}(\boldsymbol{r}_1)\times\boldsymbol{H}(\boldsymbol{r}_1)\big]\Big\} \\ & - \nabla_1 g(\boldsymbol{r}_1,\boldsymbol{r}_2)\times\big[\hat{\boldsymbol{n}}(\boldsymbol{r}_1)\times\boldsymbol{E}(\boldsymbol{r}_1)\big]\Big)\,\mathrm{d}S_1 = \begin{cases}\boldsymbol{E}(\boldsymbol{r}_2) & \boldsymbol{r}_2 \text{ outside } S_{\text{rad}} \\ \boldsymbol{0} & \boldsymbol{r}_2 \text{ inside } S_{\text{rad}}\end{cases}\end{aligned} \tag{2.1}$$

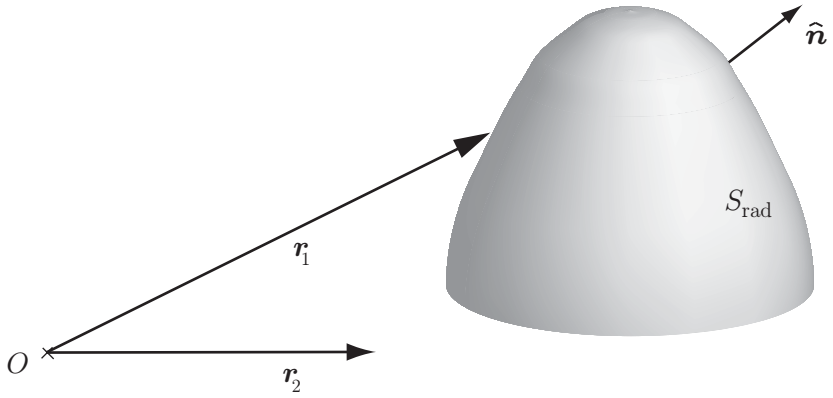

Figure 1: The surface S_{rad} of integration. The unit normal to the surface is $\hat{\boldsymbol{n}}$. The variable of integration is denoted $\boldsymbol{r}_1$ and the observation point $\boldsymbol{r}_2$.

where the time convention used is $\mathrm{e}^{\mathrm{j}\omega t}$, and the surface divergence is denoted $\nabla_S\cdot$ [9]. The variable of integration is denoted $\boldsymbol{r}_1$ and the observation point $\boldsymbol{r}_2$, see Figure 1. The relative permittivity ϵ and the relative permeability μ may depend on the angular frequency ω, *i.e.*, the material can be dispersive, but they are constants as functions of space (homogeneous material). The scalar free space Green function is

$$g(\boldsymbol{r}_1, \boldsymbol{r}_2) = \frac{\mathrm{e}^{-\mathrm{j}k|\boldsymbol{r}_2-\boldsymbol{r}_1|}}{4\pi|\boldsymbol{r}_2-\boldsymbol{r}_1|}$$

where the wave number of the material is $k = \omega\sqrt{\epsilon_0\mu_0\epsilon\mu}$. The representation (2.1) states that if the total electromagnetic field on S_{rad} is known, the total electromagnetic field outside S_{rad} can be determined [15, 28, 47]. If these integrals are evaluated at a point $\boldsymbol{r}_2$ lying in the volume enclosed by S_{rad} these integrals cancel each other (extinction). It is important to notice that this does not necessarily mean that the field $\boldsymbol{E}$ is identically zero inside S_{rad}, it only states that the values of the integrals cancel.

The electric and magnetic equivalent surface current densities, $\boldsymbol{J}$ and $\boldsymbol{M}$, are introduced to simplify the notation and they are defined as [5]

$$\begin{cases} \boldsymbol{J}(\boldsymbol{r}) = \hat{\boldsymbol{n}}(\boldsymbol{r}) \times \boldsymbol{H}(\boldsymbol{r}) \\ \boldsymbol{M}(\boldsymbol{r}) = -\hat{\boldsymbol{n}}(\boldsymbol{r}) \times \boldsymbol{E}(\boldsymbol{r}) \end{cases} \tag{2.2}$$

The lower (or upper) representation in (2.1) is transformed into an integral equation letting $\boldsymbol{r}_2$ approach S_{rad}. However, care must be taken since the integrands become singular when $\boldsymbol{r}_2$ approaches the surface [9, 16, 26, 47]. The equation consists of three components, two describing the tangential field and one describing the normal component of the field. Since the normal component can be determined by the knowledge of the tangential parts, this representation has redundancies, *i.e.*, the normal component is eliminated [27].

To this end, (2.1) splits into a surface integral representation of the electric field

$$\iint\limits_{S_{\text{rad}}} \Big\{ -\mathrm{j}\omega\mu_0\mu\; g(\boldsymbol{r}_1,\boldsymbol{r}_2)\boldsymbol{J}(\boldsymbol{r}_1) + \mathrm{j}\frac{1}{\omega\epsilon_0\epsilon}\;\nabla_1 g(\boldsymbol{r}_1,\boldsymbol{r}_2)\big[\nabla_{1S}\cdot\boldsymbol{J}(\boldsymbol{r}_1)\big] + \nabla_1 g(\boldsymbol{r}_1,\boldsymbol{r}_2)\times\boldsymbol{M}(\boldsymbol{r}_1)\Big\}\,\mathrm{d}S_1 = \boldsymbol{E}(\boldsymbol{r}_2) \qquad \boldsymbol{r}_2 \text{ outside } S_{\text{rad}} \tag{2.3}$$

and a surface integral equation in $\boldsymbol{J}$ and $\boldsymbol{M}$

$$\hat{\boldsymbol{n}}(\boldsymbol{r}_2)\times\iint\limits_{S_{\text{rad}}} \Big\{ \mathrm{j}\omega\mu_0\mu\; g(\boldsymbol{r}_1,\boldsymbol{r}_2)\boldsymbol{J}(\boldsymbol{r}_1) - \mathrm{j}\frac{1}{\omega\epsilon_0\epsilon}\;\nabla_1 g(\boldsymbol{r}_1,\boldsymbol{r}_2)\big[\nabla_{1S}\cdot\boldsymbol{J}(\boldsymbol{r}_1)\big] - \nabla_1 g(\boldsymbol{r}_1,\boldsymbol{r}_2)\times\boldsymbol{M}(\boldsymbol{r}_1)\Big\}\,\mathrm{d}S_1 = \frac{1}{2}\,\boldsymbol{M}(\boldsymbol{r}_2) \qquad \boldsymbol{r}_2 \in S_{\text{rad}} \tag{2.4}$$

When necessary, the integrals in the surface integral equation are interpreted as Cauchy's principal value [9, 34].

The integral equation is written in a weak form, *i.e.*, it is multiplied by a test function, $\boldsymbol{\Psi}$, and integrated over its domain [6, 19, 26, 33]

$$\begin{aligned}\mathrm{j}\omega\mu_0\mu \iint\limits_{S_{\text{rad}}}\iint\limits_{S_{\text{rad}}} \boldsymbol{\Psi}(\boldsymbol{r}_2)\cdot g(\boldsymbol{r}_1,\boldsymbol{r}_2)\boldsymbol{J}(\boldsymbol{r}_1)\,\mathrm{d}S_1\,\mathrm{d}S_2 \\ - \mathrm{j}\frac{1}{\omega\epsilon_0\epsilon}\iint\limits_{S_{\text{rad}}}\iint\limits_{S_{\text{rad}}} \big[\nabla_{2S}\cdot\boldsymbol{\Psi}(\boldsymbol{r}_2)\big] g(\boldsymbol{r}_1,\boldsymbol{r}_2)\big[\nabla_{1S}\cdot\boldsymbol{J}(\boldsymbol{r}_1)\big]\,\mathrm{d}S_1\,\mathrm{d}S_2 \\ - \iint\limits_{S_{\text{rad}}}\iint\limits_{S_{\text{rad}}} \boldsymbol{\Psi}(\boldsymbol{r}_2)\cdot\big[\nabla_1 g(\boldsymbol{r}_1,\boldsymbol{r}_2)\times\boldsymbol{M}(\boldsymbol{r}_1)\big]\,\mathrm{d}S_1\,\mathrm{d}S_2 \\ - \frac{1}{2}\iint\limits_{S_{\text{rad}}} \big[\hat{\boldsymbol{n}}(\boldsymbol{r}_2)\times\boldsymbol{\Psi}(\boldsymbol{r}_2)\big]\cdot\boldsymbol{M}(\boldsymbol{r}_2)\,\mathrm{d}S_2 = 0\end{aligned} \tag{2.5}$$

The evaluation of the integrals in this paper is restricted to a body of revolution, see Section 2.2, and follows the scheme in [2, 25].

2.2 Body of revolution

From now on the equations are adapted to a body of revolution (BOR) in free space, *i.e.*, $\epsilon = 1$ and $\mu = 1$. The surface is parameterized by the azimuth angle φ and the height coordinate along the surface v, *i.e.*, the position vector $\boldsymbol{r}$ can be expressed as $\boldsymbol{r}(\varphi, v) = \rho(v)\cos\varphi\,\hat{\boldsymbol{e}}_{\text{x}} + \rho(v)\sin\varphi\,\hat{\boldsymbol{e}}_{\text{y}} + z(v)\,\hat{\boldsymbol{e}}_{\text{z}}$. The normalized basis vectors are then

$$\hat{\boldsymbol{\varphi}}(\varphi) = \frac{\partial\boldsymbol{r}}{\partial\varphi}\Big/\left|\frac{\partial\boldsymbol{r}}{\partial\varphi}\right| = -\sin\varphi\,\hat{\boldsymbol{e}}_{\text{x}} + \cos\varphi\,\hat{\boldsymbol{e}}_{\text{y}} \quad \text{and} \quad \hat{\boldsymbol{v}}(\varphi, v) = \frac{\partial\boldsymbol{r}}{\partial v}\Big/\left|\frac{\partial\boldsymbol{r}}{\partial v}\right|$$

and $\{\hat{\boldsymbol{n}}, \hat{\boldsymbol{\varphi}}, \hat{\boldsymbol{v}}\}$ forms a right-handed triple of unit vectors, see Figure 2. The curvilinear components of the magnetic equivalent surface current and electric field are denoted as $E^{\varphi} = -M^{\text{v}}$ and $E^{\text{v}} = M^{\varphi}$, *cf.*, (2.2), where $M^{\varphi} = \boldsymbol{M}\cdot\hat{\boldsymbol{\varphi}}$, and $M^{\text{v}} = \boldsymbol{M}\cdot\hat{\boldsymbol{v}}$. The magnetic field and the electric equivalent current are related in a similar way.

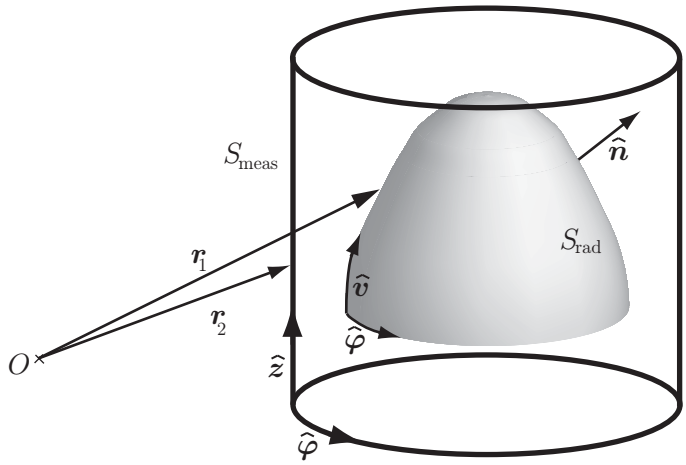

Figure 2: The regions of integration in (2.8).

Two functions, $\boldsymbol{a}^{\varphi}_{mj}$ and $\boldsymbol{a}^{\mathrm{v}}_{mj}$, are used as basis functions. They are defined as

$$\begin{aligned} \boldsymbol{a}^{\varphi}_{mj} &= f^{\varphi}_{j}(v)\, \mathrm{e}^{\mathrm{j}m\varphi}\hat{\boldsymbol{\varphi}} \\ \boldsymbol{a}^{\mathrm{v}}_{mj} &= f^{\mathrm{v}}_{j}(v)\, \mathrm{e}^{\mathrm{j}m\varphi}\hat{\boldsymbol{v}} \end{aligned} \tag{2.6}$$

The height of the radome, v_1, is discretized into points, v_j, where $j = 1, \ldots, N_{\mathrm{z}}$. The functions $f^{\varphi/\mathrm{v}}_{j}(v)$ can be chosen as a constant, linear, cubic, spline functions *etc.*, with support in a neighborhood of v_j [6, 33]. For the results in this paper, both $f^{\varphi/\mathrm{v}}_{j}(v)$ are chosen as piecewise linear functions, *i.e.*, one-dimensional rooftops. Observe that φ/v in $f^{\varphi/\mathrm{v}}$ denotes a superscript and not an exponential. In the azimuthal direction, a global function, $\mathrm{e}^{\mathrm{j}m\varphi}$, *i.e.*, a Fourier basis, is used due to the symmetry of the body, and m is an integer index. The magnetic current is expanded as

$$\boldsymbol{M} = \sum_{m,j} \left\{ M^{\varphi}_{mj}\, \boldsymbol{a}^{\varphi}_{mj} + M^{\mathrm{v}}_{mj}\, \boldsymbol{a}^{\mathrm{v}}_{mj} \right\} \tag{2.7}$$

The electric current $\boldsymbol{J}$ is expanded in a similar way, but with expansion coefficients $J^{\varphi/\mathrm{v}}_{mj}$. Galerkin's method is used [6]. That is, the test functions are according to (2.6) $\boldsymbol{\Psi}^{\varphi}_{ni} = (\boldsymbol{a}^{\varphi}_{ni})^*$ and $\boldsymbol{\Psi}^{\mathrm{v}}_{ni} = (\boldsymbol{a}^{\mathrm{v}}_{ni})^*$ where complex conjugation is denoted by a star and the indicies run through the same integers as m and j.

The surface integral representation in (2.3) is applied to the measurement set-up described in Section 3, *i.e.*, $\boldsymbol{r}_2$ belongs to the discrete set of measurement points (indexed; $q = 1, \ldots, N^{\mathrm{meas}}_{\mathrm{z}}$) on the cylindrical surface S_{meas}, see Figure 2. None of the integrals contains singularities since $\boldsymbol{r}_1$ and $\boldsymbol{r}_2$ will not coincide. From equation

(2.3) we get

$$\begin{aligned}\begin{bmatrix}\hat{\boldsymbol{v}}\\ \hat{\boldsymbol{\varphi}}\end{bmatrix}\cdot\Big\{&-\mathrm{j}\omega\mu_0\iint\limits_{S_{\mathrm{rad}}} g(\boldsymbol{r}_1,\boldsymbol{r}_2)\boldsymbol{J}(\boldsymbol{r}_1)\,\mathrm{d}S_1\\ &+\mathrm{j}\frac{1}{\omega\epsilon_0}\iint\limits_{S_{\mathrm{rad}}}\nabla_1 g(\boldsymbol{r}_1,\boldsymbol{r}_2)\big[\nabla_{1S}\cdot\boldsymbol{J}(\boldsymbol{r}_1)\big]\,\mathrm{d}S_1\\ &+\iint\limits_{S_{\mathrm{rad}}}\nabla_1 g(\boldsymbol{r}_1,\boldsymbol{r}_2)\times\boldsymbol{M}(\boldsymbol{r}_1)\,\mathrm{d}S_1\Big\}=\begin{bmatrix}\hat{\boldsymbol{v}}\cdot\boldsymbol{E}(\boldsymbol{r}_2)\\ \hat{\boldsymbol{\varphi}}\cdot\boldsymbol{E}(\boldsymbol{r}_2)\end{bmatrix}=\begin{bmatrix}E^{\mathrm{v}}(\varphi_2,v_2)\\ E^{\varphi}(\varphi_2,v_2)\end{bmatrix}\end{aligned}\tag{2.8}$$

where $\boldsymbol{r}_2$ belongs to the discrete set of measurement points and the tangential components are projected. The right hand side of (2.8) is expanded in a Fourier series. The Fourier series reduce the dimensions of the problem by one degree [25, 33, 46].

The representation in (2.8) and the integral equation in (2.5) are organized as a system of matrices, *i.e.*,

$$\begin{bmatrix} Z^{11} & Z^{12}\\ Z^{21} & Z^{22}\end{bmatrix}\begin{bmatrix} J^{\mathrm{v}}\\ J^{\varphi}\end{bmatrix}+\begin{bmatrix} X^{11} & X^{12}\\ X^{21} & X^{22}\end{bmatrix}\begin{bmatrix} M^{\mathrm{v}}\\ M^{\varphi}\end{bmatrix}=\begin{bmatrix} E^{\mathrm{v}}\\ E^{\varphi}\end{bmatrix}\tag{2.9}$$

and

$$\begin{bmatrix} \mathcal{Z}^{11} & \mathcal{Z}^{12}\\ \mathcal{Z}^{21} & \mathcal{Z}^{22}\end{bmatrix}\begin{bmatrix} J^{\mathrm{v}}\\ J^{\varphi}\end{bmatrix}+\begin{bmatrix} \mathcal{X}^{11} & \mathcal{X}^{12}\\ \mathcal{X}^{21} & \mathcal{X}^{22}\end{bmatrix}\begin{bmatrix} M^{\mathrm{v}}\\ M^{\varphi}\end{bmatrix}=\begin{bmatrix} 0\\ 0\end{bmatrix}\tag{2.10}$$

Combining the matrix systems for the integral representation (2.9) and (2.10) gives, in short-hand notation,

$$\begin{bmatrix} Z & X\\ \mathcal{Z} & \mathcal{X}\end{bmatrix}\begin{bmatrix} J\\ M\end{bmatrix}=\begin{bmatrix} E\\ 0\end{bmatrix}$$

The magnitude of the entries of the matrices may differ by several orders of magnitude. To avoid numerical errors, the system is solved for one current at a time,

$$\begin{aligned}&J=-\mathcal{Z}^{-1}\mathcal{X}M \qquad\qquad \Longrightarrow\\ &\Big\{-Z\mathcal{Z}^{-1}\mathcal{X}+X\Big\}M=E\end{aligned}\tag{2.11}$$

when $\boldsymbol{J}$ is eliminated. In the first line, $\boldsymbol{J}$ is expressed as a function of $\boldsymbol{M}$ utilizing the integral equation. The matrix $\mathcal{Z}$ is a square matrix and inverted numerically in MATLAB. The second equation is ill-posed. The matrix is no longer a square matrix and to solve for $\boldsymbol{M}$, the linear system is inverted and regularized by the singular value decomposition (SVD) in MATLAB [46]. Besides numerical errors also noise and measurement errors show up. Here, the SVD helps in suppressing the amplification of noise in the inversion [3]. The cut-off value, *i.e.*, the magnitude of the largest singular value that is excluded, is proportional to the largest singular value of the largest Fourier component of the measured field. The proportionality constant is chosen as 0.1 and 0.3 when reconstructing the co- and the cross-component, respectively [3].

In our initial investigation we have not encountered any problems with spurious modes [41] or by using the numerical inversion of MATLAB or the SVD. However, a more detailed investigation of the ill-posed equations and the choice of the cut-off value, is planned to be addressed in a forthcoming paper.

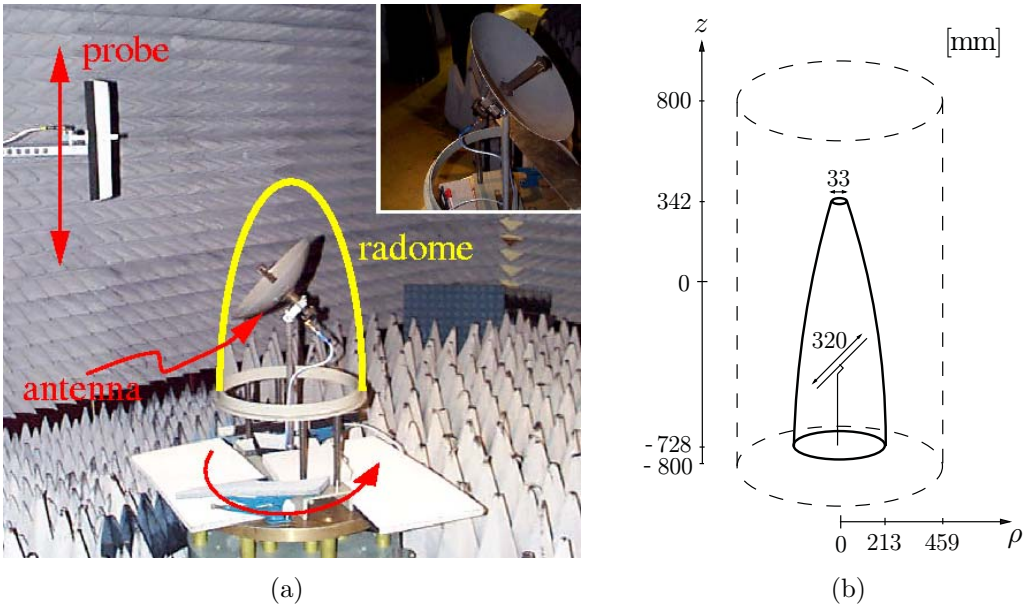

(a) (b)

Figure 3: (a) Photo of the cylindrical near-field range at SAAB Bofors Dynamics, Sweden. The antenna under test is rotated and the probe is moved in the vertical direction. A close up of the reflector antenna is shown in the upper right corner. (b) The dimensions of the reflector antenna, the radome, and the cylinder where the electric near field is measured.

3 Near-field measurements

The experimental set-up and the measured electric field is described in [30]. However, for convenience, the necessary information is summarized. The measurement set-up is shown in Figure 3. A reflector antenna, fed by a symmetrically mounted wave-guide, generates the electromagnetic field. The diameter of the antenna is 0.32 m, and the main lobe of the antenna is vertically polarized relative to the horizontal plane. The radome surface is axially symmetric and its radius, in terms of the height coordinate, is modeled by

$$\rho(z) = \begin{cases} 0.213\,\mathrm{m} & -0.728\,\mathrm{m} \le z \le -0.663\,\mathrm{m} \\ -(bz'+d) + \sqrt{(bz'+d)^2 - a(z')^2 - 2cz' - e} & \\ & -0.663\,\mathrm{m} < z \le 0.342\,\mathrm{m} \end{cases}$$

where $z' = z + 0.728\,\mathrm{m}$ and the constants are $a = 0.122$, $b = 0.048$, $c = -0.018\,\mathrm{m}$, $d = 0.148\,\mathrm{m}$, and $e = -0.108\,\mathrm{m}^2$, respectively. The height of the radome corresponds to 29 wavelengths for the frequency 8.0 GHz. The material of the radome has a relative permittivity of about 4.32 and its loss tangent is about 0.0144. The thickness of the wall of the radome varies over the surface in the interval $7.6 - 8.2\,\mathrm{mm}$.

The surface S_{rad} in (2.5) and (2.8) is defined by the radome surface, closed with smooth top and bottom surfaces. These added surfaces are needed since the integral representation applies to a closed surface and the measurements are performed under

non-ideal conditions. The turntable, on which the antenna and radome are located, see Figure 3a, reflects some of the radiation, which is taken care of by the added bottom surface. The top surface takes care of the electric field that is reflected on the inside of the radome and then radiated through the top hole. If these factors are neglected, unwanted edge effects occur, since the electric fields originating from the turntable and the top of the radome are forced to originate from the radome itself. The radome surface is divided into 8 cells per wavelength in the height direction, and in each cell 4 points are chosen where the integrations are evaluated.

The electric field is measured on a cylindrical surface by moving the probe in the z-direction and rotating the radome and the antenna under test, see Figure 3. This surface is located in the near-field zone [4]. The near-field measurement probe consists of an IEC R100 waveguide, with a collar of radar absorbing material, for which no compensation is made in the final data. The waveguide is linearly polarized, *i.e.*, one polarization is measured after which the waveguide is turned 90 degrees. The accuracy of the turntable and the probe is 0.00025 degrees and 0.12 mm, respectively. For every movement of the probe, Δz, the turntable is rotated 360 degrees. With this measurement set-up, the data on the top and the bottom of the cylindrical surface cannot be collected. It would have been preferable to measure the fields on an infinite cylinder. However, the size of the cylinder is chosen such that the turntable below the radome does not have a major influence on the measurements and such that the fields above $z = 800$ mm are negligible. In the azimuth angle, 120 points are measured in steps of 3°. The z-dimension is divided into 129 points, every two points are separated by 12.5 mm. The sample density fulfills the sampling theorem for cylindrical near-field measurements given in *e.g.*, [49].

Three different measurement configurations are considered; antenna without radome, antenna together with radome, and antenna together with defect radome. The defect radome has two copper plates attached to its surface. These are located in the forward direction where the main lobe hits the radome and centered at the heights 41.5 cm and 65.5 cm above the bottom of the radome. The side of the squared copper plates is 6 cm, corresponding to 1.6 wavelengths at 8.0 GHz. The absolute values of the measured co- and cross-polarized electric fields, E^{v} and E^{φ}, respectively, are shown in Figures 4–5, where $|E^{\mathrm{v}}|_{\mathrm{dB}} = 20\log\left(|E^{\mathrm{v}}|/|E^{\mathrm{v}}|_{\max}\right)$ and $|E^{\varphi}|_{\mathrm{dB}} = 20\log\left(|E^{\varphi}|/|E^{\mathrm{v}}|_{\max}\right)$, respectively. That is, all fields are normalized with the largest value of $|E^{\mathrm{v}}|$ when no radome is present. In particular, E^{φ} has a quite complicated pattern. The diffraction is explained as environmental reflections and an off-centered antenna feed. Observe that the amplitude of the azimuth component is smaller than the amplitude of the height component, *i.e.*, measurement errors are more likely to show up here. The differences between the three different antenna and radome cases arise from constructive and destructive interference between the radiated field and the scattered field. The absolute value of the Fourier transformed measured fields are shown in dB-scale in Figures 6–7. According to these figures, the spectrum is truncated at $n = 30$, above which the energy contents is too low.

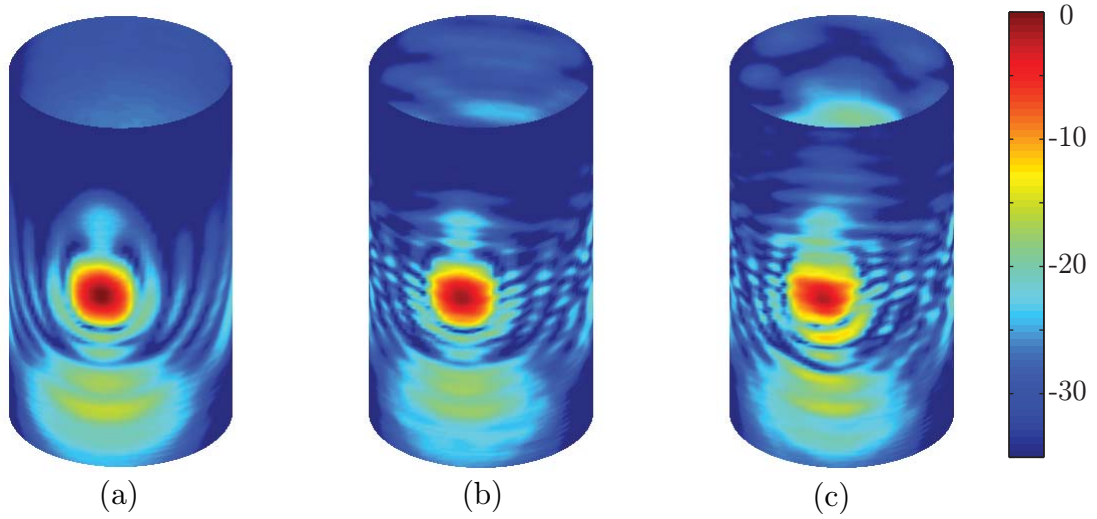

Figure 4: The co-component, $|E^{\mathrm{v}}|_{\mathrm{dB}}$, of the experimentally measured near-field data at 8.0 GHz, normalized with the largest value of $|E^{\mathrm{v}}|$ when no radome is present. (a) No radome present. (b) Radome present. (c) Defect radome present.

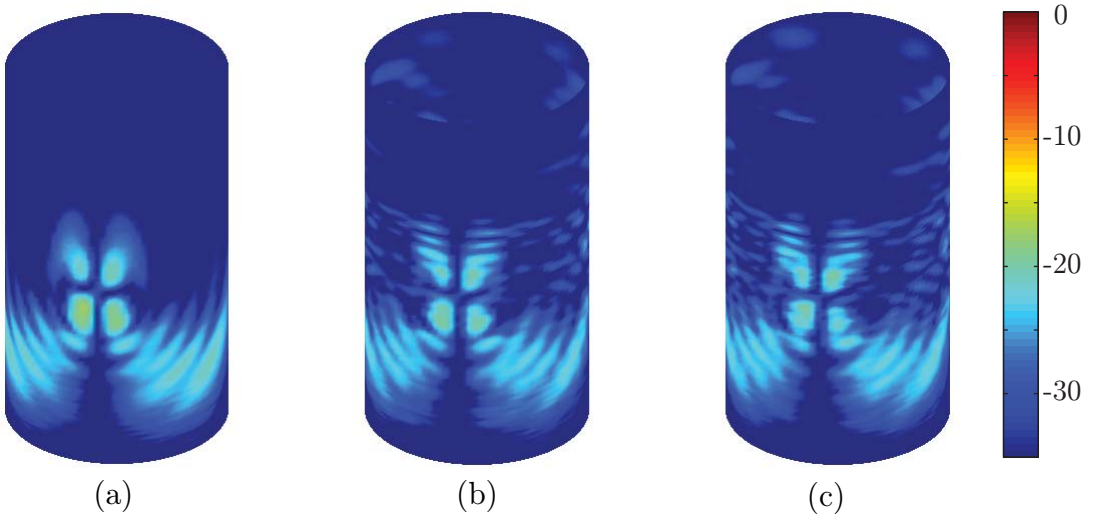

Figure 5: The cross-component, $|E^{\varphi}|_{\mathrm{dB}}$, of the experimentally measured near-field data at 8.0 GHz, normalized with the largest value of $|E^{\mathrm{v}}|$ when no radome is present. (a) No radome present. (b) Radome present. (c) Defect radome present.

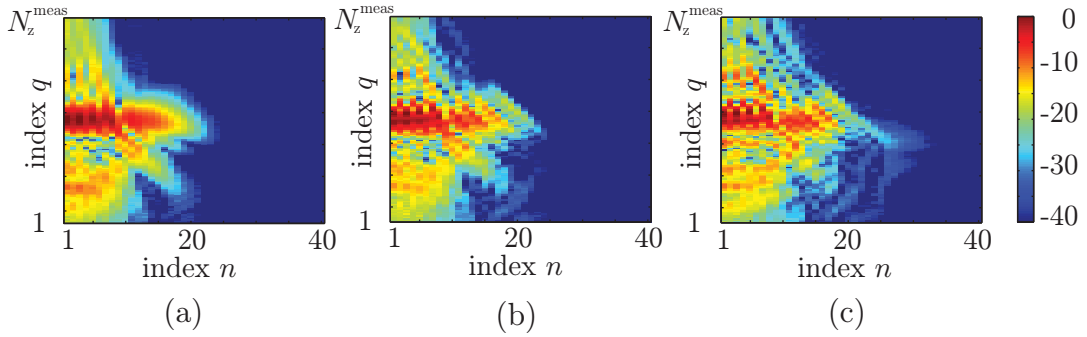

Figure 6: The Fourier transformed measured field, $|E^{v}|_{dB}$, at 8.0 GHz. All values are normalized with the largest value of $|E^{v}|$ when no radome is present. a) No radome present. (b) Radome present. (c) Defect radome present.

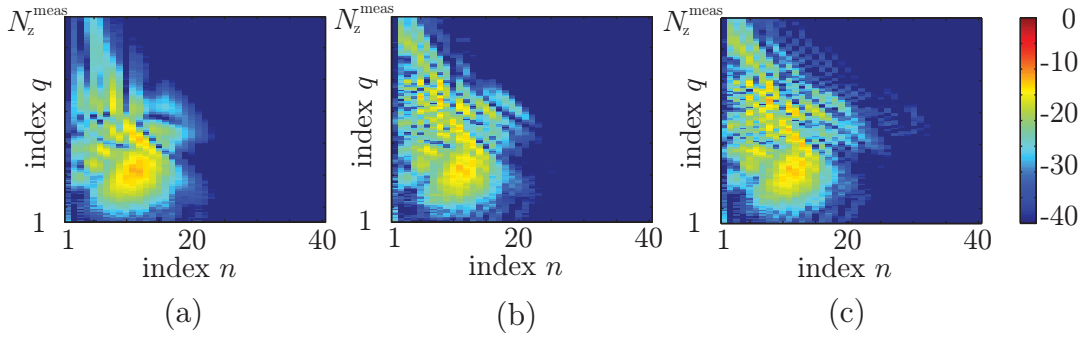

Figure 7: The Fourier transformed measured field, $|E^{\varphi}|_{dB}$, at 8.0 GHz. All values are normalized with the largest value of $|E^{v}|$ when no radome is present. a) No radome present. (b) Radome present. (c) Defect radome present.

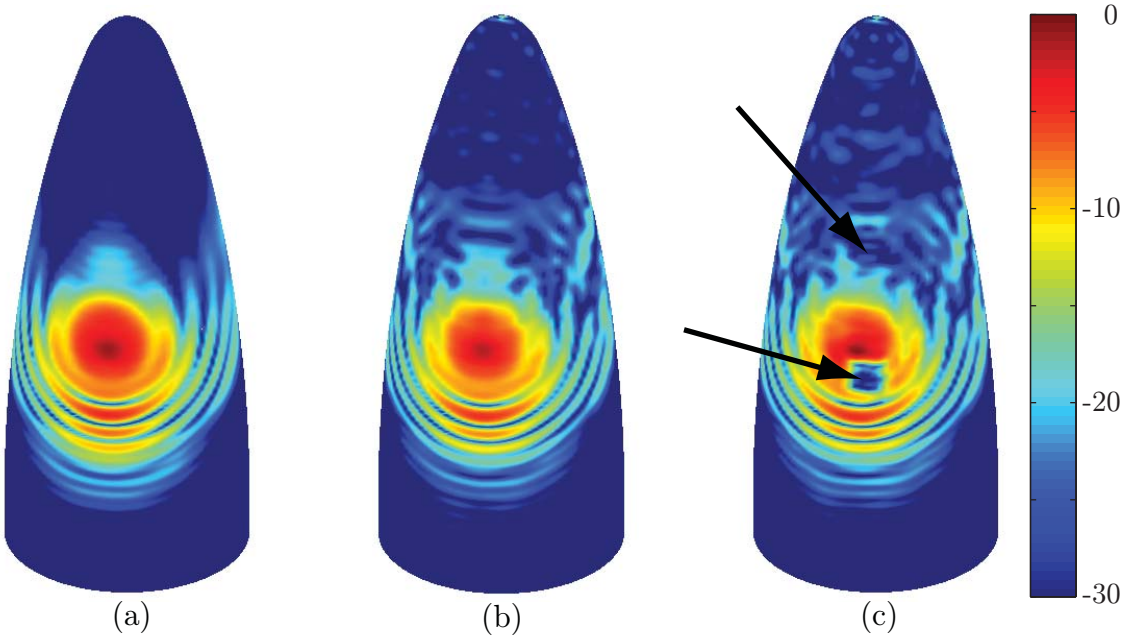

Figure 8: The recreated $|E^{\mathrm{v}}|_{\mathrm{dB}}$-component on the front side of the radome. All values are normalized with the largest value of $|E^{\mathrm{v}}|$ when the defect radome is present. (a) No radome present. (b) Radome present. (c) Defect radome present. The arrows point out the locations of the copper plates.

4 Results

The measured field on the cylindrical surface at 8.0 GHz, *cf.*, Figures 4 and 5, is transformed back onto a surface corresponding to the radome surface. Figures 8 and 9 show the recreated electric fields, $|E^{\mathrm{v}}|_{\mathrm{dB}}$ and $|E^{\varphi}|_{\mathrm{dB}}$, respectively, in the main lobe for the different configurations. Observe that all values are normalized with the largest value of $|E^{\mathrm{v}}|$ when the defect radome is present. The figures show that the near field close to the antenna is complex and hard to predict. In the case, when no radome is located around the antenna, the electric fields are calculated on a surface shaped as the radome, see Figures 8a and 9a. The case when the radome is present, see Figures 8b and 9b, shows that the radome interacts with the antenna and hence disturbs the radiated field. How this interaction affects the amplitude is depicted in Figures 10a and b, where $(|E^{\mathrm{v}}_{\text{no radome}}| - |E^{\mathrm{v}}_{\text{radome}}|)$ and $(|E^{\varphi}_{\text{no radome}}| - |E^{\varphi}_{\text{radome}}|)$ are shown in a linear scale and normalized with the maximum difference for each component. Both components of the electric field are reduced in amplitude in the main lobe whereas the field strength outside the main lobe is increased when the radome is introduced. This is most likely due to transmission loss in the radome wall and scattering against the inside wall.

The effect of the attached copper plates are detected as shown in Figures 8c and 9c, where the lower plate appears clearly. Observe that the copper plates cannot be localized directly in the near-field data, compare Figures 4c and 5c to Figures 8c

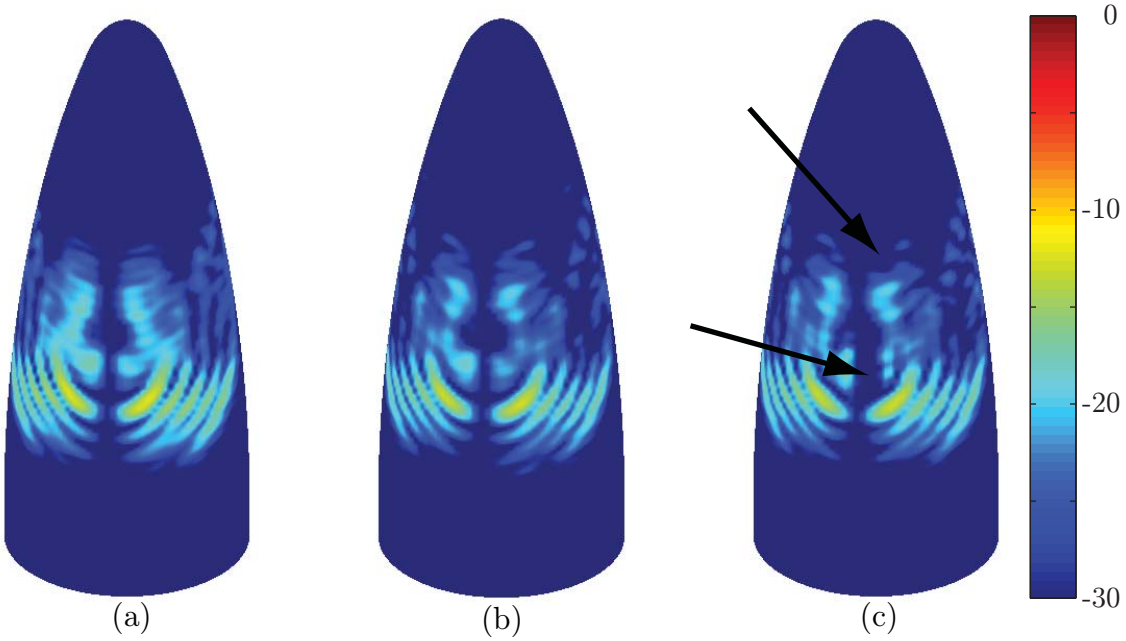

Figure 9: The recreated $|E^{\varphi}|_{\mathrm{dB}}$-component on the front side of the radome. All values are normalized with the largest value of $|E^{\mathrm{v}}|$ when the defect radome is present. (a) No radome present. (b) Radome present. (c) Defect radome present. The arrows point out the locations of the copper plates.

and 9c. The near-field data only shows that the field is disturbed, not the locations of the disturbances. The upper plate is hard to discern in Figures 8c and 9c, since it is located in a region with small field magnitudes. However, the influence of the upper copper plate can be detected in the cross section graphs, see Figures 11a and b. To determine the exact position of the defects several cross section graphs have to be examined. It is interesting to see that even though the magnitude of the cross-polarization is small, the locations of the copper plates can be found.

The presence of the radome also creates some backscattering (flash lobes) as seen in Figures 11 c–d, 12, and 13. In Figures 11 c–d, a cross section at an angle 180º from the center of the main lobe, *i.e.*, in the middle of the back side, is viewed. Figures 12 and 13 depict both components on the back side of the radome for all three configurations in a dB-scale. In these figures it is also observed that the flash lobes are altered when the copper plates are present.

The copper plates can also be detected by subtracting the field of the defect radome and the field of the non-defect radome. This result is shown in dB-scale in Figure 14 for both the components of the electric field, *i.e.*, $|E^{\mathrm{v}}_{\mathrm{radome}} - E^{\mathrm{v}}_{\mathrm{def\ radome}}|_{\mathrm{dB}}$ and $|E^{\varphi}_{\mathrm{radome}} - E^{\varphi}_{\mathrm{def\ radome}}|_{\mathrm{dB}}$, each component normalized with the maximum difference for each component. The reconstruction of the E^{φ}-component, *cf.*, Figure 14b, only shows the effects of some parts of the copper plates. The reason is that parts of the copper plates are located in an area where the amplitude of the E^{φ}-component is small, *cf.*, Figure 5 and 9a.

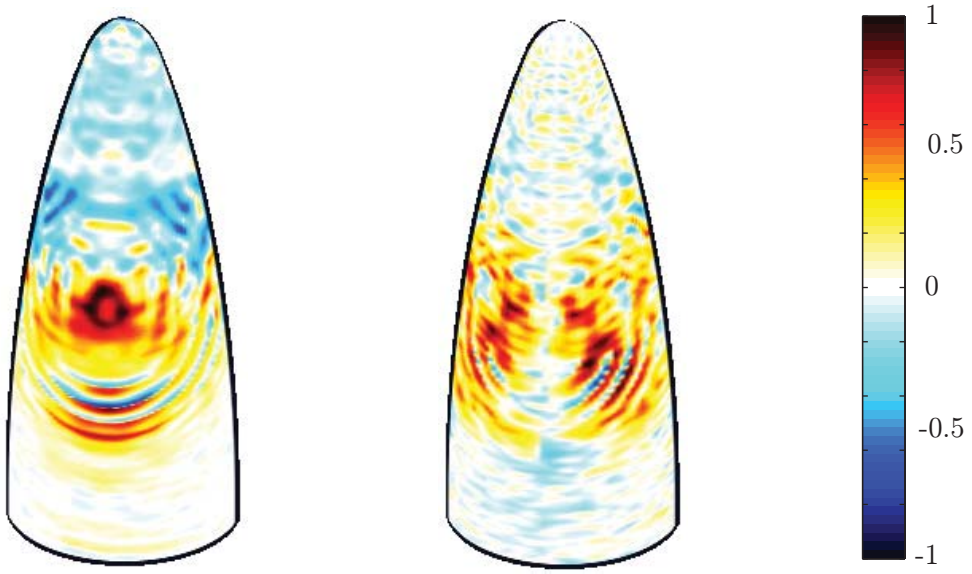

(a) (b)

Figure 10: The subtraction between the fields with and without radome present on the front side of the radome. In (a) $(|E^{\mathrm{v}}_{\text{no radome}}| - |E^{\mathrm{v}}_{\text{radome}}|)/\max||E^{\mathrm{v}}_{\text{no radome}}| - |E^{\mathrm{v}}_{\text{radome}}||$ is shown and in (b) $(|E^{\varphi}_{\text{no radome}}| - |E^{\varphi}_{\text{radome}}|)/\max||E^{\varphi}_{\text{no radome}}| - |E^{\varphi}_{\text{radome}}||$. The scale is linear.

Figure 14a indicates that there is an amplitude difference between the configurations slightly above the location of the lower copper plate. To visualize what is happening, the difference $(|E^{\mathrm{v}}_{\text{radome}}| - |E^{\mathrm{v}}_{\text{def radome}}|)$, normalized with its maximum value, in a linear scale, is depicted in Figure 15. The scale is truncated in order to see the small field difference above the copper plate. Here it becomes clear that the area, where the copper plate is attached, has a reduced electric field, when the defect radome is present. The area above the copper plate has instead an increased electric field, when the defect radome is present. This is most likely due to scattering of the copper plate.

So far only the amplitudes of the reconstructed fields has been investigated. However, even the phase can give useful information. The phase of the E^{v}-component, *i.e.*, $\angle E^{\mathrm{v}}$, where $\angle$ denotes the argument, is depicted in Figure 16 for all configurations. The vertical lines above the main lobe in Figure 16a are due to phase jumps, and are caused by the low amplitude of the fields in these areas.

Just showing the phase as in Figure 16 does not give very much information. What is interesting is to study the phase difference (antenna - antenna with radome) for the two recreated components, see Figure 17. It reveals how the phase is changed due to the influence of the radome. It is observed that the phase shift in the main lobe is almost constant, for both components. This confirms that the radome is well adapted to the frequency 8.0 GHz. Since the amplitude of E^{φ} is low, *cf.*, Figures 5 and 9, its phase contains much noise, and it is therefore somewhat more unreliable than $\angle E^{\mathrm{v}}$.

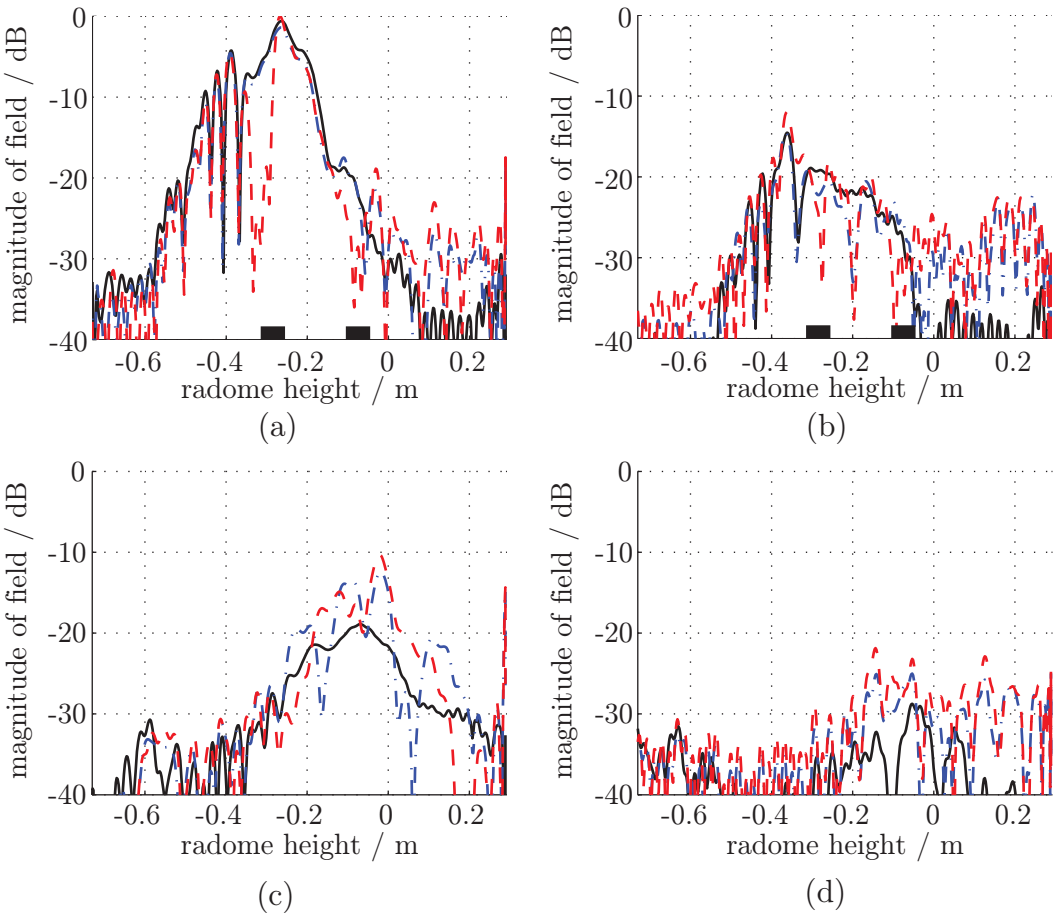

Figure 11: Cross sections of the reconstructed field components. (a) $|E^{\mathrm{v}}|_{\mathrm{dB}}$ in the main lobe. (b) $|E^{\varphi}|_{\mathrm{dB}}$ in the main lobe. (c) $|E^{\mathrm{v}}|_{\mathrm{dB}}$ on the back of the radome. (d) $|E^{\varphi}|_{\mathrm{dB}}$ on the back of the radome. All values are normalized with the maximum value of $|E^{\mathrm{v}}|$ when the defect radome is present. The solid black line corresponds to no radome, the dashed dot blue line has the radome present and the dashed red line represents the defect radome. The positions of the copper plates on the defect radome are marked by thick lines on the horizontal axis.

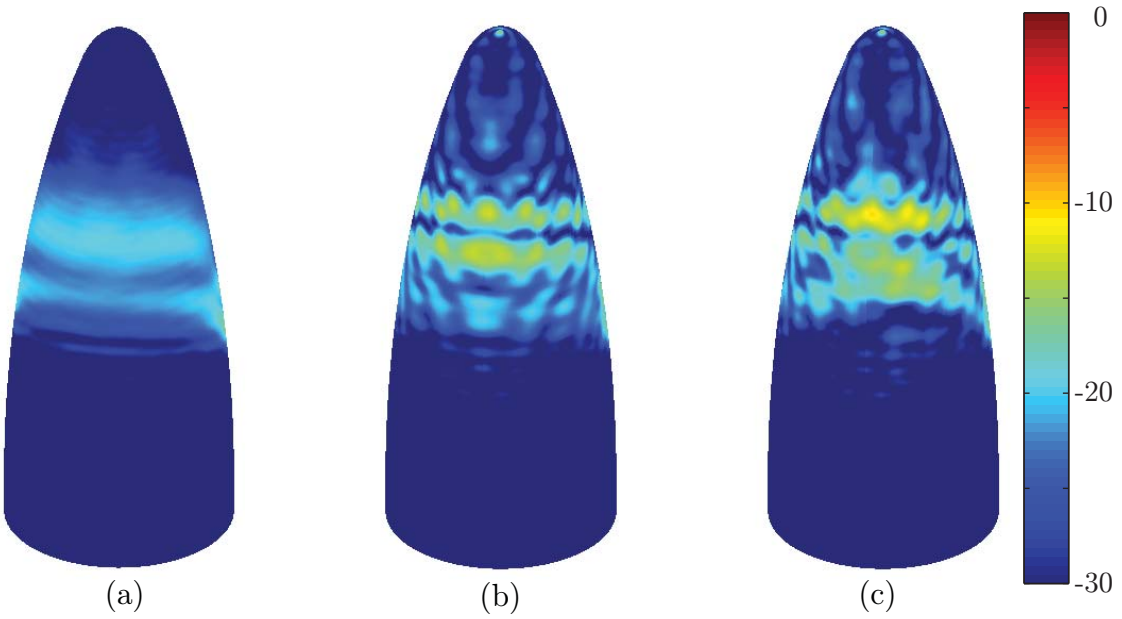

Figure 12: The recreated $|E^{\mathrm{v}}|_{\mathrm{dB}}$-component on the back side of the radome. All values are normalized with the maximum value of $|E^{\mathrm{v}}|$, on the front side, when the defect radome is present. (a) No radome present. (b) Radome present. (c) Defect radome present.

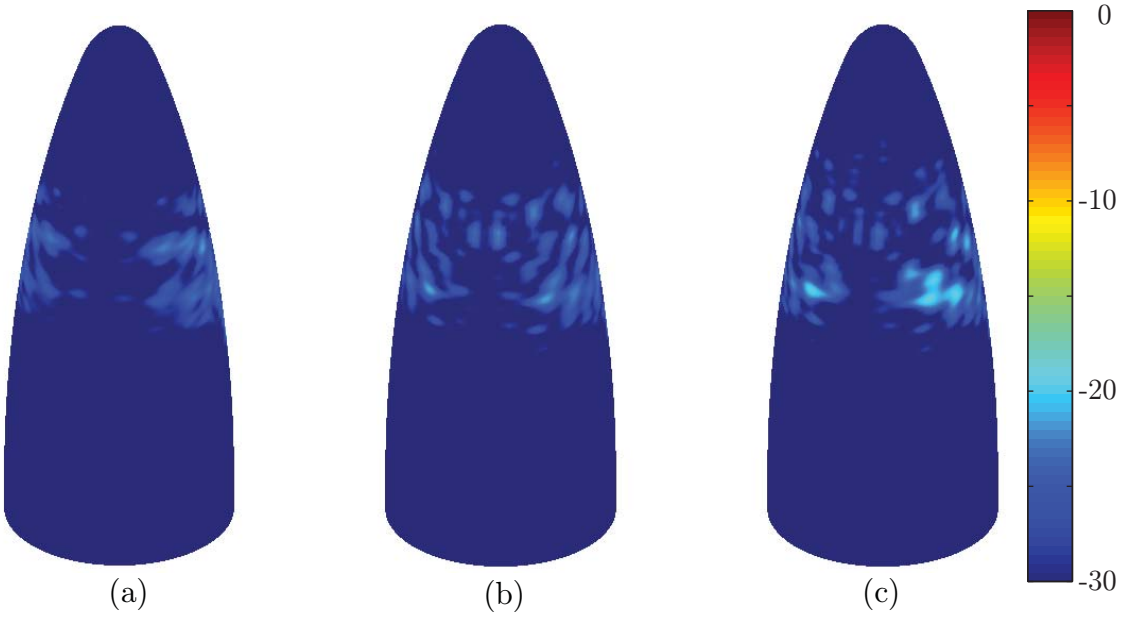

Figure 13: The recreated $|E^{\varphi}|_{\mathrm{dB}}$-component on the back side of the radome. All values are normalized with the maximum value of $|E^{\mathrm{v}}|$, on the front side, when the defect radome is present. (a) No radome present. (b) Radome present. (c) Defect radome present.

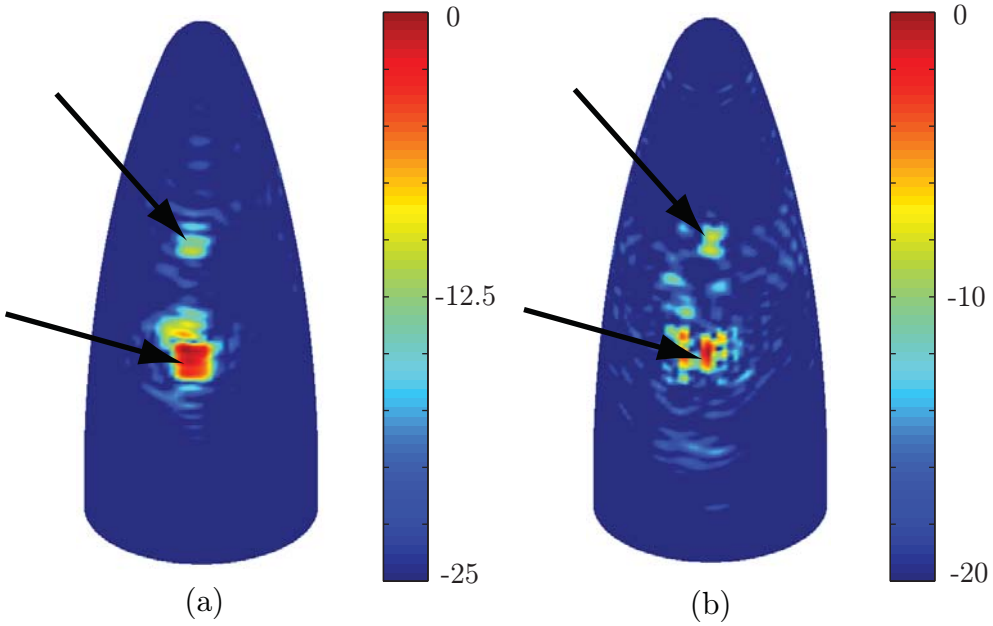

Figure 14: The logarithmic differences revealing the copper plates, (a) $20\log\{|E^{\mathrm{v}}_{\mathrm{radome}} - E^{\mathrm{v}}_{\mathrm{def\ radome}}|/\max|E^{\mathrm{v}}_{\mathrm{radome}} - E^{\mathrm{v}}_{\mathrm{def\ radome}}|\}$, and (b) $20\log\{|E^{\varphi}_{\mathrm{radome}} - E^{\varphi}_{\mathrm{def\ radome}}|/\max|E^{\varphi}_{\mathrm{radome}} - E^{\varphi}_{\mathrm{def\ radome}}|\}$ on the front side of the radome. The arrows point out the locations of the copper plates.

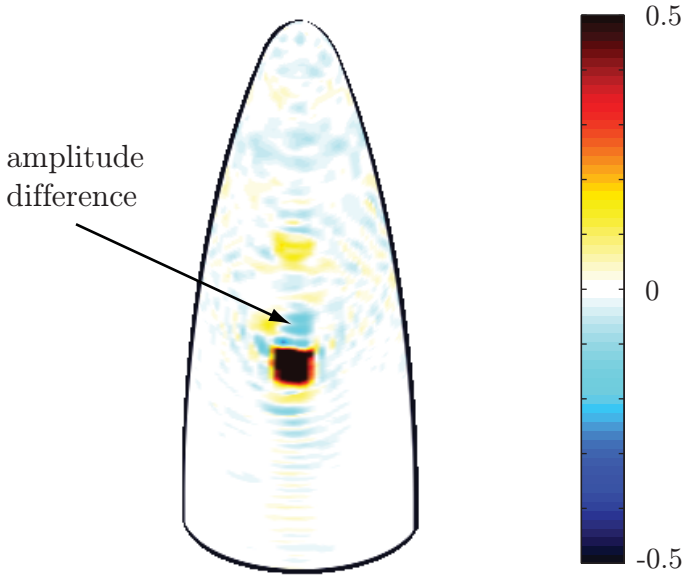

Figure 15: The difference $(|E^{\mathrm{v}}_{\mathrm{radome}}| - |E^{\mathrm{v}}{}_{\mathrm{def\ radome}}|)/\max||E^{\mathrm{v}}_{\mathrm{radome}}| - |E^{\mathrm{v}}_{\mathrm{def\ radome}}||$ in a linear scale on the front side of the radome. The scale is truncated in order to see the small field amplitude above the copper plate, marked with an arrow.

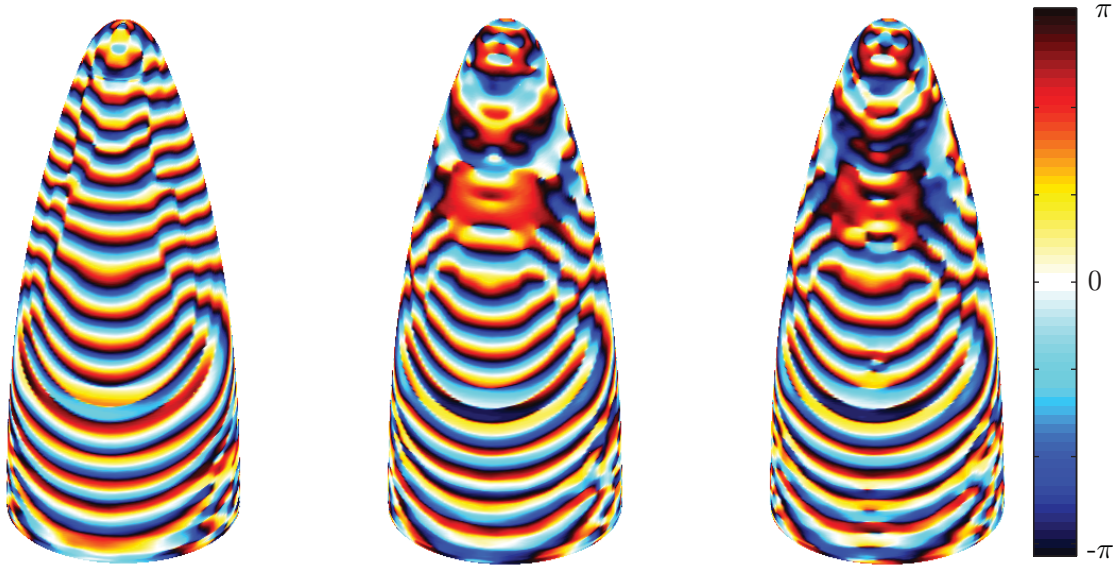

Figure 16: The recreated phase of the E^{v}-component on the front side of the radome in a linear scale. a) No radome present. b) Radome present. c) Defect radome present.

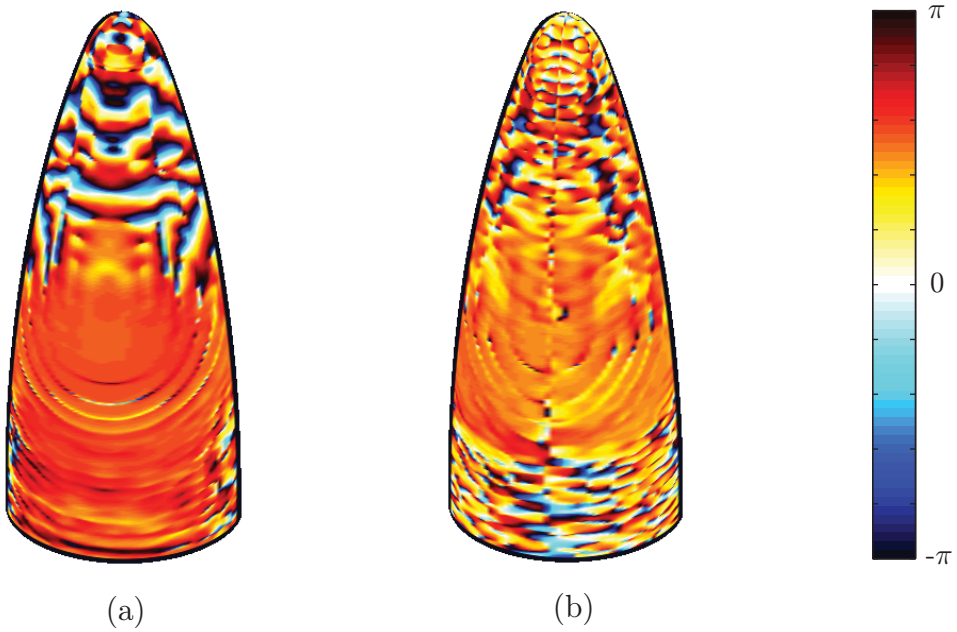

Figure 17: The IPD, *i.e.*, the phase difference between the field when no radome is present and the field when the radome is present, on the front side of the radome. a) $(\angle E^{\mathrm{v}}_{\text{no radome}} - \angle E^{\mathrm{v}}_{\text{radome}})$. b) $(\angle E^{\varphi}_{\text{no radome}} - \angle E^{\varphi}_{\text{radome}})$.

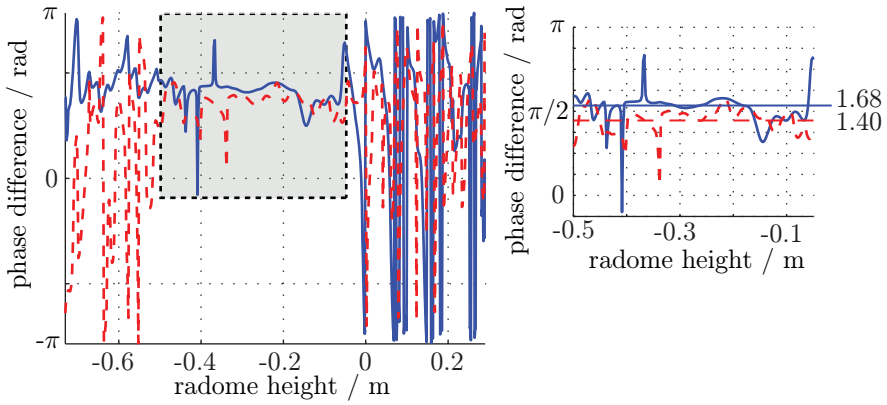

Figure 18: Cross section in the middle of the main lobe of the IPD depicted in Figure 17. The solid blue line corresponds to $(\angle E^{\mathrm{v}}_{\text{no radome}} - \angle E^{\mathrm{v}}_{\text{radome}})$ and the dashed red to $(\angle E^{\varphi}_{\text{no radome}} - \angle E^{\varphi}_{\text{radome}})$, respectively. The insert shows the area with reliable data and the medians.

In Figure 18, a cross section in the middle of the main lobe of the phase difference in Figure 17 is depicted. The cross section of $\angle E^{\varphi}$ is shown for a slightly acentric angle, since the amplitude in the center of the main lobe is very low, see Figure 9. In areas where the field is strong, the phase shift does not fluctuate as much. Outside this areas the amplitude is low and the phase is not well defined, *i.e.*, dominated by noise, and it will not give valid information. This means that when looking at the main lobe, the only area that contains reliable values is $z \in [-0.5, -0.05]$.

The phase shift arising when the radome is introduced, *i.e.*, the phase shift viewed in Figures 17 and 18, is called the IPD (Insertion Phase Delay). It is one of the parameters that quantifies the performance of the radome, and depending on the polarization, two different IPD are defined [18]

$$T = |T| \angle \mathrm{IPD} \tag{4.1}$$

where $T = E_{\mathrm{t}}/E_{\mathrm{i}}$ is the complex transmission coefficient. The incoming field is denoted E_{i}, and the transmitted E_{t}. The phase shift is only known modulus 2π. To validate the calculation of the IPD, an estimation of the thickness of the radome wall is carried out. Under the assumption of negligible reflections the IPD can be expressed as [17]

$$\mathrm{IPD} = \frac{\omega}{\mathrm{c}} \left\{ \mathrm{Re}\, \sqrt{\epsilon_{\mathrm{r}}(1 - \mathrm{j}\tan\delta)}\cos\theta_{\mathrm{t}} - \cos\theta_{\mathrm{i}} \right\} d \tag{4.2}$$

for both polarizations, where ω is the angular frequency, c is the speed of light in free space, θ_{i} is the incident angle, and θ_{t} is the transmission angle of the field on the inside of the radome wall. Approximate values of the relative permittivity, $\epsilon_{\mathrm{r}} \approx 4.32$, and the loss tangent, $\tan\delta \approx 0.0144$, are used. The thickness of the radome wall is denoted d. The incident angle is approximated to 40°, *cf.*, Figure 3b. The measured radome thickness, d, varies over the surface in the interval $7.6 - 8.2\,\mathrm{mm}$. The phase

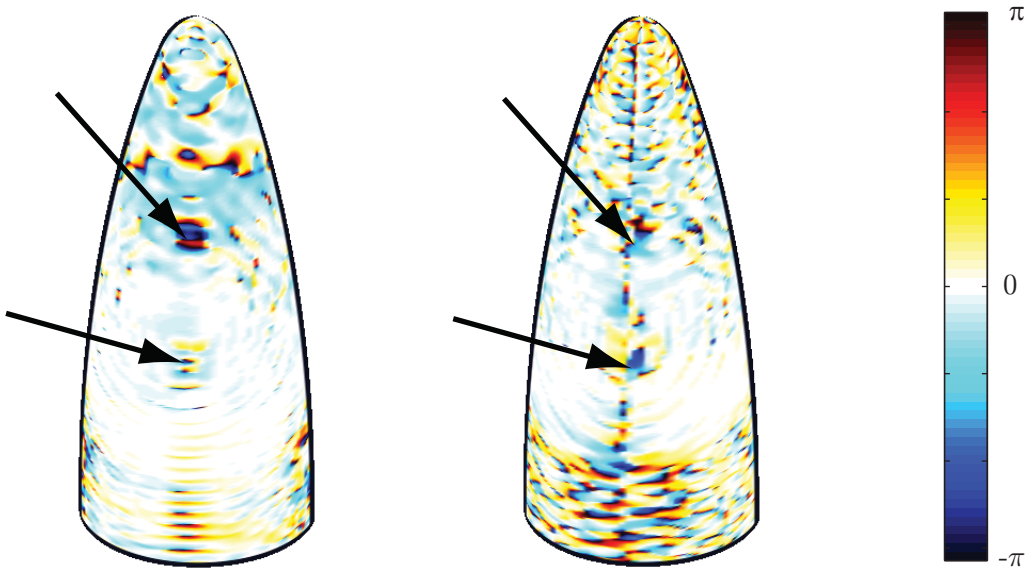

(a) (b)

Figure 19: The phase difference between the field when the radome is present and the field when the defect radome is present, on the front side of the radome. The arrows point out the copper plates. a) $(\angle E^{\mathrm{v}}_{\mathrm{radome}} - \angle E^{\mathrm{v}}_{\mathrm{def\ radome}})$. b) $(\angle E^{\varphi}_{\mathrm{radome}} - \angle E^{\varphi}_{\mathrm{def\ radome}})$.

shift in the main lobe is taken as the medians of the calculated IPD, see the insert in Figure 18. The medians, for $z \in [-0.5, -0.05]$, are 1.68 rad and 1.40 rad for the co- and the cross-component, respectively. Solving for d in (4.2) results in a radome thickness of $6.9 - 8.3$ mm. The agreement is quite well considering the approximations made.

An investigation of the phase difference (radome - defect radome), see Figures 19 and 20, reveals that its harder to localize the actual positions of the copper plates by using the phase instead of only the amplitude, *cf.*, Figures 8 and 9. Nevertheless, the upper copper plate is visible in the 3-D visualization in Figure 19a, and by looking at a cross section over the main lobe of the phase difference, the position of the upper copper plate is located for both components, see Figure 20. We only show the interval, where the phase is not too contaminated by noise, *cf.*, Figure 18. The upper copper plate is located on the boundary to where noise dominates. Thus, if the positions of the copper plate were not known in advance, the phase shift might be interpreted as noise. The lower copper plate also introduces a phase shift, but these effects are hard to interpret and not confined to the exact position of the plate.

5 Conclusions

The aim of this paper is to reconstruct equivalent currents on a surface bounding the sources of an electromagnetic field. A vector-valued surface integral representation

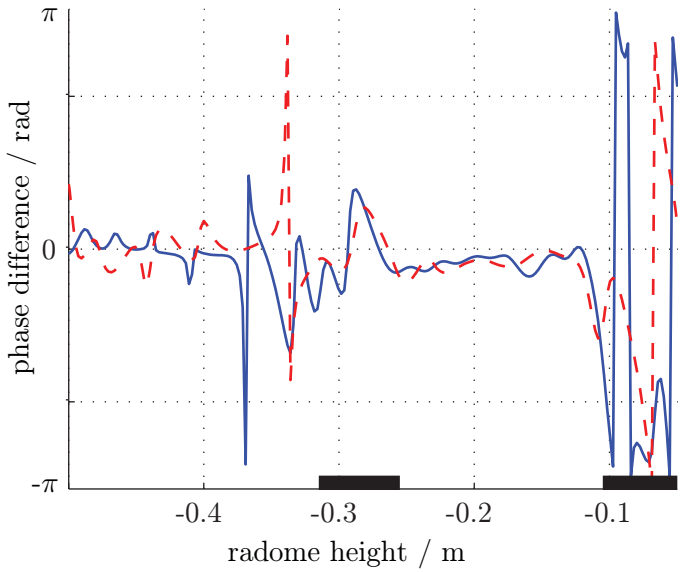

Figure 20: Cross section in the middle of the main lobe of the phase differences depicted in Figure 19. The axis describing the radome height is truncated and shows only the region where the phase information is reliable, *cf.*, Figure 18. The blue solid line corresponds to $(\angle E^{\mathrm{v}}_{\mathrm{radome}} - \angle E^{\mathrm{v}}_{\mathrm{def\ radome}})$ and the red dashed to $(\angle E^{\varphi}_{\mathrm{radome}} - \angle E^{\varphi}_{\mathrm{no\ radome}})$, respectively.

is utilized together with the extinction theorem. The surface integral representation gives a linear map between the equivalent surface currents and the near-field data for general geometries. It is shown that this map can be inverted for axially symmetric geometries with the measured near field. The theory can be adapted to geometries lacking symmetry axes. However, it is not a feasible approach for radome applications today due to the computational demand to solve the integral equations. An alternative approach would be to address this problem using fast multipoles methods [44].

In previous papers only the dominating vertical co-component of the measured field has been used in the reconstruction by using a scalar integral representation, where comparison with measured far field shows good agreement [30, 31]. In this paper it is shown that both components of the equivalent currents can be reconstructed by using a full-wave surface integral representation. The results for the cross-component show that also this component provides useful insight of the complex field close to the antenna and the field altered by the radome. It is illustrated how the radome interacts with the electric field. In particular, transmission losses in the radome wall and reflections on the inside decrease the field in the main lobe, and new side and flash lobes appear. Both components of the experimentally measured field can also be used to locate the effect of defects, *i.e.*, copper plates, not directly visible in the measured near-field data. Furthermore, the copper plates introduce scattering and alter the flash lobes.

Also, the phase of the reconstructed fields is investigated. The IPD, *i.e.*, the

phase difference, arising when the radome is located between the antenna and the measurement probe, is visualized. The results give a good estimate of the thickness of the radome wall. The effects of the copper plates are visible in the phase shift. However, the exact location of the defects is hard to determine solely from the phase images.

This paper shows the potentials of the approach in radome diagnostics. Next step is to analyze if the electric equivalent current, *i.e.*, the magnetic field, on the radome surface gives some more information. Moreover, investigations with different frequencies are expected. To localize the exact positions of the defects, a deeper analyze of 3D-pictures, *cf.*, Figures 8c and 9c, and cross-section graphs, *cf.*, Figure 11, combined with the phase shift data, is planned. To use this method in verifying radomes, *i.e.*, calculating the IPD, more analysis of the phase and its noise levels is planned to be addressed in a forthcoming paper.

Acknowledgement

The work reported in this paper was made possible by a grant from the Swedish Defense Material Administration, and their support is gratefully acknowledged. We are indebted to Saab Bofors Dynamics, in particular Ola Forslund for assistance on measurement details, and Applied Composites AB, for providing measurement data. In discussing the concepts of IPD, Michael Andersson has been most helpful, and his assistance is most appreciated.

References

[1] M. Andersson. Software for analysis of radome performance. In *Proc. International Conference on Electromagnetics in Advanced Applications (ICEAA'05)*, pages 537–539, Torino, Italy, 2005.

[2] M. Andreasen. Scattering from bodies of revolution. *IEEE Trans. Antennas Propagat.*, **13**(2), 303–310, 1965.

[3] R. Aster, B. Borchers, and C. Thurber. *Parameter Estimation and Inverse Problems*. Academic Press, New York, 2005.

[4] C. A. Balanis. *Antenna Theory*. John Wiley & Sons, New York, second edition, 1997.

[5] C. A. Balanis. *Advanced Engineering Electromagnetics*. John Wiley & Sons, New York, 1989.

[6] A. Bondeson, T. Rylander, and P. Ingelström. *Computational Electromagnetics*. Springer-Verlag, Berlin, 2005.

[7] C. Cappellin, O. Breinbjerg, and A. Frandsen. Properties of the transformation from the spherical wave expansion to the plane wave expansion. *Radio Sci.*, **43**(1), 2008.

[8] C. Cappellin, A. Frandsen, and O. Breinbjerg. Application of the SWE-to-PWE antenna diagnostics technique to an offset reflector antenna. *IEEE Antennas and Propagation Magazine*, **50**(5), 204–213, 2008.

[9] D. Colton and R. Kress. *Integral Equation Methods in Scattering Theory.* John Wiley & Sons, New York, 1983.

[10] L. E. Corey and E. B. Joy. On computation of electromagnetic fields on planar surfaces from fields specified on nearby surfaces. *IEEE Trans. Antennas Propagat.*, **29**(2), 402–404, 1981.

[11] T. F. Eibert and C. H. Schmidt. Multilevel fast multipole accelerated inverse equivalent current method employing Rao-Wilton-Glisson discretization of electric and magnetic surface currents. *IEEE Trans. Antennas Propagat.*, **57**(4), 1178–1185, 2009.

[12] J. Fridén, H. Isaksson, B. Hansson, and B. Thors. Robust phase-retrieval for quick whole-body SAR assessment using dual plane amplitude-only data. *Electronics Letters*, **45**(23), 1155–1157, 2009.

[13] M. G. Guler and E. B. Joy. High resolution spherical microwave holography. *IEEE Trans. Antennas Propagat.*, **43**(5), 464–472, 1995.

[14] J. E. Hansen, editor. *Spherical Near-Field Antenna Measurements.* Number 26 in IEE electromagnetic waves series. Peter Peregrinus Ltd., Stevenage, UK, 1988. ISBN: 0-86341-110-X.

[15] D. S. Jones. *Acoustic and Electromagnetic Waves.* Oxford University Press, New York, 1986.

[16] R. E. Kleinman and G. F. Roach. Boundary integral equations for the three-dimensional Helmholtz equation. *SIAM Review*, **16**(2), 214–236, 1974.

[17] J. A. Kong. *Electromagnetic Wave Theory.* John Wiley & Sons, New York, 1986.

[18] D. J. Kozakoff. *Analysis of Radome-Enclosed Antennas.* Artech House, Boston, London, 1997.

[19] R. Kress. *Linear Integral Equations.* Springer-Verlag, Berlin Heidelberg, second edition, 1999.

[20] F. Las-Heras, B. Galocha, and Y. Alvarez. On the sources reconstruction method application for array and aperture antennas diagnostics. *Microwave Opt. Techn. Lett.*, **51**(7), 1664–1668, 2009.

[21] F. Las-Heras, M. R. Pino, S. Loredo, Y. Alvarez, and T. K. Sarkar. Evaluating near-field radiation patterns of commercial antennas. *IEEE Trans. Antennas Propagat.*, **54**(8), 2198–2207, 2006.

[22] J.-J. Laurin, J.-F. Zürcher, and F. E. Gardiol. Near-field diagnostics of small printed antennas using the equivalent magnetic current approach. *IEEE Trans. Antennas Propagat.*, **49**(5), 814–828, 2001.

[23] J. Lee, E. M. Ferren, D. P. Woollen, and K. M. Lee. Near-field probe used as a diagnostic tool to locate defective elements in an array antenna. *IEEE Trans. Antennas Propagat.*, **36**(6), 884–889, 1988.

[24] E. A. Marengo and A. J. Devaney. The inverse source problem of electromagnetics: Linear inversion formulation and minimum energy solution. *IEEE Trans. Antennas Propagat.*, **47**(2), 410–412, February 1999.

[25] J. R. Mautz and R. F. Harrington. Radiation and scattering from bodies of revolution. *Appl. Scientific Research*, **20**(1), 405–435, 1969.

[26] N. Morita, N. Kumagai, and J. R. Mautz. *Integral Equation Methods for Electromagnetics*. Artech House, Boston, London, 1990.

[27] C. Müller. *Foundations of the Mathematical Theory of Electromagnetic Waves*. Springer-Verlag, Berlin, 1969.

[28] M. Nieto-Vesperinas. *Scattering and diffraction in physical optics*. World Scientific Publisher, Singapore, second edition, 2006.

[29] S. Nordebo, M. Gustafsson, and K. Persson. Sensitivity analysis for antenna near-field imaging. *IEEE Trans. Signal Process.*, **55**(1), 94–101, January 2007.

[30] K. Persson and M. Gustafsson. Reconstruction of equivalent currents using a near-field data transformation – with radome applications. *Progress in Electromagnetics Research*, **54**, 179–198, 2005.

[31] K. Persson and M. Gustafsson. Reconstruction of equivalent currents using the scalar surface integral representation. Technical Report LUTEDX/(TEAT-7131)/1–25/(2005), Lund University, Department of Electrical and Information Technology, P.O. Box 118, S-221 00 Lund, Sweden, 2005. `http://www.eit.lth.se`.

[32] K. Persson, M. Gustafsson, and G. Kristensson. Reconstruction and visualization of equivalent currents on a radome using an integral representation formulation. Technical Report LUTEDX/(TEAT-7184)/1–45/(2010), Lund University, Department of Electrical and Information Technology, P.O. Box 118, S-221 00 Lund, Sweden, 2010. `http://www.eit.lth.se`.

[33] A. F. Peterson, S. L. Ray, and R. Mittra. *Computational Methods for Electromagnetics*. IEEE Press, New York, 1998.

[34] A. J. Poggio and E. K. Miller. Integral equation solutions of three-dimensional scattering problems. In R. Mittra, editor, *Computer Techniques for Electromagnetics*. Pergamon, New York, 1973.

[35] J. L. A. Quijano and G. Vecchi. Improved-accuracy source reconstruction on arbitrary 3-D surfaces. *IEEE Antennas & Wireless Propagat. Lett.*, **8**, 1046–1049, 2009.

[36] Y. Rahmat-Samii, L. I. Williams, and R. G. Yaccarino. The UCLA bi-polar planar-near-field antenna-measurement and diagnostics range. *IEEE Antennas and Propagation Magazine*, **37**(6), 16–35, December 1995.

[37] D. J. Rochblatt and B. L. Seidel. Microwave antenna holography. *IEEE Trans. Microwave Theory Tech.*, **40**(6), 1294–1300, 1992.

[38] T. K. Sarkar and A. Taaghol. Near-field to near/far-field transformation for arbitrary near-field geometry utilizing an equivalent electric current and MoM. *IEEE Trans. Antennas Propagat.*, **47**(3), 566–573, March 1999.

[39] J. A. Shifflett. CADDRAD: A physical optics radar/radome analysis code for arbitrary 3D geometries. *IEEE Antennas and Propagation Magazine*, **6**(39), 73–79, 1997.

[40] R. A. Shore and A. D. Yaghjian. Dual surface electric field integral equation. Air Force Research Laboratory Report, 2001. No. AFRL-SN-HS-TR-2001-013.

[41] R. A. Shore and A. D. Yaghjian. Dual-surface integral equations in electromagnetic scattering. *IEEE Trans. Antennas Propagat.*, **53**(5), 1706–1709, 2005.

[42] S. Silver. *Microwave Antenna Theory and Design*, volume 12 of *Radiation Laboratory Series*. McGraw-Hill, New York, 1949.

[43] F. Soldovieri, C. Mola, R. Solimene, and R. Pierri. Inverse source problem from the knowledge of radiated field over multiple rectilinear domains. *Progress in Electromagnetics Research M*, **8**, 131–141, 2009.

[44] J. Song and W. Chew. FMM and MLFMA in 3-D and fast Illinois solver code. In W. Chew, J.-M. Jin, E. Michielssen, and J. Song, editors, *Fast and Efficient Algorithms in Computational Electromagnetics*, pages 77–118. Artech House, 2001.

[45] J. C.-E. Sten and E. A. Marengo. Inverse source problem in the spheroidal geometry: Vector formulation. *IEEE Trans. Antennas Propagat.*, **56**(4), 961–969, 2008.

[46] G. Strang. *Introduction to applied mathematics*. Wellesley-Cambridge Press, Box 157, Wellesley MA 02181, 1986.

[47] S. Ström. Introduction to integral representations and integral equations for time-harmonic acoustic, electromagnetic and elastodynamic wave fields. In V. V. Varadan, A. Lakhtakia, and V. K. Varadan, editors, *Field Representations and Introduction to Scattering*, volume 1 of *Handbook on Acoustic, Electromagnetic and Elastic Wave Scattering*, chapter 2, pages 37–141. Elsevier Science Publishers, Amsterdam, 1991.

[48] F. Thérond, J. C. Bolomey, N. Joachmowicz, and F. Lucas. Electromagnetic diagnosis technique using spherical near-field probing. In *Proc. EUROEM'94*, pages 1218–1226, Bordeaux, France, 1994.

[49] A. D. Yaghjian. An overview of near-field antenna measurements. *IEEE Trans. Antennas Propagat.*, **34**(1), 30–45, January 1986.

[50] A. Ziyyat, L. Casavola, D. Picard, and J. C. Bolomey. Prediction of BTS antennas safety perimeter from NF to NF transformation: an experimental validation. In *Proc. Antenna Measurement Techniques Association (AMTA)*, pages 22–26, Denver, US, 2001.

Radome diagnostics — source reconstruction of phase objects with an equivalent currents approach

Kristin Persson, Mats Gustafsson, Gerhard Kristensson, and Björn Widenberg

Paper IV

Based on: K. Persson, M. Gustafsson, G. Kristensson, and B. Widenberg. Radome diagnostics — source reconstruction of phase objects with an equivalent currents approach, Technical Report LUTEDX/(TEAT-7223), pp. 1–22, 2012, Department of Electrical and Information Technology, Lund University, Sweden. `http://www.eit.lth.se`

Submitted for publication.

Abstract

Radome diagnostics are acquired in the design process, the delivery control, and in performance verification of repaired and newly developed radomes. A measured near or far field may indicate deviations, *e.g.*, increased side-lobe levels, but the origin of the flaws are not revealed. In this paper, radome diagnostics are performed by visualizing the equivalent surface currents on the 3D-radome body, illuminated from the inside. Three different far-field measurement series at 10 GHz are employed. The measured far field is related to the equivalent surface currents on the radome surface by using a surface integral representation. In addition, a surface integral equation is employed to ensure that the sources are located inside the radome. Phase shifts, insertion phase delays (IPD), caused by patches of dielectric tape attached to the radome surface, are localized. Specifically, patches of various edge sizes ($0.5 - 2.0$ wavelengths), and with the smallest thickness corresponding to a phase shift of a couple of degrees are imaged.

1 Introduction and background

A radome encloses an antenna to protect it from *e.g.*, environmental influences. Depending on the properties of the shielding antenna and the environment in which it operates, the radome has different appearance and qualities. The radome is ideally electrically transparent, but in reality, radomes often reduce gain and introduces higher side-lobe levels, especially flash (image) lobes caused by reflections on the inside of the radome wall and reflections within the wall appear [4, 18]. Moreover, the electromagnetic wave radiated by the antenna changes its direction when passing through the radome, and, if not compensated for, boresight errors occur [4, 18].

New radomes must fulfill specified tolerance levels, and repaired radomes must be checked according to international standard and manufacturers maintenance manuals [18]. Consequently, there is a demand for diagnostics tools verifying the electrical properties of the radome. The verification test is often performed with a far-field analysis. Due to the radome, a measured far field may indicate boresight errors, amplitude reductions, introduction of flash (image) lobes, and increased side-lobe levels. However, it is not feasible to determine the cause of the alteration, *i.e.*, the location of defect areas on the radome, from the far-field data alone. Further investigations are often required, *e.g.*, cracks can be localized by employing ultrasonics [31]. Moreover, the phase alteration caused by the radome, *i.e.*, the insertion phase delay (IPD) on the surface of the radome, is commonly investigated to localize deviations. One way to measure the IPD is with two horn antennas aligned at the Brewster angle [29].

An alternative diagnostics method is presented in this paper, where the tangential electromagnetic fields — the equivalent surface currents — on the outside of the radome surface are reconstructed from a measured far field. The reconstruction is performed on a fictitious surface in free space, located precisely outside the physical surface of the radome, *i.e.*, no *a priori* information on the material of the radome is assumed. Both amplitude and phase are investigated. The effect of metallic defects

attached to a radome has previously been investigated in [24–26]. In this paper, we focus on imaging the phase changes introduced by a monolithic (solid) radome and patches of dielectric tape attached to the radome surface. These phase changes are interpreted as the IPD.

Three different far-field measurement series (at 10 GHz) are employed. In each series, both polarizations are collected over a hemisphere. Moreover, for each series, three different configurations are investigated; (0) antenna, (1) antenna together with the radome and (2) antenna together with the radome where patches of metal or dielectric material are attached to the surface. To clarify, different defects are applied to the radome in conf. (2) in the different series; defects consisting of copper plates (first series), squares of dielectric tape (second series), and the letters LU of dielectric tape (third series). The results of the first measurement series (metal defects) are employed to set the regularization parameters used in the subsequent series. In the two last measurement series, patches of dielectric tape, which mainly effect the phase of the field, are attached to the radome. The sizes of the patches vary, with a smallest dimension of 0.5 wavelengths. The dielectric patches model deviations in the electrical thickness of the radome wall, and the results can be utilized to produce a trimming mask for the illuminating areas. A trimming mask is a map of the surface with instructions of how the surface should be altered to obtain the desired properties, *e.g.*, a smooth IPD or low side- and flash-lobe levels. IPD diagnostics of the radome surface is also significant in the delivery control to guarantee the manufacturing tolerance of radomes.

The method to reconstruct the equivalent surface currents is based on a surface integral representation combined with an electric field integral equation (EFIE). The set-up is axially symmetric and a body of revolution method of moments (MoM) code is employed, with special attention taken to the calculation of the Green's function [11]. Regularization is performed by a singular value decomposition (SVD).

Prior radome diagnostics of spherical radomes utilizing a spherical wave expansion (SWE), applicable to spherical objects, are given in *e.g.*, [10], where the IPD and defects in the radome wall are investigated. Moreover, an early attempt to employ the inverse Fourier transform in radome diagnostics, is reported in [9].

The interest in surface integral representations as a tool in diagnostics has increased rapidly over the last years where different combinations and formulations based on a surface integral representation, the electric (EFIE) and magnetic (MFIE) field integral equations are utilized [1, 28]. Specifically, the influences of metallic defects attached to a radome are imaged in [24–26]. In [27] an iterative conjugate-gradient solver is utilized to find and exclude radiation contributions from leaky cables and support structures and in [8] antennas are characterized. Defect elements on a satellite antenna and a circular array antenna are localized in [16, 17], where a MoM code with higher order basis functions are implemented together with a Tikhonov regularization. Higher order basis functions and multilevel fast multipoles are utilized in [7] to recreate equivalent surface currents on a base station antenna from probe corrected near-field measurements. A surface integral representation is applied in [20, 21] to diagnose antennas. Furthermore, in [20] a conjugate-gradient solver and a singular value decomposition are shown to give similar results.

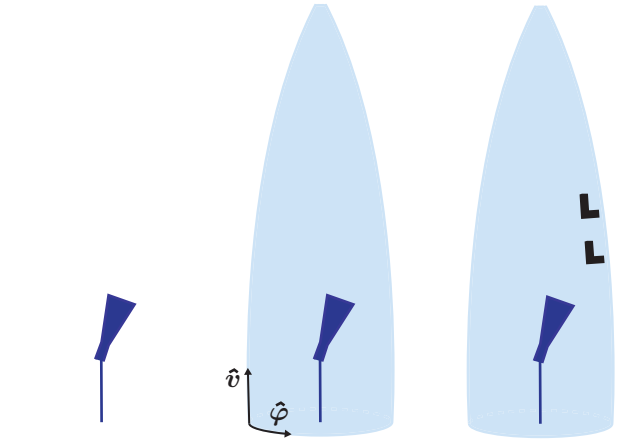

Figure 1: Description and notation of the configurations referred to throughout the paper. The middle figure shows the unit vectors of the coordinate system in which the reconstructed fields are expressed.

The focus of this paper is radome diagnostics, where patches of dielectric tape, attached to the radome surface, are localized. In Section 2.1, the set-up, the compact test range, and the measured far field are described. The IPD and different visualization options — the electric or the magnetic field — are discussed in Section 2.2. In Section 3, an outline of the reconstructing algorithm is given. Imaging results are viewed and analyzed in Section 4, whereas conclusions and discussions of future possibilities are finally given in Section 5.

2 Radome diagnostics

A measured far field of an antenna and radome configuration may indicate unwanted deviations; *e.g.*, increased and changed side lobes, and boresight errors. To find the origin of the errors, diagnostics tools are essential. Here, far-field measurements from a compact test range is utilized to localize phase shifts, insertion phase delays (IPD) on the radome surface, caused by the radome and attached patches of dielectric tape.

2.1 Measurement data and set-up

Three different measurement series are conducted at 10 GHz. Each measurement series consists of three configurations; antenna — conf. (0), antenna together with the radome — conf. (1), and antenna together with the radome where defects are attached to the surface — conf. (2), see Figure 1. Different defects are applied to the radome in conf. (2) in the different series; defects consisting of copper plates (first series), squares of dielectric tape (second series), and the letters LU of dielectric tape (third series). To clarify, conf. (0) and (1) are the same in all three series.

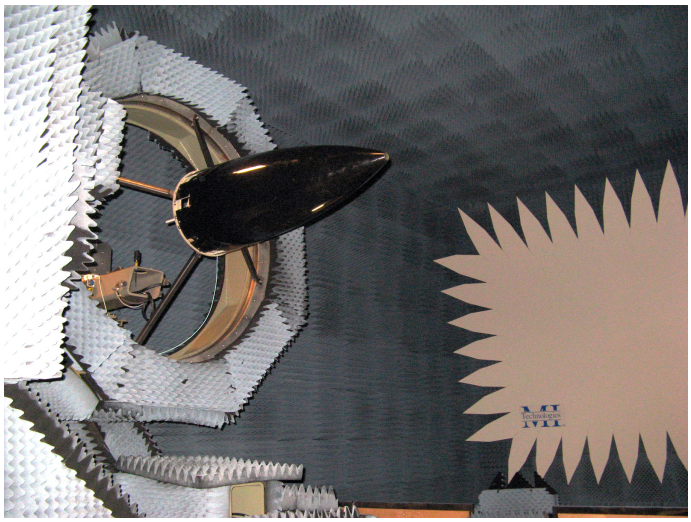

Figure 2: Photo of the measurement set-up in the compact test range.

The reason for doing these all over is that the measurement series were obtained at different times. In this way, we avoid the influence of small deviations in the mechanical and electrical set-up together with relative phase and amplitude shifts between the series. The configuration number is indicated as a superscript on the fields, whereas the field component is showed by a subscript, *i.e.*, $H_{\mathrm{v}}^{(0)} = \hat{\boldsymbol{v}} \cdot \boldsymbol{H}^{(0)}$ is the magnetic component directed along the height of the radome surface when only the antenna is present (*cf.*, notation in Figure 1).

The far-field measurements were carried out at a compact test range at GKN Aerospace Applied Composites, Linköping, Sweden, see Figure 2 [33]. The far field is measured on a hemisphere by turning the radome between $0^\circ - 90^\circ$ in the polar plane (described by θ) for each azimuthal turn (described by φ), where θ and φ are standard spherical coordinates, see Figure 3 for definitions and notational system. Measurements in the polar plane are continuously recorded at $1^\circ/\,\mathrm{s}$, whereas the measurements along the azimuthal plane are discrete and thereby more time consuming. The field is sampled every second degree in the azimuthal plane and every degree in the polar plane. A reduction of the sample density by a factor of two in the polar plane is not noticeable in the imaging results, indicating that the sample densities are satisfactory [12, 34]. Measuring one configuration, both polarizations, took approximately nine hours.

The measured far field for both the co- and cross-polarization and the three different configurations is given in Figure 4, for measurement series number three. The figure shows a cross section in the polar plane of the fields through the main lobe, and it is observed that the radome — conf. (1) — changes the far field. Attaching patches of dielectric tape in the form of the letters LU to the radome surface — conf. (2) — alters the field a little more, which is hardly visible in the figure. Moreover, the origin of the defects can hardly be determined from the far-field data alone. The far fields of the other two measurement series have similar appearance.

In the far-field measurements no probe compensation is necessary [34]. Moreover,

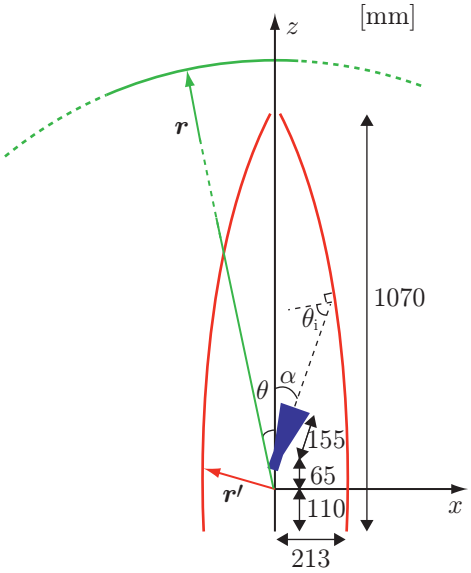

Figure 3: The geometry of the antenna, radome and far-field hemisphere. The center of rotation is located at the origin. The dominating polarization of the electric field on the antenna aperture is directed along the y-axis. The incline of the antenna is $\alpha = 22.3°$. An approximation of the incident angle is given by $\theta_i \approx 60°$. The far field is described in a spherical coordinate system with the polar angle θ.

in a compact range, where the radome and antenna is moved instead of the transmitting feed antenna, the off-set between the aperture of the antenna and the center of rotation causes a negligible amplitude change and a small phase shift during the measurement rotations. This can be corrected by probe compensation where the antenna aperture is mathematically translated to the center of rotation [12]. However, we have no interest in the absolute phase, only the phase difference between measurement configurations. This means that, as long as the set-up is rotated in the same way during all measurements, the off-set causes no problem. The far-field radius, r in Figure 3, is set to 1800 m. Larger radii give only negligible differences in the results.

The antenna is a pyramidal X-band horn antenna. The square aperture is $8 \times 8\,\mathrm{cm}^2$. The antenna is mounted at an angle $\alpha = 22.3°$, and it has a dominating electric field component in the y-direction, see Figure 3. The feed in the chamber is a linearly polarized standard X-band feed. The feed is turned 90° in order to measure both polarizations.

The radome is monolithic (solid) and covered with a thin layer of varnish. The dielectric material of the bulk has a relative permittivity of 4.32 and a loss tangent of 0.0144. The varnish has a, to us unknown, higher relative permittivity. The thickness of the radome wall varies between $7.6 - 8.2$ mm. The geometry is shown in Figure 3, and the height of the radome corresponds to 36 wavelengths at 10 GHz. In the investigations, patches of dielectric tape (Scotch Glass Cloth Electrical Tape 69-1") are attached to the radome. Waveguide measurements of the relative permittivity of the tape at Saab Dynamics, Linköping, Sweden, gave a value of $\epsilon_r \approx 4.1$

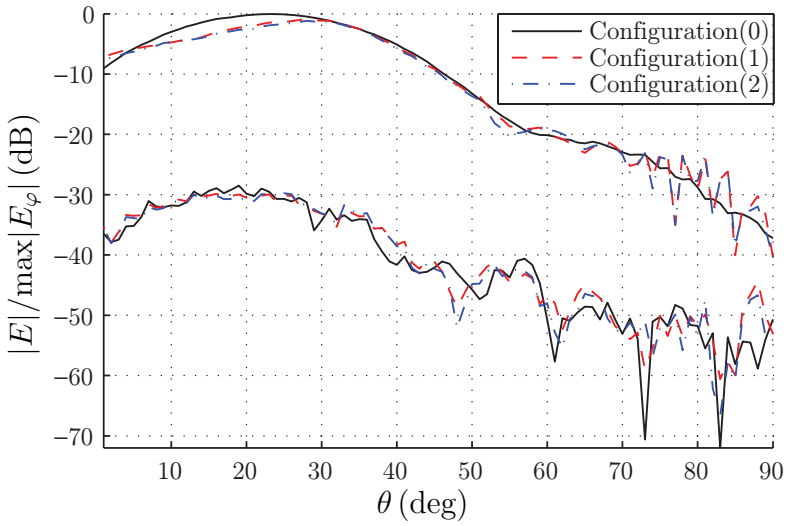

Figure 4: Co- and cross-polarization of the measured far field at 10.0 GHz through the main lobe ($\varphi = 0$). The top three lines correspond to the three different configurations of the co-polarization, $E = E_\varphi$, and the three lower ones to the cross-polarization, $E = E_\theta$, respectively. In conf. (2) the radome has dielectric letters LU attached to its surface, see Figure 1. All values are normalized to the maximum value of the co-polarization when only the antenna is present (conf. (0)).

assuming the thickness of one layer to be approximately 0.15 mm. The losses of the tape are assumed negligible.

2.2 IPD and visualization options

In performance evaluations of radomes, the phase shift of the electromagnetic field, due to the passage through the radome wall, is important. This quantity is called the electrical thickness of the radome or the insertion phase delay (IPD), and it relates the phase shift in the radome wall to the phase shift in free space [4]. For a plane wave applies

$$\mathrm{IPD} = \angle T - \frac{\omega}{\mathrm{c}_0} d \cos\theta_\mathrm{i} \tag{2.1}$$

where T is the complex transmission coefficient, which depends on the incidence angle, the parameters of the radome wall, and the polarization of the electromagnetic field [4]. The last term of (2.1) removes the phase shift of free space, where ω is the angular frequency, c_0 is the speed of light in free space, d is the thickness of the radome wall, and θ_i is the incident angle of the plane wave. In this paper, we consider reconstructed phase differences to visualize the IPD. In Section 4, the phase change of one field component, due to the radome, the defects, or both, is imaged.

The phase change, due to the attached dielectric patches, is reconstructed in Section 4. To verify the results, an approximate value of the phase change, due to one layer tape, is calculated. Thus, under the assumption of negligible reflections

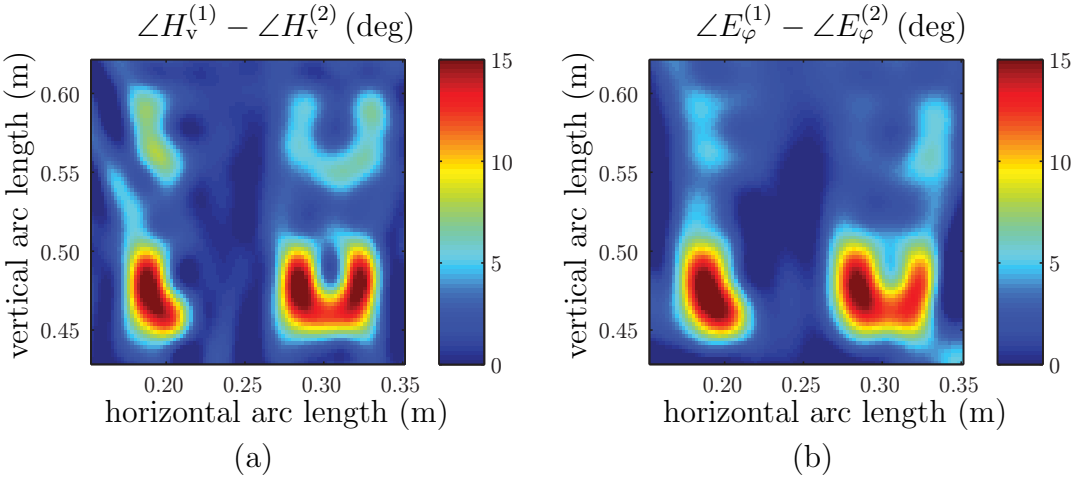

Figure 5: The reconstructed phase differences between conf. (1) and conf. (2). In conf. (2), dielectric patches in form of the letters LU are attached to the surface. The horizontal arc length corresponds to the center value of the height viewed on the y-axis, and this definition is utilized throughout the paper. a) The magnetic component H_{v}. b) The electric component E_{φ}.

and a homogeneous dielectric patch, the IPD can be expressed as [4]

$$\mathrm{IPD} = \frac{\omega}{\mathrm{c}_0}\left\{\mathrm{Re}\,\sqrt{\epsilon_{\mathrm{r}}(1-\mathrm{j}\tan\delta)}\cos\theta_{\mathrm{t}} - \cos\theta_{\mathrm{i}}\right\}d_{\mathrm{p}} \tag{2.2}$$

for both polarizations. The relative permittivity of the tape is $\epsilon_{\mathrm{r}} \approx 4.1$, the loss tangent $(\tan\delta)$ is negligible, the thickness of one layer tape is $d_{\mathrm{p}} \approx 0.15\,\mathrm{mm}$, and the transmission angle of the field is denoted θ_{t}. Assuming the incident angle to be in the interval $[40°, 80°]$, see Figure 3, gives an approximate phase shift of $2° - 3°$, per layer.

For large homogeneous slabs, the phase difference is the same for both the electric and the magnetic fields. However, a difference occurs when small patches of dielectric material are attached to the surface of the radome. In our investigations we conclude that the magnetic field gives the best image of phase defects, see Figure 5. As a consequence, this component is the one imaged in Section 4. In Figure 5a, the phase change, due to the dielectric letters LU, is visualized for the magnetic field component H_{v}, whereas the same phase difference is showed in Figure 5b for the electric field component E_{φ}. A qualified explanation of this difference is obtained by considering the induced current $\boldsymbol{J}_{\chi_{\mathrm{e}}} = \mathrm{j}\epsilon_0\chi_{\mathrm{e}}\omega\boldsymbol{E}^{(2)}$, see Appendix A for details. If the induced current is of electric nature, the electric field dominates in the near-field region, whereas the magnetic field is smoother [14]. A plausible assumption is that the induced charges in the dielectric give rise to dominating irrotational currents (electric charges) instead of solenoidal currents (loop currents). Hence, it is conjectured that this extra contribution to the electric near field, due to the defects, makes the defects appear less clear.

To further investigate the near fields, we have simulated the transmission using the software CST Microwave Studio, see Figure 6. An electric field polarized in the x-direction, propagating along the z-axis, illuminates the dielectric letter L located

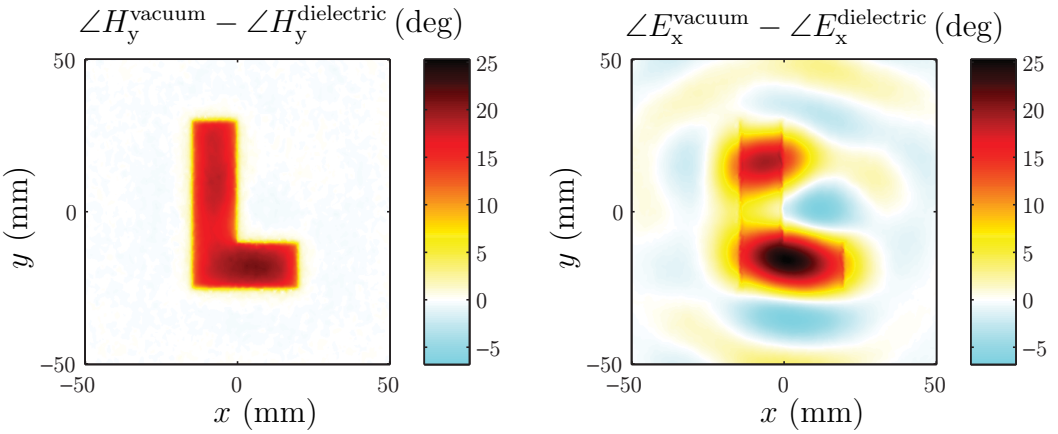

Figure 6: The phase differences simulated in CST. The incoming electric field is polarized in the $x-$direction. a) Magnetic component H_{y}. b) Electric component E_{x}.

in free space. The dielectric patch is 0.9 mm thick and has an relative permittivity of 4.32. The surrounding box of vacuum has the dimensions $100 \times 100 \times 60\,\mathrm{mm}^3$. In Figure 6, the field differences are visualized 0.02 mm above the dielectric, *i.e.*, $z = 0.92\,\mathrm{mm}$. The phase of the magnetic component H_{y} gives clearly a sharper image of the dielectric than the electric component E_{x}. Simulations with an electric field polarized in the y-direction give similar results, *i.e.*, E_{y} is less distinct than H_{x}.

3 Reconstruction algorithm

To localize the defective areas on the radome, we have utilized a surface integral representation to relate the equivalent surface currents on the radome surface to the measured far field [5, 30]. In addition, an electric surface integral equation is applied to ensure that the sources are located inside the radome [5, 30].

A surface integral representation expresses the electric field in a homogeneous and isotropic region in terms of the tangential electromagnetic fields on the bounding surface. In our case, the bounding surface, S_{radome}, is a fictitious surface, located just outside the physical radome wall, with smoothly capped top and bottom surfaces to form a closed surface. This fictitious surface is located in free space, but for convenience, it is referred to as the radome surface throughout the paper. Combining the source-free Maxwell equations and vector identities gives a surface integral

representation of the electric field [23, 30]

$$\iint\limits_{S_{\text{radome}}} \Big(-\mathrm{j}k\eta_0 \; g(\boldsymbol{r}', \boldsymbol{r}) \big[\hat{\boldsymbol{n}}(\boldsymbol{r}') \times \boldsymbol{H}(\boldsymbol{r}')\big] - \frac{\eta_0}{\mathrm{j}k} \; \nabla' g(\boldsymbol{r}', \boldsymbol{r}) \Big\{ \nabla'_S \cdot \big[\hat{\boldsymbol{n}}(\boldsymbol{r}') \times \boldsymbol{H}(\boldsymbol{r}')\big] \Big\} \\ - \nabla' g(\boldsymbol{r}', \boldsymbol{r}) \times \big[\hat{\boldsymbol{n}}(\boldsymbol{r}') \times \boldsymbol{E}(\boldsymbol{r}')\big] \Big) \, \mathrm{d}S' = \begin{cases} \boldsymbol{E}(\boldsymbol{r}) & \boldsymbol{r} \text{ outside } S_{\text{radome}} \\ \boldsymbol{0} & \boldsymbol{r} \text{ inside } S_{\text{radome}} \end{cases} \tag{3.1}$$

for the exterior problem where all the sources are located inside S_{radome}. The used time convention is $\mathrm{e}^{\mathrm{j}\omega t}$, ω is the angular frequency, and η_0 is the intrinsic wave impedance of free space. The surface divergence is denoted $\nabla_S \cdot$ [6], the unit normal $\hat{\boldsymbol{n}}$ points outward, and the scalar free-space Green's function is $g(\boldsymbol{r}', \boldsymbol{r}) = \frac{\mathrm{e}^{-\mathrm{j}k|\boldsymbol{r}-\boldsymbol{r}'|}}{4\pi|\boldsymbol{r}-\boldsymbol{r}'|}$, where the wave number is $k = \omega/\mathrm{c}_0$ and c_0 is the speed of light in free space. The representation (3.1) states that if the electromagnetic field on a bounding surface is known, the electromagnetic field in the volume, outside of S_{radome}, can be determined [30]. If these integrals are evaluated at a point $\boldsymbol{r}$ lying in the volume enclosed by S_{radome}, these integrals cancel each other (extinction).

The representation (3.1) consists of three components, two tangential fields and one normal component of the field. Since the normal component can be determined by the knowledge of the tangential parts, this representation contains redundancies. As a consequence, specifying only the tangential components suffice [23]. The measured far field consists of two orthogonal components, $\hat{\boldsymbol{\varphi}}$ (azimuth) and $\hat{\boldsymbol{\theta}}$ (polar). The tangential fields on the radome surface are decomposed into two tangential components along the horizontal, $\hat{\boldsymbol{\varphi}}$, and vertical, $\hat{\boldsymbol{v}}$, arc lengths coordinates, see Figure 1. The lower representation in (3.1) is transformed into a surface integral equation letting $\boldsymbol{r}$ approach S_{radome} from the inside [6, 30]. To simplify, the operators $\mathcal{L}$ and $\mathcal{K}$ are introduced as [15]

$$\begin{cases} \mathcal{L}(\boldsymbol{X})(\boldsymbol{r}) = \mathrm{j}k \iint\limits_{S_{\text{radome}}} \Big\{ g(\boldsymbol{r}', \boldsymbol{r}) \boldsymbol{X}(\boldsymbol{r}') - \frac{1}{k^2} \; \nabla' g(\boldsymbol{r}', \boldsymbol{r}) \big[\nabla'_S \cdot \boldsymbol{X}(\boldsymbol{r}')\big] \Big\} \, \mathrm{d}S' \\ \mathcal{K}(\boldsymbol{X})(\boldsymbol{r}) = \iint\limits_{S_{\text{radome}}} \nabla' g(\boldsymbol{r}', \boldsymbol{r}) \times \boldsymbol{X}(\boldsymbol{r}') \, \mathrm{d}S' \end{cases} \tag{3.2}$$

In this notation the surface integral representation and the surface integral equation for the electric field (EFIE) yield

$$\begin{bmatrix} \hat{\boldsymbol{\theta}}(\boldsymbol{r}) \\ \hat{\boldsymbol{\varphi}}(\boldsymbol{r}) \end{bmatrix} \cdot \Big\{ -\mathcal{L}\left(\eta_0 \boldsymbol{J}\right)(\boldsymbol{r}) + \mathcal{K}\left(\boldsymbol{M}\right)(\boldsymbol{r}) \Big\} = \begin{bmatrix} \hat{\boldsymbol{\theta}}(\boldsymbol{r}) \cdot \boldsymbol{E}(\boldsymbol{r}) \\ \hat{\boldsymbol{\varphi}}(\boldsymbol{r}) \cdot \boldsymbol{E}(\boldsymbol{r}) \end{bmatrix} \qquad \boldsymbol{r} \in S_{\text{meas}} \tag{3.3}$$

$$\hat{\boldsymbol{n}}(\boldsymbol{r}) \times \Big\{ \mathcal{L}\left(\eta_0 \boldsymbol{J}\right)(\boldsymbol{r}) - \mathcal{K}\left(\boldsymbol{M}\right)(\boldsymbol{r}) \Big\} = \frac{1}{2} \boldsymbol{M}(\boldsymbol{r}) \qquad \boldsymbol{r} \in S_{\text{radome}} \tag{3.4}$$

where S_{meas} is the set of discrete sample points (*cf.*, Figure 3), and S_{radome} is the fictitious surface located precisely outside the physical radome wall with a smoothly

capped top and bottom. In a similar manner, a surface integral equation of the magnetic field (MFIE) can be derived,

$$\hat{\boldsymbol{n}}(\boldsymbol{r}) \times \left\{ \mathcal{L}\left(\boldsymbol{M}\right)(\boldsymbol{r}) + \mathcal{K}\left(\eta_0 \boldsymbol{J}\right)(\boldsymbol{r}) \right\} = -\frac{\eta_0}{2}\boldsymbol{J}(\boldsymbol{r}) \qquad \boldsymbol{r} \in S_{\text{radome}} \tag{3.5}$$

In (3.3)–(3.5) we have introduced the equivalent surface currents on the radome surface, $\boldsymbol{J} = \hat{\boldsymbol{n}} \times \boldsymbol{H}$ and $\boldsymbol{M} = -\hat{\boldsymbol{n}} \times \boldsymbol{E}$ [15]. As mentioned above, the tangential fields on the radome surface are decomposed into two components along the horizontal and vertical arc lengths coordinates of the surface, that is $[\hat{\boldsymbol{\varphi}}, \hat{\boldsymbol{v}}, \hat{\boldsymbol{n}}]$ forms a right-handed coordinate system. Throughout the paper we use the notations, $H_{\text{v}} = \boldsymbol{H} \cdot \hat{\boldsymbol{v}} = -J_{\varphi}$, $H_{\varphi} = \boldsymbol{H} \cdot \hat{\boldsymbol{\varphi}} = J_{\text{v}}$, $E_{\text{v}} = \boldsymbol{E} \cdot \hat{\boldsymbol{v}} = M_{\varphi}$, and $E_{\varphi} = \boldsymbol{E} \cdot \hat{\boldsymbol{\varphi}} = -M_{\text{v}}$ for the reconstructed tangential electromagnetic fields.

The representation (3.3) can be used together with EFIE (3.4), MFIE (3.5), or a combination of both (CFIE), to avoid internal resonances [3, 5]. We have solved the problem by using both EFIE and MFIE separately together with the representation. The results do not differ significantly from each other. As a consequence, there are no problems with internal resonances for the employed set-up and choice of operators, since the internal resonance frequencies of EFIE and MFIE differ [3]. In Section 4, the results using (3.3) together with (3.4) are visualized.

The surface integral equations are written in their weak forms, *i.e.*, they are multiplied with a test function and integrated over their domain [3, 19]. The set-up, see Figure 3, is axially symmetric. Consequently, a Fourier expansion reduces the problem by one dimension [22]. Only the Fourier components of the fields with Fourier index $m = [-40, 40]$ are relevant, since the amplitudes of the field differences of higher modes are below $-60\,\text{dB}$, for all measurement series and configurations. Convergence studies show that this choice is sufficient.

The system of equations in (3.3)–(3.5) is solved by a body of revolution method of moments (MoM) code [2, 22]. The evaluation of the Green's functions is based on [11]. The basis function in the $\hat{\boldsymbol{\varphi}}$-direction consists of a piecewise constant function, and a global function, a Fourier basis, of coordinate φ. Moreover, the basis function in the $\hat{\boldsymbol{v}}$-direction consists of a piecewise linear function, 1D rooftop, of the coordinate v, and the same global function as the basis function in the $\hat{\boldsymbol{\varphi}}$-direction, see Figure 1 for notation. Test functions are chosen according to Galerkin's method [3], and the height (arc length) is uniformly discredited in steps of $\lambda/12$. The surface is described by a second order approximation.The in-house MoM code is verified by scattering of perfect electric conductors (PEC) and dielectric spheres [32].

The problem is regularized by a singular value decomposition (SVD), where the influence of small singular values is reduced [13]. A reference measurement series is performed to set the regularizing parameter used in the subsequent series, see Section 4.1. The inversion of the matrix system is verified using synthetic data. Moreover, the results, which localize the given defects, serve as good verifications.

The described method are applied in [24–26], to reconstruct equivalent surface currents from a measured near field. A slightly different approach is found in [16, 17]. Specifically, the surface integral representation, the EFIE, and the MFIE are solved utilizing higher order bases functions in a MoM solver with a Tikhonov regularization. In [8, 27, 28], the EFIE and MFIE are evaluated on a surface located inside the

surface of reconstruction, and the matrix system is solved by an iterative conjugate-gradient solver. Yet another approach is given in [1, 20, 21], where a surface integral representation is employed together with a conjugate-gradient solver as well as a singular value decomposition. In [7] the authors make use of dyadic Green's functions.

4 Reconstruction results

Three different configurations are investigated at 10 GHz; (0) antenna, (1) antenna together with the radome, and (2) antenna together with the radome where patches of metal or dielectric material are attached to the surface, see Figure 1. The field is measured in the far-field region, as described in Section 2.1. The equivalent surface currents, both amplitude and phase, are reconstructed on a fictitious surface shaped as the radome. Observe, even in the case when only the antenna is present — conf. (0) — the field is reconstructed on a radome shaped surface.

The magnetic component, H_v, is analyzed in this section, since it gives the sharpest image of the phase shifts (*cf.*, the discussion in Section 2.2). Moreover, the components H_φ and E_v are small cross-polarization terms, and a pronounced influence of the phase shift due to a thin dielectric patch of tape are not visible in these components. For this reason, these components are not investigated. The notation used in visualizing the phase difference between the fields from *e.g.*, conf. (1) and (2), is $\angle H_\mathrm{v}^{(1)} - \angle H_\mathrm{v}^{(2)} = \frac{180}{\pi} \angle \left\{ H_\mathrm{v}^{(1)} [H_\mathrm{v}^{(2)}]^* \right\}$, where the star denotes the complex conjugate. The employed time convention, $\mathrm{e}^{\mathrm{j}\omega t}$, gives a negative phase shift, indicating that $\angle H_\mathrm{v}^{(1)} - \angle H_\mathrm{v}^{(2)} > 0^\circ$.

4.1 Reference measurement

First, a measurement series is conducted where copper plates are attached to the radome surface in conf. (2). The imaging results agree well with the ones presented in [24–26], where near-field measurements are utilized, and these results are not further investigated in this paper. However, this first measurement series acts as a reference measurement and sets the regularization parameter of the SVD used in the subsequent measurement series. Typical graphs of the singular values are shown in Figure 7. Each curve shows the singular value for the operator with Fourier index m, normalized to the largest singular value ($i = 1$) for $m = 0$. As $|m|$ increases, the "knee" of the graph, where the singular values start to rapidly decrease, appears more quickly. The regularization parameter is chosen where the "knee" bends. Investigations have shown that the chosen value is robust for a given set-up and frequency. Furthermore, the results are not significantly altered if a slightly different value is employed. The interval Δ in Figure 7 indicates where the regularization parameter gives a reliable outcome. The regularization parameter is set to -29.8 dB, and this parameter is then utilized in the processing of the succeeding measurement series.

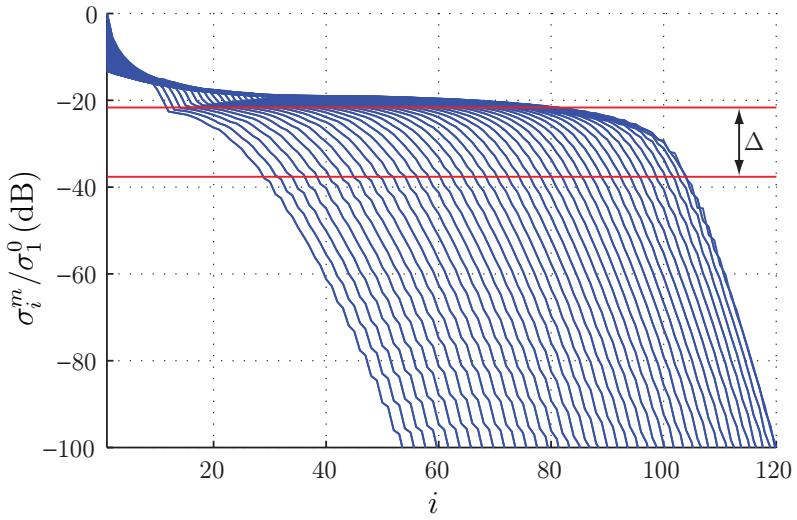

Figure 7: Singular values σ_i^m. Each curve depicts different Fourier index m, and the curves are normalized to the largest singular value for $m = 0$. The interval, Δ, where the regularization parameter gives a reliable outcome, is drawn.

4.2 Imaging of dielectric material

Obtaining a constant phase shift over the illuminated area is often important to trim radomes. The trimming is achieved by adding or removing dielectric material to the radome surface. To investigate if the proposed method can be utilized to map areas of the radome surface with a deviating electrical thickness, patches of dielectric material (defects), are attached to the radome surface in conf. (2). Defects of dielectric material mainly affect the phase of the field, and the phase differences of the fields for the different configurations give us an understanding of how the defects delay the fields.

Measurement series number two and three are employed. In each series the field from the antenna (conf. (0)), the antenna together with the radome (conf. (1)), and the antenna together with the radome where dielectric patches are attached to the surface (conf. (2)), was measured, *cf.*, Figure 1. In the second measurement series, squares are added to the area where the main lobe illuminates the radome, see Figure 8a, where the size and the thickness of the patches are shown. In the third measurement series, the letters LU are attached to the radome, see Figure 8b.

4.2.1 Dielectric squares

Eleven dielectric squares of the sizes 0.5λ, 1λ, and 2λ are added to the radome surface in conf. (2), see Figures 8a and 9. In Figure 9b, the illumination of the area of conf. (1), to which the dielectric squares will be applied to create one case of conf. (2), is shown. The largest squares are located in a field region of $[-23, -6]$ dB, the middle sized in the region $[-12, 0.3]$ dB and the smallest ones in $[-9, 0.3]$ dB, respectively. In Figures 9c and 10, the reconstructed phase shifts due to the defects, $\angle H_{\mathrm{v}}^{(1)} - \angle H_{\mathrm{v}}^{(2)}$, are visualized. The squares of size 2λ are clearly visible even though

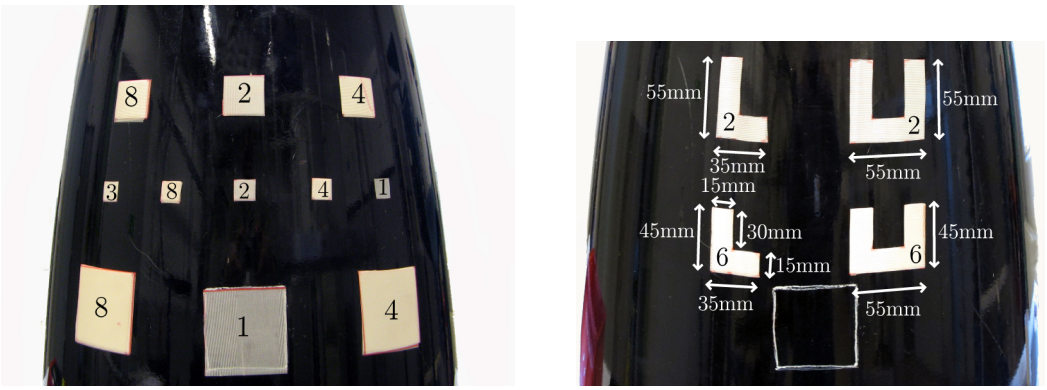

(a) (b)

Figure 8: The dielectric defects attached to the radome in conf. (2) — measurement series number two and three, respectively. The numbers on the patches indicate the number of tape layers. a) The size of the squares are; $30 \times 30\,\mathrm{mm}^2$ on the top row, $15 \times 15\,\mathrm{mm}^2$ on the middle row, and $60 \times 60\,\mathrm{mm}^2$ on the bottom row. b) Each "leg" has a width of 15 mm. The drawn square indicates where the centered lower square in the left figure was located.

they are partly located in areas with lower illumination. The ones of size 1λ are also easily found. The defects of size 0.5λ with thickness of four and eight layers are also clearly visible, even though the phase shift is not as conspicuous here. The thinner, small squares tend to blend into the background phase deviation.The rounded corners are due to the limited resolution. According to (2.2), each layer gives rise to a phase shift of approximately $2° - 3°$. To get an estimate of the phase shift due to the added squares, an average value is calculated over the areas indicated in Figure 9b. These areas are drawn according to the given coordinates of the squares, *i.e.*, their positions are not approximated from the reconstruction. The average values of the phase shifts are given in Table 1 and they agree very well for the larger squares.

	1 layer	2 layers	3 layers	4 layers	8 layers
0.5λ	$2°$	$3°$	$4°$	$5°$	$10°$
1λ		$6°$		$12°$	$22°$
2λ	$2°$			$10°$	$19°$
Phase shift due to (2.2)	$2° - 3°$	$4° - 6°$	$6° - 9°$	$8° - 12°$	$16° - 24°$

Table 1: The average phase shift due to the dielectric squares. The bottom row gives an approximate theoretical calculation, based on (2.2).

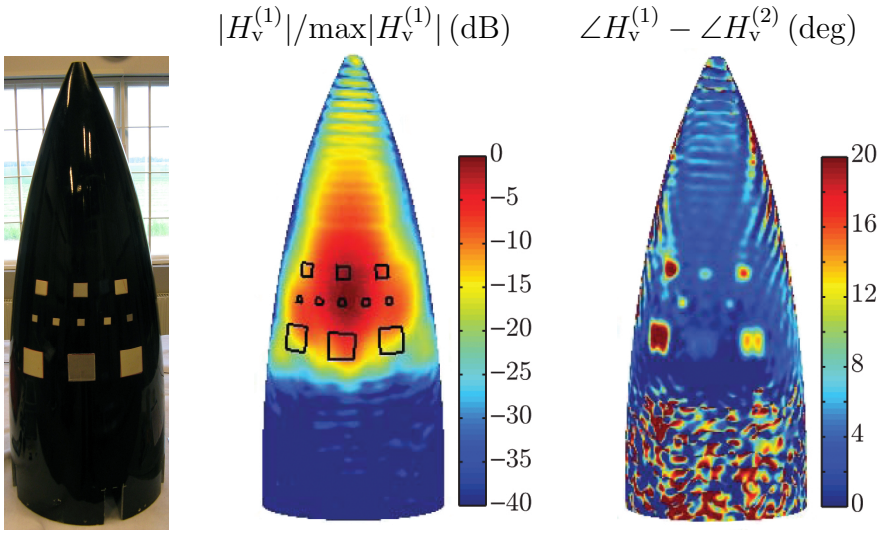

(a) (b) (c)

Figure 9: a) A photo of the radome with the dielectric squares (defects). b) The reconstructed field, H_{v}, on the radome — conf. (1). The drawn squares indicate where the defects will be located to create conf. (2). c) The phase of the reconstructed field difference between conf. (1) and (2).

4.2.2 Dielectric letters LU

In the third measurement series, defects of dielectric tape in the form of the letters LU, are investigated, see Figures 8b and 11. The thickness of the tape is six layers for the lower LU and two layers for the top one. The illumination of the area of conf. (1), to which the dielectric letters will be applied to create one case of conf. (2), is shown in Figure 11b. The ranges of the field within the defects are, from the top left to the bottom right; $[-8, -4]$ dB, $[-5, 0.3]$ dB, $[-8, -6]$ dB, and $[-9, -1]$ dB, respectively. In Figures 11c and 12a, the reconstructed phase shifts due to the defects, $\angle H_{\mathrm{v}}^{(1)} - \angle H_{\mathrm{v}}^{(2)}$, are visualized. All letters are clearly visible in the reconstruction. As stated above, each layer of tape shifts the phase by approximately $2° - 3°$. This agrees very well with the results given in Figure 12b, where the line plots reveal how the phase difference changes due to the dielectric letters. The defects on the bottom have a maximum deviation of about 16° and the top ones circa 6°.

4.2.3 Differences with the antenna as a reference

In the previous sections, we have looked at phase differences between the radome with attached defects and the radome itself, *i.e.*, the differences between conf. (1) and (2). This has given an estimate of how well phase objects can be reconstructed. In practice, it is advantageous to visualize the influence of the non-optimized radome. In our measurements, this corresponds to the difference between conf. (0) and conf. (1) or (2). The reconstructed phase shift over the illuminated area can act as a trimming mask, indicating areas where a thickness alteration is required, in

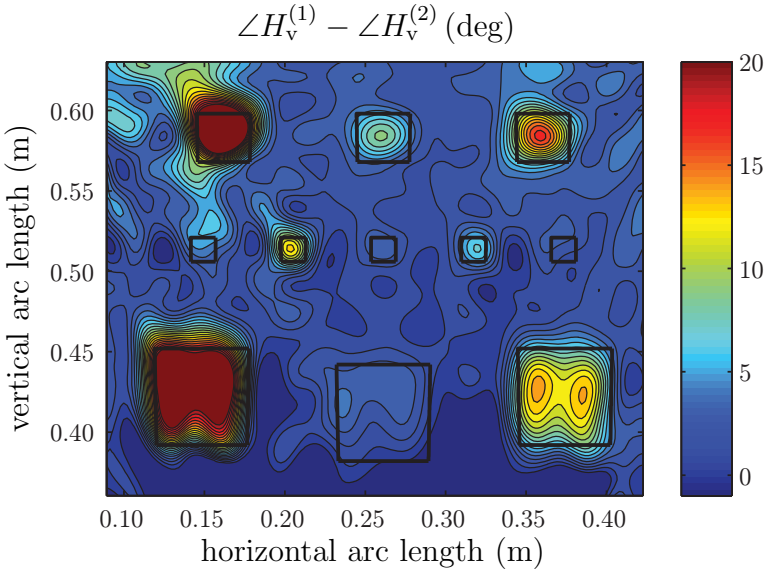

Figure 10: Enlarged view of the area with the dielectric squares in Figure 9c. The phase of the reconstructed field difference between conf. (1) and (2) is depicted. Each contour line represents one degree. The drawn squares indicate the given coordinates, *i.e.*, their positions are not approximated from the reconstruction.

order to get the phase shift into a pre-defined interval.

The influence of the radome in the main lobe, $\angle H_{\mathrm{v}}^{(0)} - \angle H_{\mathrm{v}}^{(1)}$, is visualized for the second measurement series in Figure 13a. The same difference ($\angle H_{\mathrm{v}}^{(0)} - \angle H_{\mathrm{v}}^{(1)}$) is shown in Figure 14a for the third measurement series, and it becomes clear that there is a small deviation between the conf. (0) and (1) between measurement series. Instead of a desired constant phase shift in the main lobe, Figures 13a and 14a indicate a phase shift of $115° \pm 10°$, implying that the radome surface needs to be trimmed. The drawn squares and letters, in the figures, point out where the defects are to be located to create conf. (2).

In Figures 13b and 14b, the phase difference in the main lobe between conf. (0) and conf. (2) ($\angle H_{\mathrm{v}}^{(0)} - \angle H_{\mathrm{v}}^{(2)}$) is shown for the dielectric squares and letters LU. The phase shift introduced by the dielectric patches in conf. (2) is now added to the phase shift caused by the radome itself. The upper squares in Figure 13b are mainly located in areas where the phase shift due to the radome itself is already large, therefore these squares are clearly seen. The lower ones, to the left and right, are thick enough to give rise to a visible phase shift by themselves. The square in the middle on the bottom row is only one layer thick and located in a region with a low phase shift to start with, and it cannot be resolved in the dynamic range showed. Most parts of the letters LU are seen in the reconstructed images, see Figure 14b. However, the left "legs" of the U:s are not as visible. The reason is that these parts are attached to an area, where an added patch (with the appropriate thickness) increases the phase shift to the level of the surrounding areas, and it is thereby not localized by itself.

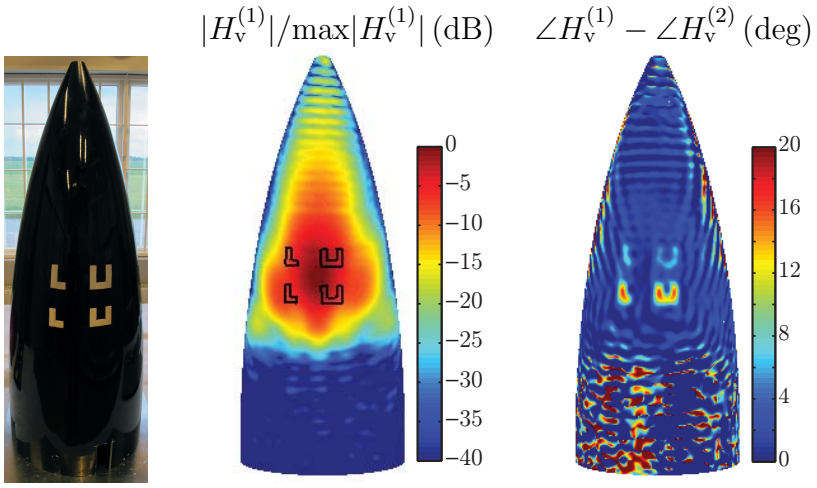

(a) (b) (c)

Figure 11: a) A photo of the radome with the attached dielectric letters LU (defects). b) The reconstructed field, H_{v}, on the radome — conf. (1). The drawn lines indicate where the letters will be located to create conf. (2). c) The phase of the reconstructed field difference between conf. (1) and (2).

4.2.4 Trimband

A horizontal band in the phase images is discovered during the investigations, see Figure 15. Visual inspection reveals a small indentation on the inside of the radome wall, originating from an earlier attempt to trim the radome. The indentation starts at the approximate height 0.6 m (arc length) with a width of 0.1 m. In Figure 15a, the reconstructed field from the antenna (conf. (0)), projected on the radome surface, is shown, to visualize the illumination. The black lines indicate where the band is located. The phase deviation between the band and the surrounding areas is approximately $-15°$ to $-10°$, see Figure 15b.

To verify the phase deviation, the phase deviation is related to a wall thickness by employing the approximate formula in (2.2). The utilized material parameters are $\epsilon_{\mathrm{r}} \approx 4.32$ and $\tan\delta \approx 0.0144$ (*cf.*, Section 2.1). Estimating the angle of incidence to 60°, see Figure 3, results in a wall thickness of $0.6 - 0.9$ mm. This approximated value agrees well with the actual indentation on the radome. The phase differences, at the top and the bottom of the radome in Figure 15b are not reliable due to low illumination.

5 Conclusions and discussions

Techniques to diagnose radomes are requested in *e.g.*, performance verifications. In [24–26], the influence of copper plates, *e.g.*, amplitude reduction and appearance of flash (image) lobes, are investigated together with the localization of the defect areas on the radome surface. In this paper, we investigate how reconstructed equivalent surface currents from a measured far field can assist in localizing phase defects on a radome. The phase defects introduce a hardly noticeable change in the far-field

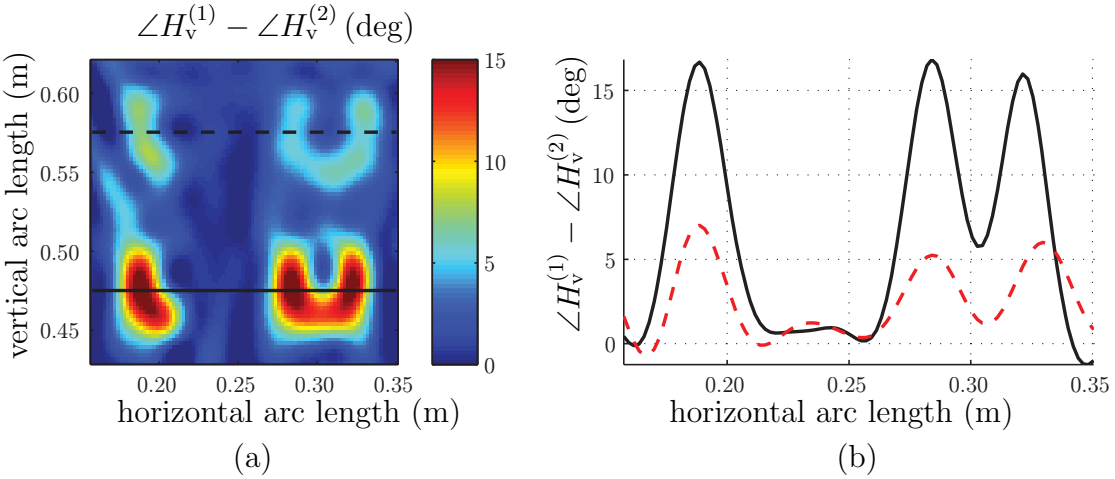

Figure 12: a) Enlarged view of the area with the dielectric letters in Figure 11c. The phase of the reconstructed field difference between conf. (1) and (2) is depicted. b) Line plot through the letters showing the phase deviations. The solid line in the left image corresponds to the solid line in the right plot *etc.*

pattern. However, by visualizing the insertion phase delay (IPD) in the illuminated area of the radome, the locations of the defects are revealed.

Dielectric squares of size 2λ — one layer thick, squares of size 1λ — two layer thick, and squares of size 0.5λ — 4 layer thick, are clearly visible in the reconstructed phase differences. One layer tape corresponds to a phase shift of a couple degrees. Furthermore, the dielectric tapes of two layers and the smallest dimension of 0.5λ in the form of the letters LU are resolved. The phase shifts of the larger squares and the letters coincide well with the approximated theoretical ones. The radiance at the upper left corner of the lower dielectric L, see *e.g.*, Figure 12a, needs to be investigated further. Possible explanations might be constructive and destructive interference due to edge effects, noise influence, or a combination thereof. Analyzes of other field components might explain this phenomenon. Future studies will address the questions of how to combine the components to increase the resolution.

Reconstructing the fields on the radome surface, the magnetic field gives sharper images than the electric field. A qualified explanation is that the induced currents on the attached patches are of electric nature. This effect is also verified by simulations in CST Microwave Studio.

The results indicate that the diagnostics method, beyond what is proposed in [24–26], can be used in constructing a trimming mask for the illuminated areas of a radome. The mask gives instructions of how to alter the radome surface, in order to change the IPD, side and flash (image) lobes, to their preferable values. To indicate how this can be implemented, we have explored the phase influence of the radome itself, and then the radome with attached patches of dielectric tape. Even if the main purpose of this paper is not to suggest how to trim the radome, we observe that adding dielectric patches gives a smoother phase shift in areas where the phase shift due to the radome itself is smaller than in the surrounding areas. In an upcoming paper, these images and their potential to alter the IPD and flash (image) lobes will be addressed.

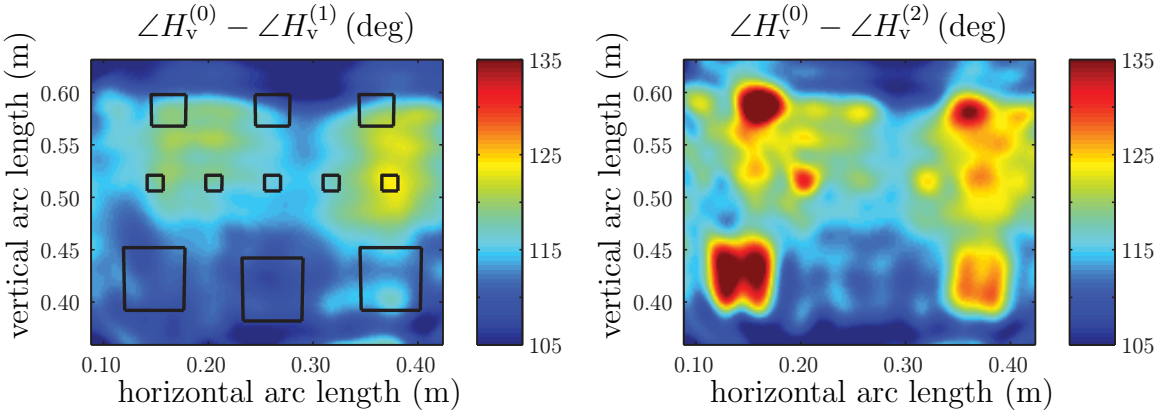

Figure 13: Enlarged view of the area illuminated by the main lobe. Phase differences reconstructed from measurement series number two. a) Phase changes due to the radome. The drawn squares indicate where the dielectric patches will be located to create conf. (2). b) Phase changes due to the radome together with the dielectric squares.

Acknowledgement

The measurements were carried out at GKN Aerospace Applied Composites' far-field facilities in Linköping, Sweden. Michael Andersson, GKN Aerospace Applied Composites, Ljungby, Sweden, has been instrumental in questions regarding radome development, measurements and manufacturing. His help has been highly appreciated. We are also grateful to Christer Larsson at Saab Dynamics, Linköping, Sweden, who did measurements on the relative permittivity of the dielectric tape. The research reported in this paper is carried out under the auspices of FMV (Försvarets materielverk) and their support is gratefully acknowledged.

Appendix A Induced currents due to dielectrics

A dielectric material introduces induced currents in the Maxwell equations. To see this, start with the Maxwell equations for time harmonic fields in a source free region (time convention $\mathrm{e}^{\mathrm{j}\omega t}$),

$$\begin{aligned} \nabla \times \boldsymbol{E} &= -\mathrm{j}\omega \boldsymbol{B} \\ \nabla \times \boldsymbol{H} &= \mathrm{j}\omega \boldsymbol{D} \end{aligned}$$

where $\boldsymbol{E}$ is the electric field, $\boldsymbol{B}$ is the magnetic flux density, $\boldsymbol{H}$ is the magnetic field, and $\boldsymbol{D}$ is the electric flux density, respectively. The constitutive relations read $\boldsymbol{D} = \epsilon_0 \epsilon_{\mathrm{r}} \boldsymbol{E}$ and $\boldsymbol{B} = \mu_0 \mu_{\mathrm{r}} \boldsymbol{H}$, where ϵ_0 is the permittivity of free space, ϵ_{r} is the relative permittivity, μ_0 is the permeability of free space, and μ_{r} is the relative permeability, respectively.

In the absence of defects, and outside the radome (conf. (1) in Figure 1) we have

$$\begin{aligned} \nabla \times \boldsymbol{E}^{(1)} &= -\mathrm{j}\mu_0 \omega \boldsymbol{H}^{(1)} \\ \nabla \times \boldsymbol{H}^{(1)} &= \mathrm{j}\epsilon_0 \omega \boldsymbol{E}^{(1)} \end{aligned}$$

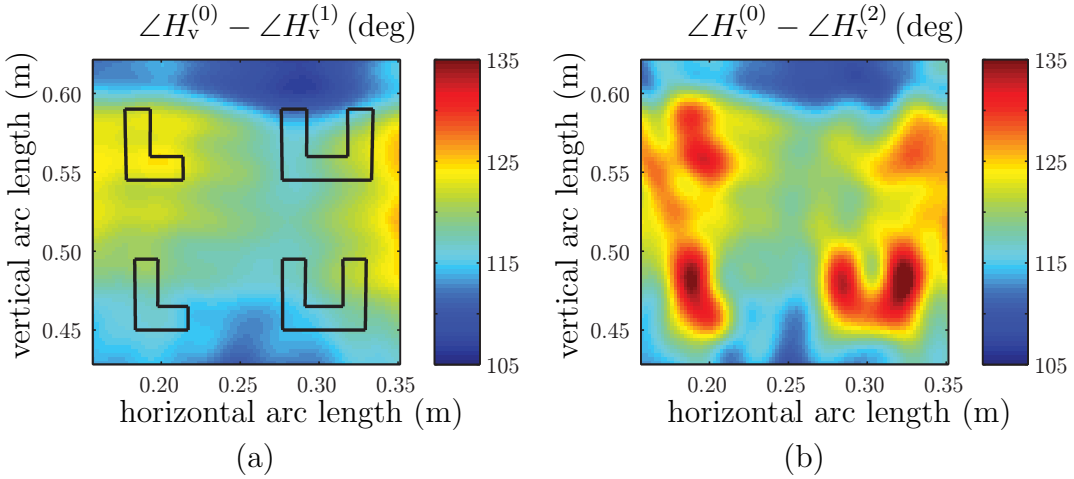

Figure 14: Enlarged view of the area illuminated by the main lobe. Phase differences reconstructed from measurement series number three. a) Phase changes due to the radome. The drawn lines indicate where the dielectric letters will be located to create conf. (2). b) Phase changes due to the radome together with the dielectric letters.

On the other hand, in the presence of a dielectric material (conf. (2)) the defects have an electric susceptibility $\chi_{\mathrm{e}} = \epsilon_{\mathrm{r}} - 1$, giving [14]

$$\begin{aligned} \nabla \times \boldsymbol{E}^{(2)} &= -\mathrm{j}\mu_0\omega\boldsymbol{H}^{(2)} \\ \nabla \times \boldsymbol{H}^{(2)} &= \mathrm{j}\epsilon_0\omega\boldsymbol{E}^{(2)} + \mathrm{j}\epsilon_0\chi_{\mathrm{e}}\omega\boldsymbol{E}^{(2)} \end{aligned}$$

The field differences $\boldsymbol{E} = \boldsymbol{E}^{(2)} - \boldsymbol{E}^{(1)}$ and $\boldsymbol{H} = \boldsymbol{H}^{(2)} - \boldsymbol{H}^{(1)}$ satisfy

$$\begin{aligned} \nabla \times \boldsymbol{E} &= -\mathrm{j}\mu_0\omega\boldsymbol{H} \\ \nabla \times \boldsymbol{H} &= \mathrm{j}\epsilon_0\omega\boldsymbol{E} + \boldsymbol{J}_{\chi_{\mathrm{e}}} \end{aligned}$$

where $\boldsymbol{J}_{\chi_{\mathrm{e}}} = \mathrm{j}\epsilon_0\chi_{\mathrm{e}}\omega\boldsymbol{E}^{(2)}$ is interpreted as the induced current.

References

[1] Y. Alvarez, F. Las-Heras, and C. Garciain. The sources reconstruction method for antenna diagnostics and imaging applications. In A. Kishk, editor, *Solutions and Applications of Scattering, Propagation, Radiation and Emission of Electromagnetic Waves*. InTech, 2012.

[2] M. Andreasen. Scattering from bodies of revolution. *IEEE Trans. Antennas Propagat.*, **13**(2), 303–310, 1965.

[3] A. Bondeson, T. Rylander, and P. Ingelström. *Computational Electromagnetics*. Springer-Verlag, Berlin, 2005.

[4] D. G. Burks. Radomes. In J. L. Volakis, editor, *Antenna engineering handbook*. pub-mcgraw, fourth edition, 2007.

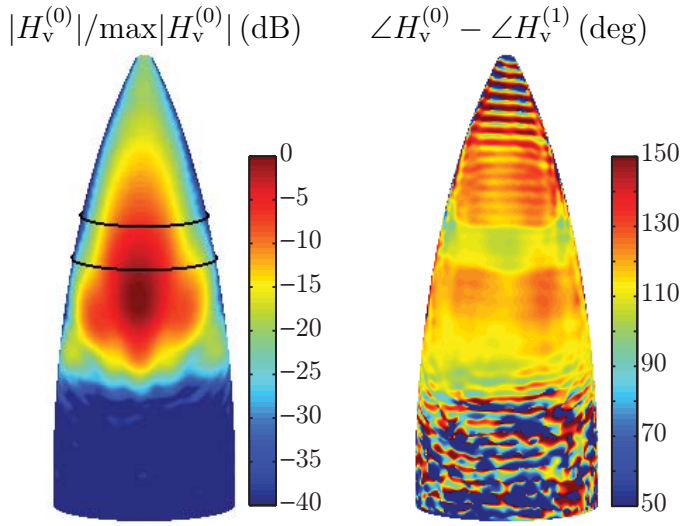

(a) (b)

Figure 15: Phase image of an earlier attempt to trim the radome. a) The illumination of the radome. The black lines indicate the location of the indentation. b) Phase change due to the radome.

[5] W. C. Chew, M. S. Tong, and B. Hu. *Integral equation methods for electromagnetic and elastic waves*, volume 12. Morgan & Claypool, 2008.

[6] D. Colton and R. Kress. *Integral Equation Methods in Scattering Theory*. John Wiley & Sons, New York, 1983.

[7] T. F. Eibert, E. Kaliyaperumal, and C. H. Schmidt. Inverse equivalent surface current method with hierarchical higher order basis functions, full probe correction and multilevel fast multipole acceleration. *Progress In Electromagnetics Research*, **106**, 377–394, 2010.

[8] L. J. Foged, L. Scialacqua, F. Saccardi, J. L. Araque Quijano, G. Vecchi, and M. Sabbadini. Practical application of the equivalent source method as an antenna diagnostics tool. *IEEE Antennas and Propagation Magazine*, **54**(5), 243–249, 2012.

[9] E. Gimonet, A. Sarremejean, J. P. David, and P. Bossuet. Determination of radome pertubation by inverse transform of radiation pattern. In *Proc. of 5th European Electromagnetic Windows Conference*, pages 183–190, Juan-les-Pins, France, 1989.

[10] M. G. Guler and E. B. Joy. High resolution spherical microwave holography. *IEEE Trans. Antennas Propagat.*, **43**(5), 464–472, 1995.

[11] M. Gustafsson. Accurate and efficient evaluation of modal Green's functions. *Journal of Electromagnetic Waves and Applications*, **24**(10), 1291–1301, 2010.

[12] J. E. Hansen, editor. *Spherical Near-Field Antenna Measurements*. Number 26 in IEE electromagnetic waves series. Peter Peregrinus Ltd., Stevenage, UK, 1988. ISBN: 0-86341-110-X.

[13] P. C. Hansen. *Discrete inverse problems: insight and algorithms*, volume 7. Society for Industrial & Applied, 2010.

[14] J. D. Jackson. *Classical Electrodynamics*. John Wiley & Sons, New York, third edition, 1999.

[15] J. M. Jin. *Theory and computation of electromagnetic fields*. Wiley Online Library, 2010.

[16] E. Jörgensen, D. W. Hess, P. Meincke, O. Borries, C. Cappellin, and J. Fordham. Antenna diagnostics on planar arrays using a 3D source reconstruction technique and spherical near-field measurements. In *Antennas and Propagation (EUCAP), Proceedings of the 6th European Conference on*, pages 2547–2550. IEEE, 2012.

[17] E. Jörgensen, P. Meincke, and C. Cappellin. Advanced processing of measured fields using field reconstruction techniques. In *Antennas and Propagation (EUCAP), Proceedings of the 5th European Conference on*, pages 3880–3884. IEEE, 2011.

[18] D. J. Kozakoff. *Analysis of Radome-Enclosed Antennas*. Artech House, Boston, London, 1997.

[19] R. Kress. *Linear Integral Equations*. Springer-Verlag, Berlin Heidelberg, second edition, 1999.

[20] Y. A. Lopez, F. Las-Heras Andres, M. R. Pino, and T. K. Sarkar. An improved super-resolution source reconstruction method. *Instrumentation and Measurement, IEEE Transactions on*, **58**(11), 3855–3866, 2009.

[21] J. A. Lopez-Fernandez, M. Lopez-Portugues, Y. Alvarez Lopez, C. G. Gonzalez, D. Martínez, and F. Las-Heras. Fast antenna characterization using the sources reconstruction method on graphics processors. *Progress In Electromagnetics Research*, **126**, 185–201, 2012.

[22] J. R. Mautz and R. F. Harrington. Radiation and scattering from bodies of revolution. *Appl. Scientific Research*, **20**(1), 405–435, 1969.

[23] C. Müller. *Foundations of the Mathematical Theory of Electromagnetic Waves*. Springer-Verlag, Berlin, 1969.

[24] K. Persson, M. Gustafsson, and G. Kristensson. Reconstruction and visualization of equivalent currents on a radome using an integral representation formulation. *Progress In Electromagnetics Research*, **20**, 65–90, 2010.

[25] K. Persson and M. Gustafsson. Reconstruction of equivalent currents using a near-field data transformation – with radome applications. *Progress in Electromagnetics Research*, **54**, 179–198, 2005.

[26] K. Persson and M. Gustafsson. Reconstruction of equivalent currents using the scalar surface integral representation. Technical Report LUTEDX/(TEAT-7131)/1–25/(2005), Lund University, Department of Electrical and Information Technology, P.O. Box 118, S-221 00 Lund, Sweden, 2005. `http://www.eit.lth.se`.

[27] J. L. A. Quijano, L. Scialacqua, J. Zackrisson, L. J. Foged, M. Sabbadini, and G. Vecchi. Suppression of undesired radiated fields based on equivalent currents reconstruction from measured data. *Antennas and Wireless Propagation Letters, IEEE*, **10**, 314–317, 2011.

[28] J. L. A. Quijano and G. Vecchi. Field and source equivalence in source reconstruction on 3D surfaces. *Progress In Electromagnetics Research*, **103**, 67–100, 2010.

[29] Z. Shengfang, G. Dongming, K. Renke, J. Zhenyuan, S. Aifeng, and J. Tian. Research on microwave and millimeter-wave IPD measurement system for radome. In *Microwave and Millimeter Wave Technology, 2004. ICMMT 4th International Conference on, Proceedings*, pages 711–714. IEEE, 2004.

[30] S. Ström. Introduction to integral representations and integral equations for time-harmonic acoustic, electromagnetic and elastodynamic wave fields. In V. V. Varadan, A. Lakhtakia, and V. K. Varadan, editors, *Field Representations and Introduction to Scattering*, volume 1 of *Handbook on Acoustic, Electromagnetic and Elastic Wave Scattering*, chapter 2, pages 37–141. Elsevier Science Publishers, Amsterdam, 1991.

[31] A. B. Strong. *Fundamentals of composites manufacturing: materials, methods and applications*. Society of Manufacturing Engineers, 2008.

[32] J. G. Van Bladel. *Electromagnetic Fields*. IEEE Press, Piscataway, NJ, second edition, 2007.

[33] B. Widenberg. Advanced compact test range for both radome and antenna measurement. In *11th European Electromagnetic Structures Conference*, pages 183–186, Torino, Italy, 2005.

[34] A. D. Yaghjian. An overview of near-field antenna measurements. *IEEE Trans. Antennas Propagat.*, **34**(1), 30–45, January 1986.

Source reconstruction by far-field data for imaging of defects in frequency selective radomes

Kristin Persson, Mats Gustafsson, Gerhard Kristensson, and Björn Widenberg

Paper V

Based on: K. Persson, M. Gustafsson, G. Kristensson, and B. Widenberg. Source reconstruction by far-field data for imaging of defects in frequency selective radomes, Technical Report LUTEDX/(TEAT-7224), pp. 1–14, 2013, Department of Electrical and Information Technology, Lund University, Sweden. `http://www.eit.lth.se`

Published as: K. Persson, M. Gustafsson, G. Kristensson, and B. Widenberg. Source reconstruction by far-field data for imaging of defects in frequency selective radomes, *IEEE Antennas and Wireless Propagation Letters*, vol. 12, pp. 480–483, 2013.

Abstract

In this paper, an inverse source reconstruction method with great potential in radome diagnostics is presented. Defects, *e.g.*, seams in large radomes, and lattice dislocations in frequency selective surface (FSS) radomes, are inevitable, and their electrical effects demand analysis. Here, defects in a frequency selective radome are analyzed with a method based on an integral formulation. Several far-field measurement series, illuminating different parts of the radome wall at 9.35 GHz, are employed to determine the equivalent surface currents and image the disturbances on the radome surface.

1 Introduction and background

Radomes enclose antennas to protect them from *e.g.*, weather conditions. Ideally, the radome is expected to be electrically transparent [10]. However, tradeoffs are necessary to fulfill properties such as aerodynamics, robustness, lightweight, weather persistency *etc.*. One tradeoff is the existence of defects. Specifically, seams appear when lightning strike protection and rain caps are applied, or in space frame radomes assembled by several panels [10, 18]. Other disturbances are Pitot tubes and the attachment of the radome to the hull of an aircraft. In all these examples of defects, it is essential to diagnose their influences, since they degrade the electromagnetic performance of the radomes if not carefully attended.

In this paper, we investigate if source reconstruction can be employed to localize and image defects on a radome surface. Employing far-field measurements removes the need for probe compensation [22]. An artificial puck plate (APP) radome with dislocations in the lattice is investigated. An APP radome is a frequency selective surface (FSS) designed to transmit specific frequencies [15, 21]. It consists of a thick perforated conducting frame, where the apertures in the periodic lattice are filled with dielectric pucks. These dielectric pucks act as short waveguide sections [15]. Due to the double curvature of an FSS surface, gaps and disturbances in the lattice may cause deterioration of the radome performance.

Source reconstruction methods determine the equivalent surface currents close to the object of interest. These methods have been utilized for various diagnostics purposes [1, 5, 8, 9, 11–14, 16, 17]. The reconstructions are established by employing a surface integral representation often in combination with a surface integral equation. The geometry of the object on which the fields are reconstructed is arbitrary. However, the problem is ill-posed and needs regularization.

Initial diagnostics studies are reported in [12–14], which focus on non-destructive radome diagnostics. The equivalent surface currents are reconstructed on a body of revolution with the method of moments (MoM), and the problem is regularized with a singular value decomposition (SVD). Other research groups have employed slightly different combinations of surface integral representations and surface integral equations to diagnose objects. Especially, radiation contributions from leaky cables are analyzed in [16], antennas are diagnosed in [1, 8, 9, 11, 17], and equivalent currents on a base station antenna are studied in [5]. A more detailed background of source reconstruction methods is found in [14].

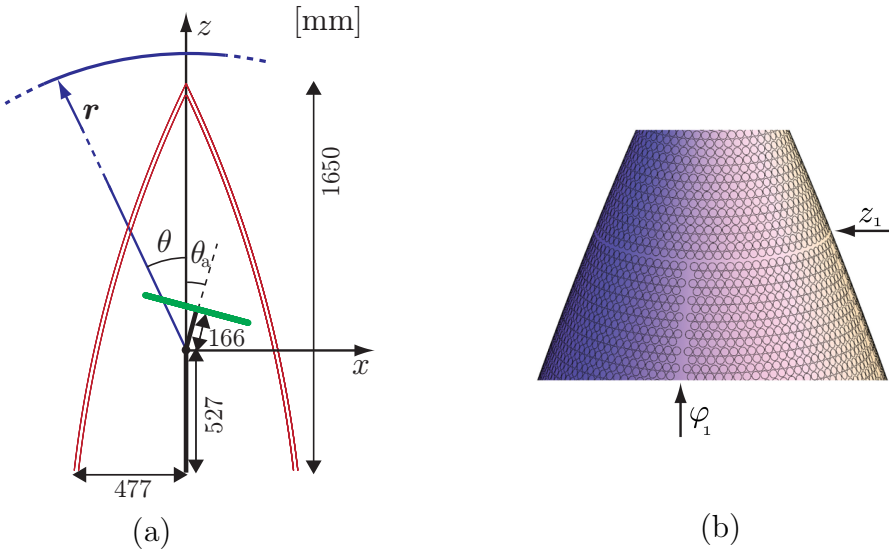

Figure 1: a) The geometry of the radome and the antenna. The center of rotation is located at the origin. b) Part of the radome visualizing the lattice structure and the defects at $\varphi_1 = -3°$ and $z_1 = 0.78\,\mathrm{m}$.

This paper revisits the reconstruction algorithm described in [12, 14] in order to investigate if defects on an FSS radome can be imaged. In Sec. 2 we describe the far-field measurements, the set-up, and the measurement series. A brief reproduction of the algorithm is given in Sec. 3. Images and analysis of the reconstructed fields revealing the defects are found in Sec. 4, whereas a discussion of future possibilities and conclusions are presented in Sec. 5.

2 Measurement data and set-up

The aim of this paper is to back propagate a measured far field using an equivalent surface currents approach to determine the tangential field components on the radome surface. The purpose is to investigate if defects on a frequency selective surface (FSS) lattice can be localized.

The geometry of the radome and the antenna set-up are illustrated in Fig. 1a. The height of the radome corresponds to 51.4 wavelengths at the investigated frequency, 9.35 GHz. The antenna is a standard 18 inch slot antenna operating in the frequency band $9.2 - 9.5\,\mathrm{GHz}$. The radiated field is linearly polarized with a dominating electric field component in the horizontal y-direction, see Fig. 1a. Several mounting angles, defined by the polar angle θ_a, and the azimuth angle φ_a, are employed to illuminate different parts of the radome surface, see Fig. 1a.

The radome is an FSS structure with a disturbed periodic lattice, depicted in Fig. 1b. A vertical line defect — a column of elements is missing — is located at $\varphi_1 = -3°$. The defect ends at $z_1 = 0.78\,\mathrm{m}$, where a horizontal line defect is located. The horizontal defect occurs due to a small vertical displacement of the elements. Owing to a large curvature of the radome, the horizontal defect also results in a

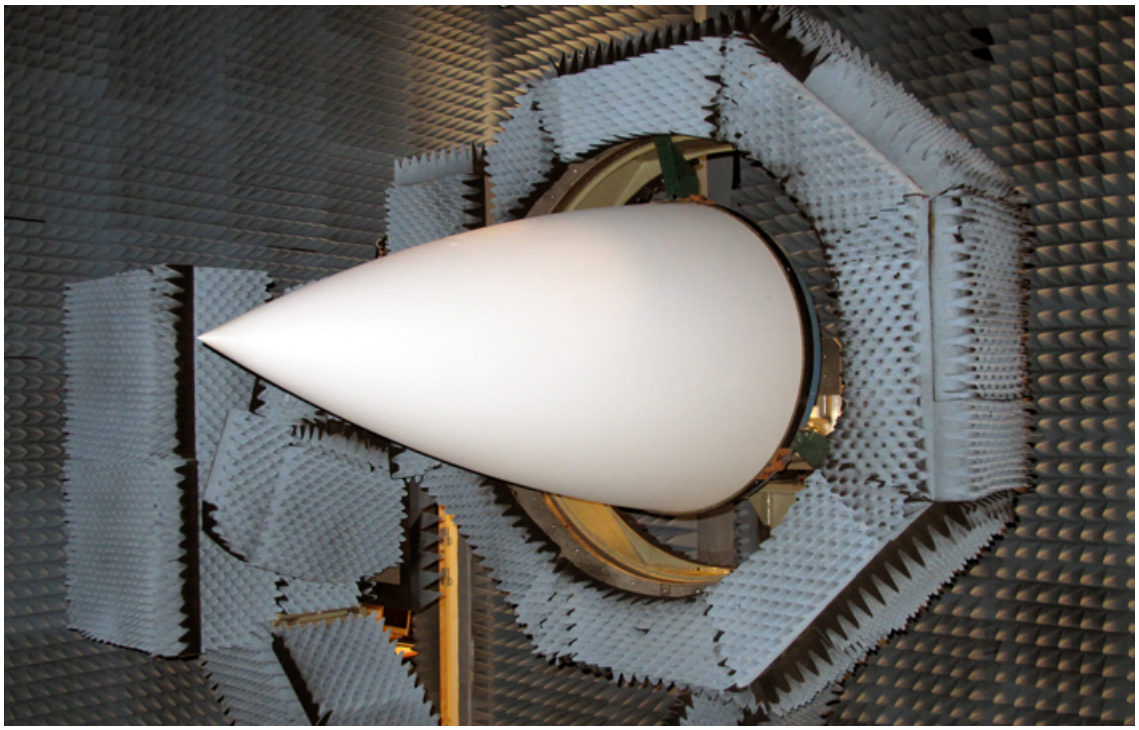

Figure 2: Photo of the radome in the compact test range.

small disturbance of the lattice in the azimuth direction. As a consequence, the vertical and horizontal defects are of different nature. Another horizontal defect is located at $z_0 = 0.38\,\mathrm{m}$, see Fig. 4a. The smaller curvature makes the disturbance of the lattice in the azimuth direction much smaller compared to the one at $z = z_1$.

Four different measurement series were performed, each with a different antenna orientation; $\{\theta_\mathrm{a} = 15°, \varphi_\mathrm{a} = 0°\}$, $\{\theta_\mathrm{a} = 12°, \varphi_\mathrm{a} = -20°\}$, $\{\theta_\mathrm{a} = 45°, \varphi_\mathrm{a} = 0°\}$, and $\{\theta_\mathrm{a} = 45°, \varphi_\mathrm{a} = -20°\}$. In the first two series, the antenna illuminates the area, where the vertical defect merges the horizontal defect at $z = z_1$, see Figs 1b and 4a. The illumination in the last two series highlights the lower cross, depicted in Fig. 4a. In this paper, we focus on the first two measurement series illuminating the top. The last two series are utilized as reference measurements to set the regularization parameter as described in [14]. Moreover, in the last series, a dielectric patch was attached to the radome surface, and the reconstruction of this patch was employed to verify the absolute position of the radome in the chamber. In each series illuminating the top, two different set-ups were measured for both polarizations. The antenna alone is referred to as configuration (0) whereas configuration (1) denotes the antenna together with the radome, also called the radome case. The configuration numbers are given as superscripts in the field notation in Sec. 4.

The far-field was measured at GKN Aerospace Applied Composites' compact test range in Linköping, Sweden, see Fig. 2 and [20]. The measurements were carried out over a spherical sector, described by the standard spherical coordinates, $\theta \in [0°, 120°]$ and $\varphi \in [0, 360°]$, see Fig. 1a for notation. The distance between two subsequent sample points was 1.5° in the azimuthal plane, and 0.75° in the polar plane, both

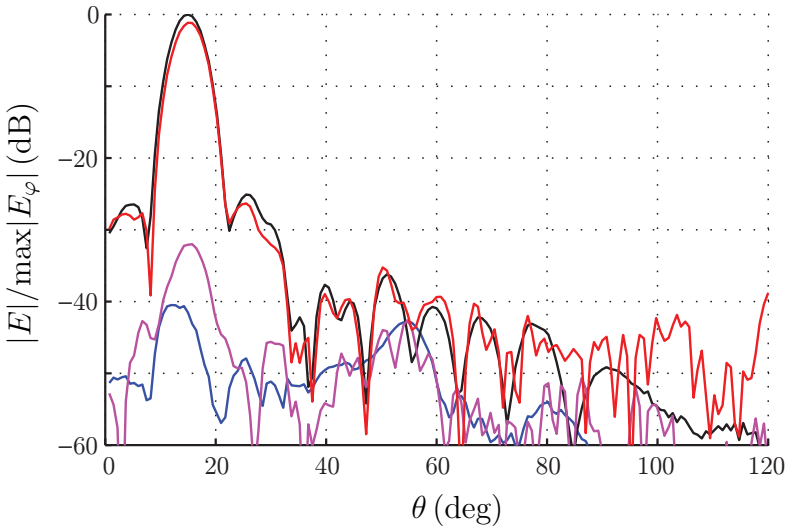

Figure 3: The measured far field through the main lobe when the antenna orientation is $\theta_a = 15°$ and $\varphi_a = 0°$. The top two lines correspond to the co-component, $E = E_\varphi$, where the black line describes the antenna case and the red one the radome case. The lower two lines correspond to the cross-component, $E = E_\theta$, where the blue line describes the antenna case and the purple one the radome case.

fulfilling the sample criteria [6, 22]. More details concerning the measurements and the chamber are found in [14, 20].

Both polarizations of the measured far field, with and without the radome, are given in Fig. 3, where the antenna orientation is $\theta_a = 15°$ and $\varphi_a = 0°$. The cross section in the polar plane, through the main lobe, $\varphi = 0$, is shown. The radome changes the main lobe of the co-polarization, E_φ, indicating transmission loss and beam deflection. The near side lobe levels are also slightly changed. Scattering effects, at large polar angles, are introduced by the radome and affect the far outside lobes in the co-polarization. The radome also changes the lobes of the cross-polarization. Bear in mind, that the antenna illuminates the top of the radome, *i.e.*, it is likely that multiple scattering inside the radome give rise to some of the changes. Moreover, it is not possible to determine the electrical influence of the defects from the unprocessed far-field data, *i.e.*, a reconstruction technique, to retrieve the fields on the radome surface, is necessary. Furthermore, the far fields show similar deviations as the ones in Fig. 3, when the antenna orientation is $\theta_a = 12°$ and $\varphi_a = 20°$.

3 Reconstruction algorithm

To investigate if a source reconstruction technique can be applied to image defects on a frequency selective surface (FSS) radome, a reconstruction algorithm is applied to relate the tangential electromagnetic fields on the radome surface to the measured far field described in Sec. 2. In this paper, we only give a short outline of the algorithm and some key implementation aspects, since the algorithm is thoroughly described in previous works, see [12, 14].

The electric surface integral equation (EFIE) [7]

$$\hat{\boldsymbol{n}}(\boldsymbol{r}) \times \Big\{ \mathcal{L}\left(\eta_0 \boldsymbol{J}\right)(\boldsymbol{r}) - \mathcal{K}\left(\boldsymbol{M}\right)(\boldsymbol{r}) \Big\} = \frac{1}{2}\, \boldsymbol{M}(\boldsymbol{r}) \tag{3.1}$$

where $\boldsymbol{r} \in S_{\text{radome}}$, and S_{radome} denotes the radome surface, smoothly closed at the bottom, is combined with the surface integral representation [4, 19]

$$\begin{bmatrix} \hat{\boldsymbol{\theta}}(\boldsymbol{r}) \\ \hat{\boldsymbol{\varphi}}(\boldsymbol{r}) \end{bmatrix} \cdot \Big\{ -\mathcal{L}\left(\eta_0 \boldsymbol{J}\right)(\boldsymbol{r}) + \mathcal{K}\left(\boldsymbol{M}\right)(\boldsymbol{r}) \Big\} = \begin{bmatrix} \hat{\boldsymbol{\theta}}(\boldsymbol{r}) \cdot \boldsymbol{E}(\boldsymbol{r}) \\ \hat{\boldsymbol{\varphi}}(\boldsymbol{r}) \cdot \boldsymbol{E}(\boldsymbol{r}) \end{bmatrix} \tag{3.2}$$

where $\boldsymbol{r}$ belongs to the set of measurement points, see Fig. 1a, and η_0 is the intrinsic wave impedance of free space. A combination of the integral representation (3.2) with a magnetic field integral equation (MFIE) does not change the results in Sec. 4 significantly. The far field is measured over a spherical sector, described by the two spherical orthogonal components, $\hat{\boldsymbol{\varphi}}$ (azimuth) and $\hat{\boldsymbol{\theta}}$ (polar), *cf.*, Sec. 2. The operators introduced in (3.1)–(3.2) are [7]

$$\mathcal{L}(\boldsymbol{X})(\boldsymbol{r}) = \mathrm{j}k \iint\limits_{S_{\text{radome}}} \Big\{ g(\boldsymbol{r}', \boldsymbol{r}) \boldsymbol{X}(\boldsymbol{r}') - \frac{1}{k^2}\, \nabla' g(\boldsymbol{r}', \boldsymbol{r}) \big[\nabla'_S \cdot \boldsymbol{X}(\boldsymbol{r}') \big] \Big\}\, \mathrm{d}S'$$

and

$$\mathcal{K}(\boldsymbol{X})(\boldsymbol{r}) = \iint\limits_{S_{\text{radome}}} \nabla' g(\boldsymbol{r}', \boldsymbol{r}) \times \boldsymbol{X}(\boldsymbol{r}')\, \mathrm{d}S'$$

where g is the scalar free space Green's function, k is the wave number, and $\nabla_S \cdot$ denotes the surface divergence [4]. Also, the equivalent surface currents on the radome surface are, $\boldsymbol{J} = \hat{\boldsymbol{n}} \times \boldsymbol{H}$ and $\boldsymbol{M} = -\hat{\boldsymbol{n}} \times \boldsymbol{E}$ [7]. The equivalent surface currents on the radome surface are decomposed into two tangential components along the horizontal, $\hat{\boldsymbol{\varphi}}$, and vertical, $\hat{\boldsymbol{v}}$, arc lengths coordinates, *i.e.*, $[\hat{\boldsymbol{\varphi}}, \hat{\boldsymbol{v}}, \hat{\boldsymbol{n}}]$ form a right-handed coordinate system. Throughout the paper we use the notations, $H_{\text{v}} = \boldsymbol{H} \cdot \hat{\boldsymbol{v}} = -J_{\varphi}$, $H_{\varphi} = \boldsymbol{H} \cdot \hat{\boldsymbol{\varphi}} = J_{\text{v}}$, $E_{\varphi} = \boldsymbol{E} \cdot \hat{\boldsymbol{\varphi}} = -M_{\text{v}}$, and $E_{\text{v}} = \boldsymbol{E} \cdot \hat{\boldsymbol{v}} = M_{\varphi}$ for the reconstructed tangential fields.

The set-up is axially symmetric, *i.e.*, a body of revolution MoM code and a Fourier expansion of the fields can be employed. Only components with Fourier index $m \in [-71, 71]$ are relevant to solve (3.1)–(3.2). The problem is regularized by a singular value decomposition (SVD), where the regularization parameter is set by the reference measurement series. The far-field radius, r in Fig. 1a, is set to 2200 m. Employing larger radii do not change the results significantly. More details, parameter choices of the MoM code, and discussions about the regularization parameter are found in [14].

4 Reconstruction results

Two measurement series are investigated at 9.35 GHz with the antenna orientations: $\{\theta_{\text{a}} = 15°, \varphi_{\text{a}} = 0°\}$, and $\{\theta_{\text{a}} = 12°, \varphi_{\text{a}} = -20°\}$, respectively, *cf.*, Fig. 1a. The

vertical lattice disturbance at $\varphi = \varphi_1$, and the horizontal one at $z = z_1$ are illuminated, *cf.*, Fig. 1b and Sec. 2. The magnetic field components, co-polarization H_v and cross-polarization H_φ, are depicted since they give clearer images of the defects, see also [14].

The calculated tangential fields are visualized in Fig. 4, where the antenna orientation is $\theta_\mathrm{a} = 15°$ and $\varphi_a = 0°$. In Figs 4ac, the field from the antenna is depicted on a surface shaped as the radome to show how the defects, marked as white lines, are illuminated. The z-axis in Fig. 4a, gives the positions of the horizontal defects, *i.e.*, $z_0 = 0.38\,\mathrm{m}$ and $z_1 = 0.78\,\mathrm{m}$, and the zooming area adapted throughout the paper, *i.e.*, $z_\mathrm{z} \geqslant 0.28\,\mathrm{m}$. The vertical defect and its top ending at z_1 appear in the field of the co-polarization on the radome, see Fig. 4b. The cross-polarized field reveals the horizontal defect at z_1, see Fig. 4d. The amplitude difference between the co- and cross-polarization, *i.e.*, $20\log|H_\mathrm{v}^{(0)}|_\mathrm{max} - 20\log|H_\varphi^{(0)}|_\mathrm{max}$, is 4.2 dB, where log denotes the 10-base logarithm and $|H_{\mathrm{v}/\varphi}^{(0)}|_\mathrm{max} = \max\limits_{\boldsymbol{r}\in S_\mathrm{radome}} |H_{\mathrm{v}/\varphi}^{(0)}(\boldsymbol{r})|$.

To verify that the defects really are imaged in Figs 4bd, another measurement series was performed, where the antenna orientation is $\theta_\mathrm{a} = 12°$ and $\varphi_a = -20°$. The influence of the radome in the main lobe is visualized in Figs 5–10. In Fig. 5, the field amplitudes are depicted. Even though the main lobe is rotated by $\Delta\theta = -3°$ and $\Delta\varphi = -20°$, the positions of the vertical defects (Figs 5ac), as well as the horizontal ones (Figs 5bd), are identical. The linear scale reveals that the defects block the field. The images of the cross-polarization, Figs 5bd, indicate an interference pattern caused by the defects, where the distance between two subsequent minima is approximately one wavelength.

The phase difference between the antenna and radome cases, the insertion phase delay (IPD), is an essential tool in diagnostics of dielectric radomes [3, 14]. Here, we investigate if defects in a frequency selective surface (FSS) lattice can be discovered or not. Fig. 6 visualizes the IPD for the two antenna orientations. Observe that the IPD is only determined modulus 2π, the phase difference $\angle H^{(0)} - \angle H^{(1)} = \frac{180}{\pi}\angle\{H_\mathrm{v}^{(0)}[H_\mathrm{v}^{(1)}]^*\}$ gives a positive phase shift due to the time convention $\mathrm{e}^{\mathrm{j}\omega t}$ used, and the star denotes the complex conjugate. The images of the vertical defect, corresponding to the two different antenna orientations, are consistent in Figs 6ac. Moreover, the position of the horizontal defect is stable in Figs 6bd. The phase reconstruction is not reliable in areas with low amplitudes. To suppress the noise in these areas, a mask is imposed in the figures, which only shows areas where the field from the antenna, $H_{\mathrm{v}/\varphi}^{(0)}$, is greater than a predefined value. Specifically, $20\log\{|H_\mathrm{v}^{(0)}|/|H_\mathrm{v}^{(0)}|_\mathrm{max}\} \geqslant -15\,\mathrm{dB}$ in Figs 6ac and $20\log\{|H_\varphi^{(0)}|/|H_\varphi^{(0)}|_\mathrm{max}\} \geqslant -10\,\mathrm{dB}$ in Figs 6bd, respectively, where $H_{\mathrm{v}/\varphi}^{(0)}$ are depicted in Figs 4ac.

A diffraction pattern is detected in both polarizations, which implies an IPD fluctuation in the main lobe. Due to rather large angles of incidence, *cf.*, Fig. 1a, the IPDs of the co- and cross-components deviate from each other [3]. In the main lobe, the cross-polarization, H_φ, has an average phase shift of 130° and the co-polarization, H_v, has an average phase shift of 160°. The vertical defect alters the IPD with an additional $20° - 30°$. As a consequence of the large phase shifts in the radome wall, the absolute difference $|H_{\mathrm{v}/\varphi}^{(1)} - H_{\mathrm{v}/\varphi}^{(0)}|$ becomes impertinent as a

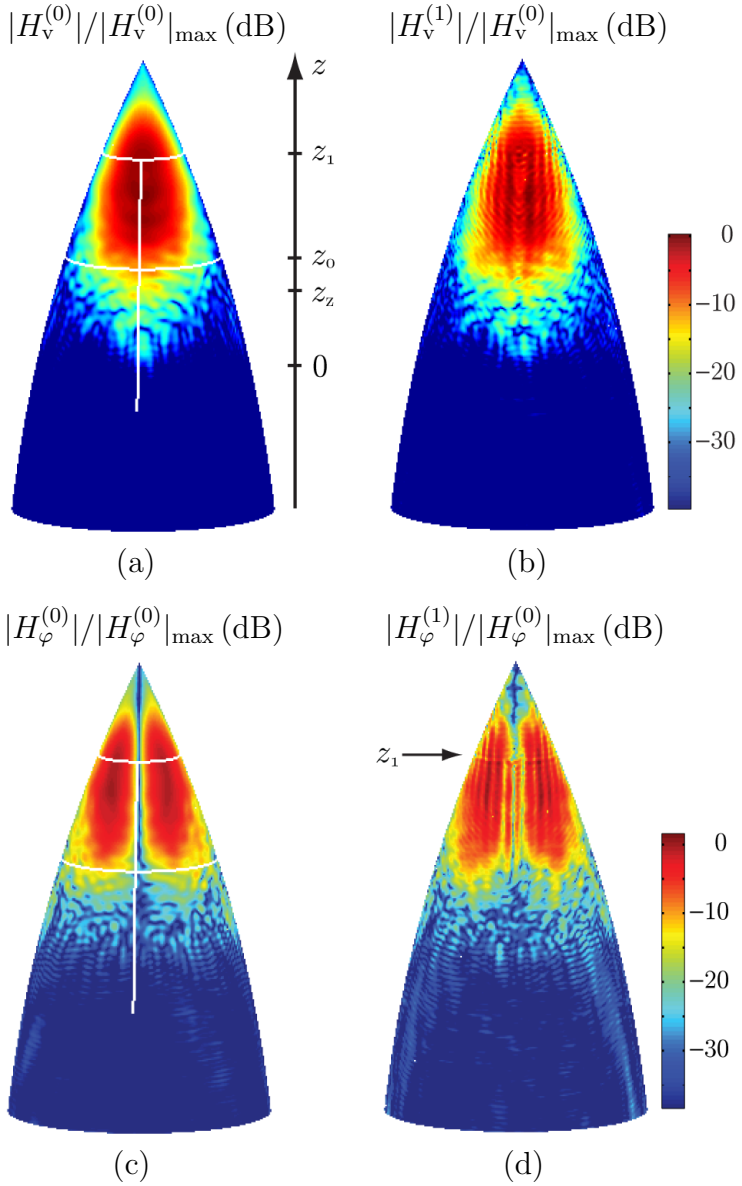

Figure 4: The H_{v}- and H_{φ}-components of the antenna alone, *i.e.*, conf. (0), are depicted in (a) and (c), respectively. The defects at z_0 and z_1, marked with white lines, are shown. Figs (b) and (d) show the H_{v}- and H_{φ}-components of the radome case, *i.e.*, conf. (1). The antenna orientation is $\theta_{\mathrm{a}} = 15°$ and $\varphi_a = 0°$.

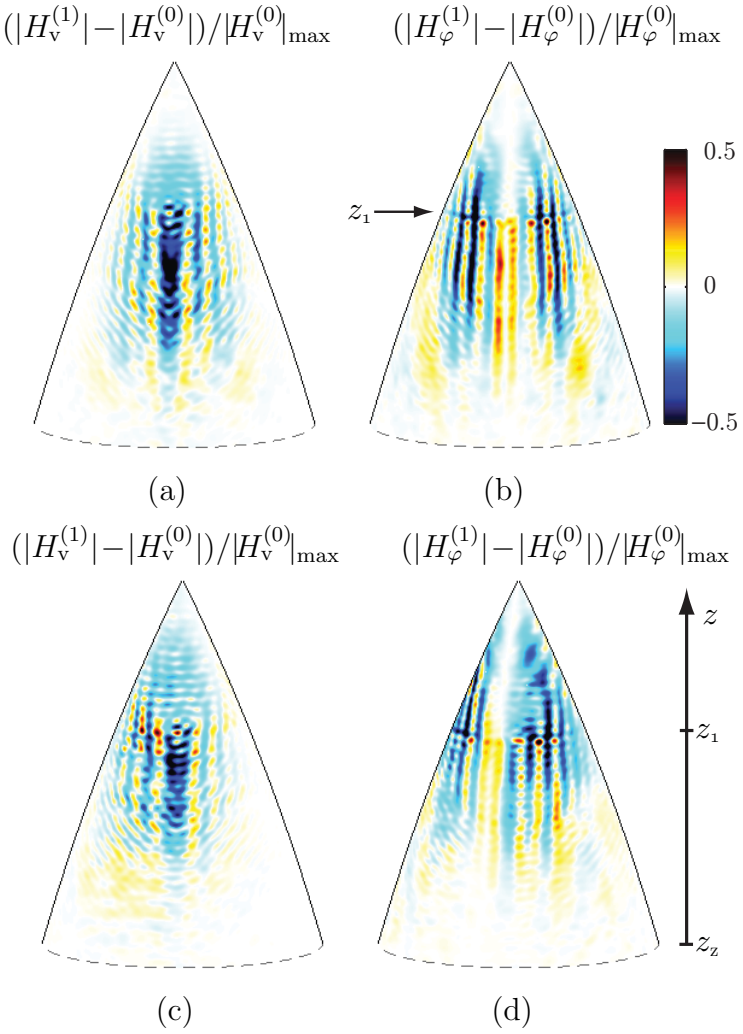

Figure 5: The reconstructed amplitude differences between the radome case and the antenna alone for $z \geqslant z_\mathrm{z}$. The top row (ab) corresponds to the antenna orientation $\theta_\mathrm{a} = 15°$ and $\varphi_a = 0°$, whereas the bottom row (cd) corresponds to $\theta_\mathrm{a} = 12°$ and $\varphi_a = -20°$. Figs (ac) show the H_v-component and (bd) the H_φ-component, respectively.

visualization tool to detect differences. The reason for this is that a phase shift close to π adds the fields instead of subtracting them.

As previously stated, the defects seem to block the incoming field, *cf.*, Fig. 5. This obstruction, which was detected in the magnetic field, is also visible in the power flow. The real part of Poynting's vector describes the time average power density that flows through the radome surface. In the right-handed coordinate system on the radome surface, $[\hat{\boldsymbol{\varphi}}, \hat{\boldsymbol{v}}, \hat{\boldsymbol{n}}]$, the normal component of Poynting's vector is [2]

$$P = \frac{1}{2}\,\mathrm{Re}\,\{\boldsymbol{E} \times \boldsymbol{H}^*\} \cdot \hat{\boldsymbol{n}} = \frac{1}{2}\,\mathrm{Re}\Big\{E_\varphi H_\mathrm{v}^* - E_\mathrm{v} H_\varphi^*\Big\} \equiv P_\mathrm{n}^\mathrm{co} + P_\mathrm{n}^\mathrm{cross} \qquad (4.1)$$

where the star denotes the complex conjugate. In Fig. 7a, the difference in the power flow between the radome and the antenna alone is depicted. This image illustrates the impact of the radome. Moreover, it filters out some of the interference pattern,

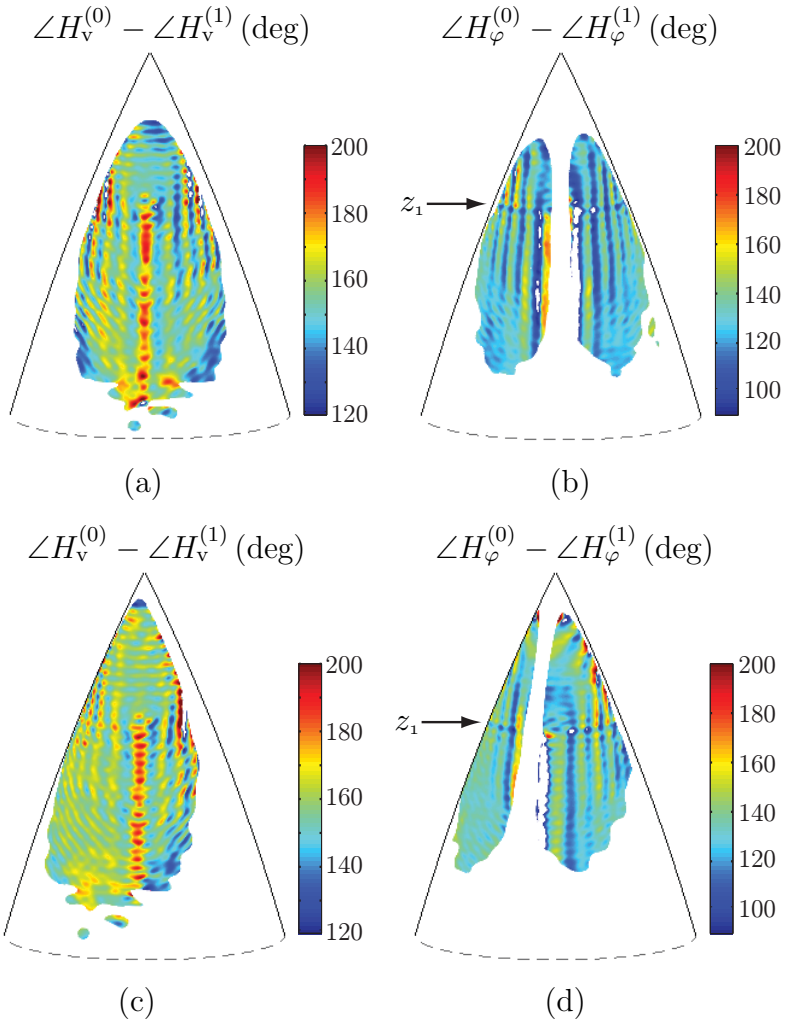

Figure 6: The insertion phase delay, IPD, $\angle H_{\mathrm{v}/\varphi}^{(0)} - \angle H_{\mathrm{v}/\varphi}^{(1)}$ for $z \geqslant z_{\mathrm{z}}$. The top row (ab) corresponds to the antenna orientation $\theta_{\mathrm{a}} = 15°$ and $\varphi_a = 0°$, whereas the bottom row (cd) corresponds to $\theta_{\mathrm{a}} = 12°$ and $\varphi_a = -20°$. Figs (ac) show the H_{v}-component in areas illuminated down to $-15\,\mathrm{dB}$, whereas (bd) visualize the H_{φ}-component in areas illuminated down to $-10\,\mathrm{dB}$.

and gives a clear view of the vertical defect. To reduce the influence of a non-even illumination, a pointwise normalization of the power flow, *i.e.*, a normalization with $P^{(0)}(\boldsymbol{r})$, is presented in Fig. 7b. A mask of $10\log\{P^{(0)}/P_{\max}^{(0)}\} \geqslant -15\,\mathrm{dB}$ is imposed, to avoid amplification of small fields in areas of low illumination. In this normalization, the horizontal defect starts to emerge. The reason why the horizontal defect is less visible in the power flow graphs is that this defect is perceived by the weaker cross-components, H_{φ} and E_{v}, and these components are suppressed by the stronger co-components in (4.1). To investigate if it is possible to get a more distinct view of the horizontal defect, the part of P with contributions from only the cross-components, *i.e.*, P^{cross} in (4.1), is mapped. This quantity is visualized in Fig. 8a, where the horizontal defect appears. An even more distinct image is obtained if the field difference, pointwise normalized with the incidence field, is depicted, see

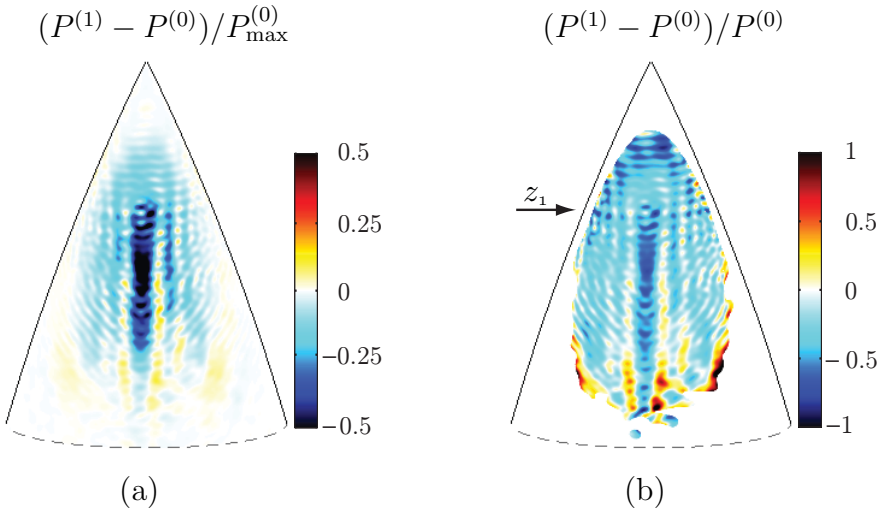

Figure 7: The time average power density through the radome for $z \geqslant z_z$. The antenna orientation is $\theta_a = 15°$ and $\varphi_a = 0°$. a) Normalized to the maximum value. b) Pointwise normalization in the illuminated areas down to −15 dB.

Fig. 8b. All values 15 dB below the maximum of $P^{(0)\text{cross}}$ are suppressed. Similar results are obtained when the antenna orientation is $\theta_a = 12°$ and $\varphi_a = -20°$, see Figs 9–10. The positions of the defects are consistent in Figs 7–10, whereas the rest of the field pattern changes slightly when the illumination is moved.

So far, the two measurement series illuminating the top have been investigated. The measurements focusing on the lower cross at $z = z_0$ are not presented in detail here, see Fig. 4a and a description in Sec. 2. However, some of the results are worth mentioning. For example, the horizontal defect at $z = z_0$ is hardly visible. The lattice is not as disturbed in the azimuth direction as it is higher up on the radome surface, and it is conjectured that this explains the weak effects, *cf.*, discussion in Sec. 2. Moreover, the diffraction pattern — clearly visible in Figs 5bd, where the top is investigated — does not appear in the cross-polarization for the lower illumination. Additionally, a flash lobe is present, revealing a vertical defect on the back of the radome wall.

5 Conclusions and discussions

Defects, giving rise to pattern distortions, are often an inevitable tradeoff in the design of radomes. To minimize the effects of these defects, diagnostics tools are valuable in the evaluation process and performance verification. In this paper, an inverse source reconstruction method is utilized to back propagate measured far-field to the surface of a frequency selective surface (FSS) radome with defects in its lattice, see Fig. 1b. Different illuminations of the radome wall help us to image these defects.

Both the amplitude and the phase differences are investigated. A vertical line defect, where a column of elements is missing, is clearly visible in the images of the magnetic co-polarization. Moreover, the visualizations of the magnetic cross-polarization reveal a horizontal line defect caused by an enlarged vertical distance

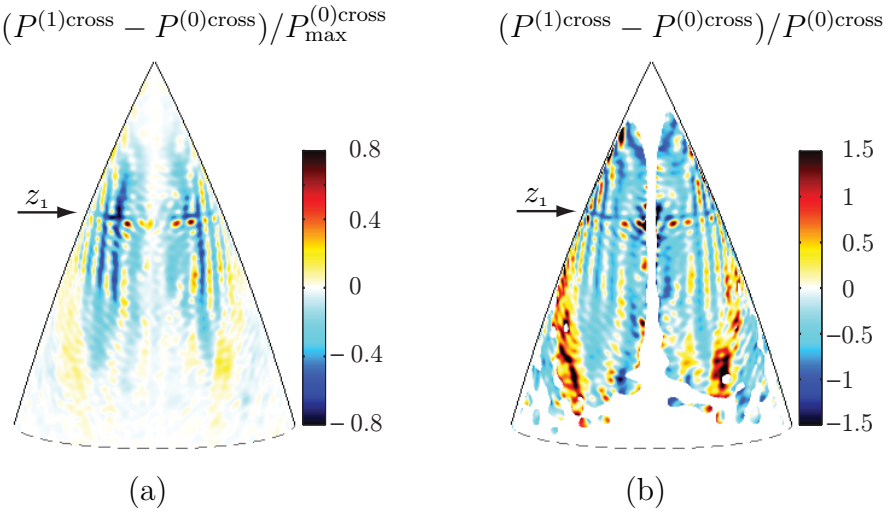

Figure 8: The cross-components of Poynting's vector for $z \geqslant z_z$. The antenna orientation is $\theta_a = 15°$ and $\varphi_a = 0°$. a) Normalized to the maximum value. b) Pointwise normalization and viewed in areas illuminated down to −15 dB.

between the center of the lattice elements. It is conjectured that the defects are blocking the field, and images of the power flow, *i.e.*, the real part of Poynting's vector, confirm this hypothesis.

Prior studies have shown the potential of the source reconstruction method as a useful tool in non-destructive dielectric radome diagnostics [12–14]. It is concluded that also defects on FSS radomes can be properly analyzed with the same technique. Further studies will address the question regarding the origin of the diffraction pattern together with a thorough analysis of the measurement data illuminating the lower cross. Another interesting aspect to be investigated is why the defects are visible in specific field components and not in others. Also, the diagnostics of other defects caused by *e.g.*, lightning strike protection or edges, are to be reported elsewhere.

Acknowledgement

The research reported in this paper is supported by a grant from FMV (Försvarets materielverk), which is gratefully acknowledged. GKN Aerospace Applied Composites' far-field range in Linköping, Sweden, has been made available for the measurements. Michael Andersson, GKN Aerospace Applied Composites, Ljungby, Sweden, is thankfully acknowledged for fruitful discussions on radome development, measurements, and manufacturing.

References

[1] Y. Alvarez, F. Las-Heras, and C. Garciain. The sources reconstruction method for antenna diagnostics and imaging applications. In A. Kishk, editor, *Solutions and Applications of Scattering, Propagation, Radiation and Emission of*

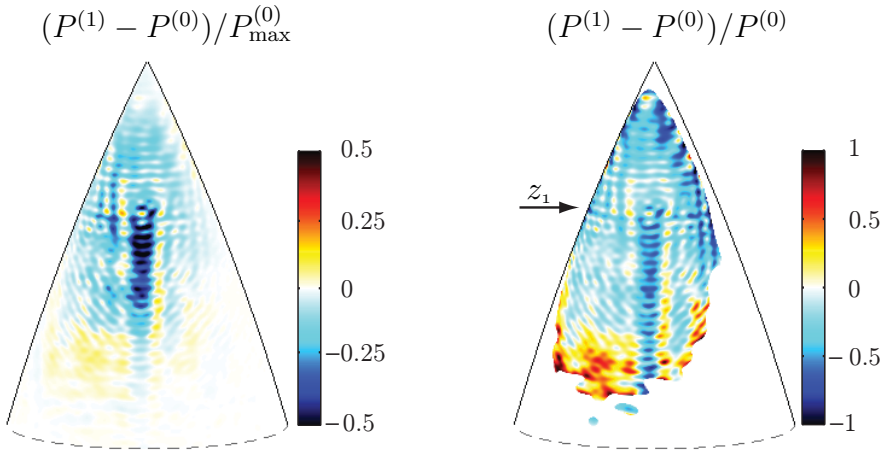

Figure 9: The time average power density through the radome for $z \geqslant z_z$. The antenna orientation is $\theta_a = 12°$ and $\varphi_a = -20°$. a) Normalized to the maximum value. b) Pointwise normalization and viewed in areas illuminated down to −15 dB.

Electromagnetic Waves. InTech, 2012.

[2] C. A. Balanis. *Antenna Theory*. John Wiley & Sons, New Jersey, third edition, 2005.

[3] D. G. Burks. Radomes. In J. L. Volakis, editor, *Antenna engineering handbook*. pub-mcgraw, fourth edition, 2007.

[4] D. Colton and R. Kress. *Integral Equation Methods in Scattering Theory*. John Wiley & Sons, New York, 1983.

[5] T. F. Eibert, E. Kaliyaperumal, and C. H. Schmidt. Inverse equivalent surface current method with hierarchical higher order basis functions, full probe correction and multilevel fast multipole acceleration. *Progress In Electromagnetics Research*, **106**, 377–394, 2010.

[6] J. E. Hansen, editor. *Spherical Near-Field Antenna Measurements*. Number 26 in IEE electromagnetic waves series. Peter Peregrinus Ltd., Stevenage, UK, 1988. ISBN: 0-86341-110-X.

[7] J. M. Jin. *Theory and computation of electromagnetic fields*. Wiley Online Library, 2010.

[8] E. Jörgensen, D. W. Hess, P. Meincke, O. Borries, C. Cappellin, and J. Fordham. Antenna diagnostics on planar arrays using a 3D source reconstruction technique and spherical near-field measurements. In *Antennas and Propagation (EUCAP), Proceedings of the 6th European Conference on*, pages 2547–2550. IEEE, 2012.

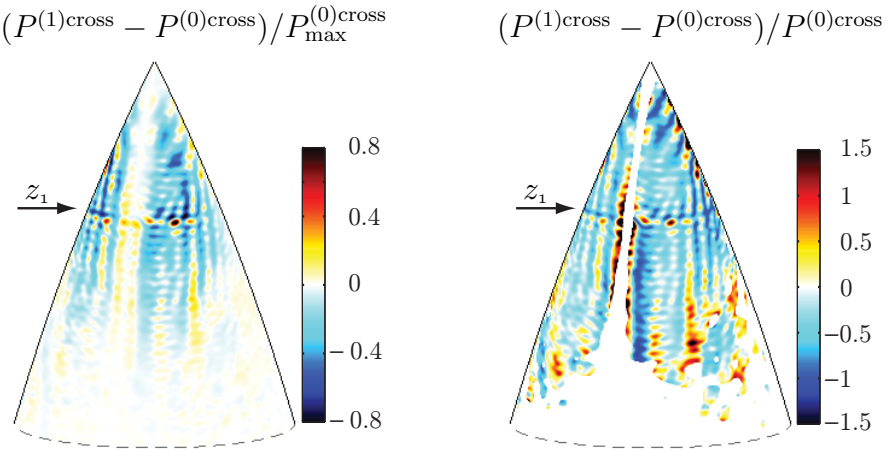

Figure 10: The cross-components of Poynting's vector for $z \geqslant z_z$. The antenna orientation is $\theta_a = 12°$ and $\varphi_a = -20°$. a) Normalized to the maximum value. b) Pointwise normalization and viewed in areas illuminated down to −15 dB.

[9] E. Jörgensen, P. Meincke, and C. Cappellin. Advanced processing of measured fields using field reconstruction techniques. In *Antennas and Propagation (EUCAP), Proceedings of the 5th European Conference on*, pages 3880–3884. IEEE, 2011.

[10] D. J. Kozakoff. *Analysis of Radome-Enclosed Antennas*. Artech House, Boston, London, 1997.

[11] Y. A. Lopez, F. Las-Heras Andres, M. R. Pino, and T. K. Sarkar. An improved super-resolution source reconstruction method. *Instrumentation and Measurement, IEEE Transactions on*, **58**(11), 3855–3866, 2009.

[12] K. Persson, M. Gustafsson, and G. Kristensson. Reconstruction and visualization of equivalent currents on a radome using an integral representation formulation. *Progress In Electromagnetics Research*, **20**, 65–90, 2010.

[13] K. Persson and M. Gustafsson. Reconstruction of equivalent currents using a near-field data transformation – with radome applications. *Progress in Electromagnetics Research*, **54**, 179–198, 2005.

[14] K. Persson, M. Gustafsson, G. Kristensson, and B. Widenberg. Radome diagnostics - source reconstruction of phase objects with an equivalent currents approach. Technical Report LUTEDX/(TEAT-7223)/1–22/(2012), Lund University, Department of Electrical and Information Technology, P.O. Box 118, S-221 00 Lund, Sweden, 2012. `http://www.eit.lth.se`.

[15] S. Poulsen. *Stealth radomes*. PhD thesis, Lund University, Department of Electroscience, Lund University, P.O. Box 118, S-221 00 Lund, Sweden, 2006.

[16] J. L. A. Quijano, L. Scialacqua, J. Zackrisson, L. J. Foged, M. Sabbadini, and G. Vecchi. Suppression of undesired radiated fields based on equivalent cur-

rents reconstruction from measured data. *Antennas and Wireless Propagation Letters, IEEE*, **10**, 314–317, 2011.

[17] J. L. A. Quijano and G. Vecchi. Field and source equivalence in source reconstruction on 3D surfaces. *Progress In Electromagnetics Research*, **103**, 67–100, 2010.

[18] R. Shavit, A. P. Smolski, E. Michielssen, and R. Mittra. Scattering analysis of high performance large sandwich radomes. *IEEE Transactions on Antennas and Propagation*, **40**(2), 126–133, 1992.

[19] S. Ström. Introduction to integral representations and integral equations for time-harmonic acoustic, electromagnetic and elastodynamic wave fields. In V. V. Varadan, A. Lakhtakia, and V. K. Varadan, editors, *Field Representations and Introduction to Scattering*, volume 1 of *Handbook on Acoustic, Electromagnetic and Elastic Wave Scattering*, chapter 2, pages 37–141. Elsevier Science Publishers, Amsterdam, 1991.

[20] B. Widenberg. Advanced compact test range for both radome and antenna measurement. In *11th European Electromagnetic Structures Conference*, pages 183–186, Torino, Italy, 2005.

[21] T. K. Wu, editor. *Frequency Selective Surface and Grid Array.* John Wiley & Sons, New York, 1995.

[22] A. D. Yaghjian. An overview of near-field antenna measurements. *IEEE Trans. Antennas Propagat.*, **34**(1), 30–45, January 1986.